

DIGITAL ACCESS TO SCHOLARSHIP AT HARVARD
DASH.HARVARD.EDU

HARVARD LIBRARY


Laser Cooling and Inelastic Collisions of the Polyatomic Radical SrOH

Citation

Kozyryev, Ivan. 2017. Laser Cooling and Inelastic Collisions of the Polyatomic Radical SrOH. Doctoral dissertation, Harvard University, Graduate School of Arts & Sciences.

Link

http://nrs.harvard.edu/urn-3:HUL.InstRepos:41140258

Terms of use

This article was downloaded from Harvard University's DASH repository, and is made available under the terms and conditions applicable to Other Posted Material (LAA), as set forth at

https://harvardwiki.atlassian.net/wiki/external/NGY5NDE4ZjgzNTc5NDQzMGIzZWZhMGFlOWI2M2EwYTg

Accessibility

https://accessibility.huit.harvard.edu/digital-accessibility-policy

Share Your Story

The Harvard community has made this article openly available.
Please share how this access benefits you. Submit a story

Laser Cooling and Inelastic Collisions of the Polyatomic Radical SrOH

A dissertation presented

by

Ivan Kozyryev

to

The Department of Physics

in partial fulfillment of the requirements

for the degree of

Doctor of Philosophy

in the subject of

Physics

Harvard University

Cambridge, Massachusetts

May 2017

©2017 Ivan Kozyryev

All rights reserved.

Dissertation advisor

John M. Doyle

Author

Ivan Kozyryev

Laser Cooling and Inelastic Collisions of the Polyatomic Radical SrOH

Abstract

Polyatomic molecules, while ubiquitous in nature, were generally perceived as too complicated and "unruly" for the majority of quantum physics experiments. However, recent theoretical analyses have pinpointed the multiple advantages of using complex molecules for diverse applications such as the creation of a universal quantum computer, quantum simulation of non-trivial many-body states, and tests of fundamental physical laws. Throughout my dissertation research I focused on extending experimental techniques from atomic physics to complex molecules. The goal of my work was to not only demonstrate new ways to control molecules, but also develop a novel experimental platform for quantum science – complex polyatomic molecules – and provide tools for physicists to conquer new frontiers in physics and chemistry.

The main theme of this thesis is the use of laser radiation to control internal and external degrees of freedom for the triatomic radical strontium monohydroxide (SrOH). The research achievements presented here can be primarily divided into the following areas: i) out-of-equilibrium studies of vibrationally inelastic collisions at cryogenic temperatures, ii) demonstration of the radiation pressure force and the direct laser cooling of polyatomic molecules, and iii) the development of concepts for laser cooling of molecules with six and more atoms. For the collisional studies, off-diagonal optical pumping was used to populate excited Sr-O stretching state and the ratio of elastic to vibrational quenching collisions was determined to be ~ 700. In the laser cooling work, using only laser light, the transverse temperature of the cryogenic buffer-gas beam of SrOH was reduced from 50 mK to below 1 mK, leading to an order of magnitude increase in phase space density of the molecular beam. Additionally, the prospects of using a coherent bichromatic force for optical

deceleration of polyatomics were analyzed and experimentally characterized with the transverse deflection of the SrOH beam. Our experimental results with SrOH and theoretical analysis of more complex strontium alkoxides not only open a wide range of future directions for laser manipulation and trapping of polyatomic molecules but also help overturn long held assumptions about the difficulties of performing "traditional" atomic physics experiments with complex molecules.

Contents

1 Introduction **1**

1.1 Motivation for cooling polyatomic molecules 3

1.1.1 Precision measurements 4

1.1.1.1 Searching for time variation of fundamental constants 4

1.1.1.2 Testing quantum statistics 6

1.1.1.3 Discrete symmetry violations 6

1.1.2 Quantum simulation and computation 7

1.1.3 Molecular collisions 10

1.1.4 State-selective chemical reactions 12

1.1.5 Controlled chemistry 12

1.1.6 Astrochemistry 13

1.2 Production of cold and ultracold polyatomic molecules 13

1.2.1 Supersonic beams 13

1.2.2 Helium nanodroplets 14

1.2.3 Buffer-gas cooling 15

1.2.4 Optoelectrical cooling 15

1.2.5 Towards laser cooling of polyatomics 16

1.3 Thesis overview 17

1.3.1 Laser manipulation of SrOH motion 17

1.3.2 Controlling internal quantum states for collisional studies 18

1.3.3 Laser cooling of complex polyatomics 19

2 Molecular Structure and Properties of Strontium Monohydroxide 20

2.1 Electronic structure of polyatomic molecules 21

2.1.1 Electronic levels of SrOH 24

2.2 Vibrational levels of linear polyatomic molecules 26

2.2.1 Bending vibrations in linear polyatomics 28

2.3 Breakdown of the Born-Oppenheimer approximation 29

2.4 Rotational energy levels of SrOH 31

2.4.1 Parity of energy levels 34

2.5 Creating a cycling transition for SrOH 35

2.6 Conclusions 39

3 Cryogenic Production and Dynamics of SrOH 40

3.1 Cryogenic buffer-gas cooling of SrOH 41

3.2 Results and discussion 43

3.2.1 SrOH-He diffusion cross section 43

3.2.2 Vibrational quenching cross sections 47

3.2.3 Rotational thermalization 50

3.2.4 Franck-Condon factor measurements 51

3.2.4.1 Off-diagonal Franck-Condon factor from molecular absorption data 52

3.2.4.2 Measurements of the off-diagonal Franck-Condon factor 53

3.2.5 Measurement of the dominant repumper frequency 56

3.3 Conclusions 58

4 Bright and Slow SrOH Cryogenic Buffer-gas Beam 60

4.1 Absorption spectroscopy 61

4.2 Eliminating SrOH-He in-beam collisions 63

4.3 Two CBGB regimes: very bright and reasonably slow vs very slow and reasonably bright . . . 68
4.4 Conclusions . . . 72

5 Photon Cycling and Radiation Pressure Force Deflection 73
5.1 Radiation pressure force in multilevel systems . . . 75
5.1.1 Radiative force on a two-level system . . . 75
5.2 Extension to a multilevel configuration . . . 77
5.3 Experimental configuration . . . 78
5.4 Photon cycling results . . . 80
5.5 Radiation pressure force deflection . . . 82
5.6 Conclusions . . . 85

6 Doppler and Sisyphus Laser Cooling 87
6.1 Doppler cooling in a multilevel system . . . 88
6.1.1 Optical molasses for a two-level atom in 1D . . . 88
6.1.2 Extension to multiple levels . . . 89
6.1.3 Limits of Doppler cooling . . . 90
6.2 Sub-Doppler laser cooling mechanisms . . . 91
6.2.1 Magnetically-assisted Sisyphus laser cooling . . . 92
6.2.2 Sisyphus cooling at high intensities . . . 93
6.2.3 Limits of sub-Doppler laser cooling . . . 96
6.3 Experimental configuration for laser cooling . . . 97
6.4 Spectroscopy of repumping transitions . . . 99
6.5 Scattering rate dependence on the remixing magnetic field . . . 101
6.6 Doppler cooling . . . 102
6.7 Sisyphus laser cooling . . . 103
6.8 Characterizing Sisyphus cooling . . . 110

6.9 Conclusions . . . 112

7 Coherent Bichromatic Force Deflection 115

7.1 Stimulated slowing for atoms . . . 118

7.2 Bichromatic force for molecules . . . 121

7.3 Experimental apparatus . . . 123

7.4 Bichromatic force deflection of SrOH . . . 125

7.5 Applications to SrOH slowing and cooling . . . 129

7.6 Conclusions . . . 131

8 Prospects of Magneto-Optical Trapping for SrOH 132

8.1 Magneto-optical trapping for atoms . . . 133

8.1.1 Type I MOT . . . 133

8.1.2 Type II MOT . . . 135

8.2 Magneto-optical trapping for diatomic molecules . . . 136

8.3 Chemical production of SrOH . . . 137

8.4 Slowing SrOH below MOT capture velocity . . . 138

8.5 SrOH Zeeman structure and MOT prospects . . . 141

8.6 Conclusions . . . 143

9 Towards Laser Cooling of Complex Polyatomics 144

9.1 Laser manipulation of quantum systems . . . 144

9.2 Photon cycling scheme . . . 147

9.2.1 Franck-Condon factors . . . 148

9.2.2 Forbidden loss channels . . . 154

9.2.3 Rotational structure . . . 155

9.3 Experimental Considerations . . . 156

9.4 Applications . . . 158

9.4.1 Ultracold hydrocarbons . . . 158

9.4.2 Laser-cooled chiral species . . . 159
9.4.3 Silicon-containing polyatomics . . . 159
9.4.4 Coherent slowing . . . 160
9.4.5 Optical loading of magnetic traps . . . 160
9.5 Conclusions . . . 161

A Selection Rules for Vibrational Angular Momentum **163**
A.1 Hamiltonian and eigenfunctions for the 2D harmonic oscillator . . . 163

B Calculation of Franck-Condon Factors for SrOH **169**
B.1 Calculation of Franck-Condon Factors for the Stretching Modes . . . 169
B.2 Calculation of Franck-Condon Factors for the Bending Modes . . . 172
B.3 Sharp and Rosenstock GF Matrix Approach . . . 174

C Intensity of Forbidden $\triangle l \neq 0$ Vibrational Decays **178**
C.1 Estimation for SrOH . . . 178
C.2 Comparison of SrOH, CaOH and BaOH . . . 181

Bibliography **181**

Citations to previously published work

Parts of this dissertation have been previously reported in the following papers.

- *Sisyphus laser cooling of a polyatomic molecule.* I. Kozyryev, L. Baum, K. Matsuda, B. L. Augenbraun, L. Anderegg, A. P. Sedlack, and J. M. Doyle. Phys. Rev. Lett. 118, 173201 (2017).

- *Proposal for laser cooling of complex polyatomic molecules*. I. Kozyryev, L. Baum, K. Matsuda, and J. M. Doyle. ChemPhysChem 17, 3641 (2016).

- *Radiation pressure force from optical cycling on a polyatomic molecule*. I. Kozyryev, L. Baum, K. Matsuda, B. Hemmerling, and J. M. Doyle. J. Phys. B: At. Mol. Opt. Phys. 49, 134002 (2016).

- *Collisional relaxation of vibrational states of SrOH with He at 2 K*. I. Kozyryev, L. Baum, K. Matsuda, P. Olson, B. Hemmerling, and J. M. Doyle. New J. Phys. 17, 045003 (2015).

Acknowledgments

First and foremost of all I would like to thank my thesis advisor Professor John Doyle. John's constant desire to learn something new about the workings of nature has been a tremendous inspiration to me throughout the graduate school. The passion with which he approaches both big picture ideas and small technical details helped drive our research in directions that are scientifically exciting despite all the technical challenges. John's willingness to take a big risk on a new project with high potential that seemed impossible at first is what allowed us to pursue laser cooling of polyatomic molecules in the first place. I could not have asked for a better advisor and mentor in graduate school than John and I am confident that scientific rigor and engineering mindset I learned from him will help me succeed in my future endeavors.

I'd also like to sincerely acknowledge encouragement and support I have received from Professors Kang-Kuen Ni and Eric Heller. I am extremely fortunate to have them as my thesis committee and would like to thank them for their constant interest in my research and various exciting discussions. Additionally, while not an official member of my thesis committee, Professor David DeMille of Yale has played a crucial role in my success in graduate school. Dave took me into his lab as a young undergraduate during my sophomore year without any previous laboratory experience and guided me though multiple challenges in becoming an experimental physicist. Throughout graduate school years, Dave continued to educate me about atomic physics and molecules for which I am immensely grateful.

The rapid progress and ultimate success of the experiments described in this thesis would not have been possible without tremendous contributions of other members of the Doyle group. Most importantly I'd like to acknowledge Louis Baum, who has helped me built the SrOH experiment from the ground up despite experimental and funding hurtles. Louis's innate intellectual drive and amazing technical competence with electronics and lasers has allowed us to move the experiment forward at a pace that I could not have previously imagined. His courageous approach to experimental challenges will definitely help him achieve great success in graduate school and beyond. With his unceasing positive attitude and support I could not have found a better lab partner and

friend than Louis in graduate school.

I'd also like to express huge gratitude to people who have helped me convert the idea I had into an actual scientific experiment. Kyle Matsuda, Ben Augenbraun, Loic Anderegg, Boerge Hemmerling, Alex Sedlack, Peter Olson and Yicheng Bao have all made important experimental contributions to results presented in this thesis. Garrett Drayna, who has played a significant role in designing and constructing "MOT9000" vacuum chamber, provided great suggestions for its operation and was always willing to answer our questions. When I first joined the Doyle group I had a great opportunity to learn multiple techniques in low temperature physics from Hsin-I Lu and Julia Piskorski; these skills served me well in the later stages of my research. Additionally, numerous scientific, political, and cultural discussions with Eunmi, Garrett, Zack, Aakash, Jacob, Elizabeth, Adam, Sandra, Dave, Nick, Colin, and other Doylies were both educational and fun.

Beyond Harvard and the Doyle group, I owe a lot of gratitude to Professors Tim Steimle from Arizona State University and Ed Eyler from University of Connecticut and their respective research groups. In addition to answering tons of questions about polyatomics throughout my dissertation research, Professor Steimle did the original high-resolution spectroscopy of SrOH that helped us get the experiment started and performed dispersed fluorescence measurements of the Franck-Condon factors that benchmarked our calculations. Professor Eyler and his student Leland Aldridge brought their unique expertise in coherent slowing techniques for molecules to our productive collaboration and without their theoretical guidance bichromatic deflection experiments with SrOH would not have been possible. Leland's extensive experience in the theory of polychromatic forces with molecules helped to propel the experiment forward and it was a huge honor to have Professor Eyler as a collaborator and colleague during this amazing project.

Many times my real experimental learning happened in the machine shop or electronics room and I was extremely fortunate to have Stan Cotreau, Steve Sansone, and Jim MacArthur educate me about various tricks and pitfalls in actually making something work. Our countless conversations made soldering and tapping holes actually enjoyable!

An important lesson that I learned at Harvard is that success of one's dissertation does not only

come from the quality of scientific results presented but also from staying on top of all the requirements and deadlines. I need to thank a lot to Lisa Cacciabaudo and Jacob Barandes for keeping me on track with all the graduation requirements throughout my time here. Harvard Physics has an outstanding group of people that enormously help grad students get their research completed and presented to the wider world. Almost every single day I have bugged such amazing people as Jan Ragusa, Carol Davis, Adam Ackerman, Paola Martinez, Silke Exner, Jean O'Connor, and others about grants, reimbursements, packages, documents, and forms and they always found time to help me out no matter how much time it took.

My parents, brother, and friends at Harvard and outside made sure to fill my graduate school life with ideas and projects disconnected from science and academia. They always helped me to keep the obstacles I faced in my studies and research in a broader perspective. Finally, but most importantly, I want to thank my amazing wife Ania, whose encouragement and support is the true secret of my success in graduate school. Though unwillingly, she became an expert on lasers, molasses and MOTs and can now definitely pass for an atomic physicist at any party. I could not have imaged a better partner than her with whom to navigate the challenges and successes of life!

To my family

Chapter 1

Introduction

Development of new experimental tools in order to fully understand and harness the complexity of individual quantum objects under fully controlled conditions has opened up new research opportunities in modern physics and chemistry. In particular, the study of cold molecules ($\sim 1\,\mathrm{K}$) and ultracold molecular quantum gases ($< 1\,\mathrm{mK}$) has led to a deeper understanding of subtle interactions within and between molecules, as well as a broad range of far-reaching applications [1]. Tiny "beakers" consisting of electric [2], magnetic [3] or optical traps [4] isolate molecules from ambient conditions and provide a new generation of chemical reaction vessels. One of the guiding goals of ultracold molecular research is the development of detailed understanding of inelastic collisions and chemical reactions at the level of a single quantum state [5–7]. The study of accurately controlled molecules in the gas phase promises to shed light on fundamental aspects of energy exchange in molecular interactions.

With the ultimate goal of achieving complete control over all degrees of freedom, the field of cold and ultracold molecules has been pursuing two directions: i) improving cooling techniques for simple species to reach lower temperatures and higher phase space density and ii) expanding research to new and more complex molecules offering broader scientific applications. However, despite the rapidly growing efforts to expand the variety of accessible ultracold molecules, the majority of ultracold molecular gases still consist of diatomic bialkalis. Such species are assembled

from atoms that are directly laser cooled to microkelvin temperatures [8]. So far, the elements of crucial importance in chemistry and astrophysics like hydrogen (H), carbon (C), nitrogen (N), and oxygen (O) are not susceptible to laser cooling and trapping, the workhorse technique of modern atomic physics.

In order to circumvent such limitations and expand the chemical diversity and complexity of ultracold molecular quantum gases and, therefore, quantum matter more generally, we embarked on a new course of research to create ultracold polyatomic molecules. The target molecule of this thesis was SrOH. As will be explained below, cooling and trapping of this species will also open the door to much more complex ones, heralding the beginning of the field of polyatomic quantum matter. SrOH provides a very convenient platform for ultracold quantum science with polyatomic molecules because of multiple "knobs" that can be tuned to achieve complete control over all degrees of freedom and the projected extendability of the molecule to related, much larger species. Both electric and magnetic fields can be efficiently used to engineer forces to bring the molecules to a halt inside electromagnetic "beakers". Very recently, accurate ab initio quantum scattering calculations were performed for SrOH colliding with Li inside a magnetic trap [9]. Favorable ratio of elastic to inelastic collisions suggests that sympathetic cooling of SrOH with Li and potentially other alkali atoms could be possible for reaching quantum degeneracy.

A single valence non-bonding electron on the strontium metal atom leads to alkali-metal-like optical properties, allowing for laser "juggling" of molecules between different internal rotational, vibrational, and electronic states with exquisite precision. While the electronic structure of SrOH favors laser manipulation, additional complexities arise from new vibrational modes absent in diatomics. Before laying out the detailed description of our experimental results with SrOH and proposed extensions to more complex polyatomic molecules, we first provide a brief background to put the project into a broader context of the currently vibrant field of cold and ultracold molecules. Additionally, we highlight the key areas where additional degrees of freedom offered by complex molecules will lead to scientific breakthroughs.

1.1 Motivation for cooling polyatomic molecules

The scientific drive to work with polyatomic molecules originates from their complexity and diversity. Physicists are interested in working with molecules that have three and more atoms because they have more rotational and vibrational degrees of freedom compared to diatomics. While diatomic molecules have one axis of rotation and one vibrational mode, a general non-linear polyatomic molecule with N atoms has $3N-6$ vibrational modes and up to three different moments of inertia. Additionally, bending vibrations with angular momenta, as well as classically forbidden motions like tunneling inversion and hindered internal rotations, exist in polyatomic spectra that have no analogs for diatomic molecules. Consequently, as the number of possible transitions between different energy levels is significantly increased compared to diatomics, the spectra become quite complex from the overlap of many lines and even different bands [10]. Therefore, cooling polyatomic molecules becomes crucial for resolving and understanding finer details of the molecular spectra. Low translational temperature leads to reduction in Doppler broadening and cooling of the internal rotations and vibrations leads to enhanced signal in low rovibrational lines as well as removal of the band overlap. Thus, in order to fully utilize the complexity provided by the polyatomic molecules scientists need to work with cold samples. A natural question to bring up is why extra internal degrees of freedom have any consequence at low temperatures when polyatomic molecules populate a single ground rovibrational level with no excited rotational and vibrational quanta. The idea is that once the molecules are cooled to very low temperatures, one can excite all of them (or a fraction) to a particular rotational and vibrational quantum state using microwave, infrared or laser light for future studies. Thus, once the molecules are cooled to very low temperatures you can very precisely and efficiently transfer them between different states at will in order to study interesting applications.

1.1.1 Precision measurements

Polyatomic molecules provide new opportunities for performing precision spectroscopy in order to test the standard model of particle physics (SM) as well as discover new physical phenomena beyond the scope of SM description (e.g. SUSY, Lorentz invariance violation). Since there are excellent reviews [1, 11, 12] of the subject aimed at fundamental physics tests with molecules, we provide only a brief overview here.

1.1.1.1 Searching for time variation of fundamental constants

Some transitions in polyatomic molecules that are not present in diatomics or atoms are very sensitive to time variation of fundamental constants as proposed in certain beyond SM theories. By either performing precise spectroscopy of polyatomic molecules in the laboratory or observational measurements from sources in outer space, we can test such predictions. The value of the fine-structure constant $\alpha \approx 1/137$ and the electron-to-proton mass ratio[1] $\beta \equiv m_e/m_p \approx 1/1836$ lead to stable protons, the formation of a large number of heavy elements, complex molecules based on carbon chemistry, and, ultimately, development of life on Earth [13]. Motivated by the desire to understand this "fine tuning", some theories predict either spatial or temporal variation of fundamental constants in the Universe [14]. The electronic transitions, including spin-orbit interactions, are sensitive to α while vibrational, rotational, and tunneling modes in polyatomic molecules are sensitive to β [13]. For example, the energy scales for electronic, vibrational and rotational intervals in molecular spectra are approximately [12]

$$E_{\mathrm{el}} : E_{\mathrm{vib}} : E_{\mathrm{rot}} \sim 1 : \sqrt{\beta} : \beta. \tag{1.1.1}$$

A number of grand unification theories predict that

$$\frac{\triangle\beta}{\beta} = R\frac{\triangle\alpha}{\alpha} \tag{1.1.2}$$

[1] Here we use β rather then commonly used μ in order to avoid confusion with reduced mass.

with the proportionality constant $R \gg 1$, thus making a β variation search more sensitive to new physics [13]. For spectroscopic measurements, the sensitivity of a particular experiment to temporal variation of β is given by

$$\left(\frac{\partial\beta}{\partial t}\right)/\beta = \left(\frac{\partial\nu}{\nu}\right)/\left(K_\beta \triangle t\right) \tag{1.1.3}$$

where K_μ is the inherent sensitivity of the probed transition to β variation, $\triangle t$ is the studied time interval, and $\partial\nu/\nu$ is the fractional frequency precision. From the dependence of the sensitivity coefficient on molecular parameters [13]

$$K_\beta = \frac{\beta}{E_e - E_g}\left(\frac{dE_e}{d\beta} - \frac{dE_g}{d\beta}\right) \tag{1.1.4}$$

one can observe that near degenerate transitions with $\triangle E \approx 0$ will lead to significantly enhanced K_β. Complex polyatomic molecules represent a fertile ground for hunting for β variation with time because near-degeneracies in their spectra for levels possessing different $dE/d\beta$ occur as a rule. For a comprehensive list of molecules and respective transitions sensitive to α and β variation please refer to Refs. [13, 15]. Particularly, spectroscopy of molecules between states associated with such motions as hindered internal rotation and tunneling inversion, which have no analogs in diatomics, lead to orders-of-magnitude enhanced sensitivity to time variation of electron-to-proton mass ratio and thus would allow for more precise tests of such new effects in physics. Spectroscopy of the vibration-rotation transitions in a supersonic beam of SF_6 were used to constrain the time variation of β to $\sim 10^{-13}\,\mathrm{yr}^{-1}$ level [16] and comparison of the torsion-rotation transitions in methanol from both astronomical and laboratory measurements led to $\triangle\beta/\beta$ limit at the 10^{-7} level with the look-back time of 7 billion years [17]. The use of cold molecular beams or dense trapped samples to perform precision molecular spectroscopy in combination with dedicated astronomical observations will lead to significant improvements in this research field [18].

1.1.1.2 Testing quantum statistics

Testing violations of the Pauli principle and the indistinguishability of identical particles is another area of fundamental physics where spectroscopy of polyatomic molecules can make a fruitful contribution. While there are some theoretical proposals for small violations of Fermi or Bose statistics [19], as of now, there appears to be a limited motivation for its existence from the theoretical side. Spectroscopy of molecules with two or more identical nuclei can place limits on the degree of quantum statistics violations. If P_{12} is an operator which exchanges indistinguishable identical nuclei, then the Pauli principle requires [20]

$$P_{12}\psi_{\text{tot}} = \pm\psi_{\text{tot}} \tag{1.1.5}$$

where "$+$" sign is for bosons ($I = 0, 1, 2, \ldots$) and "$-$" sign is for fermions ($I = \frac{1}{2}, \frac{3}{2}, \frac{5}{2}, \ldots$). Since $\psi_{\text{tot}} = \psi_{\text{space}}\psi_{\text{spin}}$, the energy levels are labeled as symmetric or antisymmetric depending of the effect of the P_{12} operator [20]

$$P_{12}\psi_{\text{space}} = \pm\psi_{\text{space}}. \tag{1.1.6}$$

Thus, for CO_2 molecule with $I = 0$, only symmetric ψ_{space} are present, leading to the absence of odd J lines. Spectroscopy of $^{12}C^{16}O_2$ was used to place a stringent limit on Bose statistics violations for two ^{16}O nuclei [21]. Two identical particles can be either in a symmetric or antisymmetric state. However, larger polyatomic molecules will be necessary for testing symmetrization postulate for three or more identical nuclei in order to place limits on finding them in a state that is neither symmetric nor antisymmetric [22]. Performing precision rovibrational spectroscopy on polyatomic molecules like SO_3 using the current state-of-the-art techniques could allow tests of symmetrization postulate for three boson at the 10^{-12} level previously achieved with CO_2 [21].

1.1.1.3 Discrete symmetry violations

Discrete symmetries like parity and time reversal and their violations play an important part in the fundamental processes of nature. Molecular spectroscopy plays a complementary role to high en-

ergy searches at the Large Hadron Collider (LHC) and could potentially provide information about the fundamental particles beyond the LHC reach [11]. For example, polar diatomic molecules are currently used to precisely test parity violation in electroweak interactions within the nucleus [23] and measure the permanent electric dipole moment of the electron [24]. A recent result from the Harvard-Yale ACME collaboration has constrained new particles at the TeV energy scale [24]. While diatomic molecules have contributed a lot to this field in the past, there are significant challenges for moving forward. For example, in the parity-violating experiments with molecules, magnetic fields as large as few Tesla are required to bring opposite parity rotational levels to degeneracy in order to enhance the signal from weak interactions [11]. In the electron electric dipole moment (EDM) search experiments, the required states that can be easily polarized and have small magnetic moment for systematic suppression are frequently metastable (like in ThO) and photon cycling and laser cooling is prevented by complex energy level structures or technically challenging wavelengths. While polyatomic molecules could potentially aid in solving some of these challenges, more careful research is necessary in order to identify suitable molecules and states. A recent theoretical paper points out the suitability of RaOH, which could potentially be laser cooled, for parity violating experiments [25] and hopefully more research in this avenue will be prompted by our results. For example, linear polyatomic molecules like SrOH in long-lived excited bending vibrational states as well as symmetric top molecules like $SrOCH_3$, which can be easily polarized with small laboratory fields, could potentially enable future sensitivity enhancements in the EDM experiments. One area where polyatomic molecules with four or more atoms are required is searching for parity violating energy differences between different enanteomers of chiral molecules [26]. Here, current state-of-the-art experiments are moving towards using cold molecular samples in order to perform high resolution spectroscopy required [27, 28].

1.1.2 Quantum simulation and computation

While initial proposals for using polar molecules for quantum computation have all studied closed-shell diatomic molecules [29], extensive recent theoretical work points to multiple advantages of

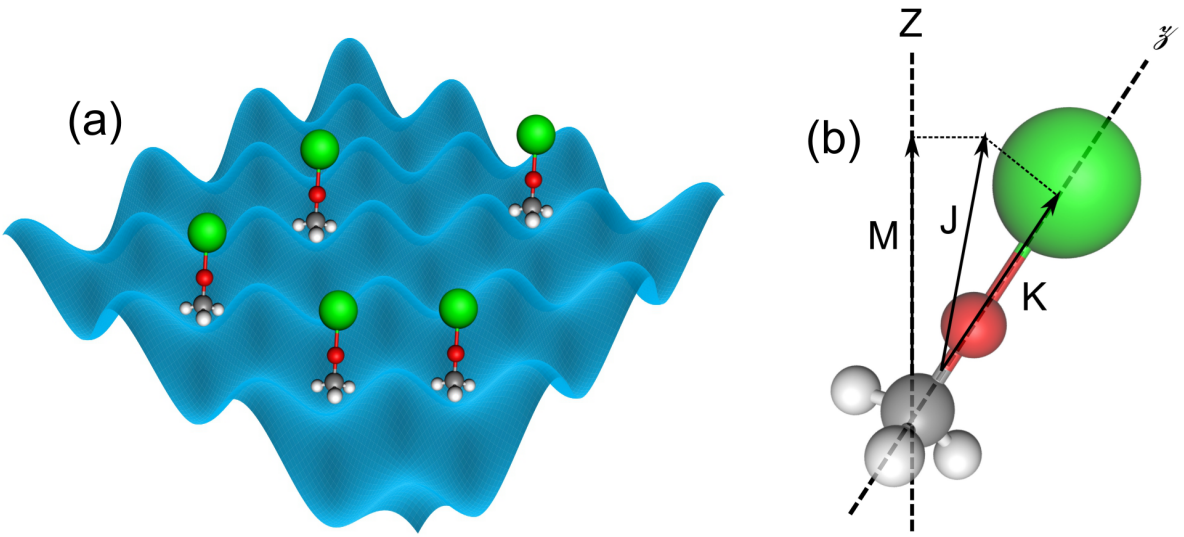


Figure 1.1.1: (a) Schematic representation of polyatomic symmetric top molecules loaded into optical lattices. Electric field applied in the vertical direction can be employed to polarize the molecules in order to perform quantum simulation or computation protocols. (b) Projections of total angular momentum J onto the molecular symmetry axis z and space-fixed quantization axis Z. Notice that unlike in diatomic or linear molecules, the rotational angular momentum J is not necessarily perpendicular to the molecular symmetry axis, leading to an additional quantum number K.

using polar symmetric top molecules (STMs) instead [30]. Relevant quantum numbers for STMs and slightly asymmetric rotors are shown in Fig. 1.1.1(b). Unlike for diatomic molecules, the effective electric dipole moment for a precessing STM in states $K, M_J \neq 0$ is independent of the electric field strength. The presence of first-order Stark effect removes the requirement for large electric fields and makes resolution of small energy shifts arising from dipole-dipole interaction during quantum logic gate operations easier. Additionally, the presence of states $|J,K,M\rangle = |1,1,1\rangle$ and $|1,1,-1\rangle$ with equal in magnitude but opposite in sign electric dipole moments enables the use of radiofrequency NMR techniques for quantum information processing. Finally, the dipole-dipole interaction can be easily turned off by transferring to states with $M_J = 0$. All of these properties make STMs well suited for rapid quantum gates operations. Moreover, $SrOCH_3$, which will later be discussed in this thesis, has an additional advantage of strong optically accessible electronic transitions for internal state manipulation and rapid state-selective readout.

There are theoretical proposals [31–33] for using a single complex macromolecule with many

vibrational modes to perform quantum computations. Each of the vibrational modes can be a separate quantum bit, and since a polyatomic molecule with N atoms contains $3N-6$ different vibrational modes, it represents an ensemble of $3N-6$ qubits. The scaling is favorable because the number of qubits grows as $3N$ vs N for NMR quantum computation or ion trapping experiments as the number of atoms increases [31]. The quantum logic gates would be realized with the shaped femtosecond laser pulses for fast implementation of quantum gates, but the experimental feasibility of these proposals and complexity comparison to other types of promising quantum computing platforms has not yet been performed. However, some experimental progress in this direction has been made and rapid classical Fourier transform has been implemented with vibrations of iodine diatomics in a supersonic beam [34].

While there are many theoretical proposals where the internal structure of the molecule does not play a significant role and they are treated as structureless dipoles [35–37], the experimental complexity of realizing specific condensed matter models can depend on the molecular internal structure. The long-range ($1/r^3$ dependence) and anisotropic (θ dependence) dipole-dipole interactions between two STMs in an electric field described by the expression[2]

$$V_{dd}(\vec{r}) = \frac{C_{dd}}{4\pi}\frac{1-3\cos^2\theta}{r^3} \tag{1.1.7}$$

is of significant interest to quantum many-body physics [38]. Since the interaction between electric dipoles is more than a thousand times stronger than for magnetic dipoles on typical atomic scales, the use of STMs like $SrOCH_3$ to simulate quantum magnetism would provide access to new physics in strongly correlated regimes on shorter time scales [39]. Direct correspondence exists between quantum magnets and STMs in $K, M_J \neq 0$ states because of the linear Stark shifts in such levels and thus enabling access to arbitrary large integer spin physics [39]. Recent theoretical work has shown that STMs can be used to simulate highly tunable and unconventional models

[2]Here we assume that the dipoles are polarized in the same direction with respect to a laboratory quantization axis $\hat{z}$, their separation vector is $\vec{r}$ and θ is the angle between the dipole moments and relative position vector. The interaction coefficient C_{dd} for two electric dipoles is approximately $1/\alpha^2$ times stronger compared to interacting magnetic dipoles under typical experimental conditions [38].

of quantum magnetic phenomena [40]. In order to experimentally realize such applications, trapping of polyatomic molecules in optical lattices will be highly desirable as shown in Fig. 1.1.1(a). While efficient lattice filling with atoms[3] is required in order to achieve strong on-site interactions to realize interesting Hamiltonians [41], the strength of electric dipole-dipole interaction with polar molecules removes strict requirements on filling efficiency as has been already demonstrated with diatomic bialkalis [42].

1.1.3 Molecular collisions

With only few exceptions [43], cooling of atomic gases into quantum degeneracy depends on atomic collisions that allow efficient thermalization without significant inelastic and chemical losses. Similarly, detailed understanding of bimolecular collisions for evaporative cooling or atom-molecule collisions for sympathetic cooling might be crucial for reaching Bose-Einstein condensates and degenerate Fermi gases with diatomic and polyatomic gases using techniques of direct cooling [4]. Additionally, accurate measurements of atom-molecule collisions play an important role in guiding theoretical calculations and development of intuitive understanding of how collisional processes occur in the non-classical regime. The use of electromagnetic fields to control the rates of inelastic processes in molecule-molecule collisions has been theoretically investigated [45–47] with experimental progress lagging behind. However, with the exception of a few outstanding papers [9, 48], the focus has been on diatomic molecules thus far because of the computational challenge of accurate scattering calculations as well as lack of experimental progress. Lifetimes of collision complexes for large molecules during cryogenic buffer-gas cooling have been explored theoretically with with both classical trajectories [49] and density-of-states approach [50] and indicate non-sticking of helium buffer-gas to hydrocarbons in the experimentally interesting regimes. These conclusions have also received experimental corroboration based on buffer-gas cooling of trans-Stilbene and Nile Red [51]. Additionally, direct observation of conformational relaxation of

[3]Highly magnetic atoms with strong dipolar interactions like Er, Cr, and Dy might be an exception here [38].

[4]Diatomic molecules directly associated from ultracold quantum gases can have initial temperatures near quantum degeneracy [44].

1,2-propanediol in cryogenic collisions with helium allowed accurate measurements of conformational relaxation cross sections informing the understanding of relevant potential energy surfaces [52]. However, all of these experimental studies have been in the regime around 10 K and extending the reach to < 1 Kcould lead to discovery of new phenomena and interesting dynamics.

For chemists, the appeal of the polyatomic molecules comes from the diversity of their constituents and structures. Motivated by the desire to understand molecular interactions and chemical reactivity, chemists embrace complexity of polyatomic molecules in order to study fundamentally interesting reactions as well as synthesize applicable compounds for drug discovery and materials. In this instance, the advantages of cooling molecular gases to cryogenic temperatures for chemical explorations are not out right obvious. Usually, chemical reactions are activated by thermal fluctuations and, accordingly, the classical reaction constants are governed by the Arrhenius' law [53]

$$k(T) \propto \exp\left(-\frac{E_A}{k_B T}\right) \tag{1.1.8}$$

with the activation energy E_A. Since as $T \to 0$, one might expect that reaction rates will drop to zero in the cold or ultracold dilute sample of atoms or molecules. However, at very low temperatures quantum mechanical effects start to dominate and such non-classical phenomena as tunneling and entanglement play crucial roles.

For example, by cooling $SrOCH_3$ from 1 K to 1 μK the thermal de Broglie wavelength of the molecules will grow from 0.2 nm to 200 nm, which is significantly larger than the classical size of $SrOCH_3$ (~ 0.5 nm). Therefore, we expect to observe significant deviation from the chemical intuition arising from studies involving high temperature collisions. While there are previous successful demonstrations of seminal studies of chemical reactions at ultracold temperatures [54, 55] they involve diatomic bialkalis only. Additionally, by selectively preparing and reading out only a single quantum state of trapped molecules we could probe inelastic collisions and chemical reactions out of thermal equilibrium for a complex symmetric top molecule. Performing studies in the regime beyond the reach of modern state-of-the-art accurate ab initio quantum scattering calculations would drive further theoretical progress in the field.

1.1.4 State-selective chemical reactions

One of the main reasons for cooling reactants beforehand is the motivation to study chemical processes out of thermal equilibrium in a state-to-state enabled control when both the initial quantum states of the incoming reactants are known as well as the final distribution of the products can be characterized. For example, in order to prepare molecules in a single rovibrational level, cooling to 1 K could be sufficient like demonstrated with CaH and Li chemical studies in a buffer-gas cell at 1 K [56] since rotational splitting for CaH is around 12 K. However, in order to prepare molecules in a particular hyperfine state or a single partial wave regime, cooling to μK temperatures might be necessary [55]. In order to benchmark and test ab initio quantum chemistry calculations, it is also necessary to determine the final states of the reaction products which is challenging because resulting molecules can end up in multiple excited rotational and vibrational levels, leading to small signals in a particular quantum state.

1.1.5 Controlled chemistry

Low temperatures also allow precise control of the chemical reaction pathway using electric, magnetic or optical fields. Laboratory electromagnetic fields allow shifting molecular energy levels by a few Kelvin and thus can be used to modify gas-phase molecular dynamics for temperatures $\lesssim 1\,\mathrm{K}$ [5]. Tuning of bimolecular chemical reactions using electric fields has been proposed [57] and spin suppression of chemical reactions has been seen for the N-NH pair from the experimental studies at 600 mK [58]. Additionally, theoretical ab initio studies of CaH-Li interactions in a magnetic field indicate that chemistry can be controlled via spin-state preparation [59]. The effects of quantum statistics and a confining geometry have also been previously observed in the ultracold chemical reactions of diatomic KRb [60]. Since the full review of theoretical and experimental results in cold and controlled chemistry is beyond the scope of this thesis we refer interested readers to Ref. [5, 7].

1.1.6 Astrochemistry

A large number of diatomic and polyatomic molecules have been detected in outer space in various interstellar environments that are characterized by diverse temperature and density regimes [61]. Studying chemical reactions between polyatomic molecules and atoms or molecules at cryogenic temperatures could help us understand diverse in astrochemistry. The quantum-mechanical tunneling reaction between the hydroxyl radical and methanol has been experimentally studied [62] in an astrochemically interesting regime and led the authors of that work to conclude that oxidation of organic molecules by OH via a tunneling mechanism could be a widespread phenomenon in low-temperature interstellar environments. This example shows that studying cold chemistry in the laboratory could aid in understanding the abundances and formation process of complex molecules including prebiotics [63] in cold interstellar environments.

1.2 Production of cold and ultracold polyatomic molecules

After motivating the exploration of cold polyatomic molecules in both physics and chemistry, we will review some experimental techniques for producing cold gas-phase samples of polyatomics. This review is not intended to be exhaustive in nature and we refer curious readers to multiple comprehensive references on the subject (e.g. [1, 8, 64]). Additionally, we are not going to describe methods for decelerating molecules that do not compress phase-space density of the molecular sample like velocity filtering or Stark and Zeeman deceleration [1].

1.2.1 Supersonic beams

Many experiments on direct cooling of molecules start with supersonic beams that are brought to rest using either electric (Stark) or magnetic (Zeeman) decelerators for further trapping and cooling [65]. While decelerators can reduce the velocity of the beams to a stop, the actual cooling of the velocity distribution happens in the supersonic expansion process. For a gas at a high initial pressure P_0 and temperature T_0 in a sealed container, upon rapid isentropic expansion into a region

with $P_1 \ll P_0$ both internal and translational degrees of freedom are cooled ($T_1 \ll T_0$) at the expanse of significant increase in the forward velocity of the beam. Since the size of the aperture is larger than the mean free path of the gas, during the expansion process the energy from internal rotations and vibrations is transferred into forward kinetic energy. While sub-kelvin temperatures in a moving reference frame have been achieved along with high number densities, large forward velocity in the laboratory frame ($v_f \sim 1,000$ m/s) presents a problem for some applications. Moving magnetic [66] and electric [67] traps that preserve phase-space density during the deceleration process appear to be a viable solution in order to bring the beams to a halt. Recently, high density samples of polyatomic [68] and diatomic [69] molecules have been achieved with magnetic deceleration as well as a molecular fountain has been demonstrated for Stark decelerated supersonic beams [70]. Even without any deceleration, supersonic beams have been used for many years for precision molecular spectroscopy [71] as well as collisional and reactive studies [72]. There are multiple extensive reviews of supersonic beams [65] and we refer the reader there for more details on the subject matter.

1.2.2 Helium nanodroplets

Under appropriate experimental conditions and using helium as a career gas, helium droplets can be formed during the process of supersonic expansion [73]. Doping of such nanodroplets consisting of hundreds or thousands of helium atoms at temperatures below 1 K with complex polyatomic molecules has been previously demonstrated and led to their spectroscopic studies [74]. Such environments provide an interesting systems for studying quantum effects of complex impurities interacting with a quantum fluid [75] but have limited applications for precision spectroscopy because of the broadening and shifts of spectral features (e.g. for example rotational constants are modified [76]). For a range of applications envisioned in this thesis, a dilute beam of polyatomic molecules with minimal collisional effects is required and therefore we did not explore this option.

1.2.3 Buffer-gas cooling

Buffer-gas cooling and beam production technique has recently attracted a lot of attention, replacing supersonic beams by producing bright and cold yet relatively slow molecular beams. Since the originally proposal in Ref. [77] and first beam demonstration in Ref. [78], there have been a few reviews covering the technical aspects of this approach [79, 80]. Briefly, upon the introduction of the hot molecular gas into the buffer-gas cell, translational motion of the molecules is cooled via scattering collisions with the inert helium buffer-gas that is maintained at 0.5-10 K temperature via collisions with the cell walls. The inelastic collisions between the buffer-gas (usually either helium or neon) and molecules lead to cooling of the rotational and vibrational motions [5]. Buffer-gas cooling has been used for loading magnetic traps of diverse atoms and molecules [79] and led to a BEC without any laser cooling throughout the process [81]. Extraction of the atoms or molecules entrained in the buffer gas flow leaving the cell through the aperture leads to beams with low forward velocities [80]. Upon the realization of the hydrodynamically enhanced buffer-gas beams [82], molecular fluxes orders of magnitude higher could be achieved compared to other beam production techniques, opening a completely new chapter in molecular beam development. Direct loading of magnetic traps for molecules [83] and magneto-optical traps for atoms [84] has been demonstrated without extra slowing. Additionally, high brightness and low forward velocities provide an almost ideal source for performing precision spectroscopy of molecules [65]. More details on buffer-gas cooling and its application to SrOH cooling will be provided in the followings chapters.

1.2.4 Optoelectrical cooling

One additional technique recently developed for direct cooling of polyatomic molecules needs to be mentioned. Optoelectrical Sisyphus cooling of polyatomics provided trapped samples below 1 mK [85]. Reaching densities required for observing molecule-molecule collisions also appears

[5] The cooling efficacy for rotations and vibrations is different and will be discussed in the later chapters.

within reach, potentially opening evaporative cooling for polyatomics (pending favorable collisional properties). However, either use of velocity filtering for chemically stable samples or additional precooling techniques like buffer-gas cooling followed by deceleration will be required for initial trapping of the molecules in order to implement the optoelectrical cooling technique [86]. To summarize succinctly, optoelectrical cooling relies on the presence of multiple low-field-seeking state-dependent energy potentials for symmetric top molecules in electric fields. In the polarized regime, STM has linear energy shifts in the electric field E characterized by [87]

$$E_{\text{Stark}} = -\mu_{\text{eff}}^{\text{el}} E = -\frac{KME\mu^{\text{el}}}{J(J+1)} \tag{1.2.1}$$

with quantum numbers[6] J, K, M_J defined in Fig. 1.1.1(b) where $\mu^{\text{el}}$is the electric dipole moment of particular molecular state. Thus, consider a specific rotational level $|J, K\rangle$, each product of the projection of the rotational angular momentum J onto the field axis M and onto the symmetry axis K will give a different energy potential. Since the technique relies on large Stark shifts, it appears to be most applicable to STMs or other molecules with linear Stark shifts.

1.2.5 Towards laser cooling of polyatomics

Revolutionary experimental tools of laser cooling and trapping developed in the 1980s and 1990s for bringing atomic gases into a new temperature and density regime led to the modern generation of atomic physics [89, 90]. While initial applications of ultracold atoms were in the study of atomic properties and interactions [91], their reach has rapidly expanded to include breakthrough results in condensed matter physics [92, 93], quantum information science [94], and particle physics [95, 96]. Presently, ultracold quantum gases are used for real-world applications in geodesy, metrology, and precision navigation [97, 98]. Our hope that extending laser cooling to complex polyatomic molecules will have similarly far reaching applications in pure and applied sciences.

[6]Good quantum numbers are associated with operators that commute with the total Hamiltonian $\hat{H}$ (i.e. $\left[\hat{H}, \hat{A}\right] = 0$) and therefore can be used for characterizing the molecular eigenstates [88].

1.3 Thesis overview

In this section we provide a broad overview of crucial experimental results presented later in the thesis. While the thesis chapters are organized according to the step-by-step experimental progress that was needed to achieve major results, the overview below is organized by conceptual similarity in order to help the reader construct a coherent picture of the thesis work.

1.3.1 Laser manipulation of SrOH motion

The choice of strontium monohydroxide (SrOH) as a molecule of interest was motivated by a number of its intriguing properties. Unlike for the isoelectronic diatomic molecule SrF, there are three vibrational modes present in SrOH with the quantum numbers denoted $\left(v_1 v_2^l v_3\right)$ for the vibrational quanta in the Sr-O stretching mode v_1, Sr-O-H bending mode v_2 with vibrational angular momentum l, and O-H stretching mode v_3. While the ground vibronic state $\tilde{X}$ has a linear geometry, the first excited degenerate bending mode (not present in diatomics) can be described by a symmetric top Hamiltonian [87]. Therefore, SrOH can be manipulated as either a linear or a symmetric top molecule depending on the requirements of the application by exciting ground state molecules into $\left(01^10\right)$ vibrational state either using off-diagonal optical pumping via an electronic state or directly. Additionally, while direct laser cooling of hydroxyl radical (OH), which plays an important role in atmospheric and interstellar chemistry, appears extremely challenging [99], addition of the strontium atom allows laser-based manipulation. In a similar vein, SrOH can be considered as a model species for extending laser cooling to more complex metal-ligand compounds (e.g. $SrCH_3$, $SrOCH_3$, and SrC_5H_5).

The presence of strong optically accessible electronic transitions at 611 nm for $\tilde{X}-\tilde{B}$ and at 688 nm for $\tilde{X}-\tilde{A}$ enable laser manipulation of SrOH external and internal motions with atomic physics techniques. As a first step towards mechanical control of its motion with laser light, we demonstrated radiation pressure force deflection of the cryogenic buffer-gas beam (CBGB) of SrOH. The

cycling transition was created by exciting $N'' = 1 \rightarrow N' = 0$ rotational transition[7] leading to a factor of 12 increase in the laser induced fluorescence (LIF) signal. By repumping the molecules lost to the excited Sr-O stretching mode, we were able to scatter more than 100 photons per each molecule leading to a mechanical deflection of the molecular beam by 0.2°. One possible application of this technique is to create a quantum-state-pure beam of SrOH molecules for collisional studies or precise measurements of the state-dependent forces. A state-pure beam of SrOH molecules in the first excited rotational level $N'' = 1$ in the vibrational ground state can be separated from the rest of the CBGB by increasing the interaction time between the molecules and laser fields, as was previously demonstrated with atoms.

Direct laser cooling of atomic gases to ultracold temperatures [89] and ultimately even into the quantum degenerate regime [43] was the true hallmark of motion control for neutral atoms. Even though laser cooling of simple diatomic molecules (SrF, YO and CaF) was very recently demonstrated [100–102], the effort of extending this technique to even the simplest polyatomic molecules seemed daunting because of the rapid growth of the vibrational degrees of freedom with the number of atoms in a molecule. However, despite the presence of three vibrational modes in SrOH, we were able to cool SrOH CBGB in 1 dimension from 50 mK to 750 μK with the same number of lasers as used for diatomic molecules SrF and YO. Our results with SrOH not only open up a wide range of future directions for laser manipulation of polyatomic molecules but also overturn long held convictions about the impossibility of performing "traditional" atomic physics experiments with complex molecular systems.

1.3.2 Controlling internal quantum states for collisional studies

In addition to controlling the external motion, we used laser light for preparing SrOH molecules in a specific quantum state in order to study state-selective inelastic collisions with cryogenic helium gas. By optically pumping molecules from the first excited rotational level $N'' = 1$ of the vibronic

[7] We follow the usual spectroscopic notation that quantum numbers for the lower state are marked with double prime symbol while those for the upper state are indicated with the prime symbol.

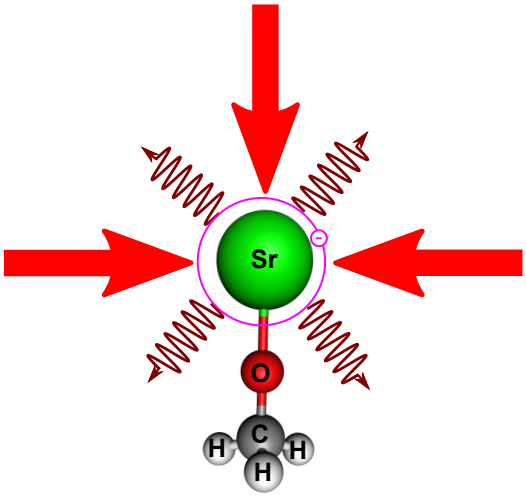


Figure 1.3.1: Photon absorption and spontaneous emission in $SrOCH_3$.

ground state $\tilde{X}\,(000)$ into first excited rotational level of the vibrationally excited state $\tilde{X}\,(100)$ we were able to measure the dependence of the molecular dynamics on the nature of vibrational state used. Dramatic differences in population lifetimes for molecules in (000) and (100) vibrational modes have been observed. Our measurements of vibrational quenching cross-sections in inelastic collisions between SrOH and helium at 2 K extended the study of relaxation in cold atom–molecule collisions to linear polyatomic radicals and contributed to an overall physical picture of the dependence of quenching rates on vibrational energy spacing in low energy collisions. Additionally, the measurement precision provided an important benchmark for future theory calculations.

1.3.3 Laser cooling of complex polyatomics

Inspired by the promising results with SrOH, we have identified a broad class of larger molecules – alkaline earth monoalkoxides (MOR) – for which similar techniques can be applied. Intuitively, since the optically active electron is located on the strontium metal, replacing H with a different ligand will not perturb electron's wavefunctions significantly, and thus preserving optical cycling ability (see Fig. 1.3.1). By performing a careful theoretical analysis of the properties of multiple complex MOR molecules with up to 15 atoms, we identified an experimentally feasible strategy to achieve laser cooling with numerous applications in physics and chemistry.

Chapter 2

Molecular Structure and Properties of Strontium Monohydroxide

A prominent class of diatomic molecules identified as suitable for direct laser cooling is alkaline earth monohalides MF like CaF [102], SrF [100], BaF [103], and RaF [104]. Pseudohalogens are polyatomic functional groups with the chemical properties reminiscent of those for halogens like fluorine (F), chlorine (Cl), and bromine (Br). As pointed out by Isaev and Berger [105], employing substitution of the halogen in a diatomic molecule with a pseudohalogen group like CN, NC, or OH, one could potentially allow identification of polyatomic molecules with optical cycling properties similar to those of MF compounds. Figure 2.1.1 provides a comparison of the electronic configurations for CaF and CaOH. As can be inferred from the diagram, similar electronic configuration of the OH^- and F^- can influence the electronic levels of Ca^+ in an identical way. However, compared to the diatomic molecule SrF, which was previously laser cooled in the DeMille group at Yale [100], the addition of a single atom to make the triatomic molecule SrOH leads to a variety of new phenomena in the structure and dynamics of SrOH compared to SrF. Therefore, before proceeding forward with with the description of the experimental results on SrOH, it is important to carefully review molecular structure of linear polyatomic molecules. After understanding the energy level details, we will consider how photon cycling can be achieved in

linear polyatomic molecules in general and what technical requirements are necessary for working with SrOH in particular.

2.1 Electronic structure of polyatomic molecules

In order to determine the electronic structure of a polyatomic molecule it is necessary to solve a time-independent Schrödinger equation

$$\hat{H}_{\text{mol}}\Psi_{\text{mol}} = E\Psi_{\text{mol}} \tag{2.1.1}$$

for a system consisting of N_{el} electrons and K_{nuc} nuclei interacting with each other via electromagnetic forces. The exact relative positions of the nuclei are determined by the averaged spatial distribution of all electrons which lead to a stable chemical bonding of the molecule despite repulsive forces between nuclei [10]. Molecular Hamiltonian[1] includes contributions from kinetic energy of the electrons and nuclei[2] as well as various potential energy terms [20]

$$\hat{H}_{\text{mol}} = \hat{T}_{\text{nuc}} + \hat{T}_{\text{el}} + \hat{V}_{\text{nuc,nuc}} + \hat{V}_{\text{el,el}} + \hat{V}_{\text{nuc,el}}. \tag{2.1.2}$$

Different terms in the equation above have the following expressions:

- kinetic energy of the nuclei with mass M_k

$$\hat{T}_{\text{nuc}} = -\frac{\hbar^2}{2}\sum_{k=1}^{K_{\text{nuc}}}\frac{1}{M_k}\nabla_k^2 \tag{2.1.3}$$

- kinetic energy of the electrons with mass m

$$\hat{T}_{\text{el}} = -\frac{\hbar^2}{2m}\sum_{i=1}^{N_{\text{el}}}\nabla_i^2 \tag{2.1.4}$$

[1] For now we have ignored contributions to $\hat{H}_{\text{mol}}$ arising from interactions associated with electronic and nuclear spins that are present in SrOH and other polyatomic radicals.

[2] We are considering a molecule at rest in the laboratory frame.

- pairwise repulsion between the nuclei with charges Z_k and $Z_{k'}$ and separation $R_{k,k'} = |R_k - R_{k'}|$

$$\hat{V}_{\text{nuc,nuc}} = \frac{e^2}{4\pi\varepsilon_0} \sum_{k'>k} \sum_{k=1}^{K_{\text{nuc}}} \frac{Z_k Z_{k'}}{R_{k,k'}} \tag{2.1.5}$$

- pairwise repulsion between the electrons separated by $r_{i,i'} = |r_i - r_{i'}|$

$$\hat{V}_{\text{el,el}} = \frac{e^2}{4\pi\varepsilon_0} \sum_{i'>i} \sum_{i=1}^{N_{\text{el}}} \frac{1}{r_{i,i'}} \tag{2.1.6}$$

- attractive force between electrons and nuclei separated by $r_{i,k} = |r_i - R_k|$

$$\hat{V}_{\text{nuc,el}} = -\frac{e^2}{4\pi\varepsilon_0} \sum_{k=1}^{K_{\text{nuc}}} \sum_{i=1}^{N_{\text{el}}} \frac{Z_k}{r_{i,k}}. \tag{2.1.7}$$

The accurate solution of Eq. 2.1.1 with an appropriate molecular Hamiltonian in Eq. 2.1.2 would explain in detail the chemical structure and spectroscopy of the species under consideration. However, since even for the simplest molecule H_2^+ with $Z_1 = Z_2 = 1$ the Schrödinger equation (Eq.2.1.1) with the molecular Hamiltonian in Eq. 2.1.2 cannot be solved exactly, resorting to either numerical methods or physically inspired approximate approaches is required [10]. While the Coulombic forces exerted on the electrons and the nuclei are similar, because of their significantly lighter mass electrons move much faster than the vibrating nuclei and therefore the electron cloud adiabatically follows the changes in the nuclear framework. By considering nuclear kinetic energy as the perturbation on the electronic Hamiltonian with a fixed nuclear framework R

$$\hat{H}_{\text{el}} = \hat{T}_{\text{el}} + \hat{V}_{\text{nuc,el}} + \hat{V}_{\text{el,el}} \tag{2.1.8}$$

the electronic structure of the molecule can be found by solving the electronic Schrödinger equation

$$\hat{H}_{\text{el}} \psi_{\text{el}}(r,R) = E_{\text{el}} \psi_{\text{el}}(r,R) \tag{2.1.9}$$

for electronic states $\psi_{\mathrm{el,m}}$ with energy[3] $E_{\mathrm{el,m}}(R)$.

In the Born-Oppenheimer approximation the coupling between rotation and vibration of the nuclei and the motion of the electron cloud is ignored and the full wavefunction can be separated into the parts coming from electronic and nuclear motions

$$\Psi_{\mathrm{mol}}(r,R) \approx \psi_{\mathrm{el}}(r)\,\chi_{\mathrm{nuc}}(R). \tag{2.1.10}$$

The total energy of the electron cloud

$$U_{\mathrm{el}} = E_{\mathrm{el}} + V_{\mathrm{nuc,nuc}} \tag{2.1.11}$$

serves as the potential energy for the nuclear motion and, therefore, nuclear wavefunctions χ_{nuc} and eigenenergies E_{nuc} can be found by solving [10]

$$\left(\hat{T}_{\mathrm{nuc}} + U\right)\chi_{\mathrm{nuc}}(R) = E_{\mathrm{nuc}}\chi_{\mathrm{nuc}}(R). \tag{2.1.12}$$

Thus, the molecular energy levels are given by the sum of the two solutions

$$E_{\mathrm{mol}} = U_{\mathrm{el}} + E_{\mathrm{nuc}} \tag{2.1.13}$$

where the first term accounts for the energy associated with electronic motion and the second term for nuclear kinetic energy from rotations and vibrations. While the Born-Oppenheimer approach enables us to separately speak of energy levels associated with electronic and nuclear (rotation and vibrations) motions, the effects of the breakdown of this approximation do play an important role in molecular spectroscopy discussed in this thesis and will be elaborated on in detail later in this chapter.

[3] The fixed $\hat{V}_{\mathrm{nuc,nuc}}$ repulsion energy can be added as an offset to $E_{\mathrm{el,m}}$.

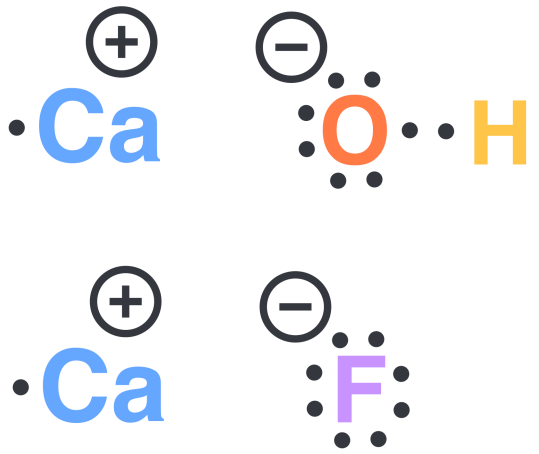


Figure 2.1.1: Electronic configurations of the isoelectronic molecules CaF and CaOH.

2.1.1 Electronic levels of SrOH

With three nuclei and more than hundred electrons the structure of a triatomic molecule like SrOH may seem to appear complex at first, however, a relatively simple one-electron hydrogenic model provides a good enough model for understanding atomic physics experiments performed here. The details of the electronic structure for SrOH can be extracted from the model including ionic bonding between positively charged Sr^{2+} closed shell and negatively charged OH^- ions with the addition of an unpaired electron located on the metal center. The presence of this valence optically active electron leads to strong low-lying electronic transitions making SrOH a particularly attractive candidate for laser spectroscopy [106]. The electronic structure of SrOH can be further understood as arising from the states of Sr^+ ion which is isoelectronic to Rb. Because of the partially positive charge on the proton in the OH group, electrostatic repulsion between the strontium ion and the proton leads to the linear geometry of SrOH that maximizes the distance between Sr^+ and H^+.

Figure 2.1.2 shows how the electronic energy levels of SrOH relevant to the experiments performed in this thesis arise from the levels of Sr ion perturbed by the negatively charged OH ligand. The single valence electron experiences the Hamiltonian of the form [107]

$$\hat{H} = \hat{H}^{(0)} + \hat{H}^{(1)} = \hat{H}_{Sr^{2+}} + \hat{H}_{LF} \tag{2.1.14}$$

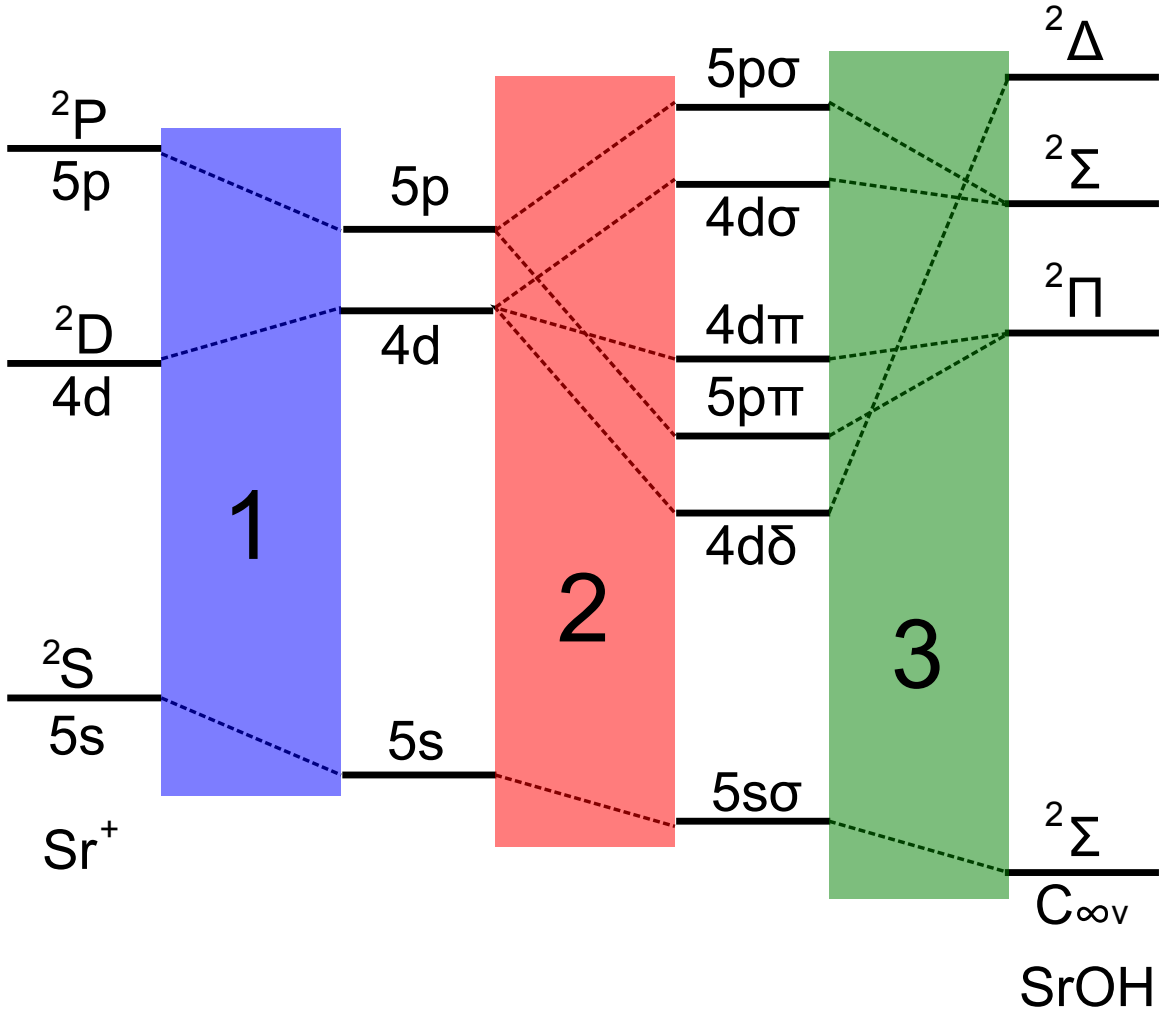


Figure 2.1.2: Correlation diagram for low lying electronic states of Sr^+ and SrOH. The three shaded regions indicate the rearrangement of the electronic energy levels in the ligand field theory due to the effect of OH^- ligand on Sr^+ ion levels. The details of the diagram are provided in the text of the chapter and the figure has been modeled after Ref. [107].

where the field of the negatively charged OH ligand is treated as the perturbation. While solving the Hamiltonian above is beyond the scope of this thesis, the results on the energy levels can be summarized qualitatively as indicated in the three regions of Fig. 2.1.2

- The energy levels of the atomic Sr ion are rearranged as demonstrated in region 1 (blue).
- The degeneracy of the atomic orbitals is lifted in the excited electronic states as shown in region 2 (red)
- Orbitals of the same m_l are mixed to create molecular states (region 3, green).

Therefore, different molecular energy levels result from the mixtures of atomic energy orbitals (except for the ground electronic state $\tilde{X}$). Understanding the energy levels of SrOH and more complex alkaline earth alkoxides in this way allows applying atomic physics intuition to such complex molecular species.

2.2 Vibrational levels of linear polyatomic molecules

Treating vibrating nuclei in a non-rotating polyatomic molecule harmonically in the normal mode coordinate system leads to no cross terms in the kinetic and potential energy parts of the vibrational Hamiltonian. Therefore, the total Hamiltonian operator is the sum of $3N-5$ independent harmonic oscillator operators in the linear case[4] [20]

$$\hat{H}_{\text{vib}} = \sum \hat{H}_i = \sum \left(-\frac{\hbar^2}{2}\frac{\partial^2}{\partial Q_i} + \frac{1}{2}\lambda_i \hat{Q}_i^2 \right) \tag{2.2.1}$$

where Q_i are the $3N-5$ normal modes. Consequently, the total vibrational wavefunction is the product of the individual wavefunctions for each mode

$$\psi_{\text{vib}} = \psi_1(Q_1)\psi_2(Q_2)\ldots\psi_{3N-5}(Q_{3N-5}) \tag{2.2.2}$$

[4]For a nonlinear molecule, there are $3N-6$ degrees of freedom for the vibrations since six degrees are associated with translation and rotation. However, for linear molecules vibrations have $3N-5$ degrees of freedom since they do not rotate around the internuclear axis [10].

where $\psi_i(Q_i)$ are the harmonic oscillator wavefunctions. The intensities of the vibronic transitions in the Born-Oppenheimer approximation are given by [88]

$$I_{e'v'e''v''} \propto |R_e|^2 q_{v'-v''} \tag{2.2.3}$$

where the Franck-Condon factor (FCF) $q_{v'-v''} = \left(\int \psi^*_{\text{vib}'} \psi_{\text{vib}''} dr\right)^2$ determines the intensity distribution among vibrational levels while $|R_e|$ is the electronic transition dipole moment. The energy levels of the vibrating polyatomic molecules become [108]

$$G(v_1 v_2 v_3 \ldots) = \sum_i \omega_i \left(v_i + \frac{d_i}{2}\right) \tag{2.2.4}$$

where d_i is the degeneracy and ω_i is the vibrational frequency of the ith vibrational mode. However, if the anharmonic contributions to the molecular potential are included[5] there exist coupling terms between different modes [20]

$$G(v_1 v_2 v_3 \ldots) = \sum_i \omega_i \left(v_i + \frac{d_i}{2}\right) + \sum_{j \le i} x_{ij} \left(v_i + \frac{d_i}{2}\right)\left(v_j + \frac{d_j}{2}\right) + \sum_{t \le t'} g_{tt'} l_t l_{t'} \tag{2.2.5}$$

where index t runs over only degenerate modes with vibrational angular momentum l_t (e.g. bending vibrations in SrOH) and x_{ij} and $g_{tt'}$ are the anharmonicity constants. For example, for SrOH with a single bending vibrational mode v_2, the term value is

$$G(v_1 v_2 v_3) \approx \omega_1 \left(v_1 + \frac{1}{2}\right) + \omega_2 (v_2 + 1) + \omega_3 \left(v_3 + \frac{1}{2}\right) + g_{22} l_2^2 \tag{2.2.6}$$

where we have neglected x_{ij} cross coupling anharmonic terms. The true wavefunctions of the complex Hamiltonian can be represented as mixtures of the harmonic oscillator wavefunctions.

[5]For example, the use of internal molecular coordinates rotating with the molecule introduces a Coriolis force that leads to rotation-vibration interaction and coupling between different normal modes for rotating diatomic and polyatomic molecules [87].

2.2.1 Bending vibrations in linear polyatomics

Bending or perpendicular modes of vibrations in linear polyatomic molecules have no analog in diatomic molecules and therefore need to be discussed in greater details since they will play a role during the laser cooling process. For a detailed treatment of the bending motion of linear polyatomics we refer the reader to great references available [20, 87, 109] and only focus on the aspects necessary for introducing the concept of vibrational angular momentum. For a two-dimensional harmonic oscillator, the wavefunction in Cartesian coordinates is given by

$$\psi(x,y) = \psi_{\mathrm{HO}}(x)\,\psi_{\mathrm{HO}}(y) \tag{2.2.7}$$

with the total energy of the oscillator becoming

$$E_v = h\nu(v+1) \tag{2.2.8}$$

for $v = v_x + v_y$ where v_i is the number of vibrational quanta in the ith oscillator. Thus, each level with energy E_v has $v+1$ degeneracy. Classically, a proper phasing of the two oscillators in the x and y directions will lead to circular or elliptical motions of the nuclei around the symmetry axis z, resulting in the associated angular momentum. Quantum mechanically, such vibrational angular momentum has to be quantized and only $\pm l\hbar$ values are possible [20]. If n_a and n_b are correspondingly the number of the left and right circularly polarized quanta then $v = n_a + n_b$ and $l = n_a - n_b$ and, therefore, possible values of $|l|$ are $v, v-2, v-4, \ldots, 0$ or 1. For a linear triatomic molecule like SrOH with only one degenerate bending vibrational mode, molecular spectra in this mode are very similar to those of symmetric top molecules with $K = l$ [87]. The degeneracy for different values of $|l|$ is split because of the anharmonic terms. For a rotating molecule, the symmetry of bending in the xz plane vs in yz plane is broken by the axis of rotation. The value of the Coriolis force depends on whether the vibration is perpendicular or parallel to the angular momentum $\vec{J}$. As a result of the vibration-rotation interaction, two degenerate levels $+l$ and $-l$ are split in the pro-

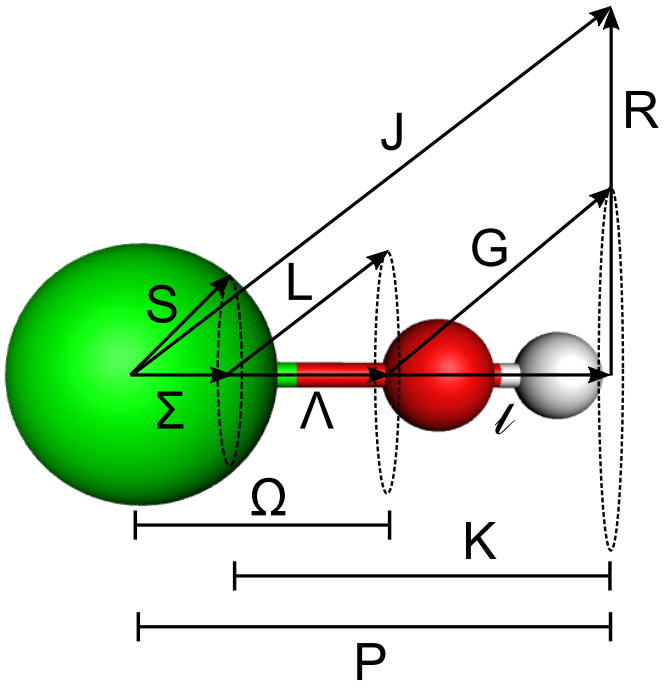


Figure 2.2.1: Coupling of angular momenta for a linear polyatomic molecule under Hund's case (a) scheme (e.g. $\tilde{A}$ state in SrOH).

cess known as l-type doubling. For $|l| = 1$, the splitting is given by $q_l (v_2 + 1) J (J + 1) /2$ where q_l is the l-type doubling constant while for $|l| \geq 2$ the splitting is even smaller [87].

2.3 Breakdown of the Born-Oppenheimer approximation

In many real molecules the description provided above is highly approximate and there are multiple perturbations to the energy levels because of the coupling between different electronic states or between different types of motion (e.g. rotation-vibration). For an exhaustive treatment of such effects in molecular spectra please see Refs. [10, 108, 110]. It is important to discuss the couplings between different angular momenta in molecules since they play an important role in determining selection rules for perturbations and symmetries of the states involved [10].

The vector models for Hund's coupling schemes (a) and (b) are shown in Figs. 2.2.1 and 2.3.1, correspondingly. In case (a), the electronic orbital and electron spin angular momenta couple strongly to the symmetry axis of the molecule and precess rapidly to form a new quantum

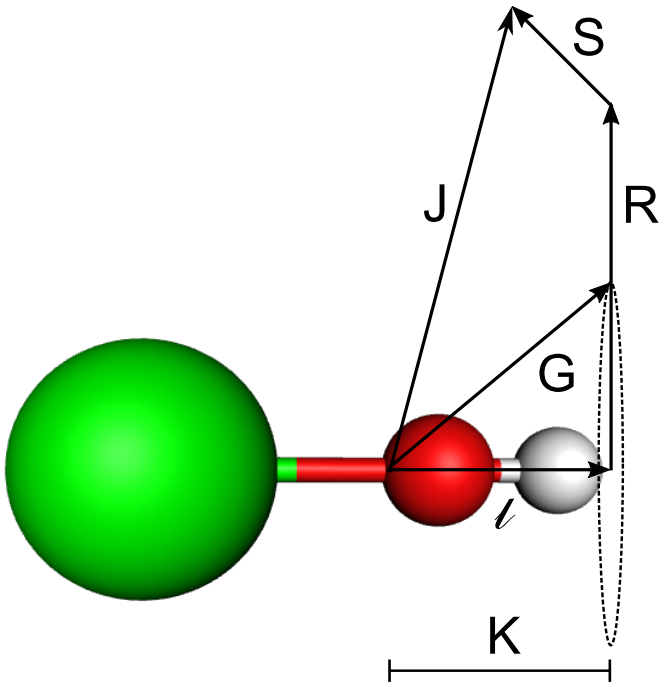


Figure 2.3.1: Coupling of angular momenta for a linear polyatomic molecule under Hund's case (b) scheme (e.g. $\tilde{X}$ and $\tilde{B}$ states of SrOH).

number $\Omega = |\Lambda + \Sigma|$. This effect arises because of the strong interaction between the spin of the unpaired electron and the magnetic field originating from the electronic angular momentum precession around the internuclear axis [10]. In the states with excited bending vibrations that have associated vibrational angular momentum G, such vibrations introduce a vibrational dipole moment to which the valence electron couples resulting in the modification of the electronic energy levels due to bending vibrations. The bending motion of the linear molecule lifts the orbital degeneracy of the state initially present because of the cylindrical symmetry. The two potential curves $E^+(\varphi)$ and $E^-(\varphi)$ become distinct

$$E^+(\varphi) - E^-(\varphi) = \alpha\varphi^2 + \beta\varphi^4, \tag{2.3.1}$$

where φ is the bond angle, and lead to the mixing between the zeroth-order vibrational and electronic wavefunctions associated with the linear molecular configuration [10]. The good quantum number for the vibronic states of symmetries $\Gamma^{\text{vib}} \otimes \Gamma^{\text{el}} = \Gamma^{\text{vibronic}}$ is $K = \Lambda + l$ [20].

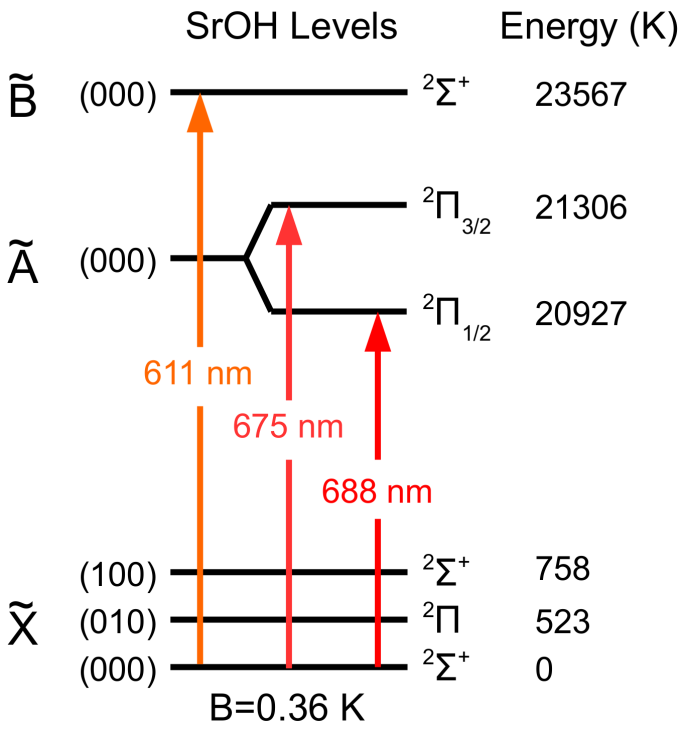


Figure 2.3.2: Three lowest optically accessible transitions in SrOH. Because of the spin-orbit splitting in the excited $\tilde{A}$ state, each of the spin-orbit manifolds can be selectively addressed with a different color laser. Two lowest-lying vibrationally excited levels in the ground state are indicated along with the rotational constant B for the ground vibronic level $\tilde{X}\,(000)$.

For case (b) scheme the spin of the electron is not coupled to the internuclear axis but instead to the rotation of the molecule as can be seen in Fig. 2.3.1. Both $\tilde{X}$ and $\tilde{B}$ states of SrOH do not have any orbital angular momentum, so we consider the case of $^2\Sigma$ electronic states here. When the bending vibration is excited as in (010) state, the vibrational angular momentum does not produce a large enough magnetic moment compared to the orbital angular momentum L in case (a) for example. Thus, the spin still remains coupled to the rotation as shown in Fig. 2.3.1.

2.4 Rotational energy levels of SrOH

Rotational energies in ground vibrational level of a linear polyatomic molecule like SrOH are essentially the same as for a diatomic molecule like SrF. For a case (b) $^2\Sigma$ state like $\tilde{X}$ and $\tilde{B}$ states

of SrOH the energy levels are given by [111]

$$F_1(N) = B_v^{''} N(N+1) - D_v^{''} N^2 (N+1)^2 + (\gamma_v/2) N \tag{2.4.1}$$

$$F_2(N) = B_v^{''} N(N+1) - D_v^{''} N^2 (N+1)^2 - (\gamma_v/2)(N+1) \tag{2.4.2}$$

where the subscript refers to the upper and lower spin-rotation component for each rotational level N and B, D, and γ are rotational, centrifugal, and spin-rotation constants, correspondingly. For case (a) molecules in the $^2\Pi$ electronic state (like $\tilde{A}$ state of SrOH), the energy levels are described by [111]

$$F_{1c}(J) = T_v - A_v/2 + B_{v(1/2)}^{'} J(J+1) - D_{v(1/2)}^{'} J^2 (J+1)^2 - (p_v/2)(J+1/2) \tag{2.4.3}$$

for the upper Λ doublet component of the $^2\Pi_{1/2}$ manifold and

$$F_{1d}(J) = T_v - A_v/2 + B_{v(1/2)}^{'} J(J+1) - D_{v(1/2)}^{'} J^2 (J+1)^2 + (p_v/2)(J+1/2) \tag{2.4.4}$$

for the lower Λ doublet component since $p_v < 0$. While for the $^2\Pi_{3/2}$ manifold we have

$$F_{2c} \approx F_{2d} \approx T_v + A_v/2 + B_{v(3/2)}^{'} J(J+1) - D_{v(3/2)}^{'} J^2 (J+1)^2 \tag{2.4.5}$$

since the Λ-doublet splitting is too small to resolve here. In order to compare the relative sizes of different spectroscopic constants in the equations above in Table 2.1 we provide the molecular constants for $\tilde{X}$ and $\tilde{A}$ states of SrOH. See Fig. 2.3.2 for the diagram of electronic states of SrOH used in this thesis. Notice that since $D \ll B$, the anharmonic terms can be ignored when calculating the transitions for laser spectroscopy in the buffer-gas cell or beam. The effective rotational constant for different spin-orbit components of $^2\Pi$ electronic state can be calculated as $B_{\text{eff}} = B\left(1 - \frac{B}{A\Lambda}\right)$ [112].

The term symbol for labeling electronic transitions in linear molecules is given by $^{\triangle N}\triangle J_{F_i' F_j''}$

Molecular Constant	cm^{-1}
$T_{000}\left(\tilde{X}\right)$	0
$B_{000}\left(\tilde{X}\right)$	0.2492032
$D_{000}\left(\tilde{X}\right)$	2.1801×10^{-7}
$\gamma_{000}\left(\tilde{X}\right)$	2.4273×10^{-3}
$T_{000}\left(\tilde{A}^2\Pi_{1/2}\right)$	14542.573
$B_{000}\left(\tilde{A}\right)$	0.2538873
$D_{000}\left(\tilde{A}\right)$	2.1735×10^{-7}
$p_{000}\left(\tilde{A}\right)$	-0.1432006
$A_{000}\left(\tilde{A}\right)$	263.51741

Table 2.1: Spectroscopic constants for the $\tilde{X}$ and $\tilde{A}$ states of SrOH taken from Refs. [113, 114].

where $\triangle N$ is specified by P, Q, or R for -1, 0, and $+1$ values correspondingly. Using notation above, some of the transitions can be calculated as $Q_{11}\left(J''\right)=F_{1d}\left(J'\right)-F_1\left(J''\right)$, $R_{12}\left(J''\right)=F_{1d}\left(J'\right)-F_2\left(J''\right)$, and $P_{11}\left(J''\right)=F_{1c}\left(J''-1\right)-F_1\left(J''\right)$.

The structure of the rotational levels for the excited stretching modes of SrOH is almost the same as that for the ground vibrational levels describe above[6]. However, for the excited bending vibrations the rotational levels and finer substructures are no longer the same as in diatomics and therefore need more attention. The expressions for the $\tilde{X}\left(010\right)^2\Pi$ rotational levels are given in the case (b) basis as [116]

$$F_1\left(N\right)=B_v\left[N\left(N+1\right)-l^2\right]-D_v\left[N\left(N+1\right)-l^2\right]^2+\frac{1}{2}\gamma_v N\pm\frac{1}{2}q_v N\left(N+1\right) \tag{2.4.6}$$

$$F_2\left(N\right)=B_v\left[N\left(N+1\right)-l^2\right]-D_v\left[N\left(N+1\right)-l^2\right]^2-\frac{1}{2}\gamma_v\left(N+1\right)\mp\frac{1}{2}q_v N\left(N+1\right) \tag{2.4.7}$$

where F_1 and F_2 are the spin-rotation components and the upper/lower sign refers to the e/f parity

[6]Like for diatomic molecules, because of the rotation-vibration interaction the rotational constant B is slightly different for excited vibrational levels, i.e. $B_v=B_e-\sum_i\alpha_i\left(v_i+\frac{d_i}{2}\right)-J\left(J+1\right)D$ [115].

level with the vibrational angular momentum $l = 1$ for (010) level of SrOH. If the term values are referenced to the rotationless levels with $N = 0$ we obtain familiar expression of

$$F_1(N) = B_v N(N+1) + \frac{1}{2}\gamma_v N \tag{2.4.8}$$

$$F_2(N) = B_v N(N+1) - \frac{1}{2}\gamma_v (N+1) \tag{2.4.9}$$

where we have ignored the anharmonic contribution. However, because of the l-type doubling each of the spin-rotation components consists of closely spaced opposite parity levels and additional constraint that $N \geq l$. For SrOH the magnitude of the splitting between the two opposite parity levels is equal to ~ 24 MHz [117].

2.4.1 Parity of energy levels

As discussed below, during the photon cycling process in SrOH, parity selection rule $+ \leftrightarrow -$ for allowed one-photon electric dipole transitions plays an important role in preventing losses to dark rotational states. The parity eigenfunctions for Σ^+ and Π states are linear combinations of the state basis functions [88]

$$\left|^{2S+1}\Lambda_\Omega \pm\right\rangle = \frac{\left|^{2S+1}\Lambda_\Omega\right\rangle \pm (-1)^{J-2\Sigma+S}\left|^{2S+1}\Lambda_{-\Omega}\right\rangle}{\sqrt{2}} \tag{2.4.10}$$

where upon application of the inversion operator E^*

$$E^*\left|^{2S+1}\Lambda_\Omega \pm\right\rangle = \pm\left|^{2S+1}\Lambda_\Omega \pm\right\rangle. \tag{2.4.11}$$

However, for a fixed electronic state Λ, Σ, and Ω quantum numbers are fixed and the total parity only changes sign because of J [107]. It is often much more instructive to use the rotationless e/f

parity instead when the J dependence is factored out. Therefore, the parity eigenfunctions become

$$\left|^2\Sigma^+_{1/2}(e/f)\right\rangle = \frac{\left|^2\Sigma^+_{1/2}\right\rangle \pm \left|^2\Sigma^+_{-1/2}\right\rangle}{\sqrt{2}} \tag{2.4.12}$$

$$\left|^2\Pi_{1/2}(e/f)\right\rangle = \frac{\left|^2\Pi_{1/2}\right\rangle \pm \left|^2\Pi_{-1/2}\right\rangle}{\sqrt{2}} \tag{2.4.13}$$

for the states involved in our experiments. While for the $\tilde{A}^2\Pi_{1/2}$ electronic state of SrOH, the levels with opposite total parity are close together in the form of Λ-type doublets, for $\tilde{X}^2\Sigma^+$ state the opposite parity levels are separated by the rotational splitting. This explains why it is easier to polarize molecules in the $^2\Pi$ electronic state than in $^2\Sigma$ states. However, for $\tilde{X}(010)$vibronic state of SrOH that has Π symmetry, closely spaced opposite parity levels arise from the linear combinations of the vibrational wavefunctions for the two-dimensional harmonic oscillator [88]

$$\psi_{\text{vib}}(e/f) = R(\rho)\frac{e^{i\phi} \pm e^{-i\phi}}{\sqrt{2}} \tag{2.4.14}$$

where $R(\rho)$ is defined in Appendix A.

2.5 Creating a cycling transition for SrOH

In order to create an optical cycling configuration for SrOH we need to consider possible electronic, vibrational and rotational loss channels upon the optical excitation. Ideally, one would pick the lowest accessible electronic transition so as to avoid losses to intermediate electronic states. For example, laser cooling of a diatomic molecule YO has been more complicated than expected due to a presence of a metastable $A'^2\triangle_{3/2}$ state [118]. From Fig. 2.3.2 we conclude that using $\tilde{X} - \tilde{A}^2\Pi_{1/2}$ as a main cycling transition will lead to an electronically closed cycle. In fact, laser slowing on the $\tilde{X}^2\Sigma^+ - \tilde{B}^2\Sigma^+$ transition has been already demonstrated for CaF making use of a small dipole moment[7] and small energy spacing between $\tilde{A}$ and $\tilde{B}$ energy levels [119]. Similarly, in addition

[7] Both $\tilde{A}$ and $\tilde{B}$ states result from the mixture of the $4p$ and $3d$ atomic orbitals.

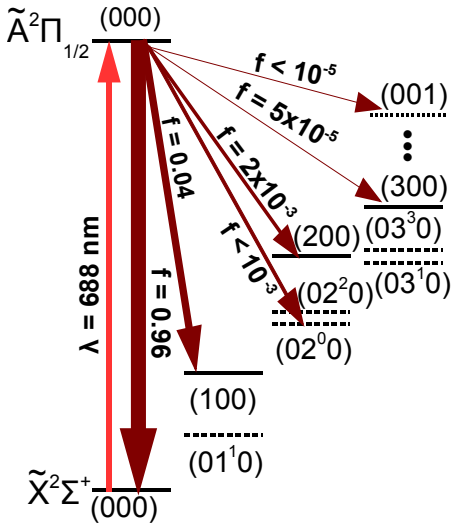


Figure 2.5.1: Details of the vibrational structure of SrOH relevant to the optical cycling scheme. The energies of the excited vibrational levels in the electronic ground state have been previously measured [114]. The main cycling laser is indicated with an upward arrow, while the spontaneous decay channels in the Born-Oppenheimer approximation are shown with the downward dark-red arrows. Thicker decay lines correspond to stronger transitions with the corresponding Franck-Condon factors (f) indicated. The rotational lines are not depicted at this scale. Vibrational levels not present in diatomic molecules are indicated with dashed lines.

to cycling on $\tilde{X}-\tilde{A}$ we could employ the $\tilde{X}-\tilde{B}$ transition for SrOH. While in the first case an injection-locked diode laser system can be used to seed a tapered amplifier, in order to address $\tilde{X}-\tilde{B}$ either a dye laser or a frequency doubling stage is necessary.

Even in the absence of any electronic loss channels, the absence of angular momentum associated with the stretching modes of vibrational motion will lead to losses to excited vibrational levels. As was previously mentioned, the vibronic transitions are governed by the values of corresponding Franck-Condon factors instead of strict selection rules. Figure 2.5.1 shows the dominant FCFs for the $\tilde{X}-\tilde{A}$ excitation. As can be seen, there are significantly more possible vibrational dark states than for a diatomic molecule like SrF. However, because of the highly diagonal FC arrays for all vibrational modes as well as the vibrational angular momentum selection rule $\triangle l_2 = 0$ only a few vibrational levels need to be addressed with additional lasers in order to bring the molecules back into the optical cycle. Table 2.2 summarizes both FCFs and VBRs[8] for the two electronic transi-

[8]Vibrational branching ratio (VBR) includes ω^3 dependence of the transition dipole.

Transition	FCF	VBR
$\tilde{X}^2\Sigma^+ - \tilde{A}^2\Pi_{1/2}$		
(000)-(000)	0.9550	0.9594
(100)-(000)	0.0425	0.0382
(200)-(000)	0.0016	0.0013
(020)-(000)	7×10^{-4}	7×10^{-4}
(001)-(000)	7×10^{-6}	3×10^{-6}
$\tilde{X}^2\Sigma^+ - \tilde{B}^2\Sigma^+$		
(000)-(000)	0.9769	0.9788
(100)-(000)	0.0185	0.0168
(200)-(000)	0.0023	0.0019
(020)-(000)	0.0022	0.0021
(001)-(000)	3×10^{-5}	1×10^{-5}

Table 2.2: Franck-Condon factors (FCFs) and vibrational branching ratios (VBRs) for SrOH $\tilde{X} - \tilde{A}$ and $\tilde{X} - \tilde{B}$ transitions. The probabilities of a transition to a combination level (e.g. $P\left[\left(12^00\right) - (000)\right]$) are smaller than values displayed in the table because they equal to the product of probabilities for the corresponding overtone levels (e.g. $P\left[(100) - (000)\right] \times P\left[\left(02^00\right) - (000)\right]$) [120].

tions considered for optical cycling in SrOH. Appendix B provides the details of how FCFs were calculated.

For polyatomic molecules with inherent symmetry, there are specific selection rules for vibrational transitions. Just like in diatomics, for allowed electronic transitions the strength of the vibronic components is determined by the value of the overlap integral $\int \psi^*_{v'} \psi_{v''} d\tau_v$. However, for the integral to be nonzero the product of the vibrational wavefunctions $\psi^*_{v'} \psi_{v''}$ must be totally symmetric with respect to all symmetry operations permitted by the point group to which the molecule belongs. Since the two vibrational levels must have the same vibrational species (i.e. $\Sigma^+ - \Sigma^+$

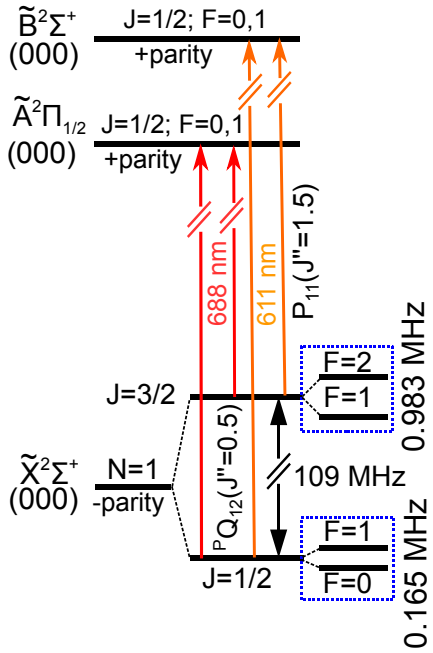


Figure 2.5.2: Relevant rotational, fine and hyperfine structure of SrOH. Rotationally closed excitations on the $\tilde{X}-\tilde{A}$ and $\tilde{X}-\tilde{B}$ electronic transitions are shown with red and orange upward arrows, correspondingly. The unresolved hyperfine splittings have been previously measured [121] and are smaller than the natural linewidth of the electronic transitions [122].

or $\Pi-\Pi$), the following selection rules apply to degenerate vibrations v_2 in SrOH: $\triangle l_2 = 0$ and $\triangle v_2 = 0, \pm 2 \pm 4, \ldots$ While $\triangle l_2 \neq 0$ transitions are strongly suppressed they have been previously observed for SrOH and CaOH and calculations in Appendix C provide the estimation of such forbidden bands.

In order to ensure that upon the electronic excitations SrOH molecules decay to the same rotational level we employ $N'' = 1 \rightarrow N' = 0$ rotational transition that prevents decays to other rotational levels because of the parity selection rule $\triangle P = \pm 1$. Figure 2.5.2 shows the the fine structure of the rotationally closed transitions used to achieve optical cycling in SrOH. Spin-rotation splitting of ~ 110 MHz can be easily addressed with an acousto-optic modulator and the hyperfine structure is smaller than the natural linewidth of the electronic transitions (~ 7 MHz). Because $F'' > F'$, for a given laser polarization there exist dark magnetic sublevels which do not couple to exciting laser light. Figure 2.5.3 shows allowed optical transitions for excitation with π polarized light and demonstrates the presence of dark $m''_F = \pm 2$ magnetic sublevels. Because of the presence

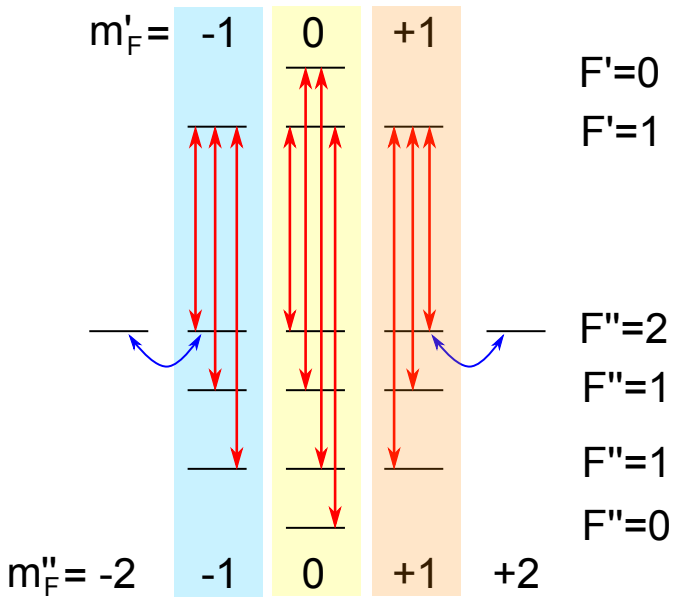


Figure 2.5.3: Hyperfine/Zeeman structure for SrOH during the photon cycling process (for clarity, relative splittings are not to scale). Allowed transitions for driving with π polarized laser light are indicated with arrows. Effectively, three separate transition bands are created (indicated with colored regions) that are mixed together because of the polarization of the spontaneously emitted photon is not controlled. Dark magnetic sublevels with $m_F'' = \pm 2$ can be remixing via Zeeman precession in the presence of an external magnetic field as indicated in the figure. With stimulated deexcitation processes, the polarization of the emitted photon can be controlled providing advantages for molecular slowing and cooling as discussed in Chapter 7.

of the unpaired electron on the strontium atom, magnetic field can be used to precess dark magnetic sublevels back into the bright states as shown in Fig. 2.5.3. Magnetic field of 10 gauss will give precession rates of $\sim 10\,\mathrm{MHz}$ enabling rapid optical cycling.

2.6 Conclusions

While the structure of polyatomic molecules can be significantly more complicated compared to atoms and diatomic molecules, optical cycling still appears possible for some species. SrOH provides an ideal testing ground for optical cycling and laser cooling of polyatomics because of its linear geometry, diagonal Franck-Condon factors, short radiative lifetimes, and convenient electronic transitions. However, additional vibrational states could potentially lead to complications as the number of scattered photons is increased.

Chapter 3

Cryogenic Production and Dynamics of SrOH

Previously, SrOH has been produced in the laboratory in the Broida ovens and supersonic beams. However, the efficiency of direct laser cooling of molecules in such experiments would be inhibited by the limited interaction time because of the fast molecular velocity in the laboratory frame. Thus, it became important to produce large numbers of SrOH molecules via cryogenic buffer-gas cooling in order to perform high resolution spectroscopy to accurately determine various transitions required for laser cooling as well as a crucial step towards producing slow buffer-gas beams for laser manipulation. Since SrOH has never been produced at cryogenic temperatures before, we carefully characterized its cooling dynamics and measured collisional properties with helium buffer gas at 2 K.

The study and control of cold atom-molecule collisions lies at the interface of physics and chemistry [1, 5, 58]. The diversity and complexity of internal molecular structures and molecular interactions provide new possibilities in precision measurement [24, 71], quantum information science [29, 123], condensed-matter physics [35], and controlled chemistry [5]. Detailed understanding of low temperature molecular collisions provides important information necessary for further development of these applications.

Compared to atomic collisions [124], low-temperature collisions of diatomic molecules are much less understood. Recently, however, significant progress has been made [125–127]. Experimental measurements of low energy collisions between simple polyatomic species (like linear triatomics) and atoms can provide crucial input for advancing theoretical models. Supersonic jet beams (sometimes Stark decelerated [128, 129]), atom association [44, 130, 131], and buffer-gas cooling [3, 132, 133] are the main experimental tools for exploring molecular collisions in the cold (1 K) and ultracold (1 μK) temperature regimes. The cold, rarefied buffer-gas environment offers a way to study cooling and molecular collisions with precise control of helium buffer-gas density and cell temperature. The efficiency of quenching vibrational motion during the atom-molecule collisional process at low temperature has been recently measured for several systems [134–137].

In this chapter, we explore inelastic collisions between strontium monohydroxide (SrOH) and helium (^{4}He) at 2.2 K. Our measurements probe the intermediate range of vibrational energy spacings, compared to previous low temperature collisional results [135–138]. For the excited Sr-O stretching vibrational mode of SrOH, we observe rapid rotational quenching and translational cooling followed by a slower vibrational quenching to the ground vibrational level. Vibrational quenching cross sections are determined with high accuracy. Our work extends the study of vibrational relaxation in cold atom-molecule collisions to linear polyatomic radicals and contributes to an overall physical picture of the dependence of quenching rates on vibrational energy spacing in low energy collisions, providing an important benchmark for theory. Additionally, we also measured the strength of the off-diagonal Franck-Condon factor for the $\tilde{X} - \tilde{A}$ electronic transition in order to confirm the feasibility of scattering multiple photons per molecule and benchmark our theoretical calculations.

3.1 Cryogenic buffer-gas cooling of SrOH

To create cold SrOH molecules we use laser ablation in combination with buffer-gas cooling [79]. A schematic diagram of the experimental apparatus is shown in Fig. 3.1.1. SrOH ($\tilde{X}^2\Sigma^+$)

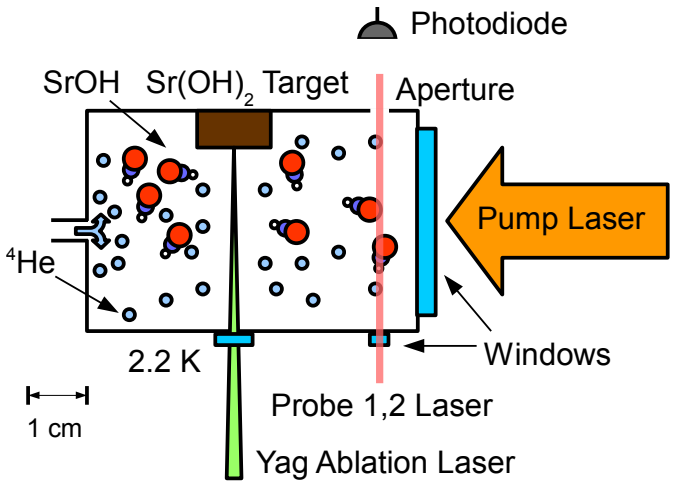


Figure 3.1.1: Schematic of the apparatus. Hot SrOH molecules produced during laser ablation of a $Sr(OH)_2$ target quickly cool translationally and rotationally after colliding with cold (~ 2 K) helium buffer gas. Thermalization dynamics are studied using a probe laser to observe molecular absorption. An optical pumping beam is used to populate $\tilde{X}$ (100) vibrational level to measure the quenching rate.

molecules are introduced into the gas phase using pulsed Nd:YAG laser ablation at 532 nm of a $Sr(OH)_2$ solid precursor with a pulse energy of $\sim 15\,\mathrm{mJ}$ and duration of $\sim 5\,\mathrm{ns}$. We continuously flow ^{4}He buffer gas into a 2.5-cm-diameter cell at rates of $0.5-10$ standard cubic centimeters per minute (SCCM). The cell is thermally anchored to a pumped helium reservoir at a temperature of $T \sim 2.2\,\mathrm{K}$. The helium density in a cell can be varied between $n_{\mathrm{He}} \approx 1\times10^{15} - 1\times10^{16}\,\mathrm{cm}^{-3}$, resulting in the typical mean time between molecule-helium diffusive collisions of $\tau \sim 0.6-0.06\,\mu\mathrm{s}$. The typical SrOH density in our experiment is a very small fraction of the helium density $n_{\mathrm{SrOH}} \approx 10^9\,\mathrm{cm}^{-3}$. A detailed description of the cryogenic apparatus used in this experiment is provided by Ref. [84].

Laser absorption spectroscopy is performed in the cell to monitor molecule production and thermalization dynamics. SrOH in the ground and excited vibrational levels is detected using "diagonal" $\tilde{A}^2\Pi_{1/2} \leftrightarrow \tilde{X}^2\Sigma^+$ transitions. We use external-cavity diode lasers (ECDLs) at 688 nm with a typical detection power of $P \sim 5\,\mu\mathrm{W}$ and a beam diameter of $\text{Ø} \sim 1\,\mathrm{mm}$. We employ the "off-diagonal" excitation $\tilde{A}^2\Pi_{1/2}(100) \leftarrow \tilde{X}^2\Sigma^+(000)$ at 662 nm (25 mW for $\text{Ø} \sim 2\,\mathrm{cm}$) followed by $\tilde{A}^2\Pi_{1/2}(100) \rightarrow \tilde{X}^2\Sigma^+(100)$ spontaneous emission ($\tau_{\mathrm{sp}} \approx 30\,\mathrm{ns}$) for optical pumping of ground

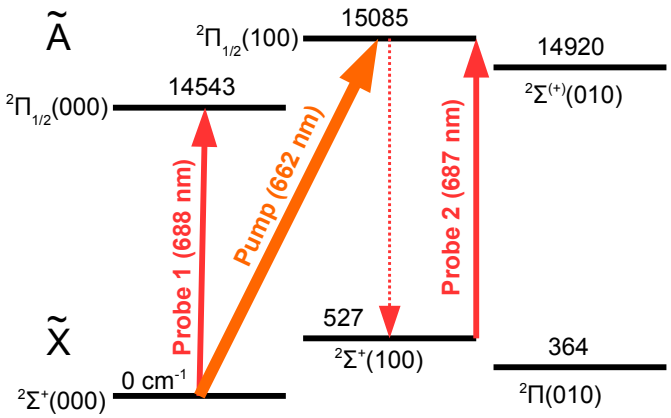


Figure 3.1.2: Optical pumping and detection procedure for SrOH. The energies are specified in cm^{-1} and taken from Ref. [114]. The vibrational quantum numbers (nml) correspond to the Sr$\leftrightarrow$OH stretching mode (n), the Sr-O-H bending mode (m) and the SrO$\leftrightarrow$H stretching mode (l). Rotational states are not shown at this scale. Excitation lasers are shown with solid lines. Spontaneous emission is depicted with a dashed line.

state molecules into $\tilde{X}\,(100)$ state. The relevant energy levels and lasers are shown in Fig. 3.1.2. We use a mechanical shutter to block the optical pumping beam with a closing time $t \leq 150\,\mu$s.

3.2 Results and discussion

3.2.1 SrOH-He diffusion cross section

We determine the SrOH-He diffusion cross section by measuring the time dynamics in the buffer-gas cell of molecules in the $\tilde{X}^2\Sigma^+\,(000)\,, N = 1$ state, which is the most populated rotational level at 2 K (Fig. 3.2.6). The spectrum of the ground vibrational level of cold SrOH in the first excited rotational level $(N = 1)$ is shown in Fig. 3.2.1. The normalized Doppler lineshape function is given by [20]

$$g_D\,(\nu - \nu_0) = \frac{2}{\triangle\nu_D}\sqrt{\frac{\ln(2)}{\pi}}e^{-4\ln(2)((\nu-\nu_0)/\triangle\nu_D)^2} \tag{3.2.1}$$

in terms of the Doppler FWHM, which is specified by

$$\triangle\nu_D = 2\nu_0\sqrt{\frac{2k_BT\ln(2)}{mc^2}}. \tag{3.2.2}$$

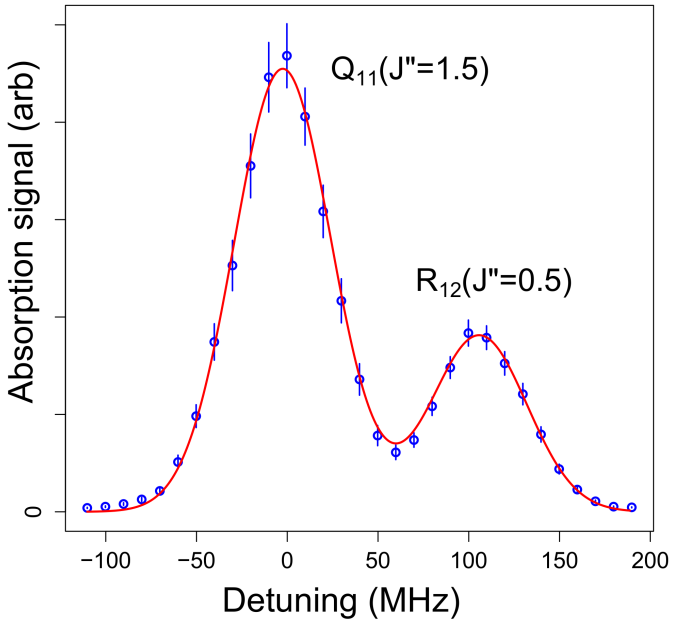


Figure 3.2.1: Spectrum of cold gas-phase SrOH molecules in the $\tilde{X}^2\Sigma^+$ (000) vibronic, first excited rotational ($N = 1$) state using $\tilde{A}^2\Pi_{1/2} \leftarrow \tilde{X}^2\Sigma^+$ electronic transition ~ 5 ms after laser ablation. The two measured peaks are for different spin-rotation components in the electronic ground state (J" $= 0.5$ and 1.5) of the $N = 1$ level. We perform a Doppler fit of the form $y = a \cdot \mathrm{e}^{-(x-b)^2/\gamma_\mathrm{D}^2}$ to each resonance line separately. Measured Doppler width $\gamma_\mathrm{D} \approx 38 \pm 1$ MHz corresponds to a translational temperature of 4.3 ± 0.1 K.

Since usually our spectrum plots are not normalized to the area of 1, we actually fit the data to the following lineshape function

$$g_{\mathrm{D}}^{(actual)} = a \times e^{-4\ln(2)((\nu-\nu_0)/\triangle\nu_{\mathrm{D}})^2} \tag{3.2.3}$$

where $(\nu - \nu_0)$ is detuning from resonance in MHz. This is the functional form we use to fit the incell and beam absorption data in order to extract the kinetic temperature of the molecules.

The time decay profile of the molecules in the $\tilde{X}\,(000)$ vibronic state is governed by the diffusion to the walls and pump-out of the cell through the aperture:

$$\frac{1}{\tau_{000}} = \frac{1}{\tau_{\mathrm{d}}} + \frac{1}{\tau_{\mathrm{p}}} \tag{3.2.4}$$

where τ_{000}, τ_{d}, and τ_{p} are the timescales for the decay of (000) vibrational mode molecules (τ_{000}) due to diffusion (τ_{d}) and cell pump-out (τ_{p}). By measuring the on-resonance absorption time profile (Fig. 3.2.2(a)) we can extract the diffusion lifetime of SrOH: $\tau_{\mathrm{d}} = \left(1/\tau_{000} - 1/\tau_{\mathrm{p}}\right)^{-1}$. For low buffer-gas flows $\tau_{\mathrm{d}}/\tau_{\mathrm{p}} < 1$ [82], and the molecule loss is primarily due to diffusion to the cell walls. Therefore, from our measurements of τ_{000} we can directly determine the diffusion lifetime of the molecules in our cell: $\tau_{\mathrm{d}} \approx \tau_{000}$.

At long times after laser ablation ($\geq 10\,\mathrm{ms}$), when higher-order diffusion modes have decayed, the in-cell $\tilde{X}\,(000)$ population profile is well fitted by a single exponential (Fig. 3.2.2(a)). We determine the SrOH-He momentum transfer cross section by measuring the diffusion lifetime of SrOH (000) mode molecules at different densities of helium buffer gas. From Fig. 3.2.2(b) we find that τ_{000} has a linear dependance on the helium density and conclude that (000) mode molecule loss is primarily dominated by diffusion. For a cylindrical cell of length L and radius r the time constant of the exponential decay for molecules diffusing through helium gas of density (n_{He}) is given by [139]:

$$\tau_{\mathrm{d}} = \frac{n_{\mathrm{He}}\sigma_{\mathrm{d}}}{\bar{v}G} \tag{3.2.5}$$

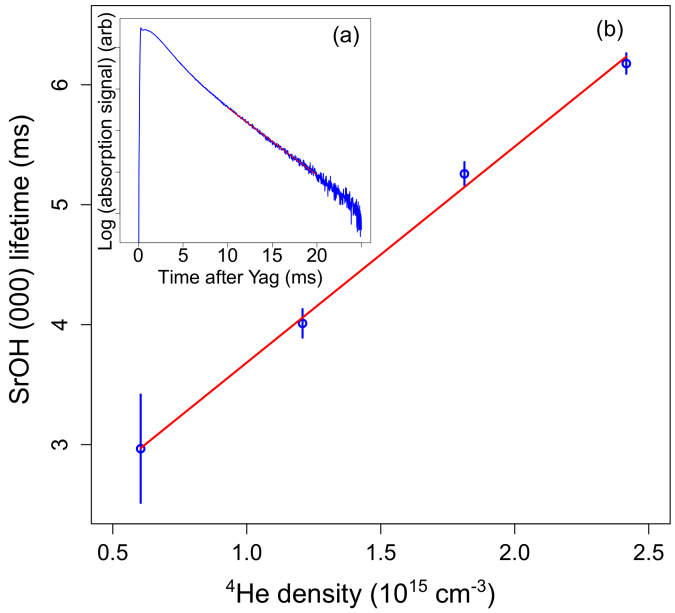


Figure 3.2.2: (a) Time decay of SrOH molecules in the (000) vibrational mode at the buffer-gas flow of 2 sccm with the linear fit shown. (b) In-cell lifetime for the ground vibronic, first excited rotational ($N = 1$) level of SrOH for various buffer-gas densities with a linear fit. For low buffer-gas flows (shown here) the molecule loss is dominated by diffusion to the cell walls.

$$G = \frac{3\pi}{32}\left(\frac{j_{01}^2}{r^2} + \frac{\pi^2}{L^2}\right) \tag{3.2.6}$$

where $\bar{v} = (8k_B T/\pi\mu)^{1/2}$ is the mean SrOH-^{4}He collision velocity at temperature T with reduced mass of the atom-molecule system μ and the diffusion cross section σ_d ($j_{01} \approx 2.405$ is the first root of the Bessel function $J_0(x)$). From Eq. 3.2.5 we determine that in the diffusive regime (τ_d/τ_p<1) the in-cell lifetime is directly proportional to the helium density, as seen in our data.

From the measurement of τ_{000} as a function of the helium density (Fig. 3.2.2(b)) using Eq. 3.2.5 we can extract the value of the diffusion cross section, $\sigma_d \approx \tau_{000}\bar{v}G/n_{He}$, finding the SrOH diffusion cross section in He at 2.2 K to be $\sigma_d\left(\text{SrOH} - ^4\text{He}\right) = (5 \pm 2) \times 10^{-14}\,\text{cm}^2$. The measured SrOH-He diffusion cross section is somewhat larger than previously measured for diatomic molecules [133, 138] at similar temperatures. The measured value of $\sigma_d\left(\text{SrOH} - ^4\text{He}\right)$ agrees with the theoretical prediction for larger polyatomic molecules colliding with helium [49].

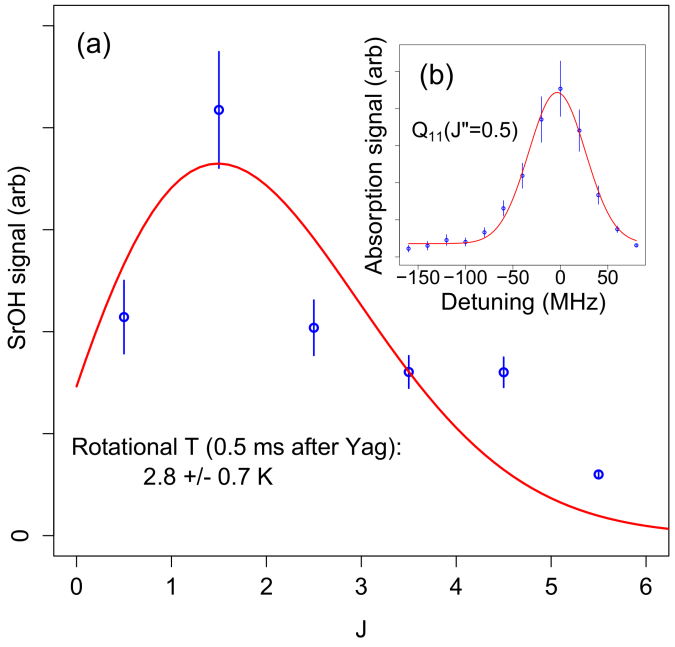


Figure 3.2.3: (a) Rotational state ($N = J - 1/2$) population for SrOH $\tilde{X}^2\Sigma^+(100)$ vibrational mode 500 μs after laser ablation. The measurement was performed using $Q_{11}(J")$ line absorption on the $\tilde{A}^2\Pi_{1/2}(100) \leftarrow \tilde{X}^2\Sigma^+(100)$ electronic transition. From the Boltzmann distribution fit, we conclude that molecules in the excited vibrational level quickly thermalize rotationally to the cell temperature of ~ 2 K. (b) Spectrum of cold gas-phase SrOH molecules in the $\tilde{X}^2\Sigma^+(100)$ vibronic, ground rotational ($N = 0$) state using $\tilde{A}^2\Pi_{1/2} \leftarrow \tilde{X}^2\Sigma^+$ electronic transition ~ 0.5 ms after laser ablation. We perform a Doppler fit of the form $y = a \cdot e^{-(x-b)^2/\gamma_D^2}$ to obtain a Doppler width $\gamma_D \approx 42 \pm 2$ MHz, corresponding to a translational temperature of 5.3 ± 0.3 K.

3.2.2 Vibrational quenching cross sections

Vibrationally excited SrOH molecules are produced during the process of laser ablation. As can be seen from Fig. 3.2.3, vibrationally excited molecules of the (100) Sr-O stretching mode quickly ($< 500\,\mu$s) thermalize rotationally to $T_r = 2.8 \pm 0.7$ K and translationally to a temperature ≤ 5.6 K. We place a bound on the translational temperature from the Doppler fit. Additional linewidth broadening mechanisms are present inside buffer-gas cells as has been seen repeatedly [138]. Vibrational temperature remains out of thermal equilibrium ($T_v \sim 400$ K) with other degrees of freedom.

In order to increase the number of molecules in the $\tilde{X}(100)$ state we optically pump SrOH molecules from the (000) mode to the (100) mode using $\tilde{A}^2\Pi_{1/2}(100) \leftarrow \tilde{X}^2\Sigma^+(000)$ electronic

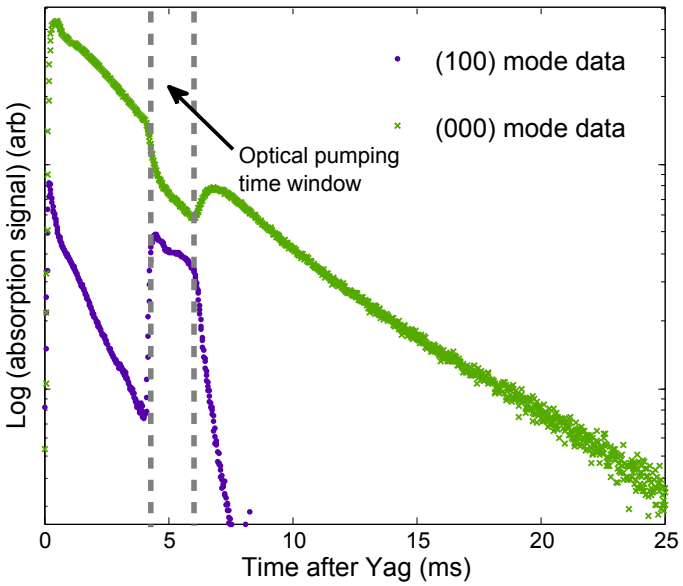


Figure 3.2.4: SrOH absorption signal vs time for different vibrational modes: vibrational ground state (000) and Sr-O stretching mode (100). The optical pumping laser excites molecules from the $\tilde{X}^2\Sigma^+(000)$ state to $\tilde{A}^2\Pi_{1/2}(100)$ state on $Q_{11}(J"=1.5)$ transition. Excited molecules predominantly decay to $\tilde{X}^2\Sigma^+(100)$ state. After the optical pumping laser is turned off, the decay of molecules in the (100) mode is dominated by vibrational quenching. We monitor populations in the different modes using $Q_{11}(J"=1.5)$ bands of the $\tilde{A}^2\Pi_{1/2} \leftarrow \tilde{X}^2\Sigma^+$ electronic transitions.

excitation (Fig. 3.1.2). Optical pumping process increases the population in $\tilde{X}(100)$ state by an order of magnitude. After the optical pumping laser is turned off, SrOH molecules in the (100) mode decay faster than those in the (000) mode (Fig. 3.2.4). The additional effect that leads to the faster decay for the (100) molecules is vibrational quenching with timescale τ_q. Using Eq. 3.2.4, we can write the decay rate of the (100) molecules in the buffer-gas cell:

$$\frac{1}{\tau_{100}} = \frac{1}{\tau_q} + \frac{1}{\tau_d} + \frac{1}{\tau_p} \tag{3.2.7}$$

In the regime where vibrational quenching dominates other loss processes ($\tau_q < \tau_d, \tau_p$), the measurement of the (100) lifetime gives quenching time: $\tau_{100} \approx \tau_q = \left(\Gamma_q n_{He}\right)^{-1}$. As can be seen from Fig. 3.2.5(a), the in-cell lifetime of the molecules in the $\tilde{X}(100), N=1$ state is inversely proportional to the helium density which indicates that (100) molecule loss is dominated by vibrational quenching.

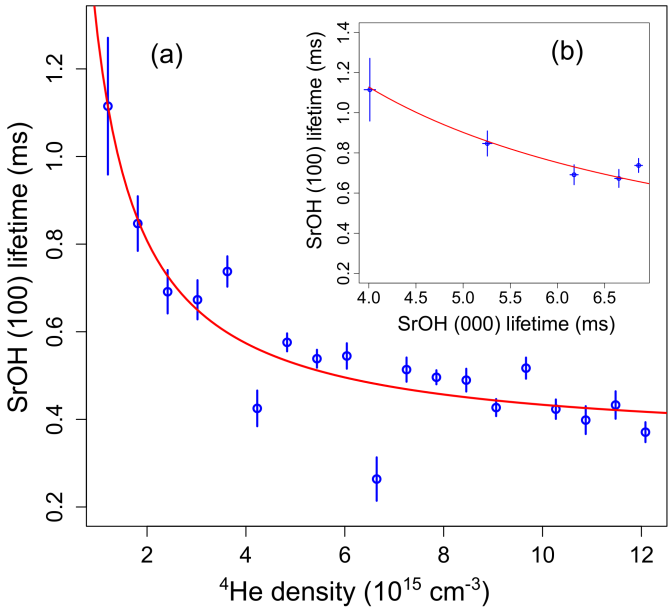


Figure 3.2.5: (a) Observed vibrational quenching for $\tilde{X}^2\Sigma^+(100)$, $N=1$ state of SrOH in collisions with ^{4}He at 2 K. Helium flow is proportional to the in-cell buffer gas density. (b) The plot of (100) mode lifetime against (000) mode lifetime for a range of in-cell helium densities. The fit is to the expected functional form $\tau_{100} \propto \Gamma/\tau_{000}$.

The dimensionless ratio of elastic to inelastic collision rates γ_{100} indicates the rate of translational versus vibrational equilibration of a molecular sample and can be determined from our measurements by:

$$\gamma_{100} = \frac{\Gamma_d}{\Gamma_q} = \frac{\sigma_d \bar{v}}{\left(\tau_q n_{He}\right)^{-1}} = \bar{v}^2 G \tau_d \tau_q \tag{3.2.8}$$

where we used Eq. 3.2.5 in the last step. After extracting lifetimes for the decays of the (000) and (100) vibrational modes (Fig. 3.2.5(b)), we calculate γ_{100} using an approximate form of Eq. 3.2.8:

$$\gamma_{100} \approx \bar{v}^2 G \tau_{000} \tau_{100} \tag{3.2.9}$$

at various buffer-gas densities. The measured value for SrOH(100)-^{4}He collisions is $\gamma_{100} = 680 \pm 80$ at 2.2 K, i.e. SrOH $\tilde{X}(100)$ molecules undergo approximately 700 momentum changing collisions before quenching vibrationally.

We can also place an upper bound on γ_{010} for the excited bending mode. The number of

collisions necessary for translational cooling of vibrationally excited SrOH molecules produced during laser ablation is given by [140]:

$$N = -\kappa \ln\left[\frac{T_f - T_{bg}}{T_i}\right] \approx 100 \tag{3.2.10}$$

for $T_f = 4\,\mathrm{K}$, $T_{bg} = 2\,\mathrm{K}$ and the coefficient $\kappa \equiv (m_{\mathrm{SrOH}} + m_{\mathrm{He}})^2 / (2 m_{\mathrm{SrOH}} m_{\mathrm{He}})$. Therefore, if $\gamma > 100$, the sample will cool translationally and rotationally, before collision-induced vibrational relaxation, leaving a metastable population, as was seen in the (100) mode of SrOH. However, if $\gamma < 100$ vibrationally excited molecules will quench before they cool translationally and rotationally. Molecules in the $\tilde{X}^2\Pi\,(010)$ vibronic state were previously detected in supersonic beams for SrOH [141] and CaOH [142] produced using pulsed laser ablation at 300 K. Experimentally, when measuring absorption on $\tilde{A}^2\Sigma^{(+)}\,(010) \leftarrow \tilde{X}^2\Pi\,(010)$ band we saw no evidence of molecules in the excited bending mode. This rapid vibrational thermalization is due to inelastic vibrational collisions with helium. This allows us to place an upper bound $\gamma_{010} < 100$, which is consistent with direct experimental measurements for low-lying bending modes in large molecules [137]. In addition to vibrational quenching, there could potentially be other unexpected contributions to the loss of (010) molecules in our experiment like state dependent chemical reactions.

The measured values of γ can be used to calculate the absolute values of collisional quenching cross sections:

$$\sigma_{\mathrm{q}} = \sigma_{\mathrm{d}} / \gamma \tag{3.2.11}$$

Combining our measurements of γ and σ_{d} we obtain the following values for the vibrational quenching cross sections $\sigma_{\mathrm{q}}\,(100) = (7 \pm 2) \times 10^{-17}\,\mathrm{cm}^2$ and $\sigma_{\mathrm{q}}\,(010) > 5 \times 10^{-16}\,\mathrm{cm}^2$.

3.2.3 Rotational thermalization

Rotational thermalization dynamics for SrOH molecules in (100) and (000) vibrational modes can be extracted by monitoring $Q_{11}\,(J')$ transitions for different rotational levels. From the data shown in Fig. 3.2.3 and 3.2.6, we estimate that rotational temperature thermalizes to $T_{\mathrm{r}} \sim 3\,\mathrm{K}$ within 1

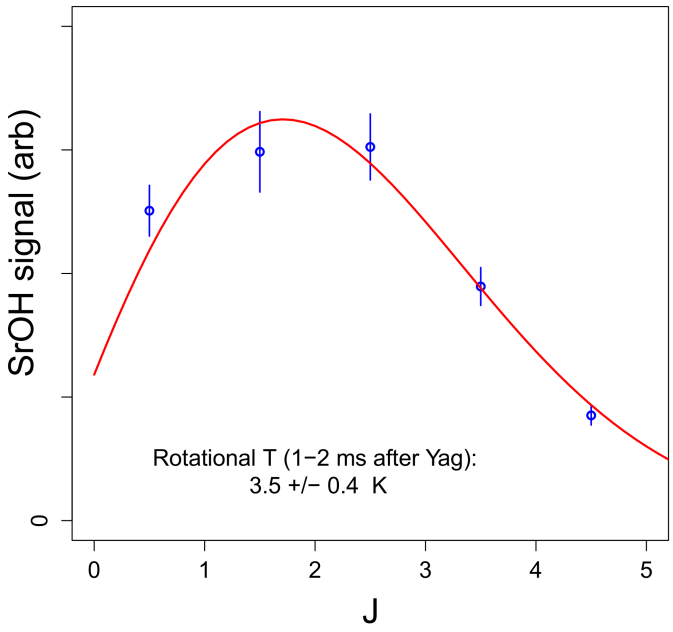


Figure 3.2.6: Thermal distribution of rotational levels ($N = J - 1/2$) for the ground vibrational mode (000) of SrOH 1-2 ms after laser ablation. From the Boltzmann distribution fit $y = a\,(2J+1)\,\mathrm{e}^{-BJ(J+1)/T}$ ($B_{\mathrm{SrOH}} = 0.36\,\mathrm{K}$), we obtain the rotational temperature $T = 3.5 \pm 0.4\,\mathrm{K}$.

ms after ablation. Since the mean time between collisions is $< 1\,\mu$s we conclude that fewer than 1,000 collisions are necessary for complete rotational thermalization after laser ablation. The initial rotational temperature following laser ablation process in a similar experiment was measured to be $> 300\,\mathrm{K}$ [143]. Typically, initial translational temperature of species immediately after the ablation process is $\sim 1000\,\mathrm{K}$ [79, 80]. Precise measurements of rotational quenching cross sections can be performed by driving rotational population out of thermal equilibrium with microwave pulses but it is beyond the scope of our work.

3.2.4 Franck-Condon factor measurements

Diagonal Franck-Condon (FC) factors are required for scattering thousands of photons necessary for laser cooling or slowing of molecules [144]. Experimental measurements of these factors have focused on diatomic molecules thus far [145–147]. We measure the ratio of FC factors by comparing the ratio of the absorption signals R_{sig} for $\tilde{A}^2\Pi_{1/2}\,(100) \leftarrow \tilde{X}^2\Sigma^+\,(000)$ and $\tilde{A}^2\Pi_{1/2}\,(000) \leftarrow \tilde{X}^2\Sigma^+(000)$ transitions using $Q_{11}\,(J\text{"} = 1.5)$ lines shown in Fig. 3.2.7(b).

3.2.4.1 Off-diagonal Franck-Condon factor from molecular absorption data

In this section, we describe how the formula for the off-diagonal Franck-Condon factor was derived from the ratio of the two absorption signals. The detection signal from the fraction of laser light absorbed is given by [148]:

$$Sig = \triangle I/I = -n_{\mathrm{m}}\sigma l \tag{3.2.12}$$

where σ is the absorption cross section for a Doppler broadened line, n_{m} is the molecular density and l is the width of the cell. Thus,the ratio of the two absorption signals with the same ground state is:

$$\frac{Sig_1}{Sig_2} = \frac{\sigma_1}{\sigma_2} \tag{3.2.13}$$

For a linear polyatomic molecule the absorption cross section for a Doppler broadened line in the electronic transition is given by [20]:

$$\sigma = \frac{2\pi^2 \nu q_{v'-v"} |R_e|^2 S_{J"}^{\triangle J}}{3\varepsilon_0 hc\,(2J"+1)} g_{\mathrm{D}}\,(\nu - \nu_0) \tag{3.2.14}$$

where $q_{v'-v"}$ is the Franck-Condon factor, R_e is the electronic transition dipole moment, and $S_{J"}^{\triangle J}$ is the rotational line strength term. The normalized Doppler lineshape function is given in Eq. 3.2.1 . Combining results of Eq. 3.2.13 and 3.2.14 we obtain the following expression for the ratio of absorption signals in our experiment:

$$\frac{Sig_1}{Sig_2} = \frac{\nu_{100\leftarrow 000}}{\nu_{000\leftarrow 000}} \times \frac{q_{100\leftarrow 000}}{q_{000\leftarrow 000}} \tag{3.2.15}$$

where Sig_1 is an absorption signal for the off-diagonal electronic transition $\tilde{A}^2\Pi_{1/2}\,(100) \leftarrow \tilde{X}^2\Sigma^+\,(000)$ and Sig_2 is an absorption signal for the diagonal transition $\tilde{A}^2\Pi_{1/2}\,(000) \leftarrow \tilde{X}^2\Sigma^+\,(000)$. Both of the signals are for $Q_{11}\,(J" = 1.5)$ lines. The measured frequency ratio is:

$$\frac{\nu_{100\leftarrow 000}}{\nu_{000\leftarrow 000}} = \frac{452.235667\,\mathrm{THz}}{435.984522\,\mathrm{THz}} \approx 1.037 \tag{3.2.16}$$

Therefore, the ratio of Franck-Condon factors is:

$$R_{FC} = \frac{q_{100\leftarrow 000}}{q_{000\leftarrow 000}} = \frac{Sig_1}{Sig_2} \times \frac{1}{1.037} \tag{3.2.17}$$

The sum of the FCFs is constrained in the following way:

$$q_{100\leftarrow 000} + q_{000\leftarrow 000} \leq 1 \tag{3.2.18}$$

From Eq. 3.2.17 and 3.2.18 we can estimate the off-diagonal FCF from the measured ratio R_{FC}:

$$q_{100\leftarrow 000} = \frac{1}{1 + (R_{FC})^{-1}} \tag{3.2.19}$$

where we assumed $q_{100\leftarrow 000} + q_{000\leftarrow 000} = 1$ since $q_{200\leftarrow 000} \ll q_{100\leftarrow 000} \ll q_{000\leftarrow 000}$.

3.2.4.2 Measurements of the off-diagonal Franck-Condon factor

Since the absorption cross section σ for a Doppler broadened line in an electronic transition is proportional to the product of the excitation frequency (ν) and FC factor ($q_{v'-v"}$) as $\sigma \propto \nu q_{v'-v"}$ [20, 149], the ratio of FC factors from our measurements is given by:

$$R_{FC} = \frac{\nu_{000\leftarrow 000}}{\nu_{100\leftarrow 000}} \times R_{sig} \tag{3.2.20}$$

where R_{sig} is the ratio of the absorption signals and ν is the frequency of the corresponding transition. The Born-Oppenheimer approximation and the Franck-Condon separation of electronic and vibrational motions was applied to the Sr-O stretching mode in the $\tilde{A}$ state of SrOH [20, 150]. We obtain $R_{sig} = 5.2 \pm 0.2\%$ which gives $R_{FC} = 5.0 \pm 0.2\%$. Combining our measurement of R_{FC} with the sum condition $FC_{000-000} + FC_{100-000} \leq 1$, we obtain the following value for the off-diagonal factor $FC_{100-000} = \left(4.8 \pm 0.2_{\text{stat}} \pm 0.8_{\text{syst}}\right) \times 10^{-2}$. The systematic error contribution is estimated from the laser frequency lock error $\triangle\nu \approx 10\,\text{MHz}$ and using the Doppler lineshape function for the measured linewidth $\triangle\nu_{\text{D}} \approx 40\,\text{MHz}$. From Eq. 3.2.14 and 3.2.1 we find that the ratio of the

absorption signals is proportional to:

$$R_{sig} \propto \frac{g_{\mathrm{D}}\left(\triangle \nu_{100\leftarrow 000}\right)}{g_{\mathrm{D}}\left(\triangle \nu_{000\leftarrow 000}\right)} = e^{-4\ln 2\left(\left(\triangle \nu_{100\leftarrow 000}\right)^2-\left(\triangle \nu_{000\leftarrow 000}\right)^2\right)/\left(\triangle \nu_{\mathrm{D}}\right)^2} \tag{3.2.21}$$

where $\triangle\nu_{\mathrm{D}}$ is the Doppler linewidth and $\triangle\nu_{v'00\leftarrow 000}$ is a detuning from resonance. Thus, if both detunings have the same magnitude $|\triangle\nu_{100\leftarrow 000}| = |\triangle\nu_{000\leftarrow 000}|$, the ratio in Eq. 3.2.21 will be 1. The measured Doppler linewidth in our experiment is $\triangle\nu_{\mathrm{D}} \approx 40\,\mathrm{MHz}$ and the estimated error in the laser frequency lock is $\triangle\nu_{v'00\leftarrow 000} \approx 10\,\mathrm{MHz}$ which results in the following estimated relative systematic error:

$$\frac{\delta R_{sig}}{R_{sig}} = 1 - e^{-4\ln 2(1/4)^2} \approx 16\% \tag{3.2.22}$$

This corresponds to an absolute systematic error of 0.8% in the measured value of $FC_{100-000} = 4.8\%$.

We assume a simple harmonic oscillator model of molecular potentials [151] to estimate $FC_{200-000} \leq 1\times 10^{-3}$. The estimation of $FC_{200-000}\left(\tilde{A}-\tilde{X}\right)$ was done using the closed-form approximate expression for FCF that uses reduced mass (μ), vibrational frequency (ω_e), and equilibrium internuclear distance (r_e) in both the ground and excited states [151]:

$$FC_{2-0}\left(\tilde{A}-\tilde{X}\right) = \left(S^4/8\right)\exp\left(-S^2/2\right) \tag{3.2.23}$$

where the subscript refers to the Sr-O stretching mode vibrational quantum number v_1 and $S \equiv \sqrt{\mu_{\mathrm{Sr-O}}\tilde{\omega}_e}\triangle r_e/5.807$ for $\tilde{\omega}_e^{1/2} \equiv 2\sqrt{\omega_e\left(\tilde{A}\right)\omega_e\left(\tilde{X}\right)}/\left(\sqrt{\omega_e\left(\tilde{A}\right)+\omega_e\left(\tilde{X}\right)}\right)$ in $\left(\mathrm{cm}^{-1}\right)^{1/2}$, $\mu_{\mathrm{Sr-O}}$ in amu and $\triangle r_e \equiv r_e\left(\tilde{A}\right) - r_e\left(\tilde{X}\right)$ in Angströms. The molecular constants used were from Ref. [114, 152].

At low vibrational quantum numbers these approximate formulae agree well with more complex models of molecular vibrations. The model assumes a simple harmonic oscillator approximation which is applicable to the Sr-O stretching mode in SrOH because the anharmonic contribution is negligible ($x_e\omega_e/\omega_e \approx 2\times 10^{-3}$ for the ground electronic state $\tilde{X}$ from the data in Ref. [113]).

From the comparison of approximate FCFs found using Eq. 3.2.23 for the isoelectronic molecule SrF and those calculated using the accurate first-order Rydberg-Klein-Rees procedure in Ref. [153] we estimate the relative error on the calculated off-diagonal FCF for SrOH to be $< 1\%$.

We can also use measured values of $FC_{000-000}$ and $FC_{000-100}$ to estimate the off-diagonal factor $FC_{000-200}$. In the harmonic oscillator approximation, using expressions in Ref. [151] and definitions provided above, we obtain the following ratios:

$$\frac{FC_{0-1}}{FC_{0-0}} = S^2/2 \tag{3.2.24}$$

$$\frac{FC_{0-2}}{FC_{0-1}} = S^2/4 \tag{3.2.25}$$

where the subscript refers to the Sr-O stretching mode vibrational quantum number. Therefore, we get the following estimation:

$$FC_{0-2} = \frac{FC_{0-1}^2}{2FC_{0-0}} \approx 10^{-3} \tag{3.2.26}$$

As previously mentioned, the break down of the harmonic oscillator approximation is on the order of 10^{-3} for SrOH [113].

The extracted value of the diagonal factor $FC_{000-000} = (95.2 \pm 0.8) \times 10^{-2}$ together with the sum condition $FC_{000-000} + FC_{000-100} \leq 1$ lead to a value for the off-diagonal factor of $FC_{000-100} = \left(4.8^{+0.8}_{-0.9}\right) \times 10^{-2}$. The error in the measured $FC_{000-100}$ accounts for a possible decay to $\tilde{X}\,(200)$ with the estimated FC factor of $FC_{000-200} \approx \frac{FC_{000-100}^2}{2FC_{000-000}} \approx 1.2 \times 10^{-3}$ in the harmonic oscillator model [151]. Our result indicates that the SrOH $\tilde{A} - \tilde{X}$ Franck-Condon array is highly diagonal, and it should be possible to scatter $\sim 10^3$ photons for SrOH using two lasers ($\lambda_{\tilde{A}(000)\leftarrow\tilde{X}(000)}$ and $\lambda_{\tilde{A}(000)\leftarrow\tilde{X}(100)}$) before the molecules will decay to the $\tilde{X}\,(200)$ state. In order to determine branching ratios to the excited bending vibrations in the $\tilde{X}$ state a more detailed experimental and theoretical analysis is necessary, which will be discussed later in the thesis. By driving $N' = 0 \leftarrow N" = 1$ transitions, the rotational loss channel can be eliminated [154]. In addition to the possibility of laser cooling, this may also have important applications for sensitive molecule detection in the

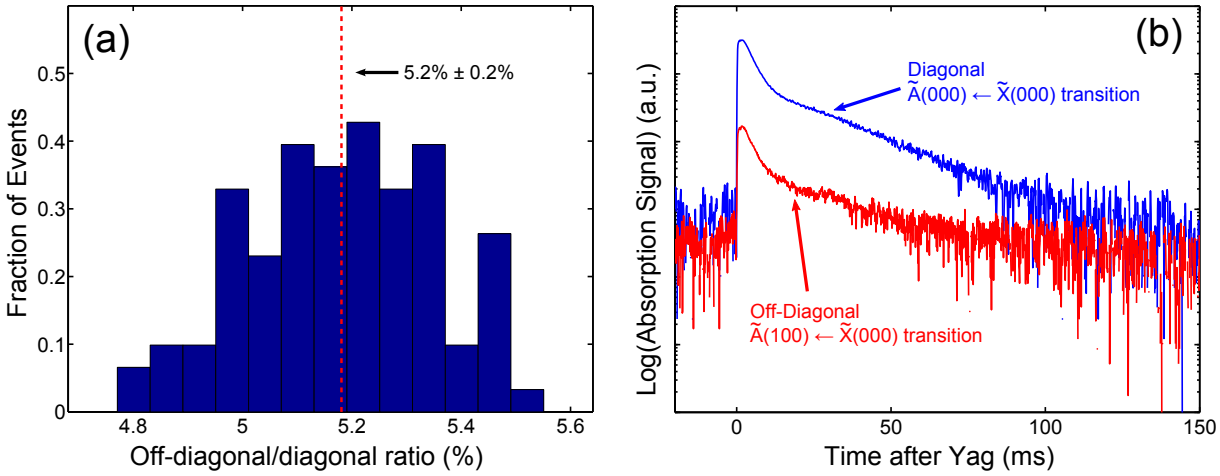


Figure 3.2.7: (a) Histogram of the ratio of the absorption signals for the $Q_{11}(J\text{''}=1.5)$ resonant lines in SrOH exiting the diagonal $\tilde{A}^2\Pi_{1/2}(000) \leftarrow \tilde{X}^2\Sigma^+(000)$ and off-diagonal $\tilde{A}^2\Pi_{1/2}(100) \leftarrow \tilde{X}^2\Sigma^+(000)$ electronic transitions. We observe an average value of 5.2% with a standard deviation of 0.2%. Figure (b) shows the corresponding absorption signals as a function of time. To determine the histogram of the measured ratios, only the signal between 0.5 ms and 10 ms is used in the analysis.

magnetic trap environment [83]. Spectrum of the rotationally closed transition in SrOH is shown in Fig. 3.2.8. The spin-rotation splitting of ~ 110 MHz is characteristic of the ground $N=1$ state. Both of the spin-rotation components separated by ~ 110 will need to be addressed during the photon cycling process.

3.2.5 Measurement of the dominant repumper frequency

As we have determined, upon the electronic excitation using the $\tilde{X}(000) \rightarrow \tilde{A}(000)$ transition, approximately 5% of the molecules will decay to the excited Sr-O stretching (100) vibrational state. Thus, on average each molecule will scatter only 20 photons before decaying to the dark (100) vibrational level. In order to bring lost molecules back into the photon cycling process, we need to optically pump them back into the ground vibrational level $\tilde{X}(000)$. While there are two possibilities for achieving this goal by optically exciting either the $\tilde{X}(100) \rightarrow \tilde{A}^2\Pi_{1/2}(000)$ or $\tilde{X}(100) \rightarrow \tilde{B}(000)$ we chose the second option since optical pumping through the $\tilde{B}$ state will allow to decouple main cycling laser from the repumping light and lead to higher scattering rate

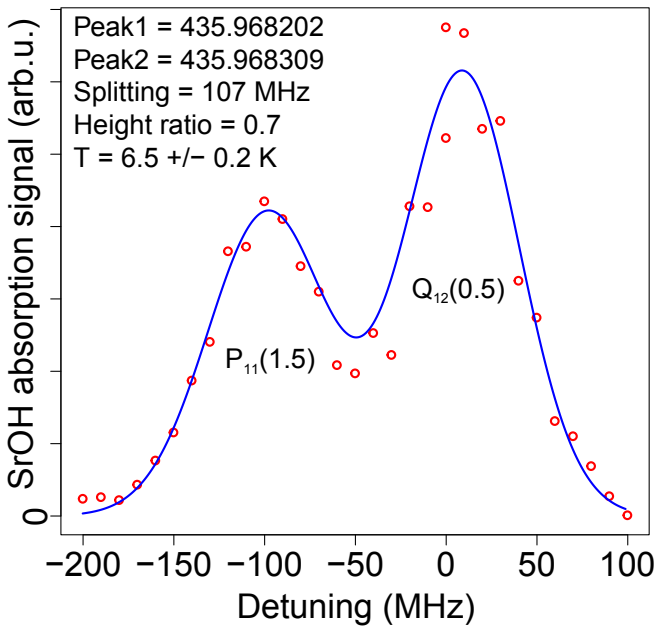


Figure 3.2.8: Spectrum of the rotationally closed transition in SrOH on the $\tilde{X}^2\Sigma^+(000) - \tilde{A}^2\Pi_{1/2}(000)$ transition. A relatively hot temperature extracted from the Doppler fit is potentially due to the overlap of the two lines that leads to additional broadening.

and thus larger radiative force.

In order to measure the spectrum of the $\tilde{X} \rightarrow \tilde{B}$ off-diagonal repumping transition, we continuously probed in-cell absorption on either one of the two spin-rotation components of the $P(N'' = 1)$ transition of the $\tilde{X}(100) \rightarrow \tilde{B}(000)$ vibronic band at 631 nm while optically pumping molecules into the excited vibrational level using $\tilde{X}(000) \rightarrow \tilde{A}(100)$ transition at 662 nm. While for the vibrational quenching studying we turned the optical pumping light for a fixed time duration, in this spectroscopy experiment we performed optical pumping in the $\tilde{X}(100)$ state continuously in order to optimally enhance the signal in the excited vibrational level. Figure 3.2.9 shows the absorption spectrum in-cell for both SR components of the rotationally closed $P_1(N'' = 1)$ branch of the $\tilde{X}(100) \rightarrow \tilde{B}(000)$ transition. By comparing the results of the $P_1(N'' = 1)$ spectrum for the $\tilde{X} - \tilde{A}$ transition data in Fig. 3.2.8 vs $\tilde{X} - \tilde{B}$ transition data in Fig. 3.2.9, we can see that while the SR splitting remains approximately the same within the experimental resolution in our measurements, the relative intensities of the two SR components are inverted because of the different symmetries of the excited electronic state.

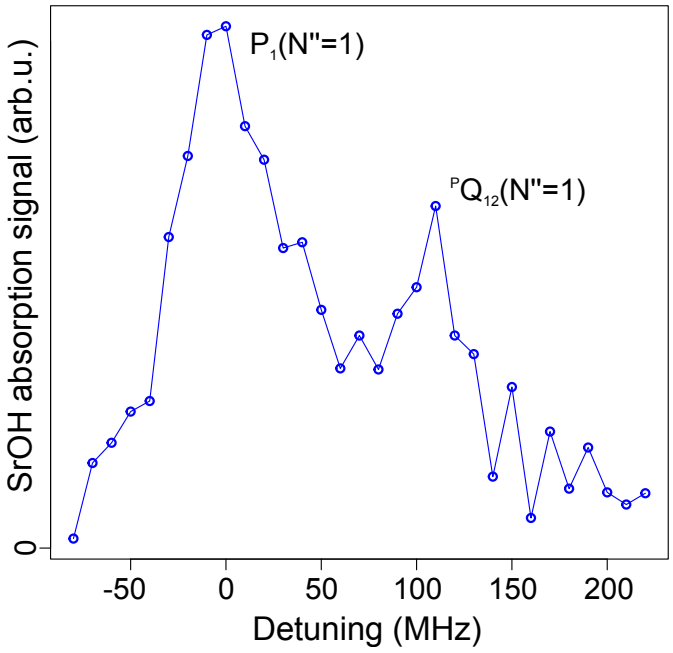


Figure 3.2.9: SrOH absorption spectrum inside the cryogenic buffer-gas cell for the $\tilde{X}^2\Sigma^+(100) \rightarrow \tilde{B}^2\Sigma^+(000)$ transition. The frequency offset is 475.171730 THz and the splitting between the peaks is 107 MHz.

3.3 Conclusions

Our measurement of the collisional quenching coefficient γ_{100} and an upper bound on γ_{010} in SrOH-^{4}He collisions provide important information on the interactions between polyatomic molecules and ^1S-state atoms at temperatures near 1 K. In Table 3.1, we compare our measurements with other experimental values for molecules in the similar collisional energy regime (multiple-partial waves and ~ 1 K).

Since SrOH is a relatively heavy molecule with a large density of rovibrational states it is not surprising that vibrational quenching proceeds relatively quickly. Our results indicate that buffer-gas cooling with helium can efficiently thermalize not only translational and rotational but also vibrational degrees of freedom in polyatomic molecules with low frequency vibrational modes ($\omega < 600\,\mathrm{cm}^{-1}$) at timescales < 1 ms. Study of SrOH-He cold collisions provides benchmark information on the dependence of vibrational quenching rates on the frequencies of molecular vibrations. The experimental techniques demonstrated in this work can be easily extended to

System	γ	ω, cm^{-1}	T, K
NH-^{3}He [135]	$> 5 \times 10^4$	3093	0.6
CaH-^{3}He [138]	$> 9 \times 10^5$	1258	0.5
ThO-^{3}He [136]	2×10^4	896	1.2
SrOH(100)-^{4}He	700	527	2.2
SrOH(010)-^{4}He	< 100	364	2.2
PhCN-^{4}He [137]	200	372	6

Table 3.1: Comparison of the vibrational quenching results for SrOH with other experiments at cryogenic temperatures.

the study of buffer-gas cooling and inelastic collisions for other linear polyatomic molecules (for example CaOH and BaOH). Future work can include experimental investigation of vibrational quenching for different modes in planar (e.g. $SrNH_2$) and symmetric-top (e.g. $SrCH_3$) molecules.

Additionally, we have measured the off-diagonal Franck-Condon factor for the $\tilde{X} - \tilde{A}$ transition that will be the limiting dark vibrational state for implementing photon cycling in SrOH. Our measurement of $FC_{000-100} = \left(4.8^{+0.8}_{-0.9}\right) \times 10^{-2}$ is consistent with the predicted value we calculated using the harmonic oscillator approximation. Using in-cell absorption spectroscopy we have also identified both of the spin-rotational components of the $P(N'' = 1)$ branch of the $\tilde{X}\,(100) \rightarrow \tilde{B}\,(000)$ vibronic transition that will be used for returning lost molecules back to the cycling process. Therefore, results presented in this chapter provide crucial information on cryogenic SrOH production and dynamics as well as its high-resolution spectroscopy required for implementing photon cycling and laser cooling in this polyatomic molecule.

Chapter 4

Bright and Slow SrOH Cryogenic Buffer-gas Beam

Helium buffer gas cooling performed inside the cell allows spectroscopy of reactive radicals in the gas phase at cryogenic temperatures and even magnetic trapping of atoms and molecules with specific collisional properties[1]. Even though Bose-Einstein condensates of metastable helium 4 have been created with buffer-gas precooling without the use of any laser cooling in the process [81], removal of residual helium buffer gas remained a formidable challenge [156]. On the other hand, initial helium densities were orders of magnitude lower for experiments performing trapping of molecules from the buffer-gas beams [83], opening possibilities for further sympathetic and evaporative cooling. Additionally, since molecular beams expanded into high vacuum provide effectively a collision-free environment, such beams play a crucial rule in precision measurement applications [65]. Because of all these considerations, production of a bright, slow, and cold beam of the SrOH radical became an important goal for our experiment. Luckily, techniques of cryo-

[1]Since only atoms and molecules in low-field seeking (LFS) states can be trapped in the conservative magnetic traps, the ratio of elastic collisions to Zeeman-state changing collisions γ_{Zeeman} has to be quite high to ensure that LFS molecules are cooled and trapped before any detrimental collisions occur that lead to the change in spin projection. For $^2\Sigma$ molecules like SrOH, SrF, CaF, and CaH this imposes a fundamental limit on the acceptable ratio of $\gamma_{\text{SR}}^2/B_{\text{rot}}^4$ for direct buffer-gas trap loading. Intuitively, this can be understood as coming from the fact that virtual excitation to the first-excited rotational level $N = 1$, which is $2B_{\text{rot}}$ above the $N = 0$ level, is necessary for direct coupling between spin-up and spin-down to arise due to spin-rotation interaction parametrized by the γ_{SR} constant. We refer the reader to Refs. [133, 155] for further details.

genic buffer-gas beams for atoms, diatomics and polyatomics have been extensively developed and reviewed in the past [79, 80].

4.1 Absorption spectroscopy

The side image of the cryogenic buffer-gas cell in the two-stage configuration where there is second low-helium density chamber attached to the main cooling cell is shown in Fig. 4.2.3(a). Since a careful characterization of such a cell design was previously performed [140, 157], here we provide only results specific to SrOH CBGB. Transverse spectrum of the SrOH beam from the two-stage cell is shown in Fig. 4.1.1. From the peak absorption signal we can extract that the beam contains approximately 10^9 SrOH molecules in the first excited rotational level in the $\tilde{X}\,(000)$ state. The transverse spread of ± 15 m/s corresponds to a transverse temperature of 2.8 K and is consistent with the measured cell temperature during ablation of $T_{\text{cell}} \approx 2.3\,\text{K}$. The on-resonance time profile of the SrOH beam is shown in Fig. 4.1.2. We can use the peak on-resonance absorption signal as well as the measured Doppler spread to extract the density in beam as well as extraction efficiency. The resonant absorption cross section[2] is given by [158]

$$\sigma_0 = \frac{\lambda^2}{2\pi}. \tag{4.1.1}$$

For a Doppler broadened line, the frequency dependent absorption cross section is given by [158]

$$\sigma(\triangle) = \sigma_{\text{D}} e^{-(\triangle/\Gamma_{\text{D}})^2} \tag{4.1.2}$$

where Γ_{D} is the Doppler width and $\sigma_{\text{D}} = \frac{\sqrt{\pi}}{2}\frac{\gamma}{\Gamma_{\text{D}}}\sigma_0 \approx 0.89\frac{\gamma}{\Gamma_{\text{D}}}\sigma_0$ and γ is the natural linewidth of the transition. Using the following experimental parameters

- $\gamma \approx 7\,\text{MHz}$
- $\Gamma_{\text{D}} \approx 33\,\text{MHz}$

[2]Here we assume $\gamma_{\text{p}} = \gamma_{\text{tot}}$ and $J'' \rightarrow J'$ transition for simplicity without sacrificing much precision.

- $\lambda = 688\,\text{nm}$

we obtain the resonance absorption cross section for a Doppler broadened SrOH line of $\sigma(\triangle = 0) \approx 1.3 \times 10^{-10}\,\text{cm}^2$.

According to the Beer's law, the fraction of laser light transmitted through the molecular beam sample is given by [20]

$$I/I_0 = e^{-\sigma(n_0 - n_1)l} \tag{4.1.3}$$

and under assumption that we are not saturating the transition we obtain $I/I_0 = e^{-\sigma n_0 l}$. Equivalently, the molecular absorption signal is given by

$$\frac{I - I_0}{I_0} = 1 - e^{-\sigma n_0 l}. \tag{4.1.4}$$

In the low absorption limit like in the beam, we obtain

$$\frac{I - I_0}{I_0} \approx \sigma n_0 l \tag{4.1.5}$$

where for our experiment with two-stage cell we have $l = 6.5\,\text{mm}$ as the aperture of the second stage cell. Therefore, the molecular density in the beam is given by

$$n_{\text{SrOH}} \approx Absorption/(\sigma l) = 0.015/\left(1.3 \times 10^{-10}\,\text{cm}^2 \times 0.65\,\text{cm}\right) \approx 2 \times 10^8\,\text{cm}^{-3}. \tag{4.1.6}$$

Thus, beam densities achievable with SrOH are comparable to those demonstrated previously with diatomic radicals like CaH and SrF [140, 159]. This result while potentially expected because of similar chemical properties of SrF and SrOH is still a bit surprising since there are more chemical reaction channels available during the violent ablation process of strontium dihydroxide $Sr(OH)_2$ than of strontium difluoride SrF_2. In fact, we have measured that more than 10^{12} strontium atoms can be produced while ablating $Sr(OH)_2$ target; Sr spectrum on the ${}^1S_0 - {}^3P_1$ line is shown in Fig. 4.1.3. Large numbers of detected strontium atoms can have two potentially useful applications. First, if a portion of them can be made to react with released hydroxyl radicals OH and hydro-

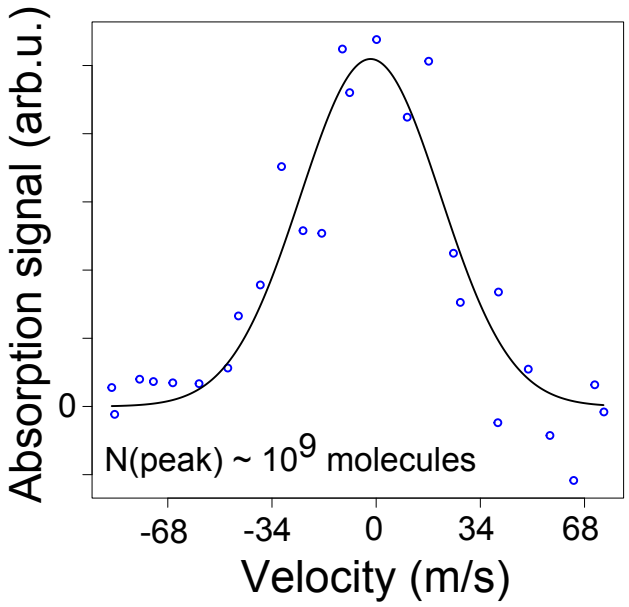


Figure 4.1.1: Transverse spectrum of SrOH cryogenic beam.

gen peroxide molecules H_2O_2, the number of SrOH molecules produce could be significantly enhanced. In this avenue, previous studies of chemical reactions between H_2O_2 and strontium around room temperature indicate that exciting strontium atoms into a metastable state $^3P_1$ makes the reaction exothermic and leads to enhanced SrOH production [160]. Potentially, introducing a high power 689 nm laser along with the Yag beam to excite unbound Sr atoms could lead to larger SrOH beam signals. In another research direction, strontium atoms from the cell can be decelerated and trapped together with SrOH in order to explore ultracold atom-molecule collisions. More details about this option will be provided in the chapter on the prospects of magneto-optical trapping of SrOH.

4.2 Eliminating SrOH-He in-beam collisions

In order to ensure that the maximum possible number of SrOH molecules is extracted from the cell, we measured on-resonance SrOH absorption signal in the beam as a function of the buffer-gas flow. Figure 4.2.1 shows that at about 5 sccm flow the extraction efficiency starts to saturate

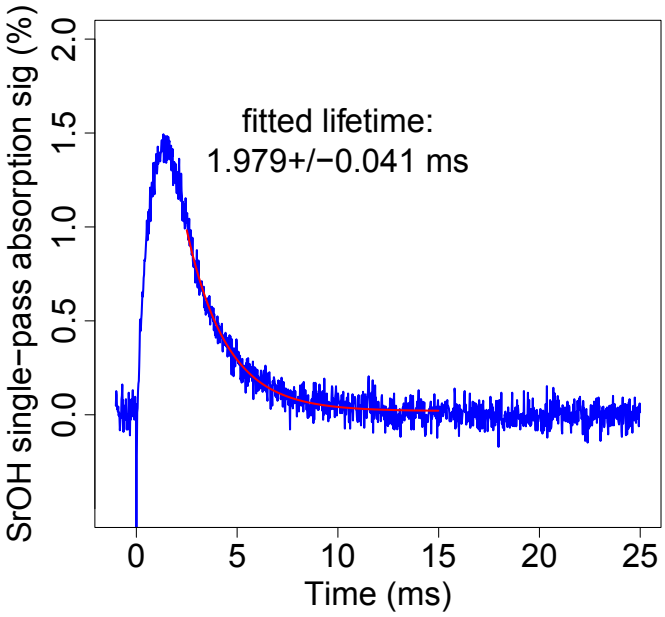


Figure 4.1.2: In-beam SrOH resonant trace with exponential decay fit for a single-stage cell. The absorption measurement is performed at most a few millimeters from the cell aperture.

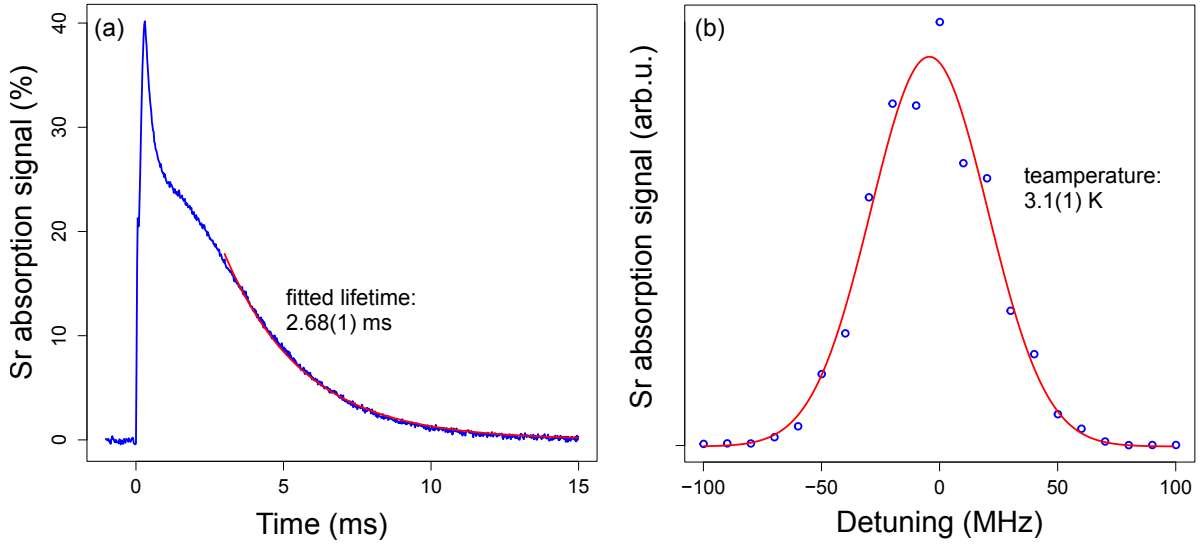


Figure 4.1.3: (a) Resonant in-cell absorption signal for atomic strontium on the $^1S_0 - ^3P_1$ line at 689 nm. (b) Absorption spectrum of buffer-gas cooled strontium. From the measured Doppler width of 35 ± 2 MHz we can extract the motional temperature of 3.1 ± 0.1 K which is consistent with the cell temperature during laser ablation. The frequency offset is 434.829101 THz.

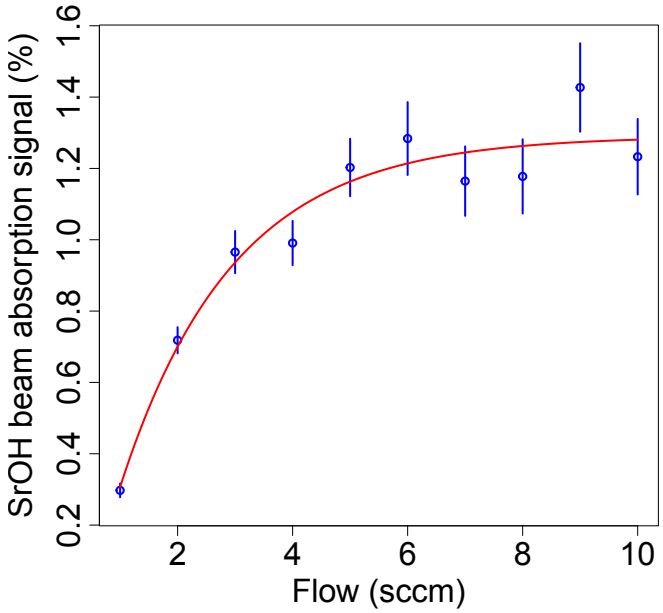


Figure 4.2.1: SrOH beam absorption signal as a function of the helium flow into the cell. Initially, the number of molecules extracted into the beam increases with the flow until full extraction is reached around 6 sccm.

and therefore flows ≥ 6 sccm should deliver the largest molecular fluxes downstream. However, upon the installation of the collimation aperture 15 cm from the cell aperture we determine that molecular fluorescence signal is decreasing with increasing flow into the cell, as can be seen in Fig. 4.2.2. Therefore, we hypothesized that helium pressure was building up in the room-temperature section of the vacuum chamber where cryogenic pumping was not available.

In order to reduce the amount of helium gas extracted into the room temperature portion of the experiment we took two crucial steps in modifying the cryogenic dewar design. First, we significantly increased the amount of charcoal inside the 4K shields in order to improve cryogenic pumping of helium buffer gas before it is extracted into the room temperature portion of the chamber. As shown in Fig. 4.2.3 the charcoal area inside the 4K shield approximately doubled after the installation of seven fins between the end of the cell and 4K exit aperture. A similar design was previously employed in the YO CBGB experiment at JILA [161]. The second improvement was also aimed at reducing the amount of helium gas flowing out of the cryogenic 4K shield by significantly reducing the open effective area as can be seen in Fig. 4.2.3 and 4.2.4. By installing

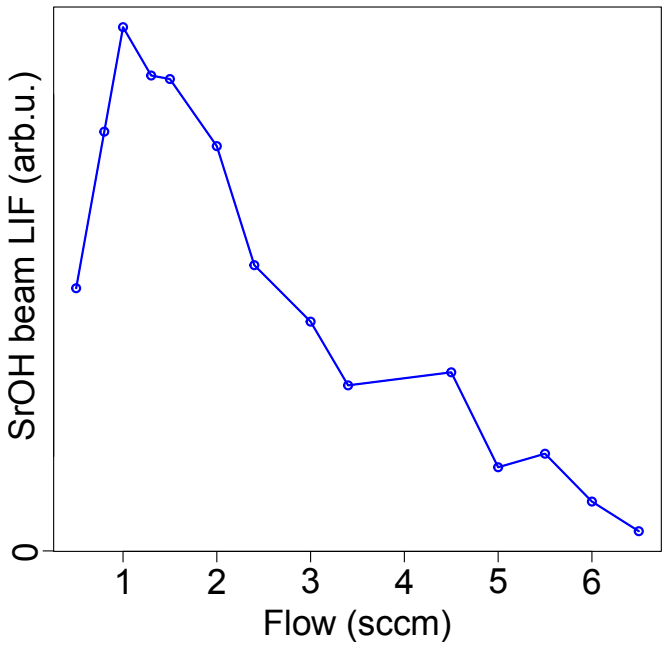


Figure 4.2.2: SrOH LIF signal 45 cm away from the cell as a function of the helium flow. The rapid drop in the signal as flow is increased provides strong evidence that helium pressure build-up in the vacuum chamber is scattering SrOH molecules.

sealed windows where previously were open holes and reducing the sizes of the remaining two apertures, the open area became less then 2 cm^2 coming from a $1 \times 1 cm^2$ aperture for the helium buffer-gas line and 6 mm diameter front aperture on the 4K shield.

Figure 4.2.5 shows the change of the SrOH LIF 45 cm away from the cell as a function of the buffer-gas flow into the cell. By comparing the results presented in this figure with those of Fig. 4.2.2 we conclude that the number of the SrOH-He scattering collisions at the collimating aperture was reduced significantly. The maximum beam signal downstream is achieved at 7 sccm which is consistent with the saturation of the cell extraction. With these improvements, the maximum SrOH LIF beam signal was increased by an order of magnitude in size enabling the signal-to-noise ratio required for the experiments presented later in this thesis.

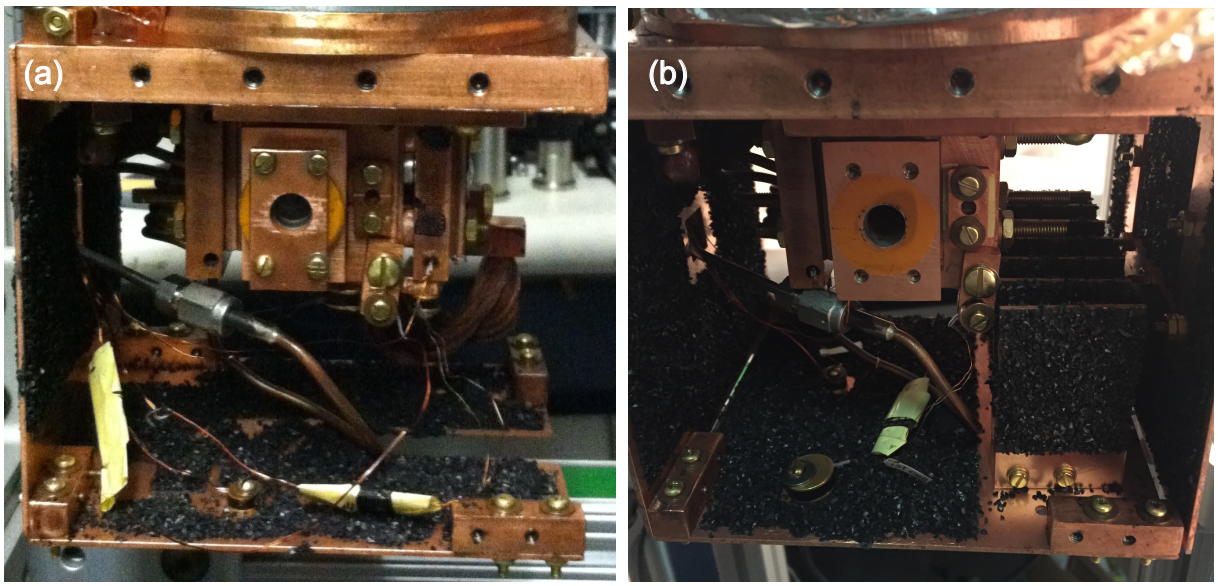


Figure 4.2.3: Inside the 4K shield before (a) and after (b) installation of the 4K fins for increasing effective cryopumping area.

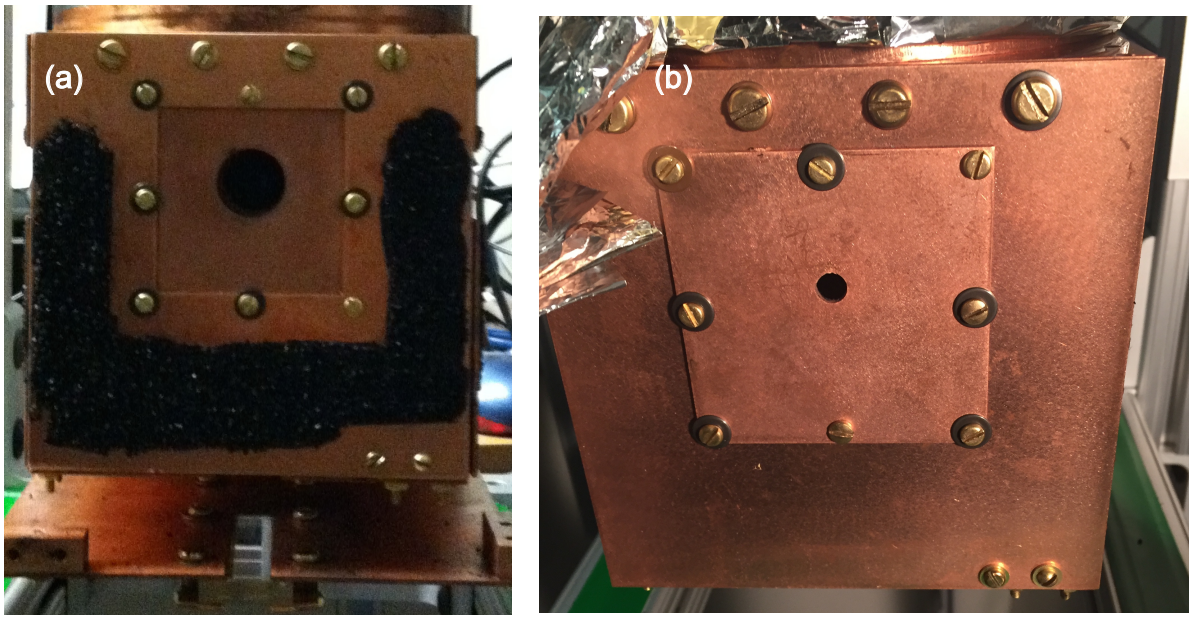


Figure 4.2.4: Front cover of the 4K shield before (a) and after (b) reduction of the 4K exit aperture. The aperture size was reduced from 25 mm to 6 mm. Additionally, the charcoal was removed from the outside of 4K shield in order to reduce the black body heating.

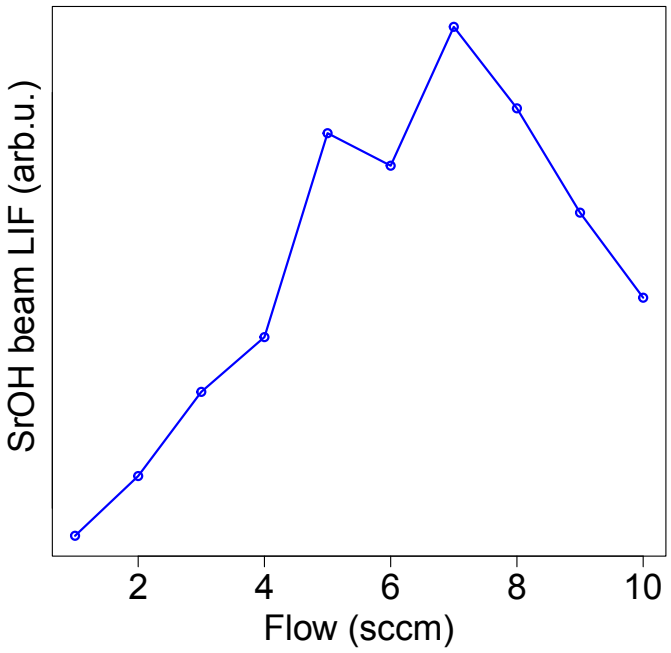


Figure 4.2.5: SrOH LIF beam signal vs flow after modification of the dewar design to reduce detrimental helium collisions.

4.3 Two CBGB regimes: very bright and reasonably slow vs very slow and reasonably bright

In order to determine the optimal beam parameters for the laser cooling experiment, we characterized the forward velocity of the SrOH beam in two different regimes. In order to achieve the slowest forward velocities we operated the experiment with the two-stage cryogenic sell that led to the velocity distribution given in Fig. 4.3.1. This CBGB already provided SrOH fluxes 2-3 orders of magnitude brighter then previous SrOH sources.This beam configuration would be ideal for implementing direct laser slowing since about 10^4 scattered photons will bring the peak velocity distribution to rest in the laboratory frame. While 2D plot containing both velocity and time of arrive is useful for understanding the general shape of the SrOH beam in the TOF-velocity space, in order to more carefully visualize the number of slow molecules we plotted the integrated beam data in Fig. 4.3.2. The slow velocity part in the range of $15-40$ m/s corresponds to kinetic energies of 1-10 K and can be directly loaded into a magnetic trap with minimal deceleration.

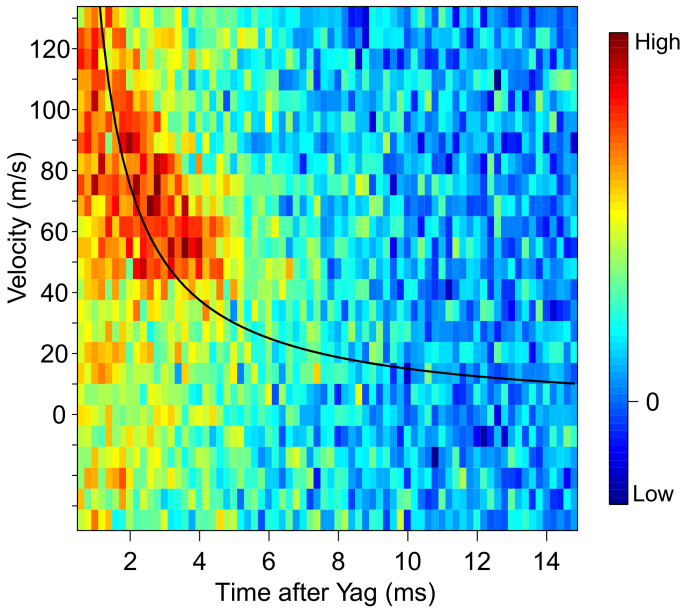


Figure 4.3.1: SrOH velocity distribution as a function of arrival time for a 2-stage cryogenic buffer-gas cell. The black line on the graph is the expected time of flight (TOF) arrival. As can be seen from the plot, there is a significant fraction of molecules between 40 and 60 m/s that can be easily decelerated for loading into a conservative trap. A fraction of molecules below the TOF line at very low velocities could be due to excitation of the other SR component. The forward velocity was measured without the collimation aperture.

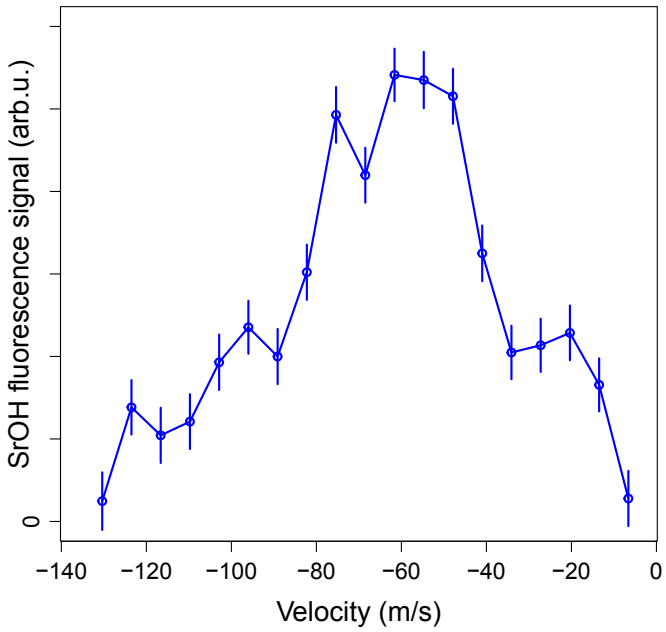


Figure 4.3.2: Integrated velocity distribution for SrOH CBGB from a 2-stage buffer-gas cell. The peak of the distribution is 55 ± 5 m/s which is consistent with the data in figure 4.3.1. While there appears to be a significant fraction of molecules at low velocities around 20 m/s, slow velocity tail needs to be studied in much more detail in order to exactly determine the number of molecules there.

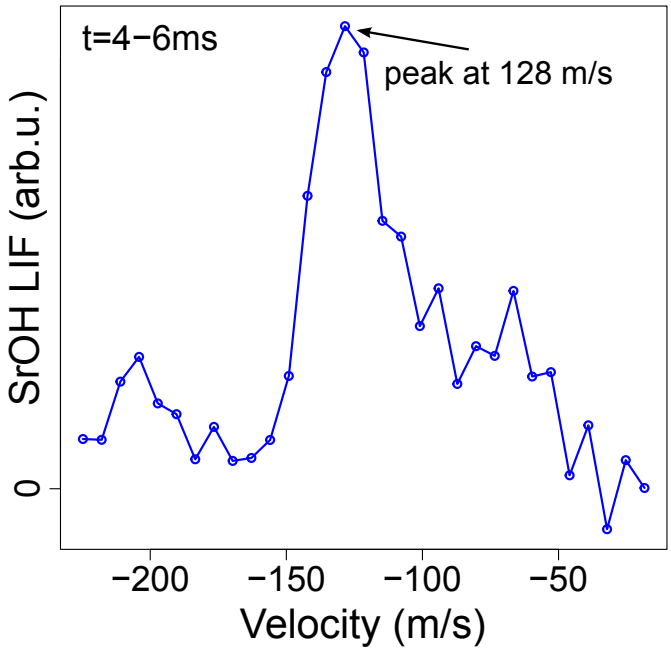


Figure 4.3.3: Forward velocity distribution of the SrOH beam in the single-stage configuration. The data was taken with the collimation aperture in place.

While such very slow CBGB of SrOH will find future applications in direct trapping and laser slowing, for initial photon cycling and laser cooling experiments we decided to work with a beam that gave us the most flux. In the single-cell configuration as shown in Fig. 4.2.3(b), the molecules are directly entering the beam after being extracted from the original cell. Figure 4.3.3 shows that with a single-stage cell we achieve velocities a factor of 2 higher compared to the two-stage set-up. However, the molecular fluxes achieved are an order of magnitude larger as measured by direct absorption outside the cell. Increased molecular number plays a crucial role once we install the collimation aperture to limit the transverse velocity spread for laser cooling experiments. After the elimination of the SrOH-He in-beam scattering described in the previous section, the forward velocity measured with and without the collimation aperture was consistent, as expected in the absence of velocity dependent scattering.

4.4 Conclusions

Using cryogenic buffer-gas beam technology [80] we have achieved SrOH beams with intensities in a single rovibrational state up to 10^{11} molecules/sr/pulse with forward velocity of 130 m/s and 10^{10} molecules/sr/pulse with velocities peaked at 60 m/s. Because of the limited photon budget due to decay to dark vibrational states, cryogenic pre-cooling in the form of CBGB played a vital role in direct laser cooling and magneto-optical trapping of diatomic molecules. Similarly, we expect bright beams of polyatomic radicals like SrOH to become a prerequisite for laser cooling and manipulation of polyatomics.

Chapter 5

Photon Cycling and Radiation Pressure Force Deflection

The use of laser radiation to control external and internal degrees of freedom for neutral atoms [89], molecules [99, 100], microspheres [162, 163], and micromechanical membranes [164, 165] has revolutionized atomic, molecular, and optical physics. In most cases, such manipulations relied on the use of resonant laser fields to change the internal state of the quantum system in a well controlled manner. Upon absorption of the light photon of wavelength λ, the momentum p of the quantum object is changed by $\triangle p = \hbar k = 2\pi\hbar/\lambda$. Even though this momentum change from a single photon can be accurately measured with modern experimental techniques [166], a large number of photon absorption-emission cycles is necessary in order to modify atomic or molecular motion significantly. For example, for Rb atomic beam moving at a forward velocity $v_f = 100$ m/s, approximately 17,000 photon scattering events are required to bring the beam to rest since one absorbed photon only modifies the velocity by $\triangle p/M_{\mathrm{Rb}} = 0.6$ cm/s. Thus, it becomes crucial to find a way for quantum objects under consideration to repeatedly get excited by the same laser field.

While a nonresonant dipole force was used to deflect a beam of CS_2 [167] and optical pumping led to rotational cooling of CH_3F [168], there has been no demonstration of the radiative force via

optical cycling for a species with more than two atoms. One of the primary reasons for the lack of previous experimental results is that polyatomic molecules are more difficult to manipulate than atoms and diatomic molecules because they possess additional constituents and their concomitant additional rotational and vibrational degrees of freedom. In this chapter, we demonstrate optical cycling and the radiation pressure force on triatomic strontium monohydroxide (SrOH). Photon cycling allows for sensitive molecular detection with close to unity experimental efficiency, while resulting light pressure force enables state-selective molecular deflection or longitudinal beam slowing.

The structure of SrOH is more complicated compared to previously laser cooled diatomic molecules: it contains three vibrational modes [114], including degenerate bending vibrations with no direct analog in diatomic molecules. Additionally, the Renner-Teller effect, which is absent in diatomics, further complicates molecular structure [169]. Therefore, while the presence of the diagonal Franck-Condon factors and closed rotational transitions provided strong indications that photon cycling can be achieved in SrOH, it was crucial to carefully characterize the photon scattering process before proceeding to more complex experiments involving laser cooling. Our experimental results demonstrate that despite the significantly increased complexity associated with even a simple polyatomic molecule like SrOH, optical cycling on a quasi-closed transition can be applied with technically straightforward modifications. In particular, for this species (and those isoelectronic to it, to be discussed later in this thesis), the additional degrees of freedom do not affect photon cycling up to the level of hundreds of photons, more than enough to implement high efficiency molecular imaging and deflection through radiative force. To reach the level of thousands of scattered photons (necessary to cool to the millikelvin regime), very similar techniques can be used, for example in SrOH by repumping the excited bending mode and will be discussed in the future chapters.

5.1 Radiation pressure force in multilevel systems

Before proceeding to experimental results on SrOH, we will briefly summarize the theory of light pressure forces in multilevel systems. Part of the complexity in working with both diatomic and polyatomic molecules comes from the absence of effective two-level systems that can be identified in many atoms. Usually, the absence of vibrational selection rules is cited as the main difficulty in laser cooling molecules but it is important to notice that even if we ignore vibrational structure completely in order to achieve optical cycling addition of multiple laser frequencies is necessary to address a multitude of ground state sublevels coupled to few excited states. This challenge comes from the combination of the need to work with rotationally excited molecules and presence of electronic spin and nuclear angular momenta in most molecules under consideration for direct laser cooling. In this section we will quantitatively describe how this additional complexity leads to the significant reduction of the radiation pressure force compared to an ideal two-level system.

5.1.1 Radiative force on a two-level system

Since we are going to be using the classical concept of force in order to describe the photon effect on a quantum molecular system it is necessary to clarify a few points here. From the classical-quantum correspondence principle and according to Ehrenfest theorem, the expectation value of the operator must agree with the classical physics picture. Therefore, when we use the force F on the atom we actually mean the expectation of the quantum mechanical force operator $\mathcal{F}$ [170]:

$$F = \langle \mathcal{F} \rangle = \frac{\mathrm{d}}{\mathrm{d}t} \langle p \rangle \tag{5.1.1}$$

where the time evolution of the momentum operator can be found as

$$\frac{\mathrm{d}}{\mathrm{d}t} \langle p \rangle = \frac{i}{\hbar} \langle [\mathcal{H}, p] \rangle = - \left\langle \frac{\partial \mathcal{H}}{\partial z} \right\rangle . \tag{5.1.2}$$

The relevant time-dependent approximate Hamiltonian for a single valence electron atom or molecule interacting with a light field is given by:

$$\mathcal{H}(t) = -e\vec{\mathcal{E}}(\vec{r},t)\cdot\vec{r}. \tag{5.1.3}$$

With the help of eq. 5.1.2 and 5.1.3 it can be rigorously shown [170] that the force on a two-level atom at rest from repeated absorption and spontaneous emission is given by

$$F_{\text{sp}} = \hbar k \gamma p_e \tag{5.1.4}$$

where $\gamma = 1/\tau_{\text{sp}}$ is the decay rate due to spontaneous emission with lifetime τ_{sp} and p_e is the probability for an atom to be in the excited state $|e\rangle$. Since the process of spontaneous emission carries away entropy from the atom, the dissipative force F_{sp} is equal to the change in momentum $\hbar k$ per scattering event multiplied by the rate of scattering γp_e. For an atom at rest, the scattering rate has the following form

$$R_{\text{sc}} = \frac{s_0\gamma/2}{1+s_0+4(\delta/\gamma)^2} \tag{5.1.5}$$

where the on-resonance saturation parameter is $s_0 = I/I_{\text{sat}} = 2|\Omega|^2/\gamma^2$ and the frequency detuning from resonance is given by $\delta = \omega - \omega_0$. The saturation intensity $I_{\text{sat}} \equiv \pi hc/3\lambda^3\tau_{\text{sp}}$ is an important experimental parameter for laser slowing and cooling experiments since it provides the guidance to achieve laser powers sufficient for $s_0 \gg 1$.

For large optical powers when Rabi frequency Ω[1] is much larger than spontaneous emission rate γ, excited state fraction p_e approaches 1/2 and, therefore, the maximum attainable dissipative force is

$$F_{\text{sp,max}} = \hbar k \frac{\gamma}{2} \tag{5.1.6}$$

and thus limited by the inherent atomic spontaneous emission rate.

[1]The Rabi frequency $\Omega \equiv \frac{-eE_0}{\hbar}\langle e|r|g\rangle$ quantified the coupling strength between the atom and the light field $\vec{\mathcal{E}}(\vec{r},t)$. Additionally, Ω is the real oscillatory frequency of the excited state population for zero detuning from resonance ($\delta = 0$).

5.2 Extension to a multilevel configuration

While the structure of SrOH requires coupling of multiple ground state sublevels to multiple excited states, complex expressions for photon scattering rate and radiative force can be presented in a form reminiscent of the familiar two-level system for which intuitive understandings have been previously developed. Because of the multiple levels coupled with laser light, expressions for scattering rate, saturation parameter, and saturation intensity have to be modified to account for additional complexity. It has been previously shown that the scattering rate for a complex molecular system like SrF and CaF can be accurately modeled as [171]

$$R_{\mathrm{sc}} = \frac{\gamma_{\mathrm{eff}}}{2} \frac{s_{\mathrm{eff}}}{1 + s_{\mathrm{eff}} + 4\left(\delta/\gamma\right)^2} \tag{5.2.1}$$

where the following notation has been adopted[2]

$$\gamma_{\mathrm{eff}} = \frac{2n_e}{n_g + n_e}\gamma \tag{5.2.2}$$

$$I_{\mathrm{sat,eff}} = \frac{2n_g^2}{n_g + n_e} I_{\mathrm{sat}} \tag{5.2.3}$$

with $s_{\mathrm{eff}} = I_{\mathrm{tot}}/I_{\mathrm{sat,eff}}$ as the new on-resonance saturation parameter. First, it is important to notice that in the two-level configuration with $n_g = n_e = 1$, we obtain $\gamma_{\mathrm{eff}} = \gamma$ and $I_{\mathrm{sat,eff}} = I_{\mathrm{sat}}$ as expected. Additionally, because the number of ground state sublevels is large, high laser intensities are required in order to saturate the transitions of interest. For example, for SrOH with cycling on the $\tilde{X} - \tilde{A}$ transition $I_{\mathrm{sat,eff}} = 18 I_{\mathrm{sat}} \approx 51\,\mathrm{mW/cm^2}$ thus requiring significantly higher laser powers for experiments that need high saturation parameters ($s_{\mathrm{eff}} \gg 1$) like laser cooling. Finally, the maximum radiative force in a multilevel system is reduced compared to a two level expression. For SrOH with $n_g = 12$ in $N = 1$ of the $\tilde{X}$ state and $n_e = 4$ in $N = 0$ of the $\tilde{A}$ state, $R_{\mathrm{sc,max}} = \gamma/4$, thus

[2]Here we consider the main cycling laser to be decoupled from the repumping lasers. Alternatively, in the so-called Λ-type configuration when multiple laser colors couple to the same excited state, the expression will have to be modified to account for the fraction of molecules remaining in the ground state vibrational level.

leading to a reduced radiative force compared to two-level atomic systems. Below we describe that despite these complexities, significant radiation pressure deflection of the SrOH cryogenic molecular beam can be achieved with experimental parameters similar to those in typical atomic physics experiments.

5.3 Experimental configuration

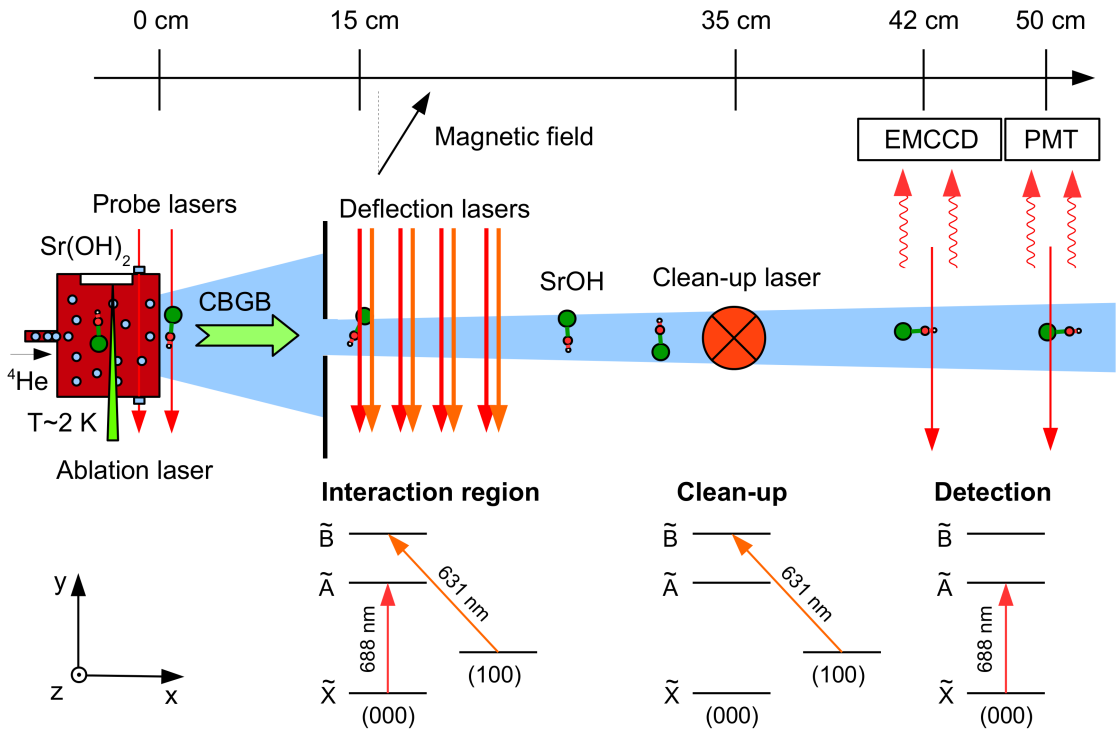


Figure 5.3.1: Schematic of the experimental setup used for radiative deflection of SrOH. A cryogenic beam of SrOH is produced using laser ablation of a pressed $Sr(OH)_2$ target followed by buffer-gas cooling with ~ 2 K helium gas. Transverse lasers, resonant with $P(N'' = 1)$ line of the $\tilde{X}^2\Sigma^+(000) \rightarrow \tilde{A}^2\Pi_{1/2}(000)$ and $\tilde{X}^2\Sigma^+(100) \rightarrow \tilde{B}^2\Sigma^+(000)$ electronic transitions, interact with the collimated molecular beam in order to apply radiation pressure force. In order to remix the dark magnetic sub-levels, a magnetic field at an angle of 60° is applied in the interaction region. Molecules remaining in the excited vibrational level of the electronic ground state are optically pumped back into the ground vibrational level using $\tilde{X} \rightarrow \tilde{B}$ off-diagonal excitation. The spatial profile of the molecular beam is imaged on the electron multiplying charge-coupled device (EMCCD) camera and the time-of-flight data is collected on the photomultiplier tube (PMT).

A schematic diagram of the experimental apparatus is shown in figure 5.3.1. Gas-phase SrOH

is produced by laser ablation of solid $Sr(OH)_2$ placed inside a cryogenic cell maintained at a temperature of ~ 2 K. SrOH molecules entrained in helium buffer gas flowing into the cell at a rate of 6 sccm (standard cubic centimeters per minute) are extracted into a beam through a 5 mm aperture. This cryogenic buffer-gas beam (CBGB) [80] contains approximately 10^9 molecules in the first excited rotational level ($N = 1$) in a pulse about 5 ms long. The forward velocity of the SrOH beam is 130 ± 20 m/s and its transverse velocity spread is ± 15 m/s. A rectangular 2×2 mm slit situated 15 cm away from the cell aperture collimates the beam. Deflection of the molecules is achieved by applying laser light perpendicular to the beam's flight path. To increase the interaction time, several laser beams are applied in a series. The deflection laser beams originate from a single-mode fiber containing two colors - 688 nm for driving the $\tilde{X}^2\Sigma^+(000) \rightarrow \tilde{A}^2\Pi_{1/2}(000)$ transition and 631 nm for driving the $\tilde{X}^2\Sigma^+(100) \rightarrow \tilde{B}^2\Sigma^+(000)$ transition. The exact scheme is for creating a cycling transition has been previously described in the chapter on SrOH molecular structure. Each color contains two frequency components separated by ~ 110 MHz to address $P_{11}(J'' = 1.5)$ and ${}^PQ_{12}(J'' = 0.5)$ lines of the spin-rotation (SR) splitting. Each dual-color beam has FWHM diameter of 1.8 mm and contains 50 mW of total laser power. In order to create multiple passes (to maximize molecule deflection), the same beam is circulated around the vacuum chamber. The light is generated using injection-locked laser diodes seeded by external-cavity diode lasers in the Littrow configuration [172]. In order to destabilize the dark states created during the cycling process [173], we apply a magnetic field of a few gauss at an angle of 60° to the polarization plane xz.

In the "clean-up" region, we repump all the molecular population from the excited vibrational level $\tilde{X}(100)$ back to the ground state in order to increase the signal in the detection region. The spatial profile of the molecular beam is extracted by imaging the laser-induced fluorescence (LIF) from a transverse retroreflected laser beam on an EMCCD camera. The laser beam addresses both SR components of the $P(N'' = 1)$ line for the $\tilde{X}^2\Sigma^+(000) \rightarrow \tilde{A}^2\Pi_{1/2}(000)$ transition with ~ 1mW each. In a similar laser configuration, time-of-flight data is recorded by collecting the LIF on a PMT 8 cm downstream.

5.4 Photon cycling results

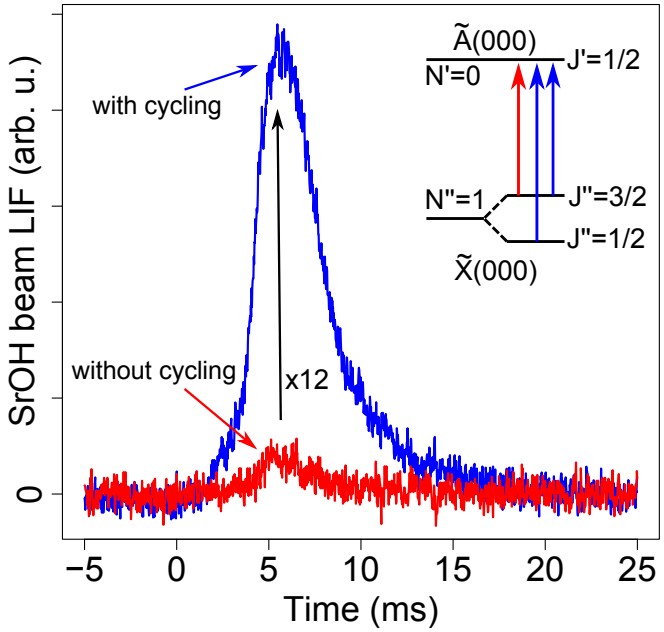


Figure 5.4.1: Laser induced fluorescence (LIF) increase due to photon cycling. The red trace shows the SrOH beam signal in the first excited rotational level ($N = 1$) when only one of the spin-rotation lines is addressed with the 688 nm laser resonant with the $P(N'' = 1)$ line of the $\tilde{X}^2\Sigma^+ \rightarrow \tilde{A}^2\Pi_{1/2}$ electronic transition. More than an order of magnitude LIF increase is observed (in blue) when two laser frequencies separated by ~ 110 MHz excite both of the spin-rotation lines. Increased fluorescence corresponds to the scattering of approximately 24 photons per each molecule limited by the decay to the dark vibrational level. The inset diagram shows which frequency components are applied during the experimental runs.

We chose the lowest frequency $\tilde{X} - \tilde{A}$ electronic excitation at 688 nm for optical cycling in the experiment because it can be addressed with all solid-state lasers. The diagonal FC factors of the $\tilde{X} - \tilde{A}$ band [113, 174] allow for scattering multiple photons before decaying to excited vibrational levels. Following a previously developed scheme for diatomics [101, 102, 154, 175], we address the molecules in the first excited rotational level on the $P(N'' = 1)$ line. Because of the rotational selection rules, molecules return to the same rotational state after the cycle $N'' = 1 \leftrightarrow N' = 0$. Hyperfine splittings in SrOH are below the natural linewidth of the electronic transition [121]. The observed fluorescence enhancement due to photon cycling is demonstrated in figure 5.4.1. The red trace shows the molecular beam signal without photon cycling when only the $P_{11}(J'' = 1.5)$

line is addressed and, therefore, on average, the molecules will scatter approximately two photons before decaying to the dark SR component. Adding the second laser frequency to excite the ${}^{P}Q_{12}(J''=0.5)$ transition, we see more than an order of magnitude increase in the LIF, which corresponds to about 24 scattered photons per molecule. We model the number of photon scattering events before a decay to the dark vibrational level $\tilde{X}(100)$ as a geometric distribution with probability of success p, identified as the "off-diagonal" FC factor[3] $f_{\tilde{A}(000)\rightarrow\tilde{X}(100)}$. Since the expected value of the geometric probability distribution is $1/p$ [176], on average, $1/f_{\tilde{A}(000)\rightarrow\tilde{X}(100)} \approx 25$ photons are scattered per molecule before the loss to the dark vibrational level, which agrees with our observations. Figure 5.4.2 shows the scan of two laser frequencies together, where the spin-rotation components manifest themselves as peaks detuned by ~ 110 MHz from the center peak. The cycling LIF is larger than the combined signal for both of the SR components alone, indicating photon cycling in the molecular system.

The experimentally relevant vibrational structure of SrOH is depicted in the inset of figure 5.4.3. Upon electronic excitation, 96% of the molecules return to the vibrational ground state while 4% decay to the excited Sr-O stretching mode (100). We repump these molecules via the $\tilde{B}$ state using the 631 nm laser, as shown in the diagram. Figure 5.4.3 depicts cycling between the (000) and (100) vibrational levels of the ground electronic state $\tilde{X}$. By applying light in the interaction region, we pump all $\tilde{X}(000)$ molecules (in black) into the excited vibrational mode $\tilde{X}(100)$ after scattering of ~ 25 photons, which is indicated by the depleted beam profile (in red). Application of the repumping beam returns the molecules to the ground vibrational level and we recover the fluorescence signal (in blue). Cycling between vibrational levels indicates that the dominant vibrational loss mechanism in the molecular system is to the excited Sr-O stretching mode $\tilde{X}(100)$. The spectrum of the repumping laser is shown in Fig. 5.4.4. It is estimated [174, 177] that the molecules will scatter about 770 photons before they decay to the second excited Sr-O stretching mode $\tilde{X}(200)$.

As previously mentioned, in addition to Sr-O stretching, SrOH contains two other vibrational

[3] Actually, p should be a branching ratio but the difference is quite small here and will not result in the number of scattered photons before loss to (100) state.

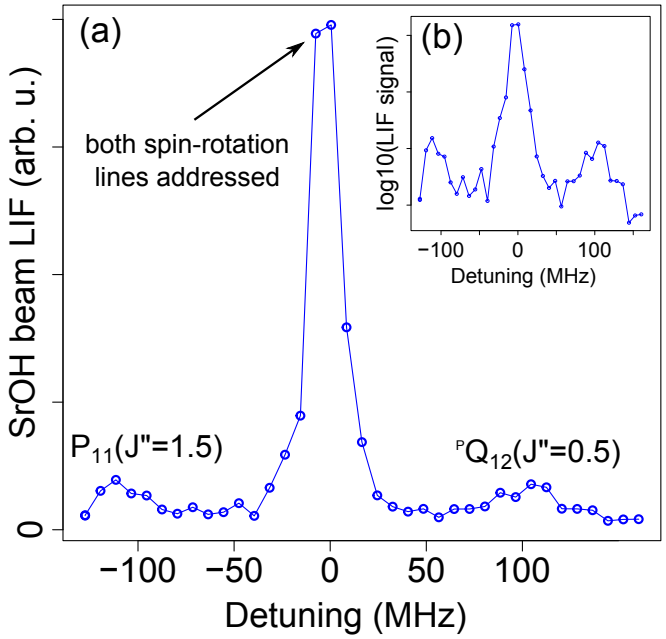


Figure 5.4.2: Fluorescence spectrum with photon cycling. (a) A three-peak spectrum is observed upon scanning of two laser frequencies separated by ~ 110 MHz through the two spin-rotation components of the $P(N''=1)$ line for the $\tilde{X}^2\Sigma^+(000) - \tilde{A}^2\Pi_{1/2}(000)$ transition. Due to the photon cycling process, collected fluorescence with both spin-rotation lines addressed is an order of magnitude larger than the sum of the individual signals. (b) Spectrum on the logarithmic scale clearly shows the three peaks. The frequency offset in the data is 435.968072 THz.

modes that can limit the photon cycling process. Because the vibrational angular momentum selection rule $\triangle l = 0$ allows only for specific decays to the excited bending mode vibrations from the $\tilde{A}(000)$ state [108], the dominant loss channel in the bending mode is to $\tilde{X}\left(02^00\right)$ energy level with $l = 0$. SrOH molecules will scatter at least 10,000 photons before decaying to the excited O-H stretching mode $\tilde{X}(001)$ [150]. Therefore, laser cooling can be effectively performed without the need for the O-H stretching mode repumping laser.

5.5 Radiation pressure force deflection

The effect of the radiation pressure force on SrOH due to photon cycling is shown in the deflection of the molecular beam (see figure 5.5.1). In order to extract the shift per photon in our setup, we perform cycling between (000) and (100) vibrational levels of the electronic ground

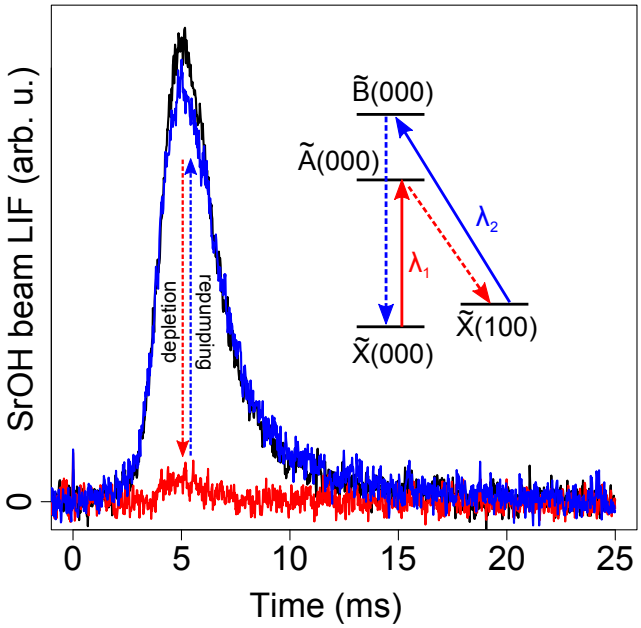


Figure 5.4.3: Cycling between vibrational levels. The molecular beam signal (black curve) is depleted (red curve) by the main cycling laser at 688 nm (light red, inset) due to off-diagonal vibrational decay to the excited vibrational mode (100). The signal is recovered (blue curve) by the application of the 631 nm repumping laser (blue, inset) in the clean-up region. The inset diagram shows the details of the vibrational structure of SrOH relevant to the optical cycling scheme. The energies of the excited vibrational levels in the electronic ground state have been previously measured [114]. The main cycling (λ_1) and repump (λ_2) lasers are indicated with the upward arrows, while the spontaneous decays are shown with downward dashed arrows.

state as described in figure 5.4.3. We measure the deflection with only the 688 nm laser applied in the interaction region and the 631 nm clean-up beam. We observe a shift of 0.007 mm/photon, which is consistent with the value estimated from the travel distance and the forward velocity of the molecular beam. The measured deflection shown in figure 5.5.1(a) corresponds to about 90 scattered photons in the interaction region or 110 total scattered photons per molecule. From the comparison of the unnormalized signals scaled by the in-cell absorption (which indicates the total number of molecules produced), we determine that $\sim 20\%$ of the molecules are lost during the deflection process. Using a Bernoulli sequence to model the absorption-emission cycles [144], we estimate from the data that the combined FC factor for loss to all dark vibrational levels above (100) is $(3 \pm 1) \times 10^{-3}$. Employing the Sharp-Rosenstock method [120], we previously calculated FC factors for decay from $\tilde{A}\,(000)$ to $\tilde{X}\,(200)$ and $\tilde{X}\,\left(02^{0}0\right)$ to be 1.6×10^{-3} and 7×10^{-4}, corre-

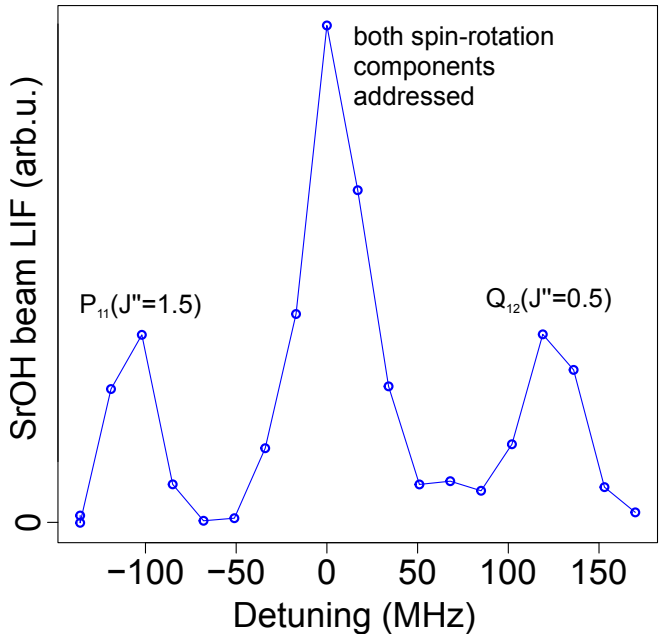


Figure 5.4.4: Spectrum of the Sr-O stretching mode repumper. $\tilde{X}\,(100) \rightarrow \tilde{B}\,(000)$ laser with 110 MHz sideband is scanned across both spin-rotation lines to optically pump molecules into the $\tilde{X}\,(000)$ state. The molecules are detected by optically cycling on the $\tilde{X}\,(000) - \tilde{A}\,(000)$ transition. The central peak has approximately twice the intensity of the sidebands as expected. The frequency offset in the plotted spectrum is 475.171626 THz.

spondingly, leading to a total loss probability of 2.3×10^{-3}. Additionally, vibronic coupling and anharmonic terms in the potential could increase these decay rates [113, 178]. In particular, the large anharmonic contribution to the bending mode potential in SrOH [114] could lead to enhanced decay to the $\tilde{X}\left(02^{0}0\right)$ state. Since our measurements of the loss rate are highly consistent with the calculations performed in the harmonic oscillator approximation, this is a strong indication that treating both stretching and bending vibrations of SrOH in this manner are appropriate for decay rates estimations. A measurement of the FC factor for $\tilde{A}\,(000) \rightarrow \tilde{X}\left(02^{0}0\right)$ transition in the laser cooling experiment will be describe in the next chapter.

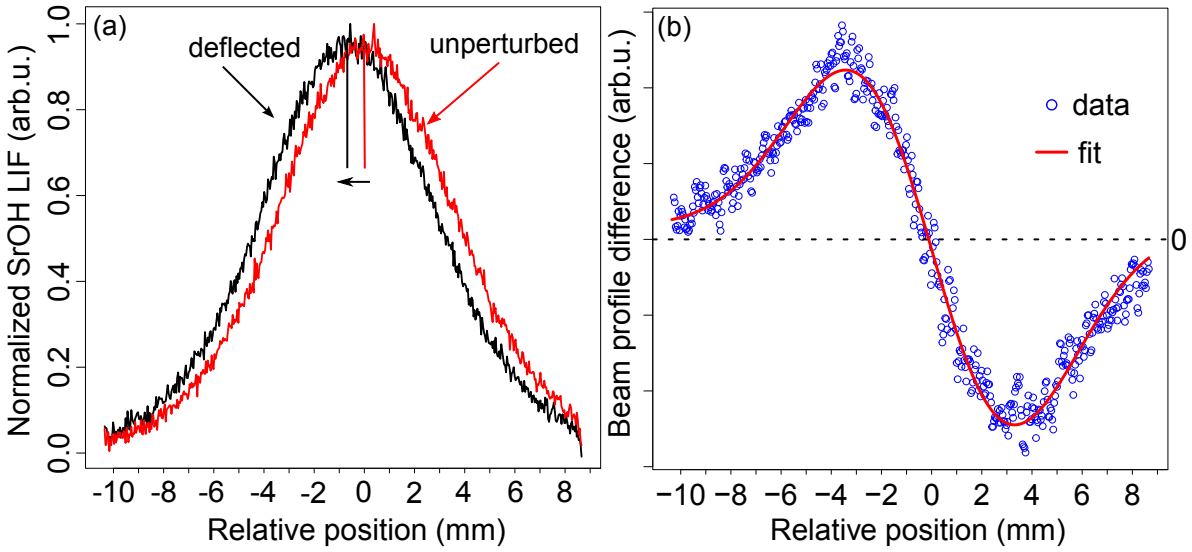


Figure 5.5.1: Deflection of the SrOH beam due to optical cycling. (a) Unperturbed spatial profile of the SrOH beam is shown in red. Upon the application of the transverse main and repump lasers in the interaction region the center of the beam distribution is shifted in the negative y direction (black curve). The shift of 0.65 mm between the centers of the peaks corresponds to the scattering of ~ 90 photons per molecule. (b) The measured difference between the normalized beam profiles vs position is shown. The deviation from zero (dashed black line) indicates the deflection of the molecular beam.

5.6 Conclusions

By repumping out of only a single excited vibrational state, we demonstrated cycling of ~ 110 photons in SrOH. The ~ 90 photons absorbed in the interaction region lead to a 0.65 mm deflection of

a cryogenic beam of SrOH. Our estimations indicate that the molecules lost from the photon cycle end up in the combination of $\tilde{X}\left(02^{0}0\right)$ excited bending state and $\tilde{X}\left(200\right)$ excited Sr-O stretching state. Additional repumping lasers to pump the molecules out of those states and back into the photon cycle would lead to scattering of $\sim 1,000$ photons per molecule, potentially allowing for laser cooling of SrOH to millikelvin temperatures [100]. Furthermore, the demonstrated optical cycling scheme opens a path towards the use of optical bichromatic forces [179–181] for rapid deceleration of SrOH originating from a CBGB [140] to near the capture velocity of a molecular MOT [175]. One potential application of the radiative force deflection for SrOH is to separate SrOH molecules in a single rovibrational level $N = 1$ of $\tilde{X}\left(000\right)$ from the cryogenic buffer-gas beam that contains not only helium atoms but also other byproducts of the violent ablation process. As described in the previous chapter, we have detected a large number of strontium atoms in the CBGB after ablating $Sr(OH)_2$ target. State-selected SrOH molecules can be used for collisional studies or trapping in an ultrahigh vacuum environment.

While SrOH has a linear geometry in the vibronic ground state, it also serves as a useful test candidate for the feasibility of applying radiative force to more complex linear and nonlinear molecules. Other strontium monoalkoxide free radicals [160] look particularly promising for laser cooling applications. Our results corroborate previous observations that the $\tilde{X} \rightarrow \tilde{A}$ electronic transition in SrOH promotes a strontium-centered, nonbonding electron, leading to highly diagonal FC factors and the dominant vibrational activity associated with the Sr-O stretching mode [113, 182]. Thus, replacing the hydrogen atom with a more complex group R (e.g. CH_3 and CH_2CH_3) should not perturb the valence electron significantly [182]. SrO-R molecules share a number of properties with SrOH that are advantageous for laser cooling, including the previously mentioned very ionic Sr-O bond, linear local symmetry near the metal, diagonal Franck-Condon factors, and technically accessible laser transitions [182]. Further work in this vein should include the evaluation of FC factors for other vibrational modes and effects of Jahn-Teller coupling [108].

Chapter 6

Doppler and Sisyphus Laser Cooling

Cooling of the external motion of neutral atoms from above room temperature into the sub-millikelvin range (leading to, e.g., Bose-Einstein condensation [43]) commonly relies on the use of velocity-dependent optical forces [170]. Laser cooling requires reasonably closed and strong optical electronic transitions, so its use for molecules has been severely limited. Recently, following initial theoretical proposals [144, 183] and proof-of-principle experimental results [154], laser cooling has been achieved for SrF [100], YO [101], and CaF [102, 175], including a 3D magneto-optical trap for SrF [171, 184, 185], and recently for CaF [186, 187]. Motivated by this progress on diatomic molecules, and building upon previous theoretical work [105], we demonstrated photon cycling – a crucial requirement for achieving light induced forces – with the triatomic molecule SrOH [188]. However, since SrOH had 3 distinct vibrational modes, including a doubly-degenerate bending mode, and because Doppler cooling required scattering an order of magnitude more photons, compared to deflection experiments, the question of direct laser cooling remained open.

In this chapter, we report direct laser cooling of a polyatomic molecule using both Doppler and sub-Doppler cooling techniques. In the Sisyphus approach the temperature of the SrOH beam is reduced from 50 mK to below 1 mK in 1 dimension. The dissipative force for compressing phase space volume is achieved by a combination of spatially varying light shifts and optical pumping into dark sub-levels, which are then remixed by a static magnetic field, as explored previously in

atomic and diatomic systems [100, 189, 190]. Since the magnitude of the induced friction force is directly related to the modulation depth of the dressed energy levels, the cooling process is much more efficient than with Doppler radiation pressure forces [191, 192]. This enhancement is especially important for complex polyatomic molecules, where scattering thousands of photons necessary for Doppler cooling becomes more challenging due to additional vibrational modes [193]. Here, we demonstrate transverse cooling (and heating) of a SrOH beam using two different electronic transitions, study loss channels to vibrational states (including the bending mode), and highlight proposed extensions to more complex strontium monoalkoxides with six and more atoms.

6.1 Doppler cooling in a multilevel system

In the previous discussion on the radiative force for a two-level atom we ignored the velocity dependence of F_{sp} and assumed a stationary atom which was a reasonable approximation for small transverse velocities used in the deflection experiment. However, because of the Doppler frequency shift $\omega_D = -\vec{k}\cdot\vec{v}$, radiative force obtains a velocity dependent component now [170]

$$F_{\text{rad}} = \hbar k \frac{\gamma}{2} \frac{s_0}{1 + s_0 + 4\left(\delta + \omega_D\right)^2/\gamma^2}. \tag{6.1.1}$$

By tuning the laser frequency below atomic resonance $\delta < 0$, the force will be higher for atoms counter-propagating to the laser beam ($\delta + \omega_D \approx 0$) and lower for atoms moving in the same direction as the photon wave vector $\vec{k}$. Thus, the force depends on the sign of $\vec{k}\cdot\vec{v}$ product.

6.1.1 Optical molasses for a two-level atom in 1D

In order to cool atomic motion in both directions, the technique of optical molasses (OM) is frequently used that relies on a pair of counter-propagating laser beams detuned below atomic resonance to dampen atomic motion. As a starting point in our analysis we will assume low intensity

regime $s_0 \ll 1$ and ignore effects arising from stimulated emission which will play an important role in the later sections. In this parameter space, the total force on the moving two-level atom is given as the sum of the force arising form the laser beams from the left $\vec{F}_{+\hat{x}}$ and right $\vec{F}_{-\hat{x}}$ directions:

$$\vec{F}_{\mathrm{OM}} = \vec{F}_{+\hat{x}} + \vec{F}_{-\hat{x}}. \tag{6.1.2}$$

The total force on the atoms becomes the product of the maximum radiation pressure force, saturation parameter, Doppler shift to linewidth ratio, as well as detuning and velocity dependent factor [194]

$$F_{\mathrm{OM}} \approx \frac{\hbar k \gamma}{2} s_0 \frac{w_D}{\gamma} \frac{16\delta/\gamma}{1 + \frac{8}{\gamma^2}\left(\delta^2 + \omega_D^2\right) + \frac{16}{\gamma^4}\left(\gamma^2 - \omega_D^2\right)^2}. \tag{6.1.3}$$

The exact expression for F_{OM} can be simplified in order to gain a better physical intuition into the damping process by considering the regime of small velocity classes such that $\omega_D \ll \gamma, \delta$. In this regime the cooling force acquires a more familiar damping form $F_{\mathrm{OM}} = -\beta v$ [194]:

$$F_{\mathrm{OM}} \approx 4\hbar k s_0 \frac{\omega_D \left(2\delta/\gamma\right)}{\left(1 + \left(2\delta/\gamma\right)^2\right)^2} \tag{6.1.4}$$

in the limit of $s_0 \ll 1$. The force decelerates atoms for $\delta < 0$ (red-detuned) and accelerated for $\delta > 0$ (blue-detuned) leading to cooling and heating of the atomic motion, correspondingly. Effective cooling happens over a finite velocity range called "capture velocity" v_c and corresponds to the Doppler shift comparable to the natural linewidth $v_c \sim \gamma/k$. For SrOH cooled on the $\tilde{X} - \tilde{A}$ transition, $v_c \approx 5\,\mathrm{m/s}$.

6.1.2 Extension to multiple levels

As was discussed previously in the context of radiation pressure force, the addition of multiple ground and excited states in real atoms and molecules complicates the two-level picture presented above. However, it was discovered recently [171, 195] that a careful analysis of Doppler laser cooling in molecules based on accurate rate equation calculations reasonably agrees with a simpler

picture of modifying two-level equations presented above and incorporating expressions for the effective decay rate γ_{eff}, saturation intensity $I_{\text{sat,eff}}$, and saturation parameter s_{eff} as discussed in the section on photon cycling in multilevel systems. There are two configurations for laser cooling employed in the SrOH experiments described below. In the first implementation, the main cycling transitions is $\tilde{X}(000) - \tilde{A}(000)$ and the repumper for the (100) state of the Sr-O stretching mode is $\tilde{X}(100) - \tilde{B}(000)$; thus the main cooling transition and the repumper transitions are decoupled, leading to $\gamma_{\text{eff}} = \gamma/2$ and $s_{\text{eff}} = s_0/18$. In the second configuration when both main cycling and (100) repumping laser are exciting the $\tilde{X} - \tilde{B}$ transitions, the number of total ground states is $n_g = 24$ now and the number of excited states is still $n_e = 4$. The effective decay rate becomes $\gamma_{\text{eff}} = 2\gamma/7$ and the effective saturation parameter is $s_{\text{eff}} = 7s_0/72 \approx s_0/10.3$ since the saturation intensity for the excitation of the $\tilde{X}(000)$ sublevels becomes [171]

$$I_{\text{sat,eff}} = \frac{2n_{g0}^2}{n_g + n_e} I_{\text{sat}} \tag{6.1.5}$$

where $n_{g0} = 12$ is the number of ground state sublevels in $\tilde{X}(000)$ and $n_g = 24$ is the total number of ground states in both $\tilde{X}(000)$ and $\tilde{X}(100)$. Despite the complexity of the presented expression in eq. 6.1.5, one possible way to interpret the scaling prefactor is to consider it as a product of the total number of (000) ground state sublevels n_{g0} that are driven by the laser excitation times the fraction of time the molecules spend in the ground vibrational state $n_{g0}/(n_g + n_e)$. The factor of 2 makes sure that when $n_g = n_{g0} = n_e$, the expression gives $I_{\text{sat,eff}} = n_g I_{\text{sat}}$. The advantage of using a decoupled scheme where the main cycling laser is not coupled to any of the repumpers is that the effective cycling rate is independent of the number of vibrational repumpers and always remains at $\gamma_{\text{eff}} = \gamma/2$.

6.1.3 Limits of Doppler cooling

While $F_{\text{OM}} \approx -\beta v$ leads to cooling of the velocity distribution at the rate of $(\mathrm{d}E/\mathrm{d}t)_{\text{cool}} = \vec{F}_{\text{OM}} \cdot \vec{v} = -\beta v^2$, atom-light interactions also lead to heating because of the finite root-mean-square scatter

value of the momentum change due to absorbed and emitted photons. For example, for an atom at rest that has undergone a single absorption and spontaneous emission event, the average energy has increased by [158]

$$\langle E \rangle = \frac{\hbar^2 k^2}{M}. \tag{6.1.6}$$

Thus, the heating rate becomes $(\mathrm{d}E/\mathrm{d}t)_{\mathrm{heat}} = R_{\mathrm{sc}}\hbar^2 k^2/M$. By analyzing the equilibrium condition $(\mathrm{d}E/\mathrm{d}t)_{\mathrm{cool}} + (\mathrm{d}E/\mathrm{d}t)_{\mathrm{heat}} = 0$, it can be shown [194] that during the Doppler cooling process the minimum temperature reached is equivalent to the energy width of the cooling transition, *i.e.* $k_B T_{\mathrm{Dop}} = \hbar\gamma/2$. For SrOH on the 689 nm transition, the Doppler cooling limit becomes $T_{\mathrm{Dop}} \approx 200\,\mu\mathrm{K}$. For regime when $s_{\mathrm{eff}} \gtrsim 1$, the minimum Doppler temperature will scale as well $T_{\mathrm{Dop}} = 200\mu\mathrm{K}\sqrt{1+s_{\mathrm{eff}}}$.

6.2 Sub-Doppler laser cooling mechanisms

There are multiple other laser cooling schemes that can reach temperatures below the Doppler limit and therefore go under the name of sub-Doppler laser cooling mechanisms. Majority of such techniques rely on the breakdown of the two-level atom approximation where multiple ground state sublevels need to be considered. Particularly, in our description of the optical forces on a multi-level system like SrOH, so far we only used statistical weights to scale the relevant experimental parameters from the two-level atom analysis like saturation intensity and scattering rate. However, we have ignored the fact that multiple ground sublevels may interact differently with the laser light. Additionally, the presence of strong electric fields from the laser oscillations leads to shifts of the atomic or molecular energy levels which we have not considered so far.

Upon the addition of the light-atom interaction $\mathcal{H}'(t)$, the energies E_n of the original Hamiltonian $\mathcal{H}_0(t)$ cease to remain eigenenergies of the new total Hamiltonian $\mathcal{H}(t) = \mathcal{H}'(t) + \mathcal{H}_0(t)$. Upon the transformation into the rotating frame, the new eigenenergies become [170]

$$E_{e,g} = \frac{\hbar}{2}\left(-\delta \mp \sqrt{\Omega^2 + \delta^2}\right). \tag{6.2.1}$$

In the limit of small Rabi frequency $\Omega \ll |\delta|$ achieved in our experiment, the energy shifts simplify to [170]

$$\triangle E_g = \mathrm{sgn}(\delta)\frac{\hbar\Omega^2}{4|\delta|} \tag{6.2.2}$$

$$\triangle E_e = -\mathrm{sgn}(\delta)\frac{\hbar\Omega^2}{4|\delta|} \tag{6.2.3}$$

with $\mathrm{sgn}(\delta) \equiv \delta/|\delta|$. Therefore, the direction of the energy shift for the ground state depends on the sign of laser detuning, with $\delta < 0$ resulting in lower energy and $\delta > 0$ giving higher energy shift for E_g. An intuitive way to understand the direction of this shift is by considering the dressed atom picture that includes the atom plus field Hamiltonian. Then, two atomic states coupled by the laser light are separated by δ. While a pair of interacting energy levels repels each other [20], the term $\mathrm{sign}(\delta)$ determines which state is higher in energy before the interaction is included. For an inhomogeneous light field like a standing wave, there will be a periodic spatially modulated light shift to atomic or molecular energy levels with largest light shifts at the antinodes and small energy shifts at the nodes. While the resulting energy gradient leads to a conservative force that averages to zero on the size of light's wavelength, spatially dependent optical pumping processes can lead to nonzero cooling forces.

6.2.1 Magnetically-assisted Sisyphus laser cooling

The simplified schematic diagram of the magnetically-induced laser cooling (MILC) mechanism utilized in our experiment is presented in Fig. 6.2.1. In the inverted level scheme of the form $F_g > F_e$ as in SrOH, for a fixed linear laser polarization, all magnetic sublevels cannot couple to the laser light, leaving some substates dark to the addressing laser light [196]. While the bright states are shifted by the amounts calculated in eq. 6.2.2 and 6.2.3, the dark states effectively have no AC Stark shifts. Also, both the magnitude of the AC Stark shifts as well as the optical pumping rate between the energy levels are largest at the antinodes of the standing light wave. Therefore, molecules originally in the bright states will loose kinetic energy as they ascend the potential hills created by the light field and are most likely to be optically pumped into the dark states at the

top of the antinodes. However, once in the dark states, the molecules will no longer couple to the laser light. In the absence of a mechanism to precess those molecules out of dark states, the cooling process would stop. Because, SrOH has an unpaired electron with a magnetic moment approximately $\mu_B = 1.4\,\mathrm{MHz/Gauss}$, the application of the magnetic fields will cause precession of the dark states back into the bright states at the rate determined by the applied magnetic field. To ensure efficient optical pumping into the dark states, the magnitude of the magnetic field is chosen such that the precession rate of the molecular magnetic sublevels is less than the optical pumping rate at the antinodes [170]. Additionally, the Sisyphus cooling will be the most effective for molecules that travel $\lambda/4$ distance in time to be pumped into the dark state [100]. If the rate of optical pumping into the dark states is γ_p, then the capture velocity range for Sisyphus laser cooling is $v_{\mathrm{Sis}} \sim \lambda\gamma_p/4 < 1\,\mathrm{m/s}$ for SrOH which is less than v_{Dop}. The force profiles for the MILC has the following functional form [189]:

$$F_{\mathrm{Sis}} = \frac{\alpha v}{1 + v^2/v_{\mathrm{Sis}}^2} \tag{6.2.4}$$

with the positive slope around $v = 0$ and smaller capture velocity.

6.2.2 Sisyphus cooling at high intensities

In low intensity regime when $\Omega \ll \gamma$, upon the electronic excitation, molecules return back to the ground state via incoherent process of spontaneous emission. However, for high laser intensities spontaneous emission starts to play a crucial role. Since in our laser cooling experiments the saturation parameter $s_{\mathrm{eff}} > 1$, it becomes important to consider coherent momentum exchange between the standing light wave of optical molasses and molecules. Such stimulated emission laser cooling has been observed for atoms in the past [191, 197] and compared to MILC has a different physical mechanism underpinning it that we describe in more detail.

In the dressed atom picture, the eigenstates of the total Hamiltonian $|\pm\rangle$ are mixtures of the

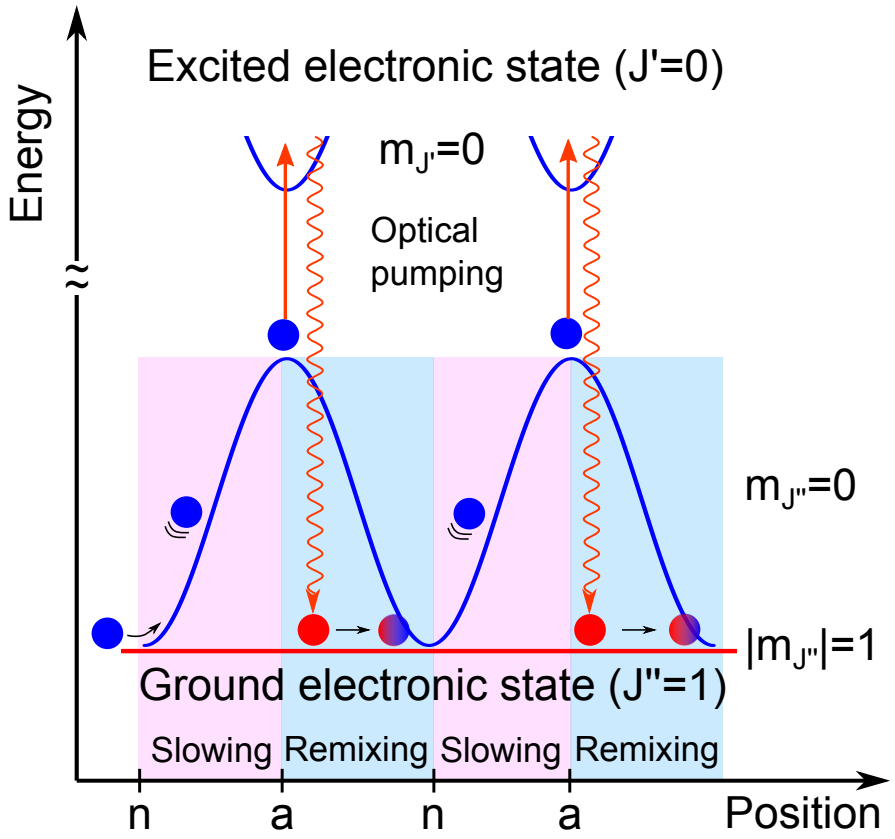


Figure 6.2.1: Diagram of the magnetically-assisted Sisyphus laser cooling for $J_g = 1 \rightarrow J_e = 0$ electronic transition with blue-detuned laser light. With the π polarized light only $m_{J''} = 0$ sublevels experience energy modifications due to AC Stark shifts. Periodic intensity modulation in the standing light wave results in a position dependent energy shift with maximums at the antinodes (denoted "a") and minimums at the nodes (denoted "n") of the standing light wave. Combination of the slowing, irreversible optical pumping, and magnetic-field induced remixing leads to the cooling of the velocity distribution.

bare atomic states $|g\rangle$ and $|e\rangle$[170]

$$|+\rangle = \sin\theta\,|g\rangle + \cos\theta\,|e\rangle \tag{6.2.5}$$

$$|-\rangle = \cos\theta\,|g\rangle - \sin\theta\,|e\rangle \tag{6.2.6}$$

where the mixing angle θ is given by

$$\cos(2\theta) \equiv -\frac{\delta}{\sqrt{\Omega^2+\delta^2}}. \tag{6.2.7}$$

Therefore, in a standing light wave created by the optical molasses beams, the composition of the eigenstates $|\pm\rangle$ acquires an oscillatory spatial dependence since the ratio of Rabi frequency Ω to detuning δ varies from node to antinode. At the node when $\Omega = 0$, dressed state $|+\rangle$ corresponds to $|g\rangle$ and therefore molecules cannot spontaneously decay. On the other hand, at the antinodes the bare states are maximally mixed with a relative energy splitting of

$$\triangle E_{|\pm\rangle} = \hbar\sqrt{\Omega^2+\delta^2}. \tag{6.2.8}$$

Consider the dynamics of molecules in a standing wave for a positive detuning $\delta > 0$. In the absence of spontaneous emission, when the atom or molecule climbs the potential hill created by the standing wave, the kinetic energy is converted into potential energy via the stimulated emission processes that redistribute the photons between two counter-propagating light waves [191]. While the atomic momentum is transferred to the light field, the total energy of the system is conserved. However, at the antinode a dressed state $|+\rangle$ which now contains a significant admixture of $|e\rangle$ and experiences a large positive Stark shift can decay via spontaneous emission to another state with a large admixture of $|g\rangle$ and significant negative Stark shift. The rate of spontaneous decays has a spatial dependence because of the differing compositions for dressed states $|\pm\rangle$ in terms of the bare states. Since on average the atoms on average climb more uphill between two consecutive spontaneous emissions, this process leads to cooling of the velocity distribution. Similar arguments

can be presented for negative detuning $\delta < 0$ when the velocity of the atoms is heating instead because spontaneous emissions are most likely at the bottoms of the potential hills at the antinodes of the standing wave. While the detuning signatures of the Sisyphus cooling at high intensities and MILC described above are identical for SrOH because of the inverted level structure, magnetic field remixing of dark substates is crucial for both cooling regimes since cooling process would cease otherwise. At high laser intensities with $s_{\text{eff}} \gg 1$ used in our experiments both cooling processes contribute to the reduction in velocity distribution and phase space compression.

6.2.3 Limits of sub-Doppler laser cooling

While in our experiment, the temperatures achieved are above T_{Dop} it is important to discuss future possibilities for reaching sub-Doppler temperatures with MILC. If sufficient interaction time is allowed between the molecules and light field, once the velocity of the molecules is such that $k_B T_{\text{lim}} < \triangle E_g$ they can no longer climb the potential hill created by the standing light wave. While the cooling arguments presented above still persist, it turns out that with a careful analysis in 1D sub-Doppler cooling schemes one obtains [170] $k_B T_{\text{lim}} = a \triangle E_g$ with $a < 1$. By changing the value of the AC Stark shift, cooling to lower and lower temperatures is possible until the recoil from spontaneous emissions involved in the optical pumping between the dark and bright sublevels starts to play an important role. The irreversible process of spontaneous emission which is a crucial requirement for laser cooling, in fact, becomes the dominant heating mechanism because of the randomness associated with spontaneous emission. Since the last spontaneously emitted photon is in the arbitrary direction, it will leave the atom or molecule with residual momentum of $\hbar k$ with the corresponding kinetic energy of

$$E_r \equiv k_B T_r = \frac{(\hbar k)^2}{2M}. \tag{6.2.9}$$

In practice, the experiments on sub-Doppler laser cooling of atoms reach temperatures on the order of $T_r \approx 10 T_r$ [170, 190]. While temperatures below T_r can be reached employing techniques

of coherent two-photon transitions [170, 198], these methods will not be described in this thesis because lowest temperatures reached with SrOH where above the Doppler cooling limit because of the limited molecule-light interaction time.

6.3 Experimental configuration for laser cooling

Our work with SrOH uses the cryogenic buffer-gas beam (CBGB) [80], which is also used in all other experiments on laser cooling of molecules. SrOH can be produced efficiently with ablation and forms an intense CBGB. Figure 6.3.1 shows a simplified schematic diagram of the current experimental apparatus used for laser cooling experiments. Laser ablation of $Sr(OH)_2$ produces SrOH molecules that are then entrained in helium buffer gas ($T_{\mathrm{He}} \sim 2$ K) that flows out of the cell into a beam. He flow is 6 standard cubic centimeters per minute (sccm), and the beam is extracted through a 5 mm diameter aperture. This CBGB contains $\sim 10^9$ molecules in the first excited rotational level ($N = 1$) in a pulse ~ 5 ms long. The forward velocity of the SrOH beam is $v_x \sim 130$ m/s and its transverse velocity spread is $\triangle v_y \sim \pm 15$ m/s. A 2×2 mm square aperture situated 15 cm away from the cell collimates the beam, resulting in an effective transverse temperature $T_\perp \sim 50$ mK. A few millimeters after the aperture, molecules enter the Interaction region with molecule-laser interaction length of 15 mm.

To laser cool, we use a photon cycling scheme that we also employed in an earlier work, as described in detail in Ref. [188]. The main photon cycling path is $\tilde{X}^2\Sigma^+(000) \rightarrow \tilde{B}^2\Sigma^+(000)$ (611 nm) and the first vibrational repump is $\tilde{X}^2\Sigma^+(100) \rightarrow \tilde{B}^2\Sigma^+(000)$ (631 nm), as shown in Fig. 6.3.1 (Interaction region). The combined main and repump laser light, with diameter of ~ 3 mm, propagates in the y direction and makes 5 round-trip passes between two mirrors before it is retroreflected back in order to create a standing wave. The molecule-laser interaction time is $t_{\mathrm{int}} \sim 115\ \mu$s. Each color (611 nm and 631 nm) includes two frequency components separated by ~ 110 MHz to address the $P_{11}(J'' = 1.5)$ and ${}^PQ_{12}(J'' = 0.5)$ lines of the spin-rotation (SR) splitting. We also study cooling using the $\tilde{X}^2\Sigma^+(000) \rightarrow \tilde{A}^2\Pi_{1/2}(000)$ excitation at 688 nm as the main

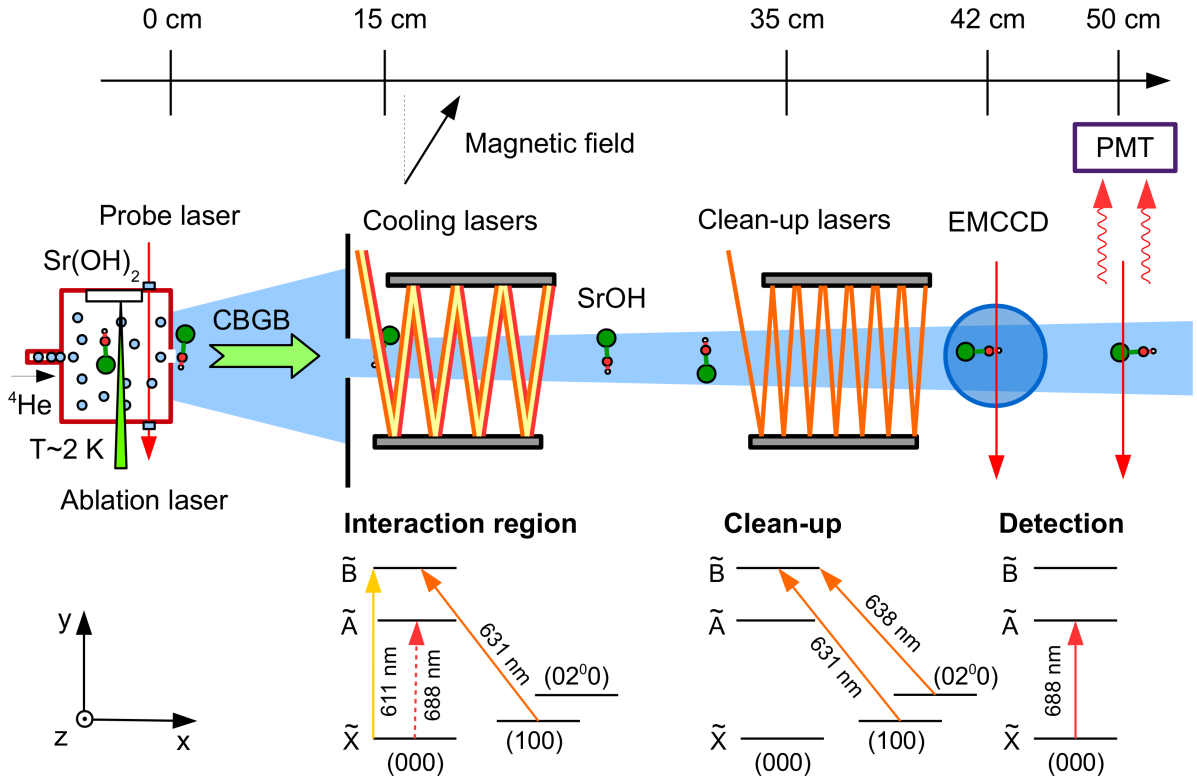


Figure 6.3.1: Schematic of the experimental apparatus (not to scale) for laser cooling experiments. A cryogenic beam of SrOH is produced using laser ablation of $Sr(OH)_2$ followed by buffer-gas cooling with ~ 2 K helium gas. To apply the cooling forces on the collimated molecular beam, we use transverse lasers retroreflected between two mirrors in order to generate a standing wave. Depending on the experimental configuration, either the $\tilde{X}^2\Sigma^+(000) \rightarrow \tilde{A}^2\Pi_{1/2}(000)$ or the $\tilde{X}^2\Sigma^+(000) \rightarrow \tilde{B}^2\Sigma^+(000)$ cooling transition is used with an additional $\tilde{X}^2\Sigma^+(100) \rightarrow \tilde{B}^2\Sigma^+(000)$ laser for repumping molecules decaying to the vibrationally excited Sr-O stretching mode. In order to remix dark magnetic sub-levels, a magnetic field is applied at an angle relative to laser polarization in the Interaction region. Before the detection is performed, molecules remaining in either (100) or (02^00) excited vibrational levels of the electronic ground state are optically pumped back into the ground vibrational level using $\tilde{X} \rightarrow \tilde{B}$ off-diagonal excitations. The spatial profile of the molecular beam is imaged on the electron multiplying charge-coupled device (EMCCD) camera and the time-of-flight (ToF) data is collected on the photomultiplier tube (PMT).

transition. Each SR component of the 688 nm light is generated using separate injection-locked laser diodes seeded by external-cavity diode lasers in the Littrow configuration [172] resulting in ~ 15 mW per SR component in the interaction region. The 611 nm light, as well as all of the repumping light, is generated by cw dye lasers passing through acousto-optic modulators resulting in ~ 50 mW per SR component. In order to destabilize dark states created during the cycling process [173], we apply a magnetic field of a few gauss. Due to the vibrational angular momentum selection rule [108], the dominant loss channel for the bending mode is to the $v_2 = 2$ state with $l = 0$ [150] denoted $\left(02^0 0\right)$. Further details regarding the photon cycling scheme used for SrOH have been previously described [188].

The spatial profile of the molecular beam is recorded by imaging laser-induced fluorescence (LIF) in the Detection region. The molecules are excited using a transverse retroreflected laser beam and LIF photons are imaged onto an EMCCD camera. The detection laser addresses both SR components of the $P(N'' = 1)$ line for the $\tilde{X}^2\Sigma^+(000) \rightarrow \tilde{A}^2\Pi_{1/2}(000)$ transition, as shown in Fig. 6.3.1 (Detection). In a similar laser configuration, time of flight (ToF) data is recorded by collecting the LIF on a PMT (further downstream). In order to boost the LIF signal there is a Clean-up region where all of the molecular population is pumped into the ground state ($\tilde{X}(000)$) from the excited vibrational levels ($\tilde{X}(100)$ and $\tilde{X}\left(02^0 0\right)$). This is done with off-diagonal excitation to $\tilde{B}(000)$, as shown in Fig. 6.3.1 (Clean-up).

6.4 Spectroscopy of repumping transitions

Our previous results on radiative force deflection of SrOH beam indicated that we were losing molecules to dark vibrational levels. Based on the estimations of the FC factors, the two dominant loss channels at approximately part per thousand each were the (200) state of the stretching mode and $\left(02^0 0\right)$ of the bending mode. Since for laser cooling experiments, we required an increase in the number of scattered photons and a larger effective laser-molecule interaction time, the fraction of SrOH molecules lost to dark vibrational levels could have become an important problem. As

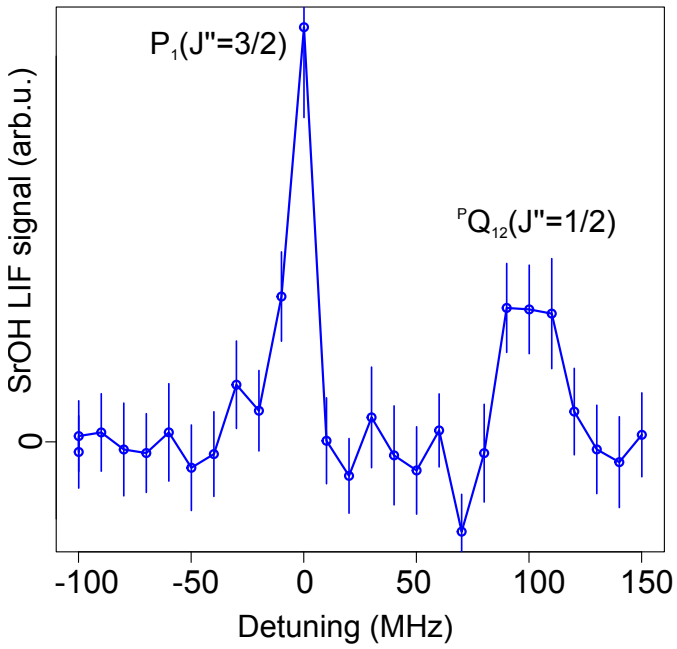


Figure 6.4.1: Fluorescence spectrum of the bending mode repumping laser. The excitation is performed on the $\tilde{X}\left(02^{0}0\right) \rightarrow \tilde{B}\left(000\right)$ transition, followed by the laser induced fluorescence signal collected for the $\tilde{B}\left(000\right) \rightarrow \tilde{X}\left(000\right)$ spontaneous decay. The offset frequency is 469.886850 THz. The integration time is 3-6 ms.

the first step, we embarked on the spectroscopy of the off-diagonal $\tilde{X}\left(02^{0}0\right) \rightarrow \tilde{B}\left(000\right)$ transition which has not been previously measured in the literature. The spectrum of this transition that we obtained is shown in Fig. 6.4.1. The splitting of ~ 110 MHz is indicative of the SR splitting in the $N = 1$ level of the $\left(02^{0}0\right)$ state.

In order to compare the calculated strength of this off-diagonal transition with our measurements we have converted the measured signal into the photon count rate to benchmark the measurement against the known $\tilde{X}\left(100\right) \rightarrow \tilde{B}\left(000\right)$ transition strength. Assuming that the population in the ground vibronic states $N_{\tilde{X}(100)}$ and $N_{\tilde{X}\left(02^{0}0\right)}$ is much larger than in the excited electronic state $N_{\tilde{B}(000)}$, the rate of excitation is given by [20]

$$-\frac{\mathrm{d}N_{\tilde{X}}}{\mathrm{d}t} = \sigma F N_{\tilde{X}} \tag{6.4.1}$$

where $F = I/h\nu$ is the photon flux and σ is the absorption cross section. For a molecular transition

σ is given by [20]

$$\sigma = \frac{2\pi^2 \nu S_{J'J''}}{3\varepsilon_0 hc\,(2J''+1)} g\,(\nu - \nu_0) \tag{6.4.2}$$

where ν_0 is the transition frequency, $S_{J'J''}$ is the transition line strength, and $g\,(\nu-\nu_0)$ is the line-shape function. The rotational line strength can be factored out into contributions from vibrational, electronic, and rotational components as follows

$$S_{J'J''} = q_{\nu'-\nu''} \left|\mathbf{R}_e\right|^2 S_{J''}^{\triangle J} \tag{6.4.3}$$

with $S_{J''}^{\triangle J}$ being the Hönl-London factor, $\mathbf{R}_e$ the electronic transition dipole moment and $q_{\nu'-\nu''}$ Franck-Condon factor between $\tilde{X}\,(\nu'')$ and $\tilde{B}\,(\nu')$ states. By looking at the ratio of fluorescence rates (LIFR) following $\tilde{X}\,(100) \rightarrow \tilde{B}\,(000)$ and $\tilde{X}\left(02^00\right) \rightarrow \tilde{B}\,(000)$ excitations, we can extract the ratio of Franck-Condon factors

$$\frac{\mathrm{LIFR}_1}{\mathrm{LIFR}_2} \approx \frac{q_1 I_1}{q_2 I_2} \tag{6.4.4}$$

if we consider the same rotational transition. Figure 6.4.2 shows the comparison of the LIF rate signals for the two off-diagonal excitations on the $\tilde{X}-\tilde{B}$ transition. The ratio of signals is ~ 6 while the ratio of the powers used is $\sim 1/2$ leading to $\times 12$ higher FC factor for $\tilde{X}\,(100)-\tilde{B}\,(000)$ than for $\tilde{X}\left(02^00\right)-\tilde{B}\,(000)$. Using the measured and calculated value of 2% for FCF for the stretching mode excitation of $\tilde{X}\,(100)$ we determine that FCF for exciting from $\tilde{X}\left(02^00\right)$ is $\sim 2\times 10^{-3}$ which is consistent with our estimation of 2.2×10^{-3} confirming the validity of our FCF calculations.

6.5 Scattering rate dependence on the remixing magnetic field

As mentioned previously, because the number of ground state sublevels is larger than for the addressed excited state ($F_g > F_e$), for a given laser polarization there exist dark magnetic sublevels that don't couple to the laser field. Thus, in the absence of the remixing mechanism the photon cycling process will cease after only a few photons have been scattered. The effect of the magnetic field on the scattering rate for SrOH excited on the $P\,(N''=1)$ subband of the $\tilde{X}-\tilde{B}$ electronic can

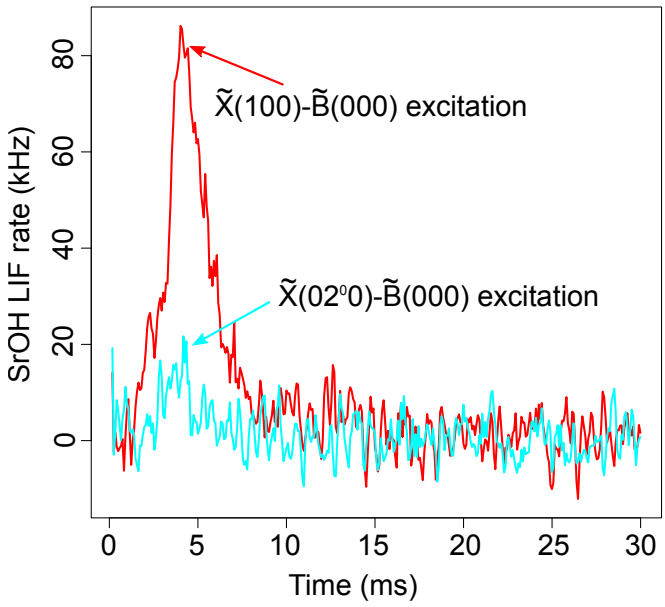


Figure 6.4.2: Comparison of the LIF rate for the two off-diagonal $\tilde{X} - \tilde{B}$ transitions.

be clearly seen from the data in Fig. 6.5.1. Without repumping lasers, the molecular beam signal should be depleted with main cycling lasers. Applied magnetic field leads to higher remixing rate and enhanced beam depletion because of the optical pumping into the excited vibrational state $\tilde{X}(100)$ after scattering ~ 50 photons per molecule.

6.6 Doppler cooling

In the regime of low cooling laser power $s_{\text{eff}} \ll 1$ and high magnetic field remixing rate, we expect to observe Doppler cooling of the SrOH beam. Figure 6.6.1 shows beam profiles for various detunings of the main cooling laser with 12 mW total laser power for $\tilde{X}(000) - \tilde{B}(000)$ and remixing rate set by the magnetic field with coil current of $I = 10$ A which corresponds to $B = 12$ Gauss [1]. As expected for Doppler cooling, we see compression of the molecular beam width for red detuning (-10 MHz) and widening for blue (+10 MHz). In the cooling configuration, the width of the beam is reduced from 8.2 ± 0.2 mm to 7.0 ± 0.1 mm which corresponds to 1D temperature

[1] The conversion factor between coil current I and the total magnetic field experienced by the molecules is $B = 1.18I$ for I in amperes and B in gauss.

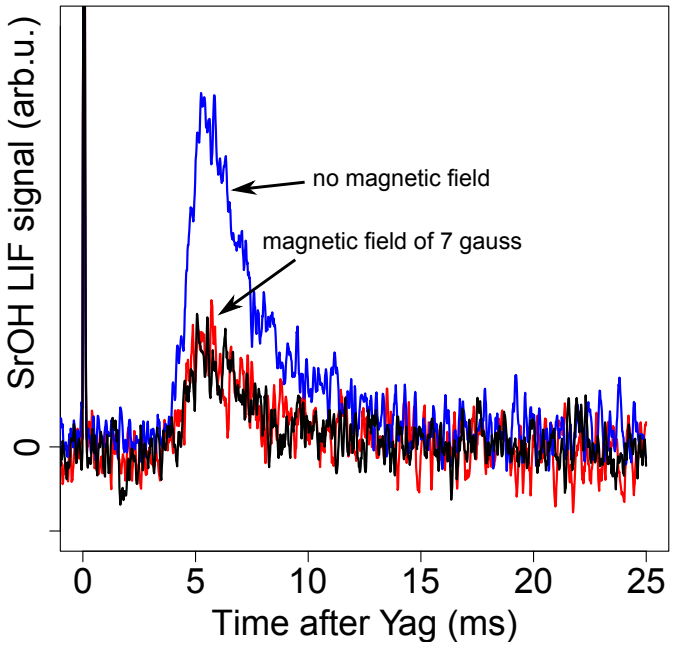


Figure 6.5.1: Depletion of the SrOH beam signal as a function of the applied remixing magnetic field.

reduction from 50 mK to 35 mK. Figure 6.6.2 shows molecular beam width vs detuning of the cooling laser. Beam compression is present for negative detunings and beam heating for positive. Once detuning is too far from resonance, both cooling and heating become less effective as seen from the plot.

6.7 Sisyphus laser cooling

Capability to perform nondestructive detection using photon cycling is almost taken for granted in atomic physics. The ability of obtain high resolution spatial images without sample destruction of not only atomic clouds but also single trapped atoms have enabled groundbreaking scientific achievement in physics of ultracold atom. However, majority of the times experiments with molecules employ photodissociation or photoionization methods that allow researchers to obtain high sensitivity to the time dynamics of studied molecules but deliver only limited spatial information. The success of our laser cooling experiments can be strongly attributed to our ability to

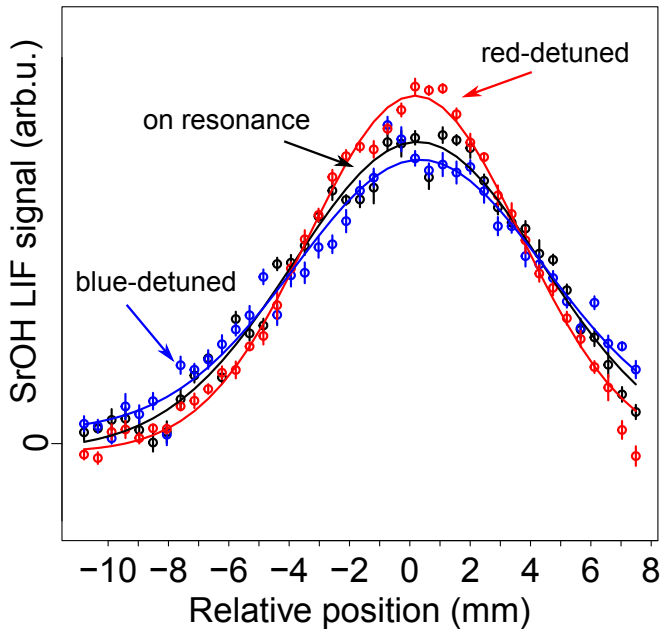


Figure 6.6.1: SrOH beam profiles for various $\tilde{X}(000) - \tilde{B}(000)$ cooling laser detunings in the Doppler configuration. The detunings are ± 10 MHz. In addition to Doppler cooling and heating, around position of -1 mm one can notice a sharp signal increase for blue detuning and signal drop for red detuning. These small effects are indicative of the Sisyphus laser cooling and heating effects to be describe later in the chapter.

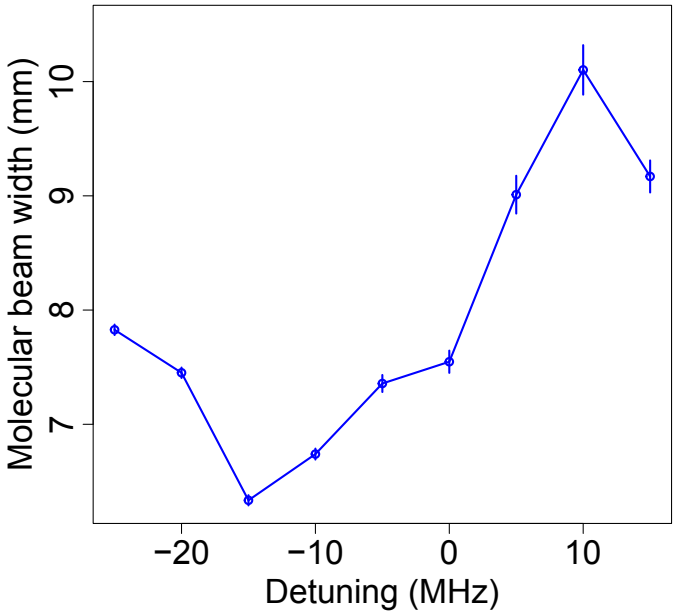


Figure 6.6.2: Molecular beam width vs detuning in the Doppler cooling and heating arrangement.

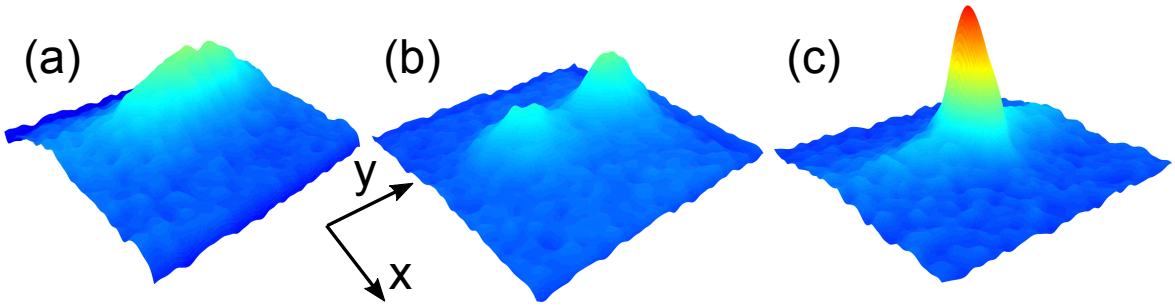


Figure 6.7.1: Camera images of the spatial fluorescence distribution of SrOH beam for various detunings of the cooling laser: (a) 0 MHz, (b) -10 MHz, and (c) +10 MHz. In the x direction the width of the fluorescence is determined by the size of the detection laser only.

obtain high resolution spatial images of SrOH molecular beam using direct photon cycling. Sisyphus laser cooling data on the $\tilde{X} - \tilde{B}$ transition visualized in 3 dimensions is shown in Fig. 6.7.1. While in the x direction, the width of the molecular cloud is limited by the size of the excitation laser, beam compression and expansion effects due to the laser light are clearly visible in the y direction.

Figure 6.7.2 shows 2D camera images of the molecular beam for various detunings of the $\tilde{X} - \tilde{B}$ cooling laser. Phase space compression is clearly visible in the comparison between images (b), $\delta = 0$, and (d), $\delta > 0$, cooling. To characterize the cooling efficacy for both $\tilde{X} - \tilde{A}$ and $\tilde{X} - \tilde{B}$ cycling transitions, we plot integrated 1D (x axis) beam profiles for both cooling configurations in Fig. 6.7.3. The most effective laser cooling was demonstrated using $\tilde{X}(000) - \tilde{B}(000)$ transition at 611 nm with laser intensity $I = 1.4$ W/cm^2, resulting in an effective on-resonance saturation parameter $s_{\text{eff}} \sim 34$ (Fig. 6.7.3(a)). The spatial distribution of the final beam is the convolution of the initial 2×2 mm beam spread, the beam spread before cooling, and the beam spread after cooling. Without cooling, the spatial width of the molecular beam is dominated by the transverse velocity distribution $v_\perp$ after the collimation aperture. In the Sisyphus configuration, the spatial profile in the detection region is influenced by the aperture's width. In order to extract $v_\perp$, Monte Carlo (MC) simulations of 2D molecular trajectories are performed by calculating the final y position in the Detection region of the molecules with forward velocity v_x that passed through the collimation aperture. The molecular velocities in the y direction are drawn from a Gaussian distribution with

a standard deviation $\sigma_{v_y} = \sqrt{k_B T_\perp / m}$, where m is the mass of SrOH. By fitting the results of the MC simulations (see Fig. 6.7.5) to the integrated molecular beam profiles, we determine the final beam temperature range of 0.5 mK $< T_\perp <$ 1 mK, which corresponds to a factor of ~ 70 reduction as compared to the $\delta = 0$ detuning and unperturbed molecular beam. Because of the high damping rate of the magnetic-field-induced laser cooling [190, 199], we achieve lower transverse temperature than previously demonstrated with a 1D MOT of diatomic molecules [101], with half the interaction length.

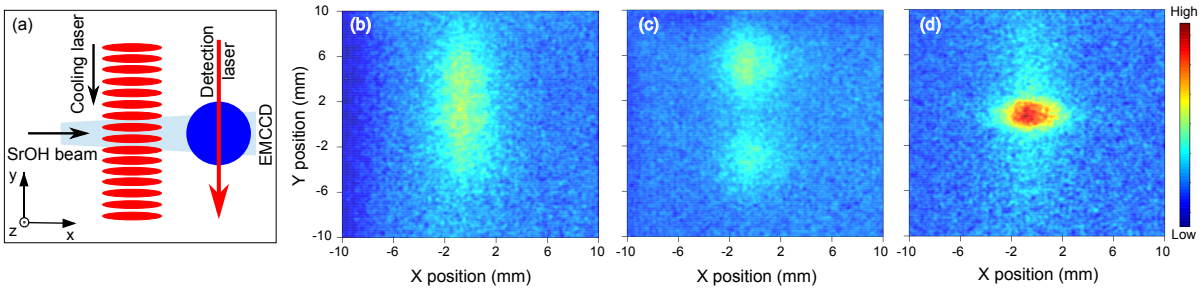


Figure 6.7.2: Spatial images of the molecular beam taken at different detunings of the $\tilde{X}\,(000) - \tilde{B}\,(000)$ cooling laser: (b) on resonance, (c) red-detuned (-10 MHz), and (d) blue-detuned (+10 MHz). The same color axis is used for all three plots. SrOH beam is moving in the x direction while the cooling and detection lasers are applied in the y direction as shown in (a). Narrowing of the spatial size of the molecular cloud with accompanying density increase in (d) compared to (b) in the y dimension indicates phase-space compression.

Cooling using the $\tilde{X} - \tilde{A}$ transition was less effective because of the lower available laser power. Figure 6.7.3(b) shows typical molecular beam profiles after interacting with a cooling laser exciting the $\tilde{X} - \tilde{A}$ transition at 688 nm with intensity of $I = 424$ mW/cm^2 and an effective on-resonance saturation parameter $s_{\text{eff}} \sim 8$. For a positive detuning we observe cooling of the SrOH beam represented by the increased molecular density near the center due to the narrowing of the spatial distribution. By comparing the fitted width of the resulting profile with a MC simulation we conclude that the beam is cooled to a final temperature of ~ 2 mK, an order of magnitude above the Doppler limit of ~ 200 μK. Figure 6.7.4 summarizes the cooling data for all configurations by plotting the full width at half maximum (FWHM) in the y dimension of the imaged molecular beam relative to the width of the unperturbed beam. While for the on-resonance configuration of the cooling lasers the width of the beam is not significantly modified, blue-detuned $\tilde{X} - \tilde{A}$ and

$\tilde{X} - \tilde{B}$ lasers compress molecular beam to 47% and 31% of the original FWHM.

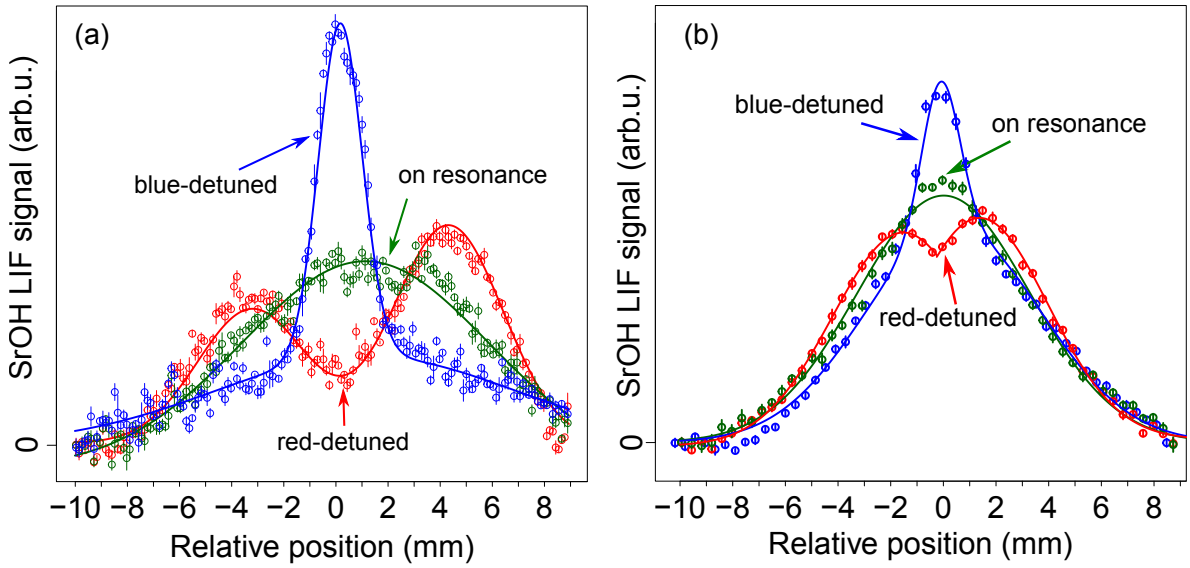


Figure 6.7.3: Integrated molecular beam profiles for different detunings of the cooling laser: (a) $\tilde{X}(000) - \tilde{B}(000)$ and (b) $\tilde{X}(000) - \tilde{A}(000)$. The detunings from resonance are given by $\delta = \pm 10$ MHz. With a positive detuning, the width of the molecular beam is reduced, which indicates cooling of the molecular beam. A "hole" around zero for $\delta < 0$ represents a heating signature of the magnetically-assisted Sisyphus effect with the widening of the total spatial distribution. An asymmetry in the height of two peaks comes from imperfect alignment between laser and molecular beams and was previously seen in similar experiments with atoms [191]. The excess signal above the fit near zero position for the on-resonance trace in (b) is potentially indicative of a slightly positive detuning of the cooling lasers.

Figure 6.7.6 shows that during the cooling process 40% of the molecules are lost to dark excited vibrational levels not addressed by the (100) and $\left(02^{0}0\right)$ repumping lasers. The phase space density Ω [2] of the molecular beam is increased due to cooling, with temperature reduction and spatial beam compression. Ω grows $\times 5$ with $\tilde{X} - \tilde{A}$ and $\times 11$ with $\tilde{X} - \tilde{B}$ cooling. With the two repumping lasers used in the experiment, $\sim 10^6$ molecules remain in the $N = 1$ (000) level. Lost molecules could be recovered with an additional repumping laser addressing the (200) vibrational level of the Sr-O stretching mode.

In order to extract the number of scattered photons during the cooling process, we determine

[2]Phase space density is given by $\Omega = n\lambda_{\mathrm{dB,x}}\lambda_{\mathrm{dB,y}}\lambda_{\mathrm{dB,z}}$, where n is the number density and $\lambda_{\mathrm{dB,i}} = h/\sqrt{2\pi m k_{\mathrm{B}} T_i}$ is the thermal de Broglie wavelength for molecules with mass m and temperature T. Ω is an important figure of merit for many experiments [1].

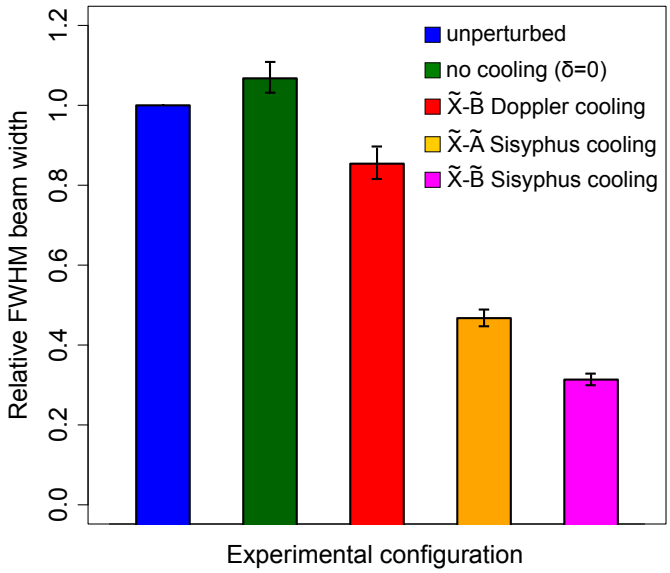


Figure 6.7.4: Summary of the laser cooling results. We plot the FWHM of the molecular cloud in the y dimension relative to the unperturbed distribution (no cooling lasers). For no cooling ($\delta = 0$) the molecular beam profile is not modified significantly. The importance of Sisyphus laser cooling for polyatomic molecules can be seen from this plot.

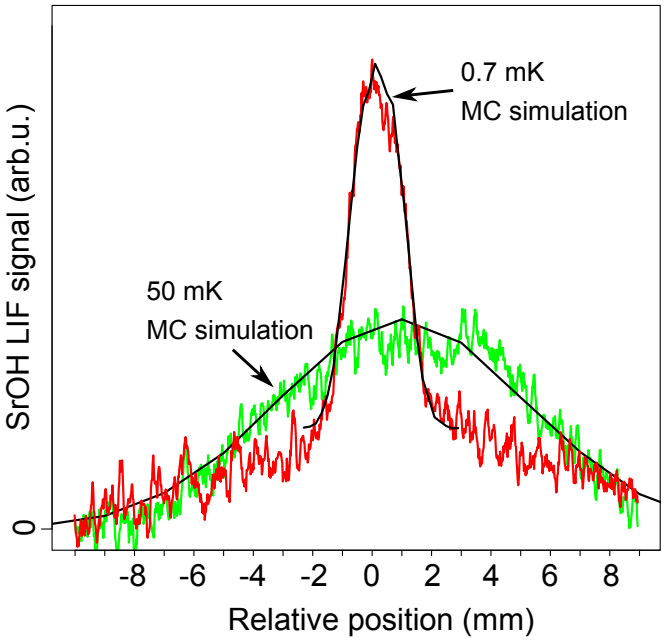


Figure 6.7.5: Extraction of beam temperature using Monte Carlo simulations of molecular dynamics.

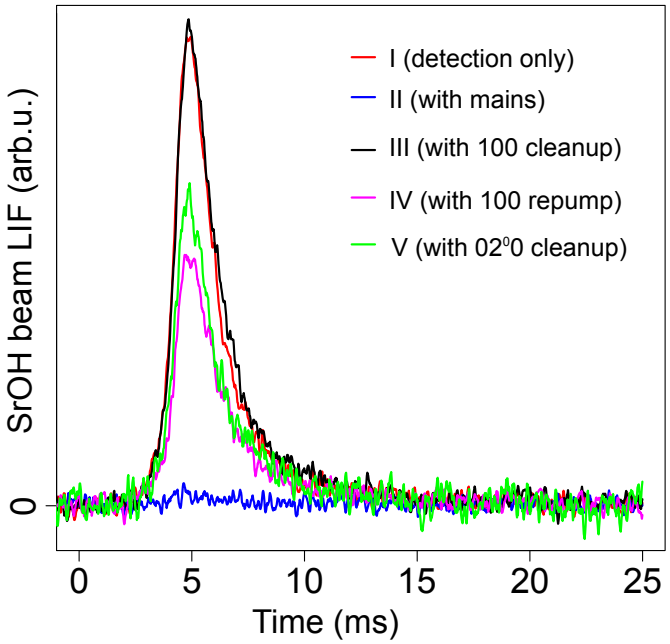


Figure 6.7.6: Molecular beam signal with various arrangements of the addressing lasers. The labeling of the traces (I-V) indicates the number of lasers interacting with the molecular beam. For trace I, only detection laser is used, while for trace V we apply five different sets of lasers (detection, main cooling laser, repump for (100) state, and clean-up lasers for (100) and $\left(02^{0}0\right)$ states.

the fraction of the remaining molecules (50%) after cooling with ToF PMT data taken without the $\left(02^{0}0\right)$ clean-up beam. Modeling absorption-emission cycles as a Bernoulli process with probability p to decay into the vibrational level not addressed by the repumping lasers [144] and using the previously measured decay rate to dark vibrational levels (above $\tilde{X}\,(100)$) of $p = (3 \pm 1) \times 10^{-3}$ [188], we calculate that on average each molecule emits 220^{+110}_{-60} photons with a scattering rate of $\Gamma_{\text{scat}} = 2 \pm 1$ MHz. In such a configuration, Doppler cooling from radiation-pressure molasses does not play a significant role [191]. By adding the $\left(02^{0}0\right)$ clean-up beam, we determine that 10% of molecules decay to the $\left(02^{0}0\right)$ state of the bending mode during the cooling stage. Therefore, we estimate the loss probability to the $\left(02^{0}0\right)$ bending mode state after the excitation to the $\tilde{A}^{2}\Pi_{1/2}\,(000)$ state to be $\sim 5 \times 10^{-4}$ which is consistent with the normal mode analysis estimations.

For negative detunings the molecules are expelled from the region around $v_y = 0$, leading to a double-peak structure that is a signature of the magnetically-assisted Sisyphus effect [189]. Compared to the results of cycling on the $\tilde{X} - \tilde{A}$ transition (Fig. 6.7.3(b)), the use of the $\tilde{X} - \tilde{B}$ transition (Fig. 6.7.3(a)) increases the separation between the peaks from 2.95 ± 0.04 mm to 7.54 ± 0.04 mm for $\delta < 0$. Our findings are in good agreement with previous studies of sub-Doppler laser cooling in complex multilevel atomic [200] and molecular systems [100, 201].

6.8 Characterizing Sisyphus cooling

In order to confirm the nature of the cooling mechanism, we characterized its effect on the molecular beam shape while modifying several key experimental parameters such as the value of detunings, laser power, and strength of the applied magnetic field. Figure 6.8.1 provides molecular beam profiles for various detunings of the main cooling laser. For $\delta < 0$ we observe widening of the beam distribution due to heating of the central portion of the beam as expected for the Sisyphus laser cooling mechanism described above. On the other hand positive detunings $\delta > 0$ lead to molecular beam compression and cooling. From the data in Fig. 6.8.1 we conclude that $\delta \geq 10$ MHz provides superior cooling results. While we did not take cooling data at detunings much larger than natural

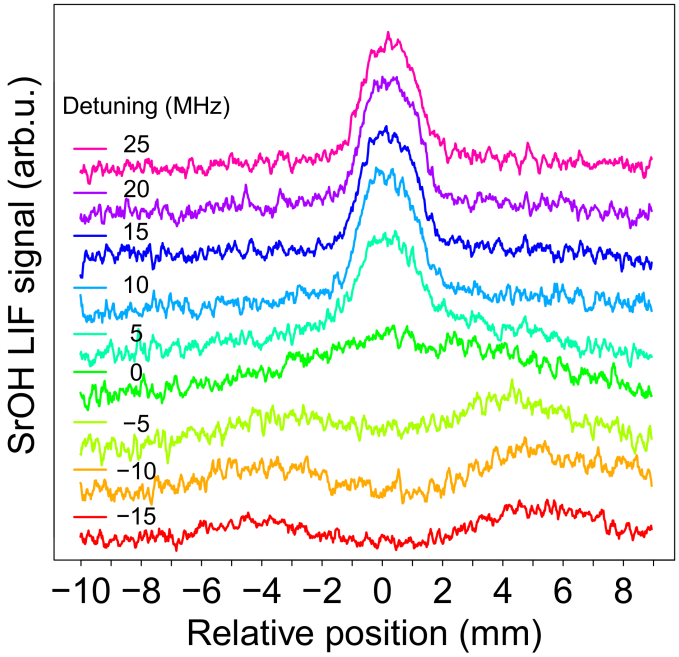


Figure 6.8.1: Beam profiles vs detuning of the $\tilde{X} - \tilde{B}$ cooling laser. The traces are vertically offset relative to each other for clarity.

linewidth ($\delta \gg \gamma$) this would be an interesting area to explore in the future experiments in order to minimize the temperature and optimize the cooled fraction of the molecules.

Figure 6.8.2 provides the comparison of the SrOH beam profiles as a function of the total laser power. For powers below 4 mW, there appears to be no significant cooling of the molecular beam. The central portion of the beam starts to compress when power of 4 mW for 3 mm diameter beam is used, resulting in an average total beam intensity of 57 mW/cm^2. For comparison, the on resonance effective saturation intensity for SrOH $\tilde{X} - \tilde{A}$ transition is 51 mW/cm^2. Because the cooling laser is detuned by one natural linewidth $\delta \approx \gamma$, the effective saturation parameter becomes $s \approx 0.22$. At the maximum intensity available for the $\tilde{X} - \tilde{A}$ cooling set-up of 33 mW, we see that a significant portion of the molecular beam is compressed. Here again, while the laser intensity of 467 mW/cm^2 is a factor of 9 larger than the effective on-resonance saturation intensity $I_{\mathrm{sat,eff}}$, because of the detuning from resonance the actual saturation parameter is $s \approx 2$. In the model of magnetically-assisted Sisyphus laser cooling described in section 6.2.1, the average kinetic energy removed from the molecules with one scattered photon is proportional to the AC Stark shift of the

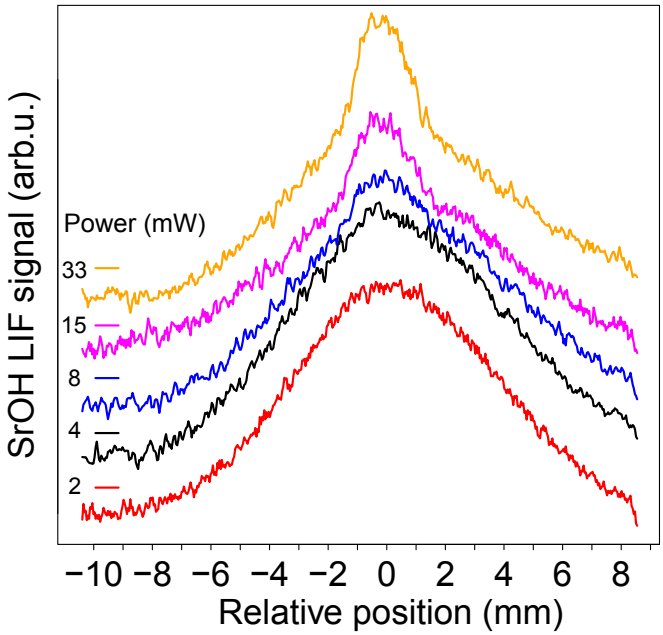


Figure 6.8.2: Beam profiles vs total power of the $\tilde{X} - \tilde{A}$ cooling laser.

ground state sub-levels. Therefore, increasing total laser power would lead to more kinetic energy removed from the molecules for a fixed number of scattered photons resulting in a larger cooled fraction as can be seen from our data in figure 6.8.2.

While magnetic potential is not directly removing kinetic energy from the molecular motion, magnetic field is crucial for remixing precessing dark magnetic projections into bright states. Figures 6.8.3 and 6.8.4 show the effect of changing magnetic field on the laser cooling process. From the data we conclude that Sisyphus laser cooling and heating processes are quite robust against magnetic field fluctuations and persist for coil currents up to 5 A which corresponds to magnetic fields of 6 gauss. However, the most effective cooling is achieved for small magnetic fields around 1 gauss.

6.9 Conclusions

In summary, we demonstrate and characterize Doppler and Sisyphus laser cooling of the polyatomic molecule SrOH. We reduce the transverse temperature of a cryogenic buffer-gas beam from 50 mK to 750 μK with ~ 200 scattered photons per molecule. Laser cooling of atoms is a mature

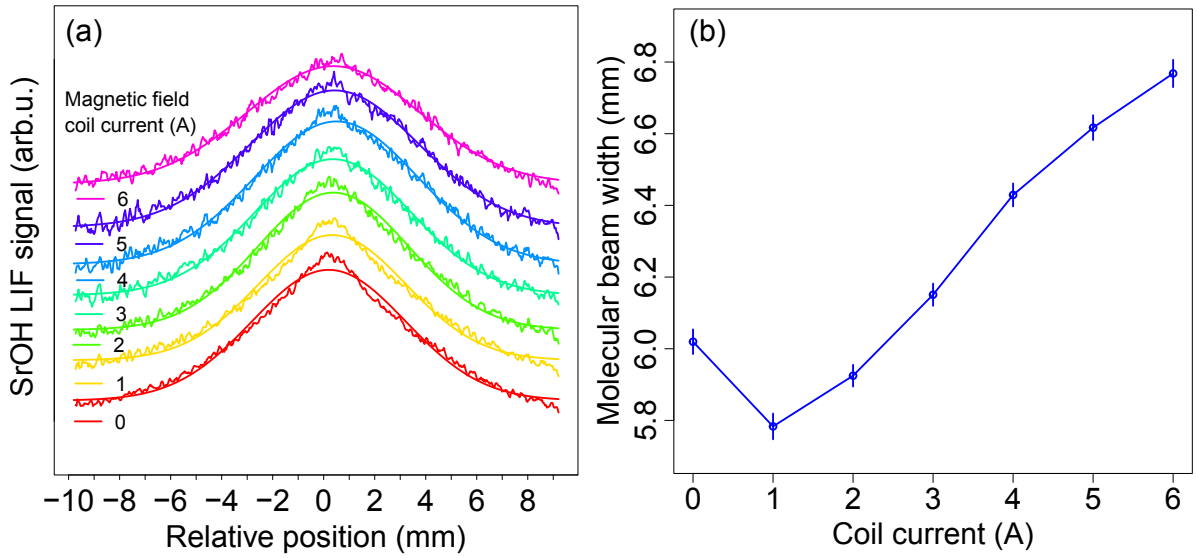


Figure 6.8.3: Sisyphus laser cooling of the molecular beam for various applied magnetic fields.

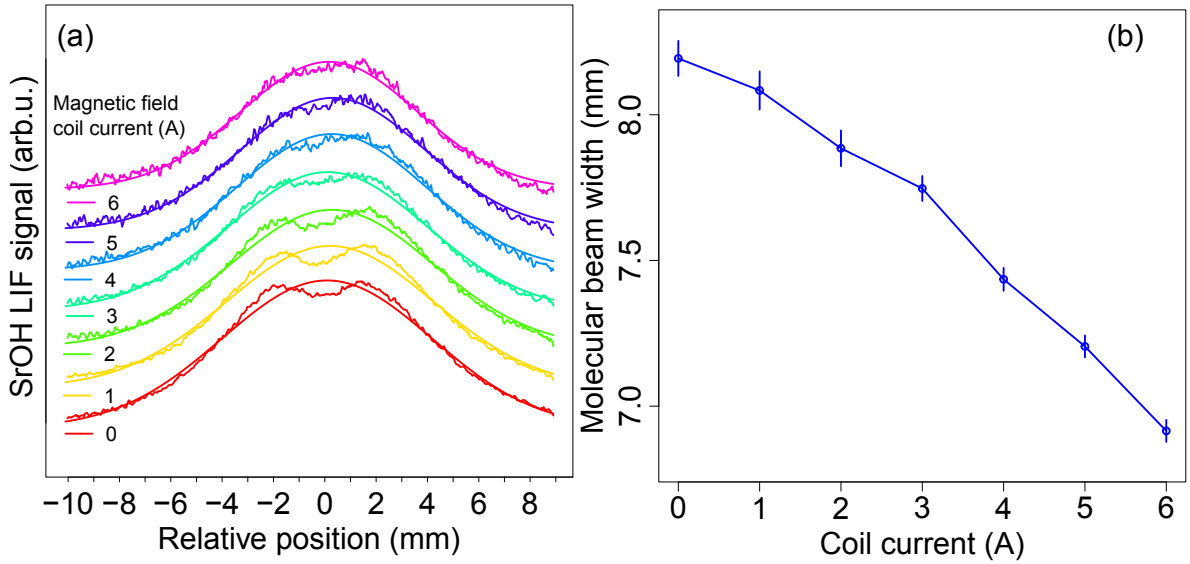


Figure 6.8.4: Sisyphus laser heating of the molecular beam for various applied magnetic fields.

scientific field [89, 90, 202] with well developed experimental [203, 204] and theoretical [205, 206] techniques. Our results with SrOH open up a wide range of future directions for laser manipulation of polyatomic molecules. By increasing the interaction time and laser intensity, cooling SrOH motion with magnetically-assisted laser cooling close to the recoil temperature of $\sim 1\,\mu$K should be possible, as previously demonstrated for atomic species under similar experimental conditions [207, 208]. Extending the scheme to 2D and using more elaborate optical configurations would lead to significantly increased brightening of the molecular beam [208, 209]. Slowing and cooling of an atomic beam in the longitudinal dimension [197, 210], e.g. for loading into a MOT, could now be extended to polyatomic molecules.

While some of these research avenues might require repumping of other vibrational states beyond the (100) and $\left(02^{0}0\right)$ states as the number of scattered photons increases, this challenge can be solved with additional repumping lasers on the $\tilde{X}-\tilde{B}$ transition. Since the strengths of higher-order Franck-Condon factors decrease rapidly [150, 151], scattering of $\sim 10,000$ photons should be possible with only two additional lasers to address (200) and $\left(01^{1}0\right)$ states. All of the required frequencies can be generated with solid-state laser diodes that have easily attainable requisite powers [211]. Moreover, by using $\tilde{X}-\tilde{A}$ electronic excitation for laser cooling and $\tilde{X}-\tilde{B}$ excitation for repumping, the scattering rate becomes independent of the number of repumping lasers, ensuring rapid optical cycling at a maximum possible rate.

While SrOH has a linear geometry in the vibronic ground state, it still serves as a useful test candidate for the feasibility of laser cooling more complex, nonlinear molecules like strontium monoalkoxide free radicals, where hydrogen is replaced by a more complex group R (e.g. $\mathrm{R}=\mathrm{CH_3}, \mathrm{CH_2CH_3}$). Because of the 180° Sr-O-C bond angle, the local symmetry near the optically active electron located on the strontium atom is linear (like in SrOH). Furthermore, SrOR molecules share a number of other important properties with SrOH, including a very ionic Sr-O bond, diagonal Franck-Condon factors, and technically accessible laser transitions [160, 182], indicating that results presented in this chapter could successfully be extended to such complex species [212].

Chapter 7

Coherent Bichromatic Force Deflection

Manipulation of external motion of gas phase atomic and molecular species with optical laser fields has a number of experimental advantages compared to using electric, magnetic, or mechanical techniques. Optical control of atomic motion allows for highly resolved state-selective control as well as compact robust vacuum chambers. Additionally, an ability to divide slowing light from a set of lasers for simultaneous delivery to various parts of the same experiment or multiple experiments with large spatial separation allows for cost effective experimental parallelization. Recently, all-optical production of a large Rb BEC has been reported [213] and previously direct laser cooling to quantum degeneracy has been achieved with Sr [43]. However, optical deceleration and cooling of atomic beams requires scattering tens of thousands of photons in order to bring room temperature atomic clouds to velocities around a few m/s when they can be confined inside electromagnetic traps for further studies. Even cryogenic buffer-gas sources producing atomic and molecular beams at velocities below 100 m/s need to be decelerated before trap loading can be accomplished. While beam deceleration employing radiation pressure force has been a standard for majority of atomic physics experiments, its application to slowing molecular beams has been severely limited by a small change in kinetic energy per scattered photon. On average, each absorption-emission cycle

changes center of mass momentum by $-\hbar k$ with the corresponding change in kinetic energy of

$$\triangle E_k = -\frac{\hbar^2 k^2}{2m}. \tag{7.0.1}$$

Employing direct Sisyphus laser cooling for SrOH as described in Chapter 6 led to reducing transverse velocity from 50 mK to below 1 mK with only 200 scattered photons. While recoil velocity of SrOH is around 1 μK each photon on average removed 250 μK worth of kinetic energy from the molecule leading to a damping force more than $2,000g$. However, the velocity capture range of this technique is limited to a few m/s. A different experimental approach is required to slow molecular beams with velocities around 100 m/s.

Optical bichromatic force (BCF) allows rapid directional momentum exchange of multiple $\hbar k$ between the light field and atoms in a single spontaneous emission cycle [210]. Therefore, it can be effectively applied to atoms and molecules that have optically accessible electronic transitions but suffer from the loss to dark states (e.g. excited electronic or vibrational levels). Particularly, application of BCF to polyatomic radicals like alkaline earth monoalkoxides that have multiple vibrational modes or diatomic molecules with complex electronic structures or non-diagonal Franck-Condon factors like ThO or WC[1] could allow production of slow, velocity controlled molecular beams for physics and chemistry applications.

SrOH provides a convenient species for exploring the effects of BCF on complex atoms and molecules with optically accessible electronic transitions. A single non-bonding valence electron allows laser addressing of internal quantum states but the loss to excited stretching and bending vibrational levels inhibits the photon cycling process. In this chapter we demonstrate and characterize optical bichromatic force by deflecting a cryogenic buffer-gas beam of SrOH. Our results are used to benchmark the theoretical calculations of BCF in complex multilevel systems in order to enable accurate predictions of BCF for other molecular species as well as different experimental parameters. Applications to molecular beam slowing are discussed.

[1] Both ThO and WC are of crucial importance for fundamental physics tests performed by searching for the permanent electric dipole moment of the electron [24, 214].

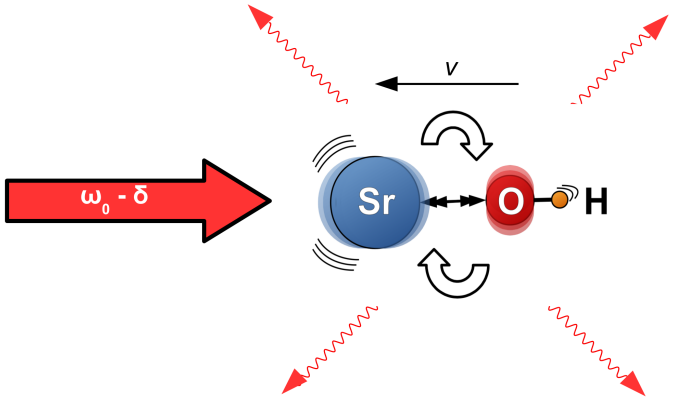


Figure 7.0.1: Schematic diagram of longitudinal slowing of SrOH beam using radiative scattering force. For simplicity, repumping lasers are not shown here. The detuning parameter δ is chosen such that incident laser frequency is Doppler shifted into molecular resonance (i.e. $\delta = -kv$). Spontaneous emission process (indicated with wavy arrows) is necessary to remove kinetic energy from the molecular beam and slow the velocity distribution.

Figure 7.0.1 shows the schematic diagram of the traditional Doppler slowing of SrOH. With effectively a single frequency counter-propagating laser beam[2] spontaneous emission is required for energy dissipation since the wavelength of the emitted light ω_e is larger than laser frequency ω_l leading to energy removal from molecules $\omega_e - \omega_l > 0$. Intuitively, a similar effect on atomic motion can be anticipated if there are two counter-propagating laser beams with frequencies $\omega_{l1} < \omega_e$ and $\omega_{l2} > \omega_e$ in a configuration when the atom absorbs a photon from laser 1 at ω_{l1} and is stimulated to emit a photon by laser 2 at ω_{l2}. If such a coherent process of momentum exchange between atom and two light fields is interrupted by a spontaneous emission after multiple cycles, the removal of the atomic kinetic energy will be irreversible. However, there is no preferred direction with only two cw light fields and additional laser frequencies are necessary. As shown in Fig. 7.0.2, slowing and cooling can be achieved with four laser frequencies total and this serves as a basis for the use of bichromatic force slowing.

[2]Here, we ignore the finer structure of SrOH electronic transitions and the presence of the repumping lasers because majority of absorbed and spontaneously emitted photons have $k \approx 2\pi/688\,\text{nm}$.

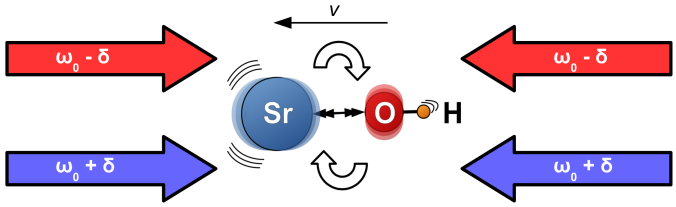


Figure 7.0.2: Schematic diagram of coherent bichromatic force slowing for SrOH. A pair of collinear laser fields (spatially separated in the diagram for clarity) of equal intensity is incident on the molecular beam from each direction. The lasers are symmetrically detuned by $\pm\delta$ relative to the transition resonance frequency ω_0. While a sequence of coherent absorption and stimulated emission processes leads to molecular deceleration within one radiative lifetime, spontaneous emissions provide the non-vanishing force over large distances by braking the coherent process.

7.1 Stimulated slowing for atoms

The idea of using stimulated cooling and slowing for atoms goes back to the end of 1980s when the rectified dipole force has been theoretically proposed and experimentally observed [215]. Using two standing light waves of different frequencies, the dipole force can be rectified to apply force on atoms on the macroscopic spatial scale. However, only the discovery of the bichromatic force, which also derives from the frequent coherent sequence of absorption-stimulated emission cycles but has a wide velocity capture range and remains robust under experimental imperfections, allowed significant advances in atom manipulation. For example, short distance deceleration of Cs atomic beam with BCF has been demonstrated [210].

There are multiple ways to understand the effects of four laser beams shown in Fig. 7.0.2 on atomic motion, including the π-pulse model, dressed atom picture, and direct solutions of the optical Bloch equations (OBEs). However, in this chapter we will only focus in the π-pulse model because it provides the most intuitive picture and allows for both qualitative and quantitative understanding of BCF in atoms. As demonstrated in Fig. 7.1.1, each pair of $\pm\delta$ detuned beams results in a series of rf beat notes. The equal intensities of each frequency beam are chosen such that the pulse area is approximate equal to π, thus leading to a series of alternating excitations and stimulated emissions. By appropriately choosing the relative phase shift between the counter-propagating beat note trains (Fig. 7.1.2), the directionality of the force can be accurately controlled.

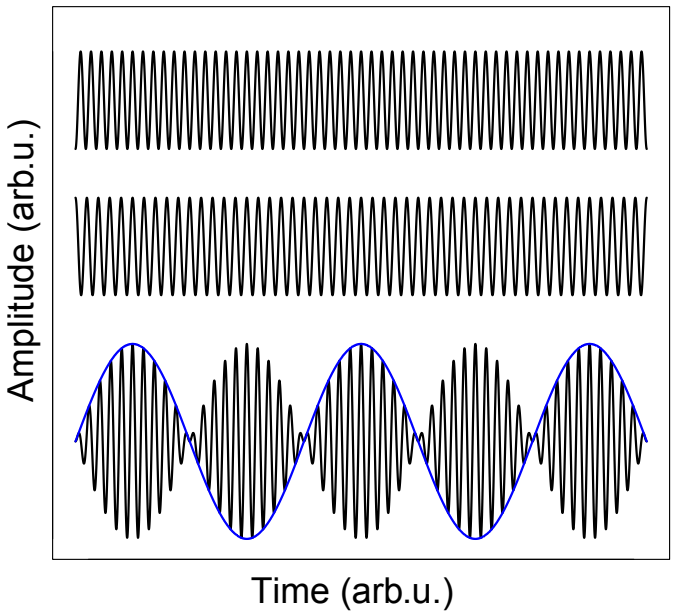


Figure 7.1.1: Beats arising from the interference of two identical sinusoidal waves with the relative frequency shift 2δ. While the amplitude envelope (depicted in blue) oscillates at frequency δ, the beat frequency is 2δ. In the ideal bichromatic force configuration, the intensity distribution and duration of each beat note is chosen such that the probability for transfering ground state molecules into an excited state (and vice versa) is equal to one (π-pulse condition).

Since in each such cycle the momentum of the atoms is modified by $\triangle P = 2\hbar k$ and the beat note modulation period is π/δ, the ideal bichromatic force is equal to [216]

$$F_{\mathrm{BCF,\,ideal}} = \frac{\triangle P}{\triangle t} = \frac{2\hbar k\delta}{\pi}. \tag{7.1.1}$$

Even though the actual force on a two-level system F_{BCF} turns out to be half of $F_{\mathrm{BCF,\,ideal}}$ because of the effects arising from spontaneous emission, it can still be much greater than the radiative force

$$\frac{F_{\mathrm{BCF}}}{F_{\mathrm{rad}}} = \frac{2\delta}{\pi\gamma} \gg 1 \tag{7.1.2}$$

if the detuning if chosen appropriately ($\delta \gg \gamma$).

From Eq. 7.1.2, we can see that the magnitude of the BCF is controlled by the laser detuning δ. However, in order to ensure that the π-pulse condition in maintained, the Rabi frequency must be scaled appropriately as $\Omega = \pi\delta/4$ [216]. While F_{BCF} scales linearly with δ, the required laser

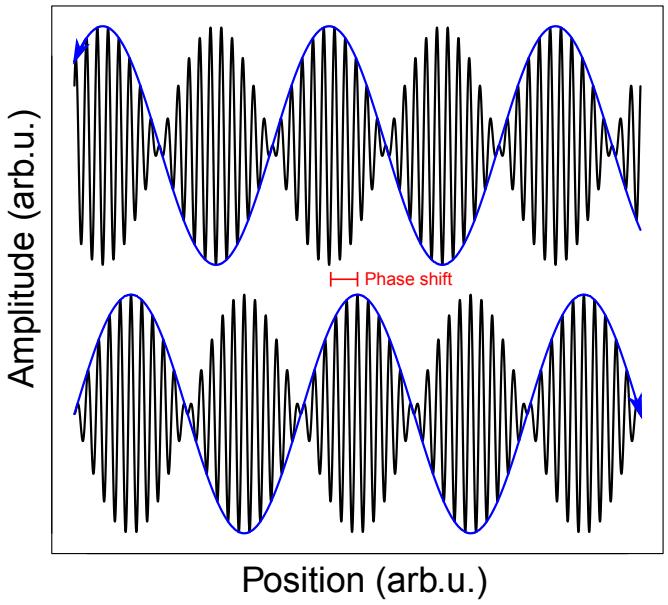


Figure 7.1.2: Bichromatic beat note pulse trains propagating in opposite directions. Relative $\pi/2$ phase shift leads to a directional force on the atoms or molecules placed in such a field configuration.

intensity [217]

$$I_{\mathrm{BCF}} = 3\left(\frac{\delta}{\gamma}\right)^2 I_{\mathrm{sat}} \tag{7.1.3}$$

has a quadratic dependence, imposing strict requirements on the size of the laser beam in the experiment.

One of the crucial advantages of using BCF compared to radiative force for atomic and molecule slowing is its large velocity capture range [179]

$$\triangle v_{\mathrm{BCF}} \simeq \frac{\delta}{k}. \tag{7.1.4}$$

While dressed atom treatment [218] is necessary in order to derive velocity capture range for BCF, it can intuitively be understood as arising when Doppler shifts kv become comparable to Rabi frequency $\Omega \sim \delta$. In the doubly-dressed atom picture, BCF arises from the spatial gradient of the field-dressed energy levels combined with Doppler shifts when atoms are propagating in standing light waves of two different frequencies $\omega_0 + \delta$ and $\omega_0 - \delta$ (Fig. 7.1.3).

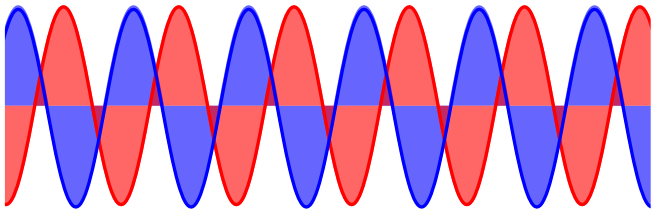


Figure 7.1.3: Standing light waves of two different frequencies in the bichromatic force configuration.

7.2 Bichromatic force for molecules

Because of the complexity of molecular structure, accurate calculations of BCF effects are not possible with the π -pulse model and direct numerical integration of the OBEs is required. Aldridge and Eyler has performed such calculation for SrOH in order to guide our experimental efforts and the details of their approach can be found in Ref. [219]. However, as shown in Ref. [179], π -pulse model can be used for a qualitative understanding of the BCF effects in multilevel systems if appropriate statistical scaling factors are applied.

There are multiple advantages of using bichromatic force slowing for molecules including

- short slowing distance $\rightarrow$ reduced transverse pluming
- short slowing time $\rightarrow$ reduced "photon budget" leading to fewer vibrational repumps
- transverse repumping possible $\rightarrow$ less repump power needed
- broad velocity capture range $\rightarrow$ no white-light EOM and spin-rotation AOM needed
- rectangular velocity dependence $\rightarrow$ velocity distribution is compressed and cooled because of abrupt flanks

However, these benefits come at a cost of high laser power required potentially small spatial capture due to tight focusing of the laser beams.

As indicated in Fig. 2.5.3, there are multiple sublevels involved in the optical cycling process of SrOH that leads to a modified saturation intensity and correspondingly appropriate bichromatic

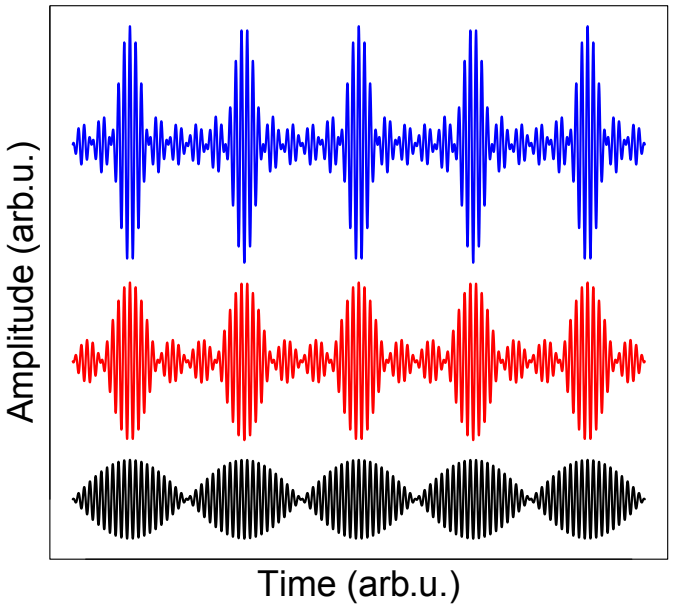


Figure 7.2.1: Comparison of bichromatic and polychromatic pulse trains that could be used for molecular slowing. Pulse trains for original BCF configuration with $\pm\delta$, as well extra harmonics at $\pm 3\delta$ and $\pm 3\delta \pm 5\delta$ are shown.

intensity

$$I_{\mathrm{BCF,eff}} = 3\left(\frac{\delta}{\gamma}\right)^2 I_{\mathrm{sat,eff}}. \tag{7.2.1}$$

Since $I_{\mathrm{sat,eff}} > I_{\mathrm{sat}}$, $I_{\mathrm{BCF,eff}} > I_{\mathrm{BCF}}$ imposing even higher laser power requirements for manipulating molecular systems with bichromatic laser light. Additionally, because of the presence of dark Zeeman and vibrational sublevels not driven by the BCF laser frequencies, effective bichromatic force $F_{\mathrm{BCF,eff}}$ will be smaller compared to a two-level system approximation. It has been shown [179] that in such a configuration

$$F_{\mathrm{BCF,eff}} = \left(\frac{n_e/2 + n_a}{n_e/2 + n_a + n_d}\eta\right)\frac{\hbar k\delta}{\pi} \tag{7.2.2}$$

where n_e, n_a, and n_d are the corresponding degeneracies for the excited state, BCF-active ground state, and BCF-inactive levels. Addition of the force reduction factor η is necessary to account for line strength variation and difference in frequency shifts relative to BCF beams.

One very attractive feature of BCF for molecules with poor FCFs is that the fraction of time

spent in the excited electronic state can be significantly reduced compared to Doppler cooling at saturation if the time between the excitation-deexcitation cycles is increased. Using simple statistical arguments for BCF in multilevel systems, the probability to be in the excited state is calculated as [217]

$$P_e \approx \frac{n_e/2}{n_e/2 + n_a + n_d} \tag{7.2.3}$$

where the form of the weighting factors is chosen to give correct $P_e \approx 1/3$ in a two-level limit. Galica et al. [181] showed that the use of polychromatic forces when higher harmonics of the original bichromatic detuning are added can lead to such improvements. Figure 7.2.1 shows how additional frequency components modify the pulse trains seen by atoms or molecules. Figure 7.1.2 shows that with BCF the counter-propagating beat trains overlap in space and time while according to Fig. 7.2.1 this can be avoided by adding higher harmonics. In fact, the use of ultrafast lasers for molecular deceleration and cooling has been recently proposed [220]. Previously, picosecond laser pulses have been used for further compression of the laser-cooled Cs sample [221].

7.3 Experimental apparatus

The apparatus used in the experiment is in many aspects similar to that described in Chapters 5 and 6, so here we focus only on the unique characteristics that were required to achieve BCF deflection. Particularly, the following experimental changes needed to be implemented:

- Collimating aperture size needed to be modified in order to ensure that most of the molecules in a beam experience laser intensities high enough for BCF effects to arise.
- Significantly larger laser intensities were required to achieve BCF effects on SrOH compared to radiative deflection and Sisyphus laser cooling.
- Because of the short laser-molecule interaction time in the experiment, there was no need for repumping vibrational states beyond (100).

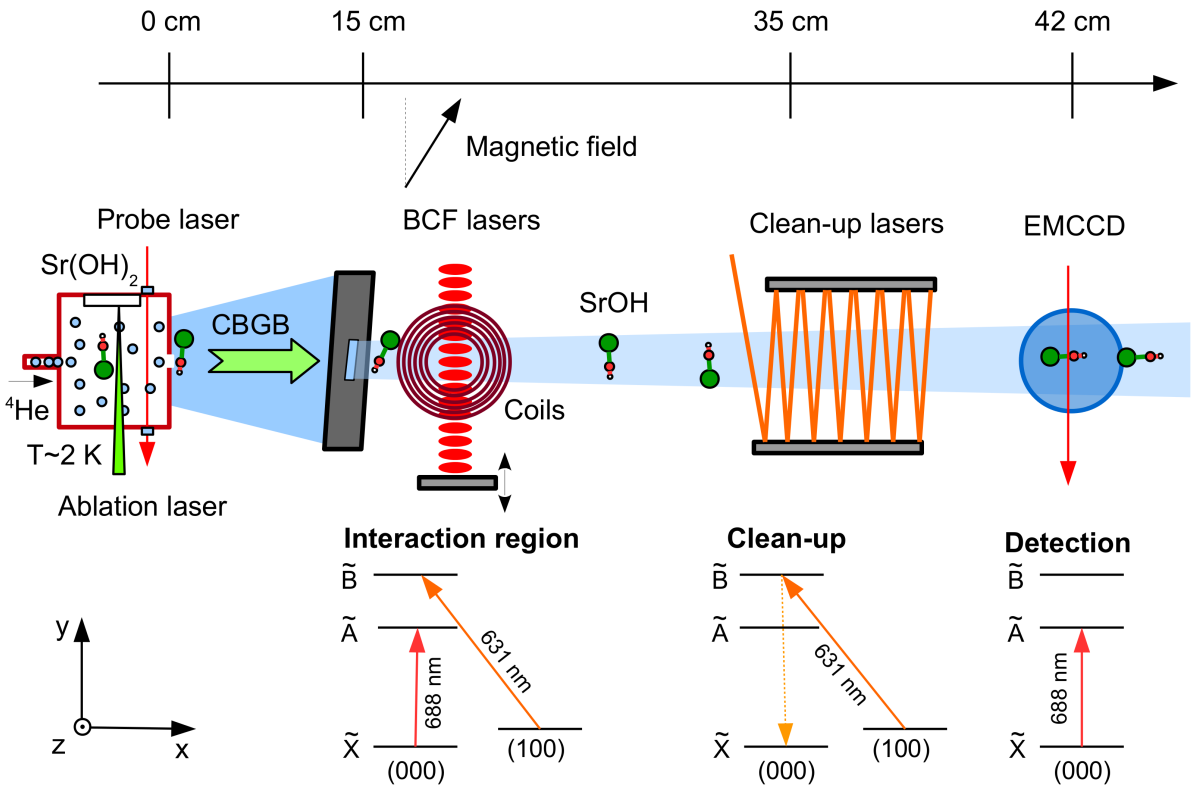


Figure 7.3.1: Experimental apparatus used for bichromatic force deflection of SrOH. For a detailed description please refer to Fig. 5.3.1. Major differences compared to Chapters 5 and 6 include, smaller collimating aperture, high-intensity standing light wave with two frequency components, and large remixing magnetic fields.The direction of the bichromatic force can be changed by moving the mirror in order to modify relative phase shifts between beat pulse trains.

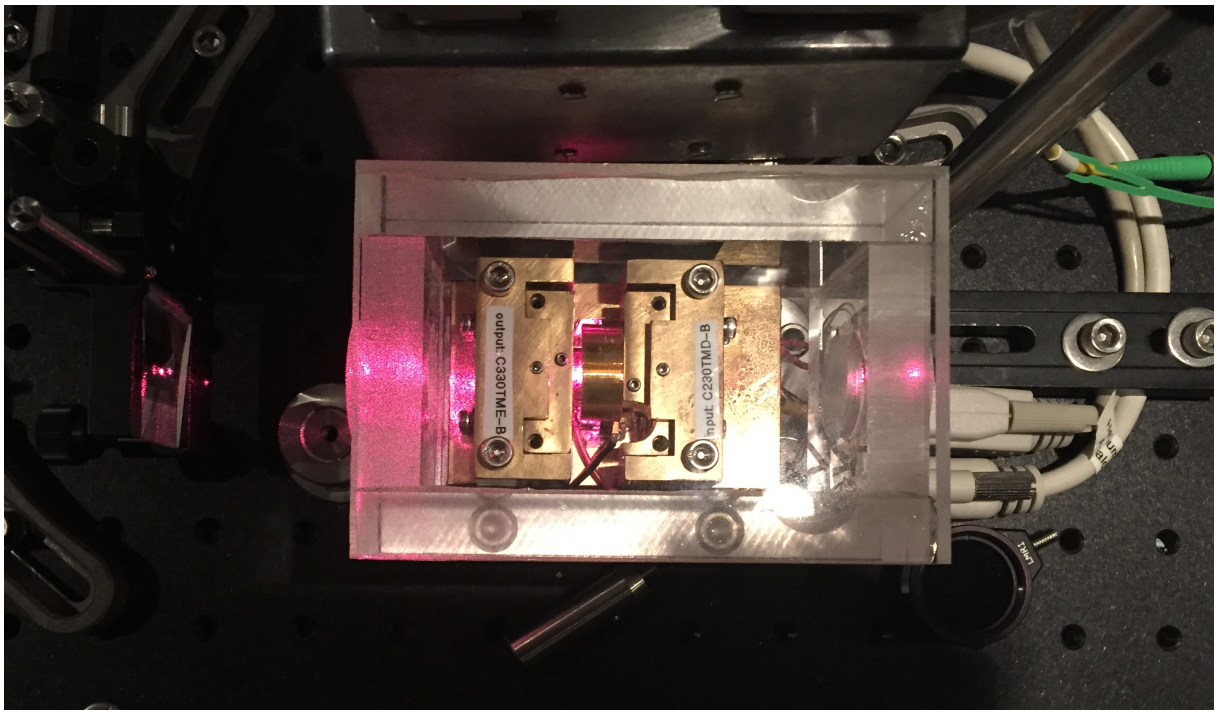


Figure 7.3.2: Custom-build tapered amplifier for generating bichromatic laser frequencies. The design was modeled after Ref. [153].

- Significantly higher magnetic fields were required for rapid remixing of dark magnetic sub-levels.

In order to achieve required laser intensities we had to construct a tapered amplifier (TA) system seeded by an injection locked laser diode. Figure 7.3.2 shows the image of the home-made TA used to generate ~ 450 mW of 688 nm laser light in order to generate two frequency components used in the BCF experiment.

7.4 Bichromatic force deflection of SrOH

Figure 7.4.1 shows the optimal configuration for BCF deflection of SrOH with 10 mW/cm^2 laser intensity. While TA delivers close to 500 mW, after the optical isolator, 260 MHz AOM for adding BCF sideband, and fiber coupling using polarization maintaining fibers only about 40 mW per each BCF frequency component remain. Thus, the laser beam $1/e^2$ diameter is limited to about 0.9 mm

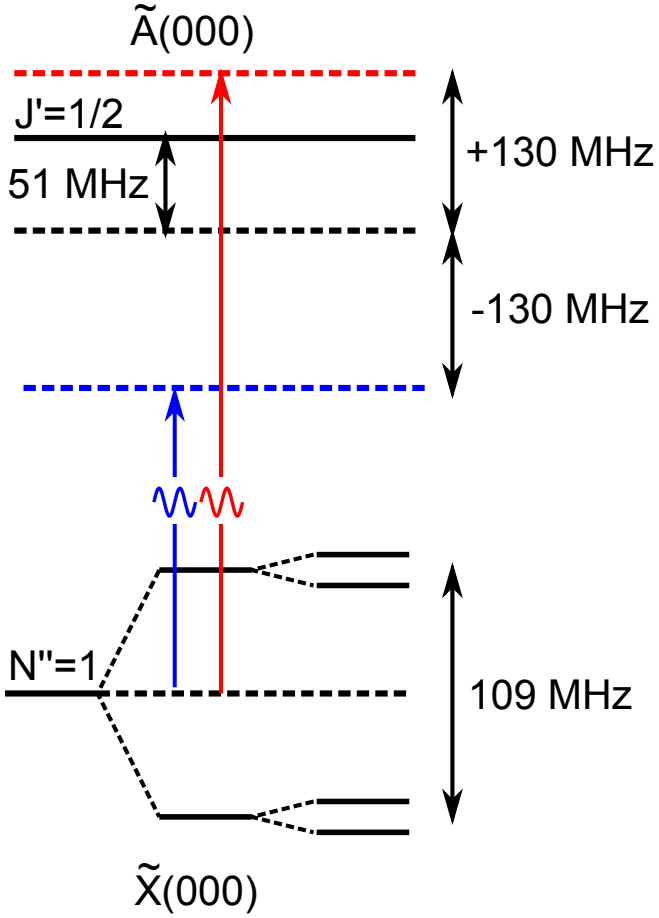


Figure 7.4.1: Optimal BCF frequency detunings for SrOH using the $\tilde{X}^2\Sigma^+(000) \rightarrow \tilde{A}^2\Pi_{1/2}(000)$ $P(N''=1)$ transition for $10\,\mathrm{mW/cm^2}$ irradiance per BCF frequency. The parameters were estimated using numerical solutions of OBEs by Aldridge in Ref. [219].

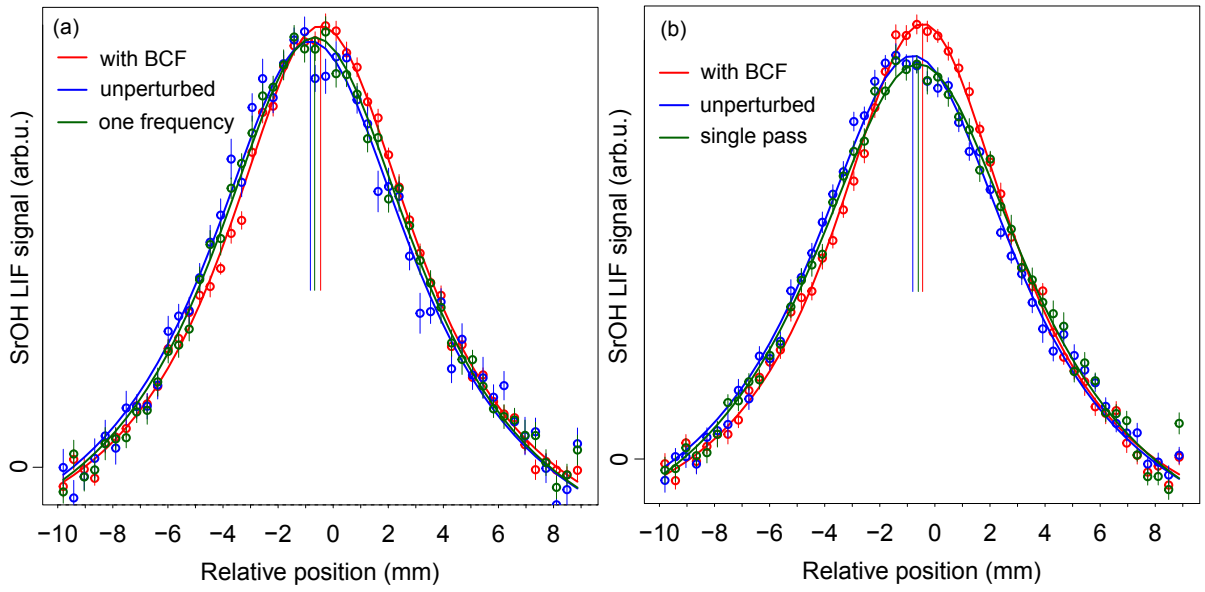


Figure 7.4.2: Bichromatic force deflection of the SrOH beam. (a) Comparison of the beam profiles for unperturbed beam, beam deflected with BCF, and beam perturbed by a single frequency standing wave. (b) Comparison of the beam profiles for unperturbed beam, beam deflected with BCF, and beam perturbed by single pass containing two laser frequencies. The fits are Lorenzians.

in order to achieve high enough laser power[3].

Results of the bichromatic force deflection for SrOH are shown in Fig. 7.4.2. As can be seen from 7.4.2(a), both BCF frequency components are necessary in order to achieve significant deflection. Additionally, Fig. 7.4.2 demonstrates that BCF beams from both directions are required, as expected. A shift of the center beam profile from a single pass beam can be attributed to off-resonant optical excitation that leads to scattering of 25 photons per molecule. We confirmed this by turning off the clean-up beam and observed depletion of the molecular signal.

According to the π-pulse model described above, the effects of bichromatic force should have a sensitive power dependence once the beat note area is no longer π. While Fig. 7.4.3(a) demonstrates the profile difference between the BCF and unperturbed molecular beams, Fig. 7.4.3 shows dependence of the BCF deflection of the total laser power in the laser beam indicating that as expected close to 10 mW/cm^2 are required to achieve optimal deflection with $\delta = 130$ MHz.

[3]The peak laser intensity for a Gaussian beam is given by $I = 2P/\left(\pi w_0^2\right)$, where w_0 is $1/e^2$ radius of the laser beam.

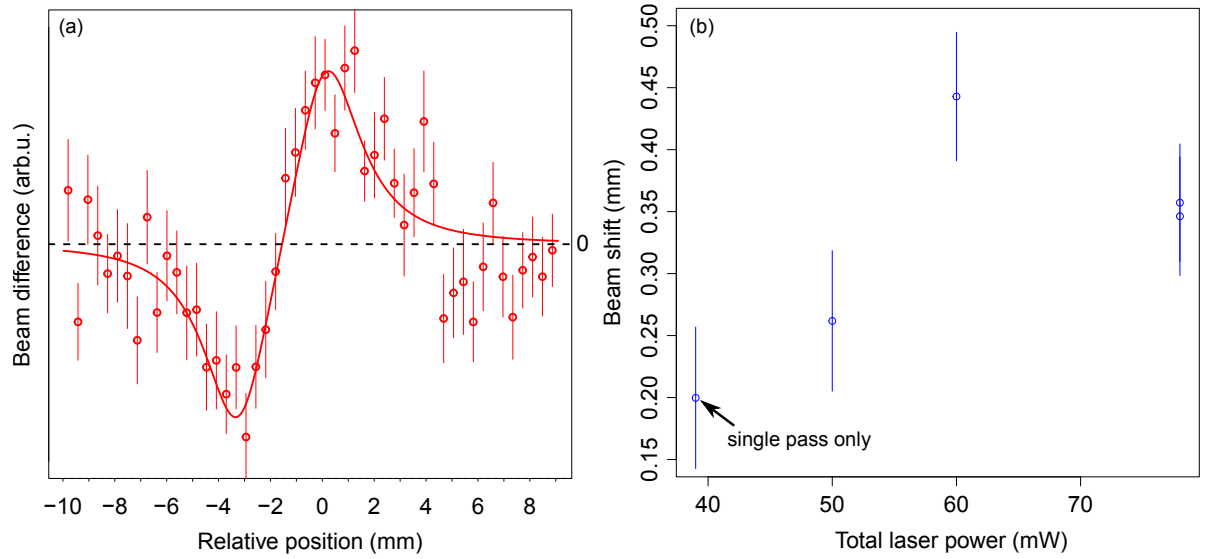


Figure 7.4.3: (a) Profile difference for an unperturbed SrOH beam and a beam deflected with BCF. (b) Power dependence of the BCF deflection.

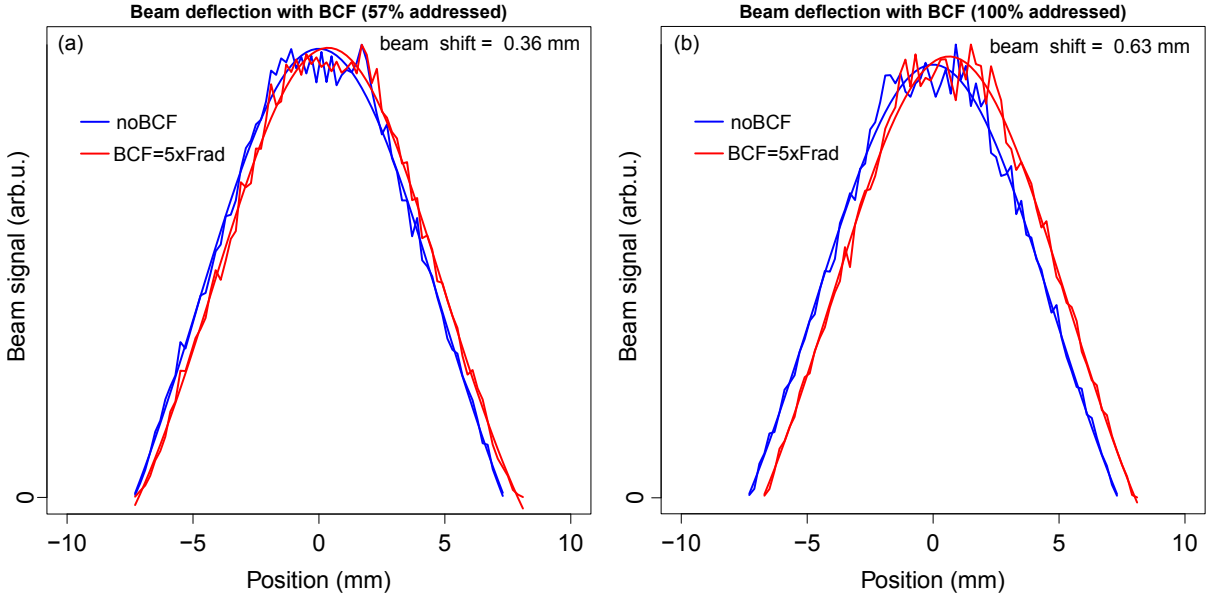


Figure 7.4.4: Molecular beam profiles simulated with Monte Carlo methods in the presence of BCF force with (a) 57% of the molecules addressed and (b) 100% of the molecules addressed.

In order to quantitatively analyze the BCF effects, we performed Monte Carlo simulations of the molecule dynamics for a different fraction of the molecules experiencing optimal bichromatic intensity. Figure 7.4.4(a) shows that our observed deflection with the used beam diameter ($2w_0 \approx$ 0.957 mm) and collimation aperture of width 0.5 mm leads to approximately 57% of the molecules addressed by the correct laser intensity I_{BCF}. If the fraction of the molecules experiencing optimal BCF conditions were increased to 100%, the shift will almost double as indicated in Fig. 7.4.3(b). From the shift in (a) we can also estimate that the BCF force is about 5 times larger than the radiative force for a given number of scattered photons.

7.5 Applications to SrOH slowing and cooling

During the Doppler slowing and cooling process the entropy increase for the photon beam is many orders of magnitude larger compared to the entropy loss for the atomic sample [222]. Previous theoretical analysis indicates that entropy removal efficiency with Doppler laser cooling is around $\eta = |\triangle S_a| / \triangle S_l \sim 10^{-5}$ [223], where $\triangle S_a$ and $\triangle S_l$ is the entropy change for atoms and light correspondingly. However, as long as $\eta \sim 1$, the light has enough capacity to absorb all the entropy lost by atoms [224]. Therefore, a larger number of scattered photons is not necessarily required for efficient laser slowing and cooling of atomic and molecular beams. Previously, bichromatic slowing and collimation was used to make an intense helium beam [225]. Using only 10 cm of interaction length, the brightness of the beam was increased by more than $3,000$. While not obvious at first sight, the bichromatic force can be set up to emulate the optical molasses but with a very large capture velocity. In order to achieve such a configuration, two different regions of counter-propagating BCF beams are required with opposite spatial phase and frequency shifts [225].

Table 7.1 illustrates the advantages and challenges of applying BCF longitudinal slowing to complex molecules like SrOH. While the slowing distance is significantly reduced compared to radiative slowing (from 3.1 cm to 3.5 mm) because of the larger force, significant laser powers are

Parameter	Two-level	$N'' = 0 \rightarrow J' = 1/2$	$N'' = 1 \rightarrow J' = 1/2$
Detuning (δ, MHz)	150 (21γ)	150 (21γ)	150 (21γ)
Velocity capture range ($\triangle v_{\mathrm{BCF}}$, m/s)	103	103	103
Optimal intensity (I_{BCF}, mW/mm^2)	39	155	697
Force ratio ($F_{\mathrm{BCF}}/F_{\mathrm{rad}}$)	27.3	5.7	11.7
Slowing time for $v_f = 50$ m/s (μs)	30	382	141
Slowing distance for $v_f = 50$ m/s (mm)	0.8	9.6	3.5
T_{loss} with $FCF_{\mathrm{loss}} = 1 \times 10^{-3}$ (μs)	68	216	216
Excited state probability (P_e)	0.33	0.11	0.14

Table 7.1: Bichromatic force slowing calculations for SrOH. The estimations were performed using the scaled two-level model described in Section 7.2 and Ref. [217].

Parameters used in the calculations:

- Two-level saturation I_{sat}: 2.8 mW/cm^2
- Effective saturation for $N'' = 0 \rightarrow J' = 1/2$ transition $I_{\mathrm{sat,eff}}$: 11.2 mW/cm^2
- Effective saturation for $N'' = 1 \rightarrow J' = 1/2$ transition $I_{\mathrm{sat,eff}}$: 50.6 mW/cm^2
- Force reduction factor η: 0.25

required to achieve optimal BCF conditions. As can be seen from the table, the main challenge in applying BCF to molecules is the presence of multiple levels so saturation requirements grow significantly. If one could find a molecules in the $^1\Sigma$ configuration, the power requirements could be reduced significantly. Since the calculations were performed using a simplified model, they can only be used as an order of magnitude estimate and for relative comparisons only. Interested readers should refer to the numerical solutions of the OBEs for SrOH provided in Ref. [219] for more detailed calculations.

7.6 Conclusions

Bichromatic and polychromatic optical forces based on coherent momentum exchange between light and atomic matter promise to play a crucial role in extending laser manipulation to complex polyatomic molecules and diatomics with poor Franck-Condon factors. Our experimental results with SrOH demonstrate that deflection forces $\sim 4-5$ times larger than radiative are possible with BCF, corroborating previous theoretical calculations [219] and paving the way for efficient laser slowing of complex molecules. Achieving larger Rabi frequencies with bigger laser beam sizes and applying this technique to longitudinal slowing will significantly aid in creating a three dimensional MOT of SrOH and similar polyatomics.

Chapter 8

Prospects of Magneto-Optical Trapping for SrOH

While the technique of optical molasses described in Chapter 6 leads to cooling of the velocity distribution and compression of the phase space in 3D[1], it does lead to spatial trapping of the atomic or molecular clouds[2]. Even though various methods have been previously explored [226], usually atomic physics experiments rely on the inhomogeneous magnetic fields to provide required spatial dependence of the scattering force and enable true trapping in free space [148]. While an atomic MOT is a very robust trap with relatively modest technological requirements for construction and operation[3], recently demonstrated MOTs of diatomic molecules have shown that significant challenges need to be faced when transferring this versatile technique to molecular species. In this

[1]Following Ref. [170], we define phase space density in 6D $\rho(\vec{r}, \vec{p}, t)$ at time t as the probability that a single particle is at position $\vec{r}$ with momentum $\vec{p}$. Thus, defining a new vector $\vec{q} = (\vec{r}, \vec{p})$and using $\int \rho(\vec{q}, t)\, \mathrm{d}^6 q = 1$, we can calculate the probability to find one particle in a subspace $\mathcal{V}$ as $P(\mathcal{V}) = \int_{\mathcal{V}} \rho(\vec{q}, t)\, \mathrm{d}^6 q$. During the laser cooling process, the use of the velocity dependent optical forces leads to an exponential gain in phase space density as [170]

$$\frac{\mathrm{d}\rho(\vec{q}, t)}{\mathrm{d}t} = 3\frac{\beta}{M}\rho(\vec{q}, t) \tag{8.0.1}$$

where β is the damping coefficient for optical molasses and M is the mass of the atom.

[2]While initially the atoms will concentrate in a small region of space, they will eventually diffuse out of the laser beams.

[3]For example, required magnetic field gradients and laser powers can be achieved with air-cooled coils and external cavity diode lasers.

chapter, we briefly provide the theory of magneto-optical trapping for atoms before highlighting extra hurtles arising when working with diatomic molecules. Finally, we break down the steps necessary for achieving magneto-optical trapping for polyatomic molecules, primarily focusing on SrOH.

8.1 Magneto-optical trapping for atoms

In a MOT, just like in optical molasses discussed earlier, the cooling effect on the atoms comes from the scattering force. However, the application of the magnetic field gradient leads to a spatially dependent Zeeman splitting of atomic energy levels. The use of circularly polarized laser beams combined with particular Zeeman selection rules and spatial dependence of the energy shifts leads to the imbalance in the radiative force imparted from the counter-propagating laser beams [148]. While the general idea is effectively the same, the details of implementation depend on the exact relationship between the ground state and excited state angular momenta, leading to type I and type II MOTs discussed in more detail below.

8.1.1 Type I MOT

Figure 8.1.1 shows a schematic diagram for achieving a MOT in atomic system with $J_g < J_e$ in a so-called type I MOT configuration which is most frequently used in atomic physics experiments. As can be seen from the diagram, for $B > 0$ the Zeeman energy level for $m_J = -1$ is shifted into resonance with the σ^- polarized red-detuned laser beam incident from the right, resulting in a restoring force towards the trap center. The situation is reversed for $B < 0$, where $m_J = +1$ level is shifted into resonance with σ^+ polarized laser light leading to spatially restoring optical force towards $B = 0$ position.

In order to provide a quantitative analysis of the MOT trapping forces, it is necessary to con-

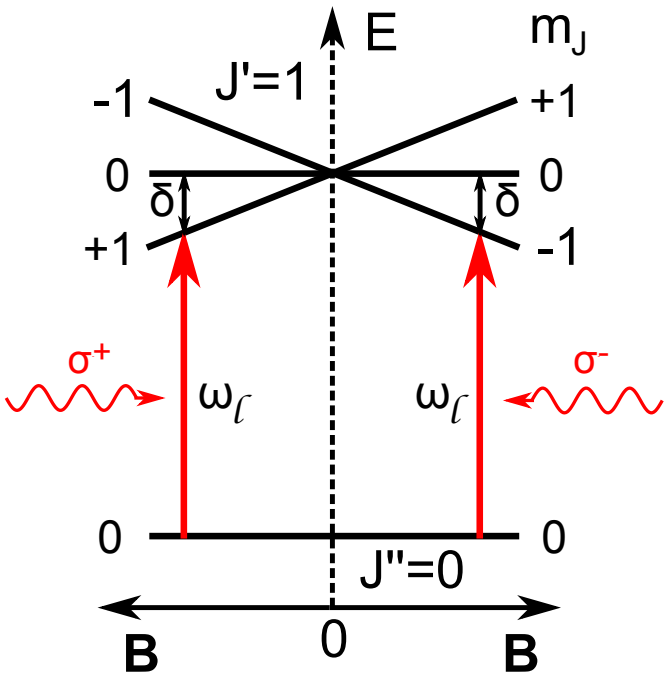


Figure 8.1.1: Schematic diagram of magneto-optical trapping in 1D using $J'' = 0 \rightarrow J' = 1$ optical transition.

sider the total force on atoms arising from both counter-propagating laser beams

$$\vec{F}_{\text{MOT}} = \vec{F}_{+} + \vec{F}_{-} \tag{8.1.1}$$

where the force from each beam takes the form found previously in the description of optical molasses in Chapter 6 [170]

$$F_{\pm} = \pm \frac{\hbar k \gamma}{2} \frac{s_0}{1 + s_0 + 4\left(\delta_{\pm}/\gamma\right)^2}. \tag{8.1.2}$$

However, effective detuning needs to incorporate both Doppler and Zeeman shifts in the MOT configuration of Fig. 8.1.1 [170]

$$\delta_{\pm} = \delta \pm \omega_D \pm \omega_Z \tag{8.1.3}$$

with $\omega_D = -\vec{k} \cdot \vec{v}$ and $\omega_Z = \mu' B/\hbar$ with the effective magnetic moment of the transition specified as $\mu' \equiv (g_e m_e - g_g m_g)\mu_B$. The spatial dependence of the MOT forces comes from the linearly inhomogeneous magnetic field of the form $B \equiv Ax$ along the $\hat{x}$ direction. Notice that MOT operation

relies of the differential magnetic moment $\mu' \neq 0$.

In the regime when ω_D, $\omega_Z \ll \delta$, the total force profile becomes identical to a damped harmonic oscillator

$$F_{\mathrm{MOT}} = -\beta v - \kappa x \tag{8.1.4}$$

with the damping coefficient of the optical molasses and the spring constant $\kappa = \mu' A/(\beta\hbar k)$. Thus, the damping rate of the MOT is $\Gamma_{\mathrm{MOT}} = \beta/M$ and the oscillation frequency is $\omega_{\mathrm{MOT}} = \sqrt{\kappa/M}$ for mass M atoms, resulting in an overdamped atomic motion of characteristic restoring time $2\Gamma_{\mathrm{MOT}}/\omega_{\mathrm{MOT}}^2$ [170]. While both the qualitative and the quantitative descriptions of a MOT provided here use a 1D model, they capture majority of the essential conceptual details required for understanding the process of three-dimensional magneto-optical trapping. The steady-state temperature of type I MOTs is usually comparable to the temperature of optical molasses, leading to sub-Doppler cooling in certain configurations.

8.1.2 Type II MOT

The advantage of using type I MOT configuration presented in Fig. 8.1.1 is that while both laser polarization and magnetic field orientation are kept constant, all of the atoms in the ground state are addressed with incident laser beams in the proper orientation. However, in some atomic species the use of ground states with larger angular momentum than in excited state is required (i.e. $J'' > J'$) [227]. The way to achieving magneto-optical trapping in such a configuration is illustrated in Fig. 8.1.2 for a simple case of $J'' = 1 \rightarrow J' = 0$ atomic transition. While the laser frequency is still detuned below the atomic resonance ($\omega_l < \omega$), the laser polarization and the direction of the magnetic field are synchronously modulated in order to ensure that the direction of the Zeeman shift is reversed in order for dark magnetic sublevels to scatter photons from the correct direction. While higher order effects have led to MOT demonstrations in type II configurations without such reversals, intuitively one would expect the MOT forces to average out to zero value if the dark magnetic sublevels are not actively remixed.

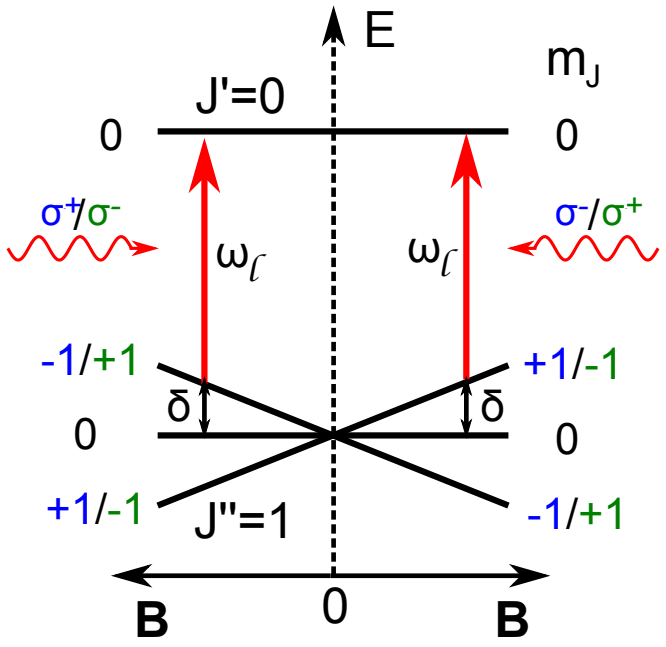


Figure 8.1.2: 1D MOT schematic diagram using $J'' = 1 \rightarrow J' = 0$ optical transition.The direction of applied magnetic field and laser polarizations are modulated to achieve the restoring force.

8.2 Magneto-optical trapping for diatomic molecules

Probably, the first practical proposal for achieving magneto-optical trapping for diatomic molecules was provided by Stuhl et al. [228], who suggested to use pulsed electric fields to non-adiabatically remix the ground state magnetic sublevels. Five years later, Hummon et al. have experimentally demonstrated magneto-optical compression of the YO beam in 1 and 2D using oscillating magnetic fields and time-dependent optical polarizations [101]. True magneto-optical trapping in 3D was demonstrated with SrF for both DC [229] and RF [171] configurations. At the time this thesis was written, two research groups have demonstrated 3D MOTs of CaF [186, 187] and one group has achieved 3D MOT of YO. This rapid experimental progress combined with detailed theoretical work [201, 230] aimed at explaining the origin of 3D MOT trapping forces for molecules as well as carefully predicting specific characteristics of molecular MOTs have already provided a lot of insight into the differences between magneto-optical trapping process for atoms vs molecules.

Even in the optimal RF MOT configuration presented in Fig. 8.1.2, the effective scattering rate of the trapped molecules is modified because of the presence of multiple ground states n_g coupled

to excited electronic state with multiplicity n_e [231]

$$R_{sc} = \Gamma \frac{n_e}{n_e + n_g + 2\sum_{j=1}^{n_g} \left(1 + 4\triangle_j^2/\Gamma^2\right) I_{\mathrm{sat,j}}/I_j} \tag{8.2.1}$$

where $I_{\mathrm{sat,j}} = \pi hc\Gamma/\left(3\lambda_j^3\right)$ is the corresponding two-level saturation intensity and $\triangle_i$ is the detuning. Additionally, other experimental MOT parameters like T_{MOT}, Γ_{eff}, s_{eff}, and κ_{MOT}have to be modified appropriately to account for the coupling of multiple ground and excited state levels [171]. Recent combined experimental and theoretical advanced in magneto-optical trapping for diatomic molecules empower us to consider the prospects of making a 3D MOT of polyatomic molecules like SrOH or CaOH.

8.3 Chemical production of SrOH

While MOTs of SrF have been achieved using buffer-gas beam source relying on the ablation of a solid molecular precursor SrF_2 [153], the stable and robust operation of CaF MOTs has necessitated the development of the chemical beam sources relying on the reaction between ablated Ca metal and SF_6 gas [186, 187]. Based on our experience with the SrOH production using ablation of the pressed $Sr(OH)_2$ powder, development of the new SrOH beam source relying on the chemical production mechanism might also be necessary in order to achieve large stable SrOH beam signals over prolonged periods of time required for MOT optimization and characterization. Fortunately, relying on the previous experimental studies of supersonic beams of CaOH and SrOH, it seems highly likely that large numbers of SrOH can be produced by ablating strontium metal targets inside the buffer-gas cell while simultaneously flowing helium gas seeded with water (H_2O) or hydrogen peroxide (H_2O_2) through a thermally disconnected fill line. While gas-phase reaction between ground state strontium atoms and water is endothermic by 0.8 eV, it was previously

determined that the chemical reaction

$$\mathrm{Sr}^{*}\left({}^{3}\mathrm{P}_{1}\right)+\mathrm{H_2O\,(g)}\rightarrow\mathrm{SrOH\,(g)}+\mathrm{H\,(g)} \tag{8.3.1}$$

is exothermic by about 1.0 eV [232]. While Sr^* atoms are naturally produced during the laser ablation process, promotion of the strontium using 689 nm intercombination line to the $^3P_1$metastable state will lead to enhanced SrOH production.

8.4 Slowing SrOH below MOT capture velocity

Radiative slowing of the cryogenic buffer-gas beam of SrOH below the capture velocity of a 3D MOT will require scattering a large number of photons. Additionally, small loss rate to dark vibrational levels is required to demonstrate reasonably long MOT lifetimes. Figure 8.4.1 demonstrates the optical cycling scheme in SrOH that can be used for both radiative slowing as well as direct trapping in a MOT. With four repumping lasers indicated in the diagram, scattering of $> 10^4$ photons should be possible per molecule. Assuming half of the maximum possible scattering rate, MOT lifetimes of ~ 20 ms should be possible with 10^5 scattered photons. Comparison of the radiative force slowing for SrOH and diatomic molecules that have been trapped in a 3D MOT is provided in Table 8.1. Employing $\tilde{X}-\tilde{A}$ as the main cycling light and repumping using the $\tilde{X}-\tilde{B}$ transitions as shown in Fig. 8.4.1 leads to a reasonably fast cycling rate allowing for SrOH beam deceleration in a short distance compared to heavy diatomic molecules like SrF and YO. Figure 8.4.2 provides a comparison between SrOH and CaF of the required number of photons to stop a slow cryogenic buffer-gas beam. As can be seen from the plot, the use of either $\tilde{X}-\tilde{A}$ or $\tilde{X}-\tilde{B}$ transition for SrOH ($m_{\mathrm{SrOH}} = 105$ amu) necessitates $\sim 10^4$ scattered photons to bring 60 m/s beam to a stop. Lighter molecular species like CaF ($m_{\mathrm{CaF}} = 59$ amu) or CaOH ($m_{\mathrm{CaOH}} = 57$ amu) require only about half as many scattered photons because of the larger single photon recoil velocity.

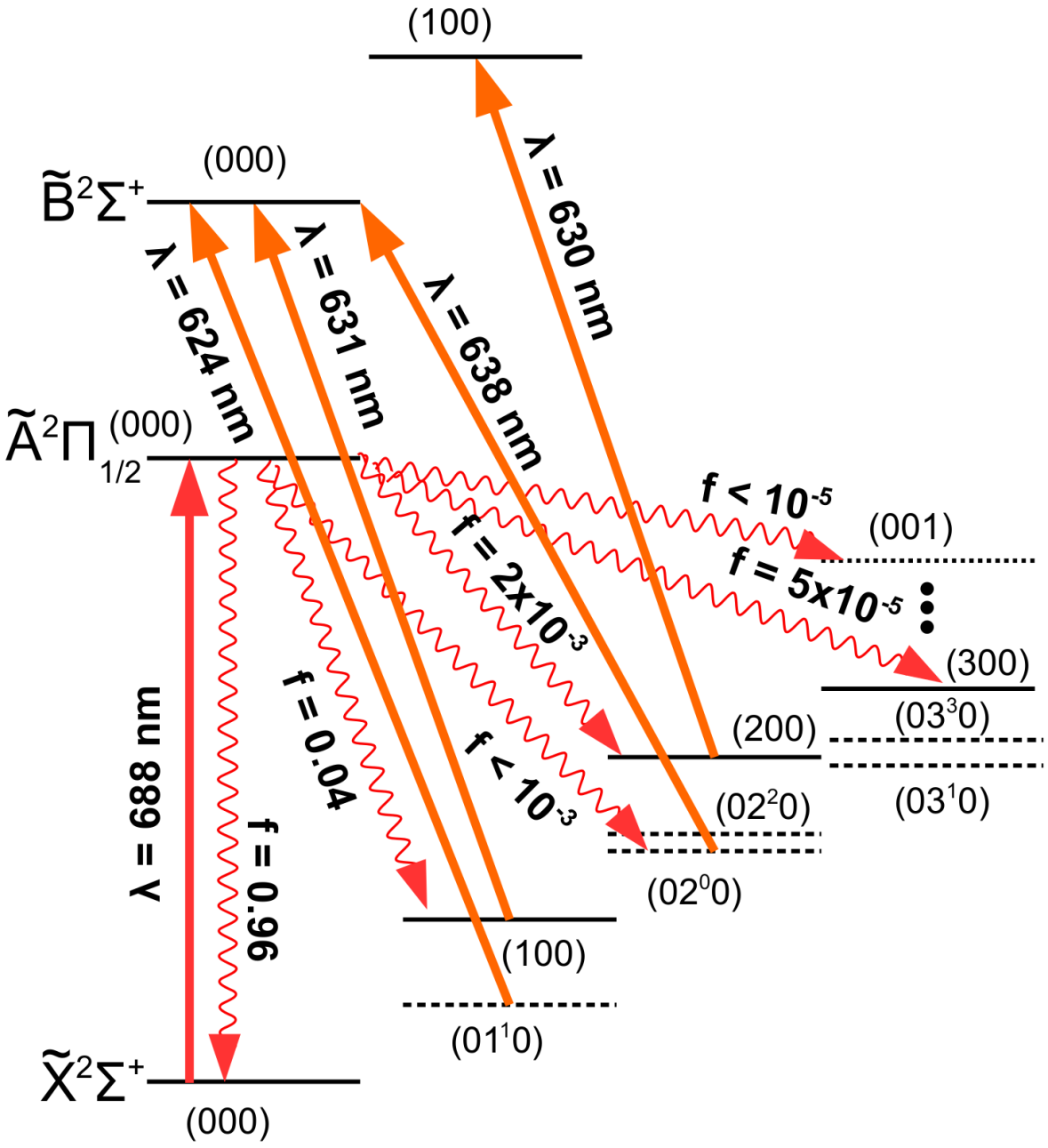


Figure 8.4.1: Optical cycling scheme for SrOH required to achieve magneto-optical trapping. Scattering 10,000 photons per molecule seems feasible with four repumping lasers indicated.

Parameter	SrOH	SrF	YO	CaF
Cycling wavelength, nm	688	663	614	606
Recoil velocity, mm/s	5.5	5.6	6.2	11
Mass, amu	105	107	105	59
Max scattering rate/2π, MHz	$7 \times 1/4$	$7 \times 1/7$	$5 \times 1/13$	$8 \times 1/7$
Photons to stop (100 m/s)	18,000	18,000	16,000	9,000
Photons to stop (50 m/s)	9,000	9,000	8,000	4,500
Time to stop, ms (100 m/s)	1.6	2.8	7.0	1.2
Time to stop, ms (50 m/s)	0.8	1.4	3.5	0.6
Distance to stop, cm (100 m/s)	12	21	52	9
Distance to stop, cm (50 m/s)	3.1	5.3	13	2.3

Table 8.1: Radiative force slowing comparison for SrOH, SrF, YO and CaF. For SrOH, the main cycling and repumping transitions are decoupled. Additional reduction in scattering rate for YO comes from microwave remixing of rotational states required because of the presence of the metastable $^2\triangle_{3/2}$ state. Half of the maximum possible radiative force was assumed to allow for experimental deviations from ideal conditions.

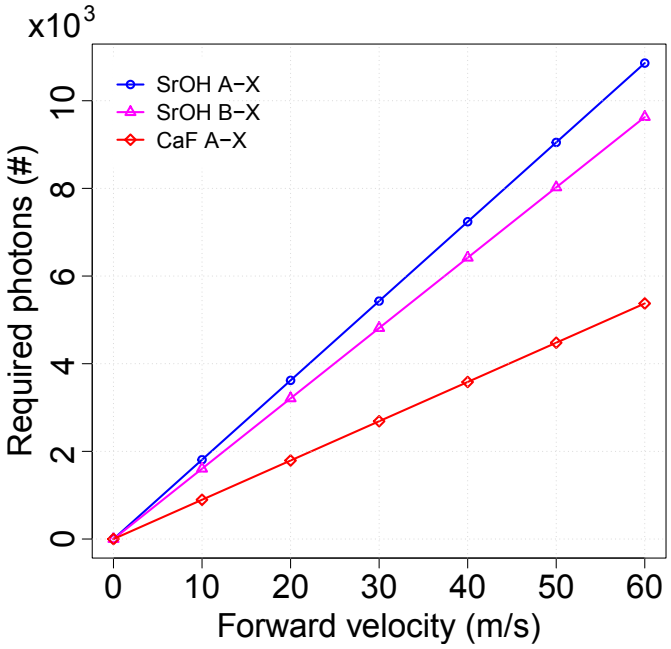


Figure 8.4.2: Comparison of the required number of photons to stop SrOH and CaF cryogenic buffer-gas beams.

8.5 SrOH Zeeman structure and MOT prospects

In order to achieve rotationally closed optical excitations for SrOH, transitions with $F'' > F'$ are used and therefore only type II MOTs could be constructed. While the Zeeman structure of SrOH shown in Fig. 8.5.1 is more complicated than the canonical $J'' = 1 \rightarrow J' = 0$ transition, it is still simpler to analyze compared to $^2\Sigma$ diatomics used for laser cooling like SrF and CaF. As previously mentioned, the hyperfine structure of SrOH is unresolved and therefore effectively only spin-rotation structure needs to be considered. Using red-detuned frequencies as indicated in the diagram, magneto-optical trapping could potentially be achieved. Because of the relatively large spin-rotation splitting compared to the natural linewidth of the electronic transitions, frequency component red-detuned relative to $J = 1/2$ manifold will not cause heating of the $J = 3/2$ sublevels.

While the Zeeman structure of the excited electronic states $\tilde{A}$ and $\tilde{B}$ will need to be analyzed in

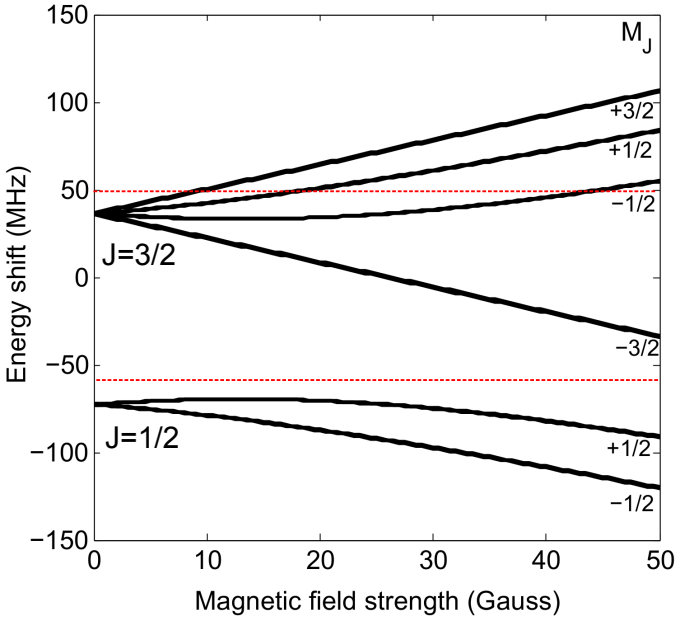


Figure 8.5.1: Zeeman structure of SrOH in the first excited rotational level of the vibronic ground state. The hyperfine structure is unresolved at this level of detail.

more detail, approximately the magnetic moment in the $\tilde{A}$ state is given as [10]

$$\mu_\Omega = (\Lambda + 2\Sigma)\,\mu_B = 0 \tag{8.5.1}$$

since M_L and M_S have opposite signed for $\Omega = 1/2$ state. However, because of the mixing between relatively close lying $\tilde{A}$ and $\tilde{B}$, the magnetic moment in the $\tilde{A}$ state becomes $\mu_\Omega \neq 0$. The size of the Zeeman shift for the rotational levels of the $\tilde{A}$ state can be estimated as [233]

$$\triangle E_{Z\pm} = \pm\frac{1}{3}\left(g_l^{'} - g_r^{e'}\right)\mu_B B_Z M_F \tag{8.5.2}$$

where the Zeeman coefficients are calculated from the Λ doubling constants of the $\tilde{A}$ state as[4] $g_l^{'} = p/(2B_{\rm rot})$ and $g_r^{e'} = -q/B_{\rm rot}$ where $p = -0.1432\,{\rm cm}^{-1}$, $q = -1.51\times10^{-6}\,{\rm cm}^{-1}$, and $B_{\rm rot} =$

[4]In order to avoid notation confusion we use B_Z to denote applied magnetic field and $B_{\rm rot}$ to indicate molecular rotational constant.

$0.2539\,\mathrm{cm}^{-1}$ [234]. Thus, the magnitude of the Zeeman shift for the $\tilde{A}$ state of SrOH is given as

$$\left| \frac{\triangle E_{Z\pm}}{\mu_B B_Z M_F} \right| \approx \frac{g_l^{'}}{3} = 0.094. \tag{8.5.3}$$

It is interesting to note that $\frac{1}{3}\left(g_l^{'} - g_r^{e'}\right)$ parameter which quantifies the Zeeman shift magnitude for the excited $\tilde{A}$ state is larger for SrOH compared to SrF and CaF. Since non-zero excited state g-factor of SrF in the $\tilde{A}$state has been suggested as the origin of type II DC MOT operation, even stronger confining force for DC MOT is expected for SrOH. However, it has been confirmed both experimentally and theoretically that RF MOTs operated as shown in Fig. 8.1.2 provide stronger confinement for molecules compared to DC and therefore present a more attractive option for SrOH trapping. In order to characterize RF MOT parameters for SrOH, initial experiments can be performed in 1D or 2D configurations as done with YO [101] and CaF [231] before proceeding to 3D confinement. Experimental chamber used for SrOH laser cooling can be modified in a straightforward manner to allow such magneto-optical compression of SrOH CBGB.

8.6 Conclusions

Based on the analysis presented here combined with the experimental results on direct laser cooling of SrOH in Chapter 6, loading of SrOH cryogenic buffer-gas beam into a 3D magneto-optical trap appears possible. Using four repumping lasers, radiation pressure longitudinal deceleration should enable slowing below the capture velocity of a 3D MOT. Use of the bichromatic force deceleration described in Chapter 7 or Zeeman-Sisyphus type slower [Ref] should reduce the number of required repumping lasers even further. The Zeeman structure of SrOH appears "simpler" compared to related diatomic molecules like SrF and CaF and either DC or RF MOT can be accomplished using $\tilde{X} - \tilde{A}$ or $\tilde{X} - \tilde{B}$ electronic transitions.

Chapter 9

Towards Laser Cooling of Complex Polyatomics

While cooling SrOH is interesting in its own right, we consider it as a model system for how laser cooling can proceed in much more complex species. In order to productively pursue applications outlined in the Introduction chapter, preparation of laser cooled samples of diverse polyatomic molecules with different geometries and properties will be required. In this chapter we outline how techniques developed with SrOH can be effectively extended to other alkaline earth monoalkoxide free radicals and what potential applications can be achieved.

9.1 Laser manipulation of quantum systems

The ability to repeatedly scatter multiple photons from a quantum object, photon cycling, has led to numerous scientific advances [89, 90]. For external state manipulation, the use of the radiation pressure force from optical cycling to slow, cool, and trap atomic species has facilitated the creation of a diverse set of degenerate quantum gases [235–237], atomic clocks [238, 239], and other forefront quantum science successes [240, 241]. For example, atom imaging in optical lattices with single-site resolution [92, 93, 242, 243] enabled quantum simulation of certain condensed matter theoretical models [244, 245]. When applied to solid-state materials, the use of anti-Stokes

fluorescence made possible optical cooling of solids to cryogenic temperatures [246, 247] as well as laser cooling of micromechanical membranes to the quantum backaction limit [164, 165]. However, the application of photon cycling to gas-phase neutral molecules has been relatively limited, until recently.

In his proposal [144], Di Rosa outlined three criteria that need to be fulfilled in order for direct laser cooling to be applicable to molecules, including i) the existence of strong electronic transitions, ii) diagonal Franck-Condon (FC) factors, and iii) the absence of metastable loss states. Later Stuhl et al. [183] pointed out that to reduce the number of required laser frequencies $J' = J'' - 1$ type transitions could be used to eliminate rotational branching. Following these initial proposals, laser cooling and slowing has been demonstrated on the diatomic radicals SrF [100, 248], YO [101, 118], and CaF [102, 175, 249], and led to the creation of a magneto-optical trap (MOT) for SrF [171, 184, 185].

Polyatomic molecules possess extra atoms compared to diatomics, leading to additional degrees of freedom and complexity. This complexity is the essential property that makes them interesting but from a practical point of view has the potential to inhibit the photon cycling process. For example, direct laser cooling of complex nonlinear polyatomic molecules (e.g. alcohols) is prevented by their non-diagonal FC factors, technically challenging wavelengths, and the absence of strong bound-to-bound electronic transitions. Recently, Isaev and Berger pointed out that quasidiagonality of the FC matrix can be expected for polyatomics with a bonding scheme where a valence electron is "over" a closed shell and undergoes transitions to nonbonding orbitals that are shifted away from the bonding region [105]. They also highlighted a few molecules that have this characteristic including CaOH, CaNC, $CaCH_3$, and $MgCH_3$. In parallel to that theory work, we experimentally demonstrated radiation pressure force deflection of a polyatomic molecule by scattering ~ 100 photons from strontium monohydroxide (SrOH) [188]. Very recently we have also achieved Sisyphus laser cooling of SrOH, reducing the transverse temperature of a cryogenic buffer-gas beam of SrOH from 50 mK to 750 μK with ~ 220 scattered photons per molecule [250]. Inspired by our experimental results on SrOH and insights provided by Isaev and Berger, here we

identify a general scheme for optical cycling in SrO-R type molecules, allowing for laser cooling of species with six or more atoms.

Cold, dense samples of diverse, large polyatomic molecules could open new research avenues in fundamental physics and chemistry as well as quantum science. In particular, enhanced spectral sensitivity of polyatomic molecules to the time variation of fundamental constants arising from phenomena beyond the standard model [13, 15], including interactions with cosmic fields [251, 252], could allow for new astrophysical detectors [17]. The importance of complex organic molecules for astronomy is also indicated by previous observations of over fifty different molecular species containing six or more atoms in interstellar space in a variety of environments [61]. Also, unique degrees of freedom provided by polyatomic molecules have been proposed for applications in quantum simulation [39, 40] and computation [31, 32, 253]. Finally, polyatomics offer an extensive platform for studying violations of fundamental symmetries of nature [26, 254].

Motivated by the variety of possible applications, significant progress on the control of neutral gas-phase complex molecules has been demonstrated previously [255], including electric [2, 256], magnetic [257], and optical field deceleration [258], rotating centrifugal slowing [259], and buffer-gas cooling [260, 261]. Recently, optoelectrical Sisyphus cooling of the electrically trapped sample [86] led to creation of formaldehyde at sub-millikelvin temperatures [85]. The use of an optical cycling scheme for molecules explored in this chapter could significantly enhance these experiments and also lead to direct laser cooling of large molecules into the ultracold regime.

The general concept for photon cycling in a complex polyatomic molecule involves the attachment of a "two-level" atom to facilitate the scattering of photons. As was previously demonstrated experimentally [182], replacing hydrogen (H) in alcohols (HOR) with an alkaline earth metal atom (M) like Ca or Sr leads to alkaline earth monoalkoxide free radicals (MOR), which have a number of ideal properties for direct laser cooling. Like in SrOH, which we recently laser cooled [250], the M-O bond is very ionic, so the orbitals of the metal are only slightly affected by the nature of R on the ligand, leading to a locally linear symmetry near the metal. Diagonal FC factors, laser accessible strong electronic transitions, and a small hyperfine structure make MOR a convenient class

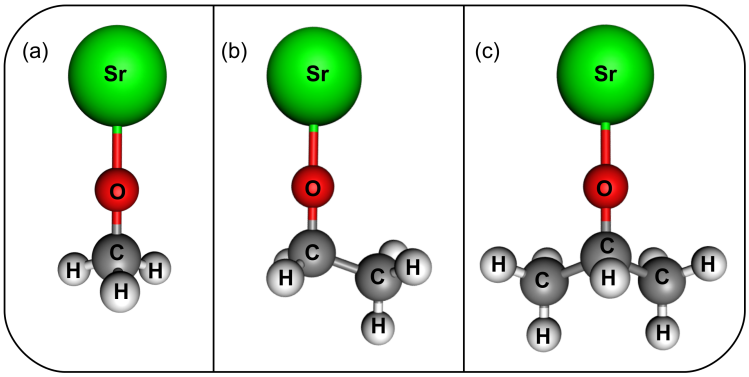


Figure 9.1.1: Three representatives of alkaline earth monoalkoxide free radicals explored in this chapter: (a) strontium monomethoxide, (b) strontium monoethoxide, and (c) strontium isopropoxide. In all cases here, Sr-O-C bond is linear as previously confirmed by the direct laser spectroscopy of these molecules [182]. 3D molecular structures were generated using MolView [262].

of polyatomic molecules for direct laser cooling. The structures of three example MOR molecules are shown in Fig. 9.1.1.

In this chapter, we detail our calculations of the dominant vibrational loss channels for a large number of calcium and strontium monoalkoxide free radicals, identify specific optical cycling approaches, and describe experimental considerations for the Doppler and Sisyphus laser cooling of large polyatomic molecules.

9.2 Photon cycling scheme

In order to understand the emergence of photon cycling in MOR polyatomic molecules, it is important to consider the details of their molecular structure. The electronic levels of the alkaline earth monoalkoxide radicals closely resemble those of monohalides (e.g. CaF or SrF) [160]. The ionic character of the metal-oxygen bond leads to an approximate electronic distribution of the form M^+O^-R which can be analyzed with a simple one-electron, hydrogenic model [182]. While alkaline earth metals have a ns^2 electron configuration in the ground state, during the molecule formation one of the outer-shell electrons is transferred to the ligand, leaving a nonbonding valence electron in a ns state on the M^+ ion. Therefore, the electronic ground state $\tilde{X}$ is mostly formed from the valence $ns\sigma$ molecular orbital leading to alkali metal-like structure. For example, the

Sr^+ ion is isoelectronic to Rb (with ^2S ground state), and the addition of the OH^- ligand results in the molecular ground state $5s\sigma\tilde{X}^2\Sigma^+$ in SrOH. Because of the effectively linear symmetry for M^+-O^--R, the lowest excited atomic state $(n-1)\,d$ produces $(n-1)\,d\sigma$, $(n-1)\,d\pi$, and $(n-1)\,d\delta$ molecular orbitals. The second excited atomic state np gives $np\sigma$ and $np\pi$ orbitals. We explore a photon cycling scheme where we focus on only two excited molecular electronic states $\tilde{A}$ and $\tilde{B}$, which come from the mixture of $(n-1)\,d\pi$-$np\pi$ and $(n-1)\,d\sigma$-$np\sigma$ orbitals, correspondingly.

9.2.1 Franck-Condon factors

Because the electronic transitions considered here involve the promotion of a metal-centered non-bonding electron of M^+, the decay bands are expected to be highly diagonal with $\triangle v = 0$. While previous experimental studies have confirmed this reasoning in some cases [182, 263], no precise measurements of small off-diagonal FC factors were performed. In order to estimate the dominant vibrational loss channels in the MOR systems, which are of crucial importance during the cycling process, we use a harmonic oscillator model to treat atomic motion. This approximation is employed because of the modest anharmonic contribution to the molecular potentials for the states under consideration (e.g. from the data in Ref. [263] $x_e\omega_e/\omega_e \approx 1\times10^{-3}$ for the ground electronic state $\tilde{X}$ of $SrOCH_3$). As a starting point of the analysis, we estimate the FC factors associated with the M-O stretching mode, which involves the motion of the metal atom and, therefore, is expected be the dominant off-diagonal loss channel during photon cycling. Our calculation is performed with the closed-form approximate expressions for FC factors that use the reduced mass (μ), vibrational frequency (ω_e), and equilibrium internuclear distance (r_e) in both the ground and excited states [151]. Considering only the $M^+\leftrightarrow O^-R$ vibrational mode, the expressions for the dominant FC factors are [151]

$$FC_{00} = \exp\left(-S^2/2\right) \tag{9.2.1}$$

$$FC_{01} = FC_{0-0}S^2/2 \tag{9.2.2}$$

where the subscript refers to the M-O stretching mode vibrational quantum number v_1 and $S \equiv \sqrt{\mu_{\mathrm{Sr-O}}\tilde{\omega}_e}\triangle r_e/5.807$. The denominator incorporates numerical prefactors for using convenient units with $\tilde{\omega}_e^{1/2} \equiv 2\sqrt{\omega_e\left(\tilde{A}\right)\omega_e\left(\tilde{X}\right)}/\left(\sqrt{\omega_e\left(\tilde{A}\right)}+\sqrt{\omega_e\left(\tilde{X}\right)}\right)$ in $\left(\mathrm{cm}^{-1}\right)^{1/2}$, $\mu_{\mathrm{Sr-O}}$ in amu, and $\triangle r_e \equiv r_e\left(\tilde{A}\right) - r_e\left(\tilde{X}\right)$ in Angstroms. For low vibrational quantum numbers these approximate formulas agree well with more complex models of molecular vibrations. From the comparison of approximate FC factors found using Eq. 9.2.1 for the isoelectronic molecule SrF and those calculated using the accurate first-order Rydberg-Klein-Rees procedure in Ref. [153], we estimate the relative error on the diagonal FC factors for MOR to be $< 1\%$.

Tables 9.1 and 9.2 provide a summary of the calculated FC factors for the M-O stretching mode for strontium and calcium monoalkoxides. The sum of the two decay channels $FC_{00} + FC_{01}$ is $\gtrsim 99.8\%$ for SrOR and $\gtrsim 99.9\%$ for CaOR confirming the qualitative arguments presented above and indicating that a single repumping laser for the M-O stretching mode will result in only a part in $\gtrsim 500$ loss to higher levels of this vibrational mode. By benchmarking the calculated value of $FC_{00} + FC_{01}$ against isoelectronic molecules SrF and SrOH for which experimental measurements are available [153, 177], we estimate the error in the sum of the two FC factors for the M-O stretching mode to be $\lesssim 2 \times 10^{-3}$. Since λ_{main} is 690 ± 2 nm for SrOR and 630 ± 2 nm for CaOR, these main transition wavelengths are highly independent of the R chain, indicating that a single set of external cavity diode lasers [172] could be used to address the whole range of MOR molecules. While $\lambda_{\mathrm{repump}}$ varies with the species because of the approximately linear dependence of the M-O vibrational frequency on the effective reduced mass of the M-OR complex [182], the expected range of tens of nanometers can be easily covered with a single laser diode by temperature tuning. The recoil velocity is larger for the CaOR class of molecules compared to SrOR but the difference between the lightest and heaviest species we consider is less than a factor of 3. While radiative lifetimes have not been precisely measured for the MOR molecules under consideration, the similarities of their electronic structure with alkaline earth halides indicate expected lifetimes of $20 - 30$ ns [267] leading to strong electronic transitions.

In order to estimate the effects of other vibrational modes, beyond the M-O stretching, we

Molecule	# atoms	# modes	FC_{00},%	λ_{main}, nm	v_{recoil}, mm/s	FC_{01}, %	λ_{repump}, nm
$SrOCH_3$	6	12	95.1	688.7	4.9	4.8	708.5
$SrOCH{=}CH_2$	7	15	95.2	–	–	4.7	–
$SrOCH_2CH_3$	9	21	94.0	689.3	4.4	5.8	706.1
$SrOC(CH_3){=}CH_2$	10	24	95.0	–	–	4.9	–
$SrOCH(CH_3)_2$	12	30	94.3	690.4	3.9	5.6	703.7
$SrOCH_2CH_2CH_3$	12	30	94.4	689.1	3.9	5.5	702.6
$SrOC(CH_3)_3$	15	39	94.2	690.6	3.6	5.7	702.6
$SrO(CH_2)_3CH_3$	15	39	93.6	689.3	3.6	6.2	702.1

Table 9.1: Relevant experimental parameters as well as estimated dominant Franck-Condon factors for strontium monoalkoxide radicals. The calculations are performed for the $\tilde{X}-\tilde{A}$ electronic transition with the spectroscopic constants taken from Refs. [182, 263, 264]. For a non-linear molecule with N atoms, there are $(3N-6)$ degrees of freedom for the normal vibrations with some of the modes possibly degenerate [10]. Based on the similarity of the electronic structures between the listed molecules we expect $\lambda_{main} \sim 690$ nm and $\lambda_{repump} \sim 705$ nm for the unfilled entries.

Molecule	# atoms	# modes	FC_{00}, %	λ_{main}, nm	v_{recoil}, mm/s	FC_{01}, %	λ_{repump}, nm
$CaOCH_3$	6	12	95.1	628.3	8.9	4.8	648.0
$CaOCH_2CH_3$	9	21	95.2	630.9	7.4	4.7	646.6
$CaOCH_2CH_2CH_3$	11	27	95.0	630.5	6.4	4.9	644.7
$CaOCH(CH_3)_2$	12	30	95.6	632.0	6.4	4.3	645.0
$CaOCH(CH_3)CH_2CH_3$	15	39	95.0	632.4	5.6	4.9	645.9
$CaOC(CH_3)_3$	15	39	95.4	632.2	5.6	4.5	644.5

Table 9.2: Relevant experimental parameters as well as estimated dominant Franck-Condon factors for calcium monoalkoxide radicals. The calculations are performed for the $\tilde{X}-\tilde{A}$ electronic transition with the spectroscopic constants taken from Refs [182, 265, 266]. For a non-linear molecule with N atoms, there are $(3N-6)$ degrees of freedom for the normal vibrations with the possibility of degenerate modes [10].

consider a more complete model of the molecular vibrations. Here we use the **GF** matrix formalism [268] and Sharp-Rosenstock approach [120] to calculate FC factors in the M-O-R triatomic approximation [269]. The main reason for treating these complex molecules with such a simplified picture comes from i) the availability of the spectroscopic data and ii) the strength of the off-diagonal decay channels. Because the $\tilde{X}-\tilde{A}$ electronic transitions are highly localized on the metal ion, significant FC factor contributions are expected only for the modes that involve the motion of the metal [270]. Ref. [120] uses the harmonic oscillator approximation, a method of generating functions and the linear transformation of the normal mode coordinates between the initial and final states, to obtain general analytic expressions for calculating FC factors for polyatomic molecules. The main advantage of this approach is that it can be extended to include all of the vibrational modes present in complex molecules [271].

Fig. 9.2.1 displays the essential laser cooling transition scheme and summarizes the values of the calculated FC factors for the dominant loss paths for strontium monomethoxide. $SrOCH_3$ is a prolate symmetric top of C_{3v} symmetry and has 12 vibrational modes with 4 of them being doubly-degenerate leading to a total of 8 distinct vibrations [263]. Because the electronic transitions are highly localized on the Sr^+ ion, only the three modes which are involved in the motion of the strontium are expected to have appreciable FC factors: Sr-O stretching, Sr-O-C bending, and O-C stretching. While cycling is possible on either $\tilde{X}-\tilde{A}$ or $\tilde{X}-\tilde{B}$ electronic transitions, we choose to focus on the prospects of cycling with 689 nm on the $\tilde{X}^2A_1 \leftrightarrow \tilde{A}^2E_{1/2}$ and repumping on $\tilde{X}^2A_1 \rightarrow \tilde{B}^2A_1$ (632, 637, and 668 nm). Decoupling the main laser from the repumps leads to a higher cycling rate that is independent of the number of repumpers [249]. In this way cycling rates up to $\sim 10^7$ s^{-1} should be achievable [250]. Since the repumping lasers for (100), $\left(02^00\right)$, and (001) are coupled to the same excited state, laser powers for $\lambda_{3,5,6}$ should be matched in order to achieve the optimal cycling rate. All of the necessary wavelengths λ_{1-6} can be obtained with high power diode lasers and tapered amplifiers, resulting in a compact experimental setup.

Using spectroscopic data from Refs. [182, 265, 272], we performed a similar FC factors analysis for the calcium monomethoxide ($CaOCH_3$) molecule in order to determine the feasibility of

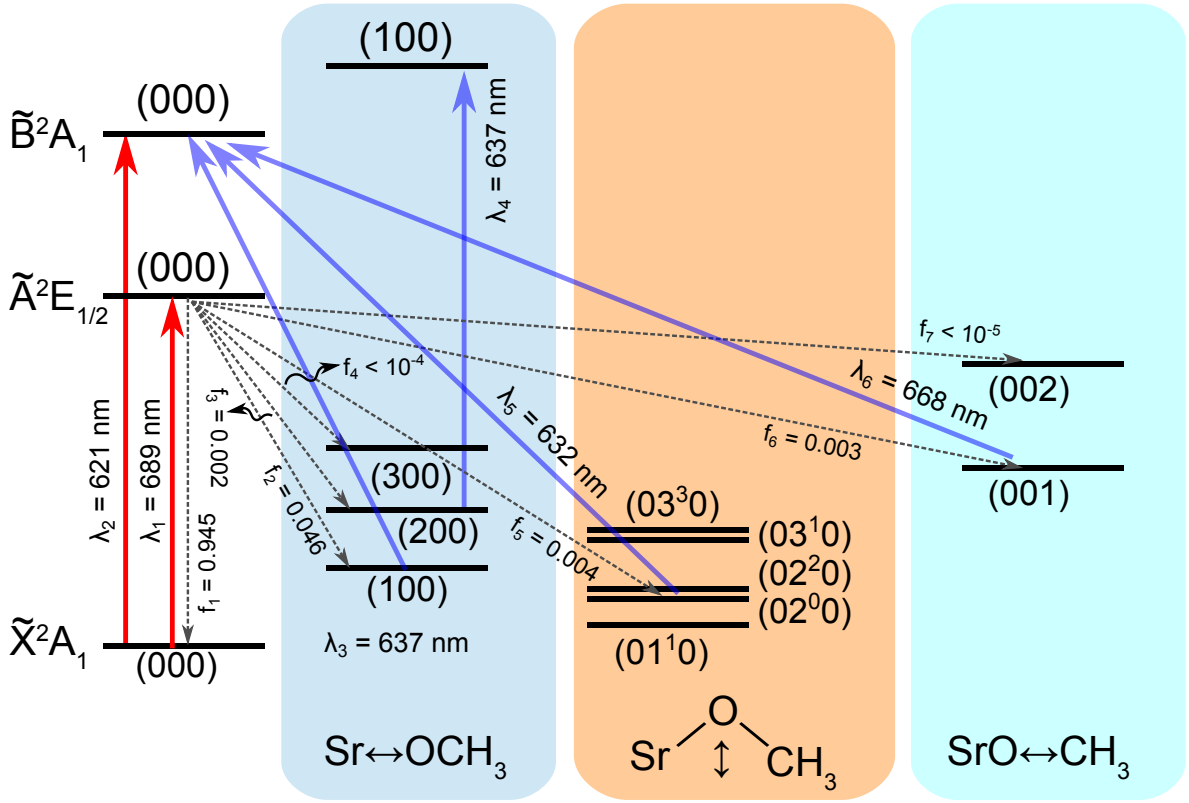


Figure 9.2.1: Photon cycling scheme for strontium monomethoxide ($SrOCH_3$). The energies of certain excited vibrational levels (100) (405 cm^{-1}), (200) (809 cm^{-1}), (020) (271 cm^{-1}), and (001) (1138 cm^{-1}) in the electronic ground state have been previously measured [263]. Two possible main cycling transitions (λ_1 and λ_2) are indicated with upward red arrows. Spontaneous decay channels in the Born-Oppenheimer approximation are shown with downward gray dashed arrows with a corresponding Franck-Condon factor labeled (f_{1-7}). Upward blue arrows labeled with an excitation wavelength (λ_{3-6}) represent the necessary repumping lasers to scatter $\gtrsim 1{,}000$ photons per molecule. The rotational states are not depicted at this scale. The vibrational quantum numbers $\left(v_1 v_2^l v_3\right)$ correspond to the Sr↔O stretching (v_1), Sr-O-C bending (v_2), and SrO↔C stretching (v_3) vibrational modes. The superscript l next to the bending mode vibrational quantum number (v_2^l) indicates the projection of the vibrational angular momentum on the symmetry axis.

laser cooling. Using the notation from Fig. 9.2.1, we obtain the following values for $CaOCH_3$: $f_{000} = 0.943$, $f_{100} = 0.045$, $f_{200} = 0.001$, $f_{02^00} = 0.006$, and $f_{001} = 0.005$ for the dominant vibrational decay channels. Therefore, using four vibrational repumpers exciting through the $\tilde{A}$ state, $\lambda_{100} = 648$ nm, $\lambda_{200} = 669$ nm, $\lambda_{02^00} = 640$ nm, and $\lambda_{001} = 677$ nm, photon cycling and laser cooling can be achieved using the main transition $\tilde{X} - \tilde{A}$ at $\lambda_{000} = 628$ nm. All of these laser wavelengths can be created using solid-state diode lasers with enough power [211] to perform laser cooling to sub-mK temperatures. Coupling of the main and three repumping lasers through the excited $\tilde{A}$ state will require balanced laser powers across all vibronic transitions and lead to the reduced scattering rate. However, this problem can be resolved by cycling on the $\tilde{X} - \tilde{B}$ transition at 566 nm instead.

9.2.2 Forbidden loss channels

The selection rule for the vibrational angular momentum in the electronic transitions is given by $\triangle l = 0$ [108]. Therefore, to first order the decay from the $\tilde{A}(000)$ excited state to the $\tilde{X}\left(01^10\right)$ state should be forbidden in MOR molecules. However, it was previously seen that the intensity of $\tilde{A}(000) \rightarrow \tilde{X}\left(01^10\right)$ is about $\frac{1}{8}$ of the allowed $\tilde{A}(000) \rightarrow \tilde{X}\left(02^00\right)$decay for SrOH [113]. The non-zero intensity of the $(000) - (010)$ band comes from spin-orbit vibronic coupling [178]. In particular, the $\tilde{A}^2\Pi_{1/2}(000)$ level interacts with $\tilde{B}^2\Sigma^+(010)$ level, leading to intensity borrowing [116]. Since the coupling between the electronic and vibrational angular momenta manifested by the Jahn-Teller effect in symmetric-top molecules [10] like $MOCH_3$ is on the same order as the Renner-Teller effect for linear isoelectronic counterparts like MOH [270], using experimentally measured intensity ratios for SrOH [113] together with our estimations of the $\tilde{A}(000) \rightarrow \tilde{X}\left(02^00\right)$ FC factor for $SrOCH_3$, we obtain the decay rate $\tilde{A}(000) \rightarrow \tilde{X}\left(01^10\right)$ to be $\sim 5 \times 10^{-4}$, which is consistent with our estimations using the Renner-Teller Hamiltonian perturbation terms [269]. Therefore, scattering of $\sim 1,000$ photons per molecule can be achieved without repumping vibrational levels with $l \neq 0$.

9.2.3 Rotational structure

Since each vibrational level contains many rotational levels, it is important to consider rotational selection rules even if the majority of the vibrational dark states are repumped as discussed previously. For the case of strontium and calcium monomethoxides considered above, the cycling process is obtained by driving the $\tilde{X}^2A_1 \rightarrow \tilde{A}^2E_{1/2}$ vibronic transition. In this case the dipole moment μ lies perpendicular to the symmetry axis along MOC and therefore the evaluation of the transition dipole moment integral

$$\int \Psi_f \left(^2E\right)^* \mu \Psi_i \left(^2A_1\right) \tag{9.2.3}$$

results in the following selection rules:$\triangle K = \pm 1$ and $\triangle J = 0,\ \pm 1$ [107]. By choosing to drive the $K'' = 1 \rightarrow K' = 0$ transition we obtain a sub-band similar to $(b)^2\Sigma - (a)^2\Pi$ in linear molecules with the letter upfront indicating the Hund's coupling case [112]. As shown in Fig. 9.2.2(a), a rotationally closed system of levels can be obtained by driving the ${}^pQ_{12}(1,0.5)$, ${}^pP_{11}(1,1.5)$, and ${}^pP_{12}(1,1.5)$ transitions simultaneously, where we use ${}^{\triangle|K|}\triangle J_{F_i'F_j''}\left(|K|'', J''\right)$ notation for electronic transitions in polyatomic molecules.

For the repumping scheme outlined previously, we need to excite off-diagonal $\tilde{X}^2A_1 \rightarrow \tilde{B}^2A_1$ vibronic transitions. Since the transition dipole moment points along the MOC symmetry axis in this case, the evaluation of the transition dipole moment integral

$$\int \Psi_f \left(^2A_1\right)^* \mu \Psi_i \left(^2A_1\right) \tag{9.2.4}$$

gives the following selection rules: $\triangle K = 0$ and $\triangle J = 0,\ \pm 1$ [107]. Excitation of the $K'' = 1 \rightarrow K' = 1$ branch results in a sub-band similar to $(b)^2\Pi - (b)^2\Pi$ for linear molecules. Molecules lost to the excited vibrational levels can be returned to the ground vibrational level and back into the cycling scheme by driving the ${}^qQ_{22}(1,0.5)$, ${}^qP_{21}(1,1.5)$, and ${}^qP_{22}(1,1.5)$ branches at the same time (see Fig. 9.2.2(b)). Therefore, it appears feasible to maintain a high cycling rate for

$MOCH_3$ type molecules with only three distinct frequencies per each vibrational transition. These frequencies can be generated from a single laser with a combination of electro- and acousto-optic modulators, as done for diatomic molecules [154, 175, 273]. Additionally, rotational levels can be remixed by microwave fields [118]. Alternatively, since $K'' = 0 \rightarrow K' = 0$ branch of the $\tilde{X}^2A_1 \rightarrow \tilde{B}^2A_1$ manifold resembles $(b)^2\Sigma - (b)^2\Sigma$ sub-band for linear molecules [274] both cycling and repumping can be achieved with only two frequencies ${}^qQ_{12}(0,0.5)$ and ${}^qP_{11}(0,1.5)$ per $\tilde{X} - \tilde{B}$ vibronic excitation at a price of reduced scattering rate (see Fig. 9.2.2(c)). A separate analysis will be necessary to identify a rotationally-closed cycling scheme for molecules with lower degrees of symmetry.

As done with both diatomic molecules [154] and SrOH [188], additional frequencies might be necessary to address the spin-rotation and hyperfine splittings for each rotational transition. Because the hydrogen nuclear spins are even further removed from the metal-centered valence electron in MOR molecules as compared to MOH, the hyperfine structure is expected to be below the natural linewidths of the explored electronic transitions. Measurements performed on $CaOCH_3$ using pump/probe microwave optical double resonance (PPMODR) technique [275] confirm the small value of the hyperfine parameters compared to CaOH.

9.3 Experimental Considerations

Production of a wide range of MOR molecules has been previously demonstrated in both Broida ovens [160, 182] and supersonic beams [275]. At the heart of the production mechanism lies the following chemical reaction:

$$\mathrm{M}^*\left({}^3P_1\right) + \mathrm{HOR} \rightarrow \mathrm{MOR} + \mathrm{H} \tag{9.3.1}$$

which is exothermic for the metal atoms in the excited metastable state. While in the oven experiments an excitation laser is necessary to promote alkaline earth metals via ${}^1S_0 \rightarrow {}^3P_1$ to initiate the reaction, direct ablation of the metallic target with a pulsed nanosecond laser creates enough

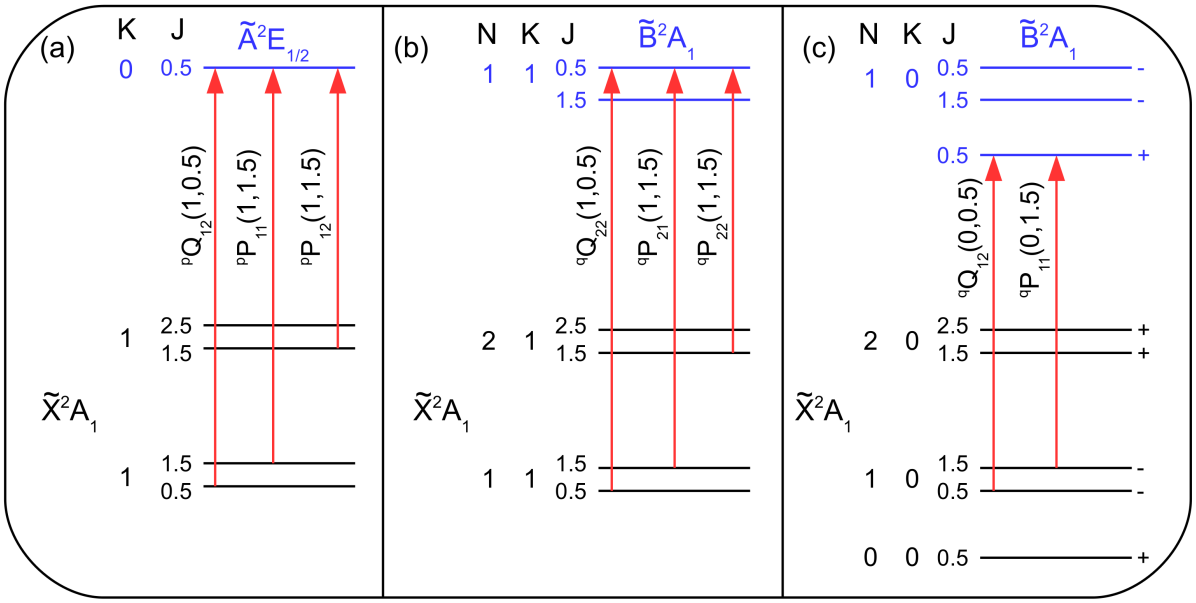


Figure 9.2.2: Relevant rotational levels of $MOCH_3$ molecules for (a) photon cycling on the $K'' = 1 \rightarrow K' = 0$ branch of the $\tilde{X} - \tilde{A}$ electronic transition and (b) repumping from excited vibrational levels on the $K'' = 1 \rightarrow K' = 1$ branch of the $\tilde{X} - \tilde{B}$ transition as well as (c) both cycling and repumping on the $K'' = 0 \rightarrow K' = 0$ branch of the $\tilde{X} - \tilde{B}$ transition (c). Energy levels are labeled by the symmetric-top quantum numbers J and K. Necessary laser frequencies are indicated with upward arrows. Splittings between $N = 1$ and $N = 2$ rotational levels of the $\tilde{X}$ state are approximately 10 GHz for $SrOCH_3$ [263] and 14 GHz for $CaOCH_3$ [265]. In the diagram (c) parity of the energy levels is indicated with "+" and "-".

atoms in the metastable state for efficient molecule production. The reaction of the ground state atoms with alcohols has been shown to proceed via an HMOR intermediate but with a much lower yield for the alkoxides of interest [182].

In order for the proposed laser cooling scheme to be feasible, it is necessary to first "pre-cool" rotational and vibrational motions of MOR molecules so that only a small number of rotational states are populated in the ground vibrational level. This initial step could be achieved either via broadband optical cooling [276, 277] or buffer-gas cooling [79]. For example, experimental techniques for injecting "hot" molecular gases into cryogenic buffer-gas cells followed by chemical reaction with the ablation produced metals have been previously demonstrated [249, 278] and can be extended in a straightforward manner to produce MOR samples at Kelvin temperatures. Following this initial step, laser cooling can be applied on a cryogenic buffer-gas beam (CBGB) in a low pressure environment suitable for further trap loading [80].

9.4 Applications

In this section we outline a number of possible applications in different sub-fields for the photon cycling scheme presented in this chapter for MOR molecules.

9.4.1 Ultracold hydrocarbons

While the presence of alkaline earth metals is crucial for applying the proposed laser cooling scheme to MOR, certain applications might require a sample of neutral alkoxy radicals (OR). For example, understanding the abundance of complex molecules like CH_3O in interstellar clouds requires precise measurements of the gas-phase reactions at cold temperatures [62]. Related, precision spectroscopy of the hydroxyl radical (OH) was used to constrain the time evolution of the fine structure constant [279]. Inspired by the recent progress on laser-cooled diatomic molecules, extensive theoretical calculations have been performed for using photo-fragmentation (PF) to obtain ultracold hydrogen [280], fluorine [281], chlorine [282], and carbon [283], which cannot be

readily laser cooled with the current technologies. One intriguing possibility of the PF approach is achieving a Bose-Einstein condensate of atomic hydrogen [280] without the use of a dilution refrigerator or evaporative cooling, as was done previously [284]. While, as of now, no similar studies have been performed for polyatomic molecules, structural similarities between MF, MOH, and $MOCH_3$ indicate a possibility of obtaining ultracold alkoxy radicals by zero-energy PF. Hydroxyl radical (OH) obtained from laser cooled SrOH at the Doppler limit of ~ 200 μK using fragmentation will have a temperature of ~ 30 μK, which is more than two orders of magnitude lower than the demonstrated temperature of the evaporatively cooled sample [285].

9.4.2 Laser-cooled chiral species

Preparation of asymmetric methyl groups has a long and rich history in organic chemistry [286–289] with recently identified applications in fundamental physics for measuring parity-violating energy differences between enanteomers [290]. The use of a chiral methyl group CHDT in MOR could lead to chiral molecules that can be directly laser cooled: SrOCHDT and CaOCHDT. While Isaev and Berger previously considered the prospects of laser cooling chiral MgCHDT using two repumping lasers to eliminate dominant vibrational loss channels [105], such a scheme would correspond to scattering $1/(1-0.86) \approx 7$ photons per molecule. In the MOR molecules explored in this chapter, the methyl group is situated further from the photon cycling center M and, therefore, we expect a small perturbation to the cycling process from the isomeric substitutions on the methyl group. Using a similar scheme to Fig. 9.2.1 would allow scattering of $\sim 1,000$ photons per chiral molecule, allowing direct laser cooling and opening ultracold chemistry with chiral molecules.

9.4.3 Silicon-containing polyatomics

Another way to expand the chemical diversity of laser-cooled polyatomic samples explored in this chapter is by using silicon atoms (Si) instead of carbon. A variety of silanol (HOSi) containing compounds have been previously explored both theoretically [291, 292] and experimentally [293] in order to construct alcohol analogs. In the manner outlined in Sec. 9.3, flow of $HOSiR_3$ into

a buffer-gas cell containing laser ablated alkaline earth metals should lead to efficient production of diverse siloxide radicals ($MOSiR_3$) that could potentially possess favorable properties for direct laser cooling. For comparison, indirect creation of silicon containing molecules via assembly from laser cooled atoms will be technically challenging since laser cooling of Si requires a continuous-wave laser source in the deep-ultraviolet region at 252 nm [294].

9.4.4 Coherent slowing

Using Doppler radiation pressure force to slow the CBGB of molecules requires scattering of $\gtrsim 10^4$ photons [248] which would necessitate additional repumping lasers beyond those outlined in Fig. 9.2.1 and thus lead to increased technical complexity of the experiment. However, our proposed optical cycling scheme delivering $\sim 10^3$ scattered photons per molecule opens a path towards the use of coherent optical bichromatic forces (BCF) for rapid deceleration of MOR originating from a CBGB to near the capture velocity of a molecular MOT, $v_{\mathrm{cap}} \sim 10\ \mathrm{m/s}$ [295]. Following successful experimental results for atomic beams, there has been different new schemes proposed for efficient laser slowing of diatomic molecules on both electronic [179, 180, 296] and vibrational transitions [297]. While we surmise that these techniques could be applied to MOR species, detailed simulations of the bichromatic force in complex multilevel systems (e.g. like done for CaF [180]) will be necessary in order to precisely determine suitable experimental parameters.

9.4.5 Optical loading of magnetic traps

The presence of an unpaired electronic spin for MOR molecules makes them amenable to magnetic trapping after longitudinal slowing and transverse cooling steps. We have demonstrated magnetic slowing and optical loading of CaF from a two-stage CBGB into a magnetic trap via scattering of only a few photons [83], a method which can be straightforwardly extended to either CaOR or SrOR class of molecules. Accumulation of a MOR sample in a magnetic trap will be a promising starting point for exploring elastic and inelastic collisions with either alkali metal atoms (e.g. Li or K) or helium. Previously, rigorous ab initio theoretical calculations have indicated that certain

polyatomic molecules have small spin-depolarization rates with helium [48, 298], compared to those of CaH [59], but these exciting predictions have never been tested experimentally. Studies with magnetically-trapped spin-polarized samples of MOR molecules would not only accurately benchmark state-of-the-art quantum scattering calculations but also explore the limits of sympathetic cooling with atoms.

9.5 Conclusions

Using a harmonic oscillator approximation for the stretching and bending vibrations of the alkaline earth monoalkoxide polyatomic molecules we estimate the dominant off-diagonal Franck-Condon factors that could limit the optical cycling process in MOR molecules (M=Ca, Sr). Our calculations indicate that scattering of $\sim 1,000$ photons per molecule is feasible with four vibrational repumpers for at least several molecules with six or more atoms. Photon cycling for such complex species will open up many applications not only in control of molecular motion but also in the sensitive measurements of fundamental processes and constants in physics and chemistry.

This approach, together with recent insights by Isaev and Berger [105], could initiate a fertile research area at the crossroads of AMO physics and physical chemistry. On the experimental side, further work could include precise experimental measurements of the predicted FC factors using dispersed laser induced fluorescence [299, 300]. In the theoretical direction, either ab initio or normal mode analysis [120] with the inclusion of all vibrational modes would allow identification of small loss channels with $\lesssim 1/1000$ decay rates. With the addition of extra repumping lasers to limit the dark state losses to below $\sim 10^{-4}$ level, radiative pressure slowing of molecules in a cryogenic molecular beam could be achieved either via the "white-light" or chirped techniques [118, 248]. Another intriguing research question to address is how phenomena present only in polyatomic molecules like Jahn-Teller coupling [108] and internal vibrational redistribution (IVR) [10] will influence the photon cycling process. Finally, determining the largest or most complex OR group that could be attached to the metal atom without eliminating the photon cycling ability

completely would answer a fundamental question in the laser cooling community. Cold collisions and chemical reactions of such molecules could be of crucial interest in various fields [5, 62].

Appendix A

Selection Rules for Vibrational Angular Momentum

Here we give the explanation of the vibrational angular momentum selection rules for linear polyatomic molecules like SrOH. Such selection rules play an important role in the choice of specific molecules and cycling transitions for the laser cooling of polyatomics. We also discuss the origin of the breakdown of the vibrational angular momentum selection rule for particular molecules.

A.1 Hamiltonian and eigenfunctions for the 2D harmonic oscillator

Consider a linear triatomic molecule with the Hamiltonian of the form (ignore the stretching modes for now):

$$H_{total} = H_{xy} + H_z = \frac{1}{2\mu}\left(p_x^2 + p_y^2\right) + \frac{1}{2}\mu\omega^2\left(x^2 + y^2\right) + \frac{1}{2\mu}p_z^2. \tag{A.1.1}$$

Notice that the restoring force is a function of x and y only, and therefore the problem is reduced to solving 2D harmonic oscillator with the Hamiltonian of the form:

$$H_{xy} = -\frac{\hbar^2}{2\mu}\left(\frac{\partial^2}{\partial x^2} + \frac{\partial^2}{\partial y^2}\right) + \frac{1}{2}\mu\omega^2\left(x^2 + y^2\right), \tag{A.1.2}$$

where μ is the reduced mass of the harmonic oscillator and $f = \mu\omega^2$ is the force constant (we have assumed an isotropic SHO). The eigenvalue equation for the oscillator is:

$$H_{xy}\Psi = E_{xy}\Psi. \tag{A.1.3}$$

After performing the change of variables: $x' \equiv x\sqrt{\frac{\mu\omega}{\hbar}}$ and $y' = y\sqrt{\frac{\mu\omega}{\hbar}}$ we obtain the following equation:

$$-\frac{1}{2}\left(\frac{\partial^2\Psi}{\partial x'^2} + \frac{\partial^2\Psi}{\partial y'^2}\right) + \frac{1}{2}\left(x'^2 + y'^2\right)\Psi = E\Psi \tag{A.1.4}$$

where E is in the units of $\hbar\omega$. Moreover, the equation easily factorizes into the x and y components:

$$-\frac{1}{2}\left(\frac{\partial^2}{\partial x'^2} - x'^2\right)\psi_{n_{x'}}\left(x'\right) = \left(n_{x'} + \frac{1}{2}\right)\psi_{n_{x'}}\left(x'\right) \tag{A.1.5}$$

$$-\frac{1}{2}\left(\frac{\partial^2}{\partial y'^2} - y'^2\right)\psi_{n_{y'}}\left(y'\right) = \left(n_{y'} + \frac{1}{2}\right)\psi_{n_{y'}}\left(y'\right) \tag{A.1.6}$$

where the total wavefunction in 3D is given by:

$$\Psi\left(x', y', z\right) = \psi_{n_{x'}}\left(x'\right)\psi_{n_{y'}}\left(y'\right)\psi\left(z\right) \tag{A.1.7}$$

The total energy of the 2D harmonic system then becomes:

$$E_{xy} = \left(n_{x'} + n_{y'} + 1\right)\hbar\omega = \left(v + 1\right)\hbar\omega. \tag{A.1.8}$$

Let's exploit the symmetry of the problem and consider the molecule in cylindrical coordinates around the internuclear axis (z). Since $x' = \rho\cos\phi$ and $y' = \rho\sin\phi$ we obtain the following

Hamiltonian in the new coordinate system:

$$H_v = \frac{1}{2}\rho^2 - \frac{1}{2}\left(\frac{1}{\rho}\frac{\partial}{\partial\rho} + \frac{\partial^2}{\partial\rho^2} + \frac{1}{\rho^2}\frac{\partial^2}{\partial\phi^2}\right) \tag{A.1.9}$$

with the eigenvalue equation:

$$H_v\psi_v(\rho,\phi) = E\psi_v(\rho,\phi) \tag{A.1.10}$$

where $E = v+1$ in the units of $\hbar\omega$.

Consider a separable solution of the form $\psi_v(\rho,\phi) = R(\rho)\Phi(\phi)$. After a substitution into the eigenvalue equation and manipulation we obtain:

$$\left(\rho^4 - \frac{\rho}{R}\frac{dR}{d\rho} - \frac{\rho^2}{R}\frac{d^2R}{d\rho^2} - 2E\rho^2\right) - \frac{1}{\Phi}\frac{d^2\Phi}{d\phi^2} = 0 \tag{A.1.11}$$

where the first part depends only on ρ and the second part only on ϕ. Define the separation constant as l^2 to obtain:

$$\frac{1}{\Phi}\frac{d^2\Phi}{d\phi^2} = -l^2 \tag{A.1.12}$$

$$\rho^2 R - \frac{1}{\rho}\frac{dR}{d\rho} - \frac{d^2R}{d\rho^2} - 2ER + \frac{l^2}{\rho^2}R = 0. \tag{A.1.13}$$

In this manner the wave-functions for bending and angular motions are separated. The solution of the first equation is given by:

$$\Phi(\phi) \propto e^{il\phi} \tag{A.1.14}$$

where l has to be an integer because of the periodicity of the physical system in ϕ and can take positive and negative values (i.e. $l = 0, \pm1, \pm2, \ldots$). Consider the vibrational contribution to the transition moment integral for an electronic transition between two different states g and e with different values of l:

$$\int \Phi_e^* \Phi_g d\phi \propto \int e^{i(l_g - l_e)\phi} d\phi \tag{A.1.15}$$

which is equal to zero unless $l_g = l_e$. Therefore, $\triangle l = 0$ in the electronic transitions.

Next let's solve the second equation for $R(\rho)$. First, let's consider the asymptotic limit at $\rho \to \infty$ of the differential equation for $R(\rho)$:

$$\frac{d^2R}{d\rho^2} = \rho^2 R. \tag{A.1.16}$$

The physically acceptable solution is $R(\rho) \propto e^{-\rho^2/2}$. Now consider the asymptotic form of the differential equation at the limit $\rho \to 0$:

$$\frac{d^2R}{d\rho^2} + \frac{1}{\rho}\frac{dR}{d\rho} - \frac{l^2}{\rho^2}R = 0 \tag{A.1.17}$$

with the physically acceptable solution $R(\rho) \propto \rho^{|l|}$.

Combining both asymptotic results we obtain the following form of the solution $R(\rho) = \rho^{|l|}e^{-\rho^2/2}L(\rho)$. After substitution into the original equation for $R(\rho)$, we obtain the following differential equation for $L(\rho)$:

$$\frac{d^2L(\rho)}{d\rho^2} + \frac{dL(\rho)}{d\rho}\left(\frac{2|l|+1}{\rho} - 2\rho\right) + 2L(\rho)(E - 1 - |l|) = 0 \tag{A.1.18}$$

since $E = v + 1$ and using a change of variables $r = \rho^2$ we obtain:

$$r\frac{d^2L(r)}{dr^2} + \frac{dL(r)}{dr}(|l| + 1 - r) + L(r)\frac{v - |l|}{2} = 0 \tag{A.1.19}$$

where we have used the following results to perform change of variables in the differential equation:

$$\frac{dL}{d\rho} = \frac{dL}{dr}\frac{dr}{d\rho} = 2\rho\frac{dL}{dr} \tag{A.1.20}$$

$$\frac{d^2L}{d\rho^2} = \frac{d}{d\rho}\left(2\rho\frac{dL}{dr}\right) = 2\frac{dL}{dr} + 4\rho^2\frac{d^2L}{dr^2} \tag{A.1.21}$$

since $\frac{d}{d\rho} = 2\rho\frac{d}{dr}$. After making a substitution $k \equiv |l|$ and $n \equiv \frac{v-|l|}{2}$ we obtain the following equation:

$$r\frac{d^2L(r)}{dr^2} + \frac{dL(r)}{dr}(k + 1 - r) + nL(r) = 0 \tag{A.1.22}$$

which is an associated Laguerre differential equation (see Arfken and Weber for more details)

with solutions given by the associated Laguerre polynomials $L_n^k(r)$ where n is an integer. Thus, $v = |l|, |l|+2, |l|+4, \ldots$

Combining all the results together, we obtain the wavefunctions for the 2D harmonic oscillator:

$$\psi_{v,l}(\rho,\phi) = e^{il\phi}\rho^{|l|}e^{-\rho^2/2}L^{|l|}_{\frac{v-|l|}{2}}\left(\rho^2\right) \tag{A.1.23}$$

where the vibrational angular momentum selection rules comes from the first term as was shown before. Notice that the wavefunctions are not normalized yet. Also, observe that the wavefunctions are doubly degenerate because $\psi_{v,l} = \psi_{v,-l}$.

In order to normalize the wavefunctions, consider the integral in polar coordinates using the change of variables $r = \rho^2$ as before:

$$\int_0^{2\pi}\int_0^{\infty}\psi^*_{v,l}\psi_{v',l'}\rho d\rho d\phi = \int_0^{2\pi}e^{i(l'-l)\phi}d\phi\int_0^{\infty}r^k e^{-r}L^{k'}_{n'}L^k_n(r)\frac{dr}{2} = \pi\frac{(n+k)!}{n!}\delta_{n',n} \tag{A.1.24}$$

which is zero unless $v = v'$ and $|l| = |l'|$. Therefore, the normalized wavefunctions are given by:

$$\psi_{v,l}(\rho,\phi) = \left(\frac{\mu\omega}{\hbar}\right)^{\frac{1}{2}}\left[\frac{\left(\frac{v-|l|}{2}\right)!}{\pi\left(\frac{v+|l|}{2}\right)!}\right]^{\frac{1}{2}}e^{il\phi}\rho^{|l|}e^{-\rho^2/2}L^{|l|}_{\frac{v-|l|}{2}}\left(\rho^2\right) \tag{A.1.25}$$

where, as was defined previously, $\rho = \sqrt{\frac{\mu\omega}{\hbar}}\left(x^2+y^2\right)$. Sometimes the wavefunctions are given in terms of $\mathcal{L}^{|l|}_{\frac{v+|l|}{2}} = \mathcal{L}^{|l|}_{n+|l|}$ where we can use the conversion factor (see Ref. [301] Eq. 13.39):

$$L^{|l|}_{\frac{v-|l|}{2}} = (-1)^{|l|}\mathcal{L}^{|l|}_{\frac{v+|l|}{2}}. \tag{A.1.26}$$

Actually, a lot of references (for example Ref. [87]) write the wavefunctions in terms of $\mathcal{L}^{|l|}_{\frac{v+|l|}{2}}$. The associated Laguerre polynomials can be expressed by the regular Laguerre polynomials in the following manner:

$$L^k_n(x) = (-1)^k\frac{d^k}{dx^k}\left[L_{n+k}(x)\right]. \tag{A.1.27}$$

Now that we have found the wavefunctions for the bending motion of the linear polyatomic molecule, we can confirm that l is indeed the vibrational angular momentum. Let z axis be along the internuclear axis of the molecule. The angular momentum operator then becomes:

$$L_z = -i\hbar\frac{\partial}{\partial\phi}. \tag{A.1.28}$$

Notice that the eigenvalues of L_z are given by $\hbar l$:

$$L_z\psi_{v,l} = \hbar l\psi_{v,l}. \tag{A.1.29}$$

Therefore, the bending motion of a linear molecule has vibrational angular momentum $l\hbar$ along the z-axis. Observe that the energy of the oscillator is doubly degenerate in l since

$$E_v = \hbar\omega(v+1) = \hbar\omega(2n+|l|+1). \tag{A.1.30}$$

Also, even though states of different l designated by v_2^l are degenerate for the 2D harmonic oscillator, they become split for the anharmonic oscillator.

Appendix B

Calculation of Franck-Condon Factors for SrOH

In this appendix we describe in detail how the calculation of Franck-Condon factors (FCFs) for SrOH was done. Specifically, we calculate FCFs for $\tilde{A}^2\Pi_{1/2} \leftarrow \tilde{X}^2\Sigma^+$ and $\tilde{B}^2\Sigma^+ \leftarrow \tilde{X}^2\Sigma^+$ electronic transitions for both stretching and bending vibrational mode configurations. The results are compared to the recent measurements from the Steimle group at ASU and the applications to Doppler cooling of SrOH are outlined.

B.1 Calculation of Franck-Condon Factors for the Stretching Modes

In order to calculate diagonal and off-diagonal FCFs for the stretching modes we use the harmonic oscillator model. From eq. (III,38) in [112] the eigenfunctions of the Schrödinger equation of the harmonic oscillator are given by:

$$\psi_v = N_v e^{-\frac{1}{2}\alpha(r-r_e)^2} H_v\left(\sqrt{\alpha}(r-r_e)\right) \tag{B.1.1}$$

where N_v is the normalization constant, $\alpha = 4\pi^2\mu\nu/h$ and $H_v\left(\sqrt{\alpha}(r-r_e)\right)$ is an Hermite polynomial of the vth degree. Since we are primarily interested in the FCFs for the 2 lowest vibrational states, the corresponding wavefunctions are:

$$\psi_0 = N_0 e^{-\frac{1}{2}\alpha(r-r_e)^2} \tag{B.1.2}$$

$$\psi_1 = N_1 e^{-\frac{1}{2}\alpha(r-r_e)^2} 2\sqrt{\alpha}(r-r_e). \tag{B.1.3}$$

Using previously measured values of equilibrium internuclear distance r_e and vibrational frequency $\omega = \nu/c$, as well as calculated reduced mass μ we can estimate the wavefunctions ψ_v for each of the electronic states $\tilde{X}$, $\tilde{A}$ and $\tilde{B}$ that we are interested in. The normalization constants are calculated as:

$$1/N_v = \left(\int_{-\infty}^{\infty} \psi_v^* \psi_v \mathrm{d}r\right)^{1/2} \tag{B.1.4}$$

for each state independently. Thus, the FCFs of interest can be found in the following way:

$$q\left(\tilde{A}(000) \leftarrow \tilde{X}(000)\right) = \left(\int_{-\infty}^{\infty} N_0\left(\tilde{A}\right)\psi_0^*\left(\tilde{A}\right) N_0\left(\tilde{X}\right)\psi_0\left(\tilde{X}\right)\right)^2 \tag{B.1.5}$$

$$q\left(\tilde{A}(000) \leftarrow \tilde{X}(100)\right) = \left(\int_{-\infty}^{\infty} N_0\left(\tilde{A}\right)\psi_0^*\left(\tilde{A}\right) N_1\left(\tilde{X}\right)\psi_1\left(\tilde{X}\right)\right)^2 \tag{B.1.6}$$

and the expressions for $q\left(\tilde{B}(000) \leftarrow \tilde{X}(000)\right)$ and $q\left(\tilde{B}(000) \leftarrow \tilde{X}(100)\right)$ are of the same form as above. Table B.1 summarizes the calculated FCFs for the Sr-O stretching mode assuming a diatomic approximation for now.

In a similar way we can perform the calculations for the excitation of the O-H stretching mode and obtain a bound $q_{01} < 10^{-4}$. Notice that the calculated FCFs using this simple harmonic oscillator model agree quite well with the measurements performed by the Steimle group. Here are the differences between the calculated and measured values: $\triangle q_{00}\left(\tilde{A}^2\Pi_{1/2} \leftarrow \tilde{X}\right) = 0.001$, $\triangle q_{00}\left(\tilde{B} \leftarrow \tilde{X}\right) = 0.004$, $\triangle q_{01}\left(\tilde{A}^2\Pi_{1/2} \leftarrow \tilde{X}\right) < 10^{-3}$, and $\triangle q_{01}\left(\tilde{B} \leftarrow \tilde{A}\right) = 0.005$. In the calculation above we used the spectroscopic parameters summarized in Table B.2.

$v_1^{"}(\tilde{X})$	Upper state	$v_1^{'}(upper)$	$q_{v'v"}$
0	$\tilde{A}$	0	0.956
1	$\tilde{A}$	0	0.043
0	$\tilde{B}$	0	0.981
1	$\tilde{B}$	0	0.018

Table B.1: Summary of the calculated Franck-Condon factors for the Sr-O stretching mode using a diatomic approximation.

Parameter	Value	State	Reference
r_e	2.111 Å	$\tilde{X}$	[152]
ω_1	526.991 cm^{-1}	$\tilde{X}$	[114]
r_e	2.091 Å	$\tilde{A}$	[152]
ω_1	542.097 cm^{-1}	$\tilde{A}$	[114]
r_e	2.098 Å	$\tilde{B}$	[152]
ω_1	582 cm^{-1}	$\tilde{B}$	[122]

Table B.2: SrOH spectroscopic parameters used in Franck-Condon factor calculations.

B.2 Calculation of Franck-Condon Factors for the Bending Modes

Here we describe the details of the FCF calculations for the bending mode. The model we use is that of 2D simple harmonic oscillator. The eigenfunctions in polar coordinates (ρ, ϕ) are given by [87, 150, 302]:

$$\psi_{vl} = N_{vl} \left(\sqrt{\alpha}\rho\right)^{|l|} e^{-\frac{1}{2}\alpha\rho^2 + il\phi} F^{|l|}_{\frac{1}{2}(v+|l|)} \left(\alpha\rho^2\right) \tag{B.2.1}$$

where $F^{l}_{\frac{1}{2}(v+l)}$ is an associated Laguerre polynomial and $\alpha = 4\pi^2\nu_2/hG_{33}$ where $G_{33} = \mu_1 + \mu_2 + \mu_3 \left(r_{e,13} + r_{e,23}\right)^2 / \left(r_{e,13} r_{e,23}\right)$. We follow the notation in Ref. [150]: $\mu_1 = 1/m\left({}^{88}\mathrm{Sr}\right)$, $\mu_2 = 1/m\left({}^{1}\mathrm{H}\right)$ and $\mu_3 = 1/m\left({}^{16}\mathrm{O}\right)$ and r_e corresponds to the equilibrium internuclear distance. The normalization factor N_{vl} is calculated in the same way as in Eq. B.1.4:

$$1/N_{vl} = \left(\int_0^{2\pi}\int_0^{\infty} \psi^*_{vl}\psi_{vl}\rho d\rho d\phi\right)^{1/2} \tag{B.2.2}$$

Because of the vibrational angular momentum selection rule $\triangle l = 0$ we consider decay to $\tilde{X}^2\Sigma^+(020)$ vibronic level as the dominant off-diagonal loss in the bending mode. We used the following wavefunctions in our calculations:

$$\psi_{00} = N_{00} e^{-\frac{1}{2}\alpha\rho^2} \tag{B.2.3}$$

$$\psi_{02} = N_{02} e^{-\frac{1}{2}\alpha\rho^2} \left(-\alpha\rho^2 + 1\right) \tag{B.2.4}$$

The Franck-Condon for the bending mode transition is calculated as:

$$q_{v',v"} = \left(\int_0^{2\pi}\int_0^{\infty} \psi^*_{v'l}\psi_{v"l}\rho d\rho d\phi\right)^2 \tag{B.2.5}$$

The results of the calculation are summarized in Table B.3.

From the data obtained in the Steimle group shown in Fig. B.2.1 we can place a bound on the bending mode off-diagonal decay as $q_{02} \leq 0.005$ which is consistent with the calculated values.

In the calculation above we used the following spectroscopic constants (in addition to the ones

v_2" $(\tilde{X})$	Upper state	$v_2'\,(upper)$	$q_{v',v"}$
0	$\tilde{A}$	0	0.9992
2	$\tilde{A}$	0	0.0008
0	$\tilde{B}$	0	0.998
2	$\tilde{B}$	0	0.002

Table B.3: Summary of the calculated Franck-Condon factors for the bending mode.

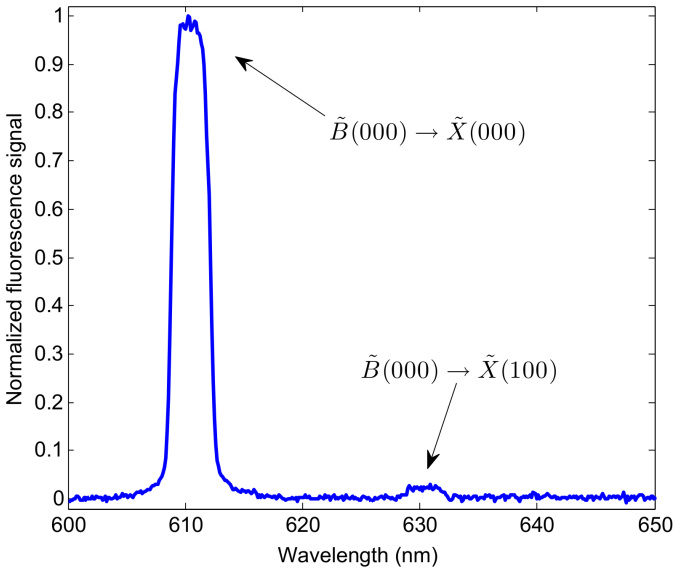


Figure B.2.1: Dispersed laser induced fluorescence for SrOH $\tilde{B}\,(000) \leftarrow \tilde{X}\,(000)$ laser excitation. Data was taken by the Steimle group at ASU.

Parameter	Value	State	Reference
ν_2	361 cm^{-1}	$\tilde{X}$	[113]
ν_2	381 cm^{-1}	$\tilde{A}$	[114]
ν_2	397 cm^{-1}	$\tilde{B}$	[122]

Figure B.2.2: SrOH molecular constants used for bending mode FCF calculations.

given previously) summarized in Table B.2.2.

B.3 Sharp and Rosenstock GF Matrix Approach

Here we use the **GF** matrix formalism and Sharp-Rosenstock approach [120] to calculate FCF for SrOH. They use the harmonic oscillator approximation, the method of generating functions and the linear transformation of the normal mode coordinates between the initial and final states to obtain general expressions for calculating FCFs for polyatomic molecules. The main advantage of this approach is that it can be easily extended to more complex species like $SrNH_2$ and $SrCH_3$. Following the approach presented in Ref. [150], first we set up the kinetic-energy related matrix **G** for each of the states involved ($\tilde{X}$, $\tilde{A}$, and $\tilde{B}$):

$$\mathbf{G} = \begin{bmatrix} G_{11} & G_{12} & 0 \\ G_{21} & G_{22} & 0 \\ 0 & 0 & G_{33} \end{bmatrix} \tag{B.3.1}$$

Notice that the G matrix is block diagonal and therefore the bending mode is not coupled to the stretching modes. The individual entries are given by [268]:

$$G_{11} = \mu_1 + \mu_3 \tag{B.3.2}$$

$$G_{12} = G_{21} = -\mu_3 \tag{B.3.3}$$

$$G_{22} = \mu_2 + \mu_3 \tag{B.3.4}$$

$$G_{33} = \mu_1 + \mu_2 + \mu_3 \frac{(r_{31} + r_{32})^2}{r_{31} r_{32}} \tag{B.3.5}$$

where the internal coordinates were chosen to be $r_{31} = R_{\text{eq}}(\text{Sr} - \text{O})$, $r_{32} = R_{\text{eq}}(\text{O} - \text{H})$, and $(r_{31} r_{32})^{1/2} \triangle\phi$ so that all force constants have the same dimensions and $\mu_1 = 1/\text{mass}\left({}^{88}\text{Sr}\right)$, $\mu_2 = 1/\text{mass}\left({}^{1}\text{H}\right)$ and $\mu_3 = 1/\text{mass}\left({}^{16}\text{O}\right)$. The force matrix for each state of interest in given by:

$$\mathbf{F} = \begin{bmatrix} F_{11} & 0 & 0 \\ 0 & F_{22} & 0 \\ 0 & 0 & F_{33} \end{bmatrix} \tag{B.3.6}$$

where the off-diagonal couplings were ignored (refer to Ref. [150] for details). The **GF** product matrix is calculated then for each state ($\tilde{X}$, $\tilde{A}$, and $\tilde{B}$) separately. Eigenvalues of the **GF** matrix are found by solving:

$$|\mathbf{GF} - \lambda \mathbf{I}| = 0 \tag{B.3.7}$$

where λ is the vector of coefficients:

$$\lambda = \begin{bmatrix} \lambda_1 \\ \lambda_2 \\ \lambda_3 \end{bmatrix} \tag{B.3.8}$$

and $\lambda_k = 4\pi^2 \nu_k$. Solving the secular equation above Eq. B.3.7 for the diagonal entries of the force matrix, we obtain F_{11}, F_{22}, and F_{33} coefficients for each state separately. The normalized eigenvectors of the **GF** matrix give the entries of the **A** matrix which gives the amplitudes of position A_{tk} for a specific internal coordinate S_t and normal coordinate Q_k. For example, the A matrix we obtain for the ground state is:

$$\mathbf{A}\left(\tilde{X}\right) = \begin{bmatrix} -0.9998 & 0.0599 & 0 \\ -0.0178 & -0.9982 & 0 \\ 0 & 0 & 1 \end{bmatrix} \tag{B.3.9}$$

Imposing the normalization condition for each column $\mathbf{A}_k$ of $\mathbf{A}$:

$$N_k^2 \left(\mathbf{A}_k^T F \mathbf{A}_k\right) = \lambda_k \tag{B.3.10}$$

we obtain the $\mathbf{L}$ matrix which consists of normalized columns of $\mathbf{A}$ matrix in the manner described above. The $\mathbf{L}$ matrix can be used to convert from internal coordinates S to the normal coordinates Q in the following way:

$$S = \mathbf{L}Q \tag{B.3.11}$$

Following Sharp and Rosenstock [120] we calculate the difference vector of equilibrium positions $R = R_{eq} - R'_{eq}$ and matrices $\mathbf{J} = (\mathbf{L}')^{-1}\mathbf{L}$ and $\mathbf{K} = (\mathbf{L}')^{-1}R$. The diagonal matrix of reduced frequencies Γ' is given by:

$$\Gamma' = \begin{bmatrix} 4\pi^2\nu'_1/h & 0 & 0 \\ 0 & 4\pi^2\nu'_3/h & 0 \\ 0 & 0 & 4\pi^2\nu'_2/h \end{bmatrix} \tag{B.3.12}$$

where ν_1, ν_2, and ν_3 frequencies refer to the Sr-O stretching, bending and O-H stretching modes. For the calculation of the FCF ratio we use the following constructed matrices following Sharp and Rosenstock:

$$\mathbf{C} = 2\Gamma^{\frac{1}{2}} \left(\mathbf{J}^\dagger \Gamma' \mathbf{J} + \Gamma\right)^{-1} \Gamma^{\frac{1}{2}} - \mathbf{1} \tag{B.3.13}$$

$$\mathbf{D} = -2\Gamma^{\frac{1}{2}} \left(\mathbf{J}^\dagger \Gamma' \mathbf{J} + \Gamma\right)^{-1} \mathbf{J}^\dagger \Gamma' \mathbf{K} \tag{B.3.14}$$

The ratio of FCFs is given by [120] and results for SrOH are summarized in Table B.4.

n_1	n_2	n_3	Excited State	$q(\mathbf{0},\mathbf{v})/q(\mathbf{0},\mathbf{0})$	Calculated	Measured
0	0	0	any	1	1	1
1	0	0	$\tilde{A}$	$\mathbf{D}_1^2/2$	4.5×10^{-2}	4.5×10^{-2}
1	0	0	$\tilde{B}$	$\mathbf{D}_1^2/2$	1.9×10^{-2}	2.4×10^{-2}
2	0	0	$\tilde{A}$	$\left(2\mathbf{C}_{11}+\mathbf{D}_1^2\right)^2/8$	1.7×10^{-3}	-
2	0	0	$\tilde{B}$	$\left(2\mathbf{C}_{11}+\mathbf{D}_1^2\right)^2/8$	2.3×10^{-3}	-
0	1	0	any	$\mathbf{D}_2^2$	0	-
0	2	0	$\tilde{A}$	$\mathbf{C}_{22}^2$	8×10^{-4}	-
0	2	0	$\tilde{B}$	$\mathbf{C}_{22}^2$	2×10^{-3}	-
0	0	1	$\tilde{A}$	$\mathbf{D}_3^2/2$	7×10^{-6}	-
0	0	1	$\tilde{B}$	$\mathbf{D}_3^2/2$	3×10^{-5}	-

Table B.4: Summary of the calculated FCF ratios.

Appendix C

Intensity of Forbidden $\triangle l \neq 0$ Vibrational Decays

In this appendix we calculate the order of magnitude estimates for the intensity of the forbidden transition $\tilde{A}^2\Pi_{1/2}(000) \rightarrow \tilde{X}^2\Sigma^+\left(01^10\right)$which will lead to molecule loss in the SrOH laser cooling experiment. We also compare this loss mechanism for CaOH, SrOH and BaOH.

C.1 Estimation for SrOH

The selection rule for the vibrational angular momentum in the electronic transitions is given by $\triangle l = 0$. Therefore, to first order the decay from $\tilde{A}^2\Pi_{1/2}(000)$ excited state to $\tilde{X}^2\Sigma^+\left(01^10\right)$ state should be forbidden. However, it was previously seen in the literature that the intensity of $\tilde{A}(000) \rightarrow \tilde{X}\left(01^10\right)$ is about $\frac{1}{8}$ of the allowed $\tilde{A}(000) \rightarrow \tilde{X}\left(02^00\right)$decay [113]. The non-zero intensity of the $000-010$ band comes from the spin-orbit vibronic coupling [178]. The $\tilde{A}^2\Pi_{1/2}(000)$ level interacts with $\tilde{B}^2\Sigma^+(010)$ level which leads to intensity borrowing. In mode detail, mixing occurs in second order via $H_{RT} \times H_{SO}$ Hamiltonian term. Dipolar term of the Renner-Teller (RT) perturbation operator connects basis functions with $v_2 = \pm 1$ and $\triangle l = -\triangle\Lambda = \pm 1$ and is given by (eq. 18 in [116]):

$$H_{RT} = \frac{1}{2} V \left(q_+ L_- + q_- L_+ \right) \tag{C.1.1}$$

where the ladder operators $q_\pm$ and $L_\pm$ act on the vibrational and electronic orbital angular momenta, correspondingly. The effective spin-orbit operator is given by (from eq. 19 in [116]):

$$H_{SO} = A L_z S_z + \frac{1}{2} A \left(L_+ S_- + L_- S_+ \right). \tag{C.1.2}$$

Thus, the second order interaction $H_{RT} \times H_{SO}$ has non-zero matrix elements within the $^2\Pi$ manifold that mix basis states with $v_2 = \pm 1$ and $\triangle P = 0$ which leads to the $\tilde{A}(000) \sim \tilde{A}(010)$ mixing. The second order energy shift is given by:

$$\frac{\left\langle \tilde{A}(000) \left| H_{RT} \right| \tilde{B}(010) \right\rangle \left\langle \tilde{B}(010) \left| H_{SO} \right| \tilde{A}(010) \right\rangle + \left\langle \tilde{A}(000) \left| H_{SO} \right| \tilde{B}(000) \right\rangle \left\langle \tilde{B}(000) \left| H_{RT} \right| \tilde{A}(010) \right\rangle}{E_{\tilde{A}-\tilde{B}}} \tag{C.1.3}$$

which is approximately given by:

$$\frac{2 \left\langle \tilde{A}(000) \left| H_{RT} \right| \tilde{B}(010) \right\rangle \left\langle \tilde{B}(010) \left| H_{SO} \right| \tilde{A}(010) \right\rangle}{E_{\tilde{A}-\tilde{B}}}. \tag{C.1.4}$$

In order to calculate the decay rate we need to find the corresponding second order wavefunction correction which is given by:

$$\propto \frac{\left\langle \tilde{A}(000) \left| H_{RT} \right| \tilde{B}(010) \right\rangle \left\langle \tilde{B}(010) \left| H_{SO} \right| \tilde{A}(010) \right\rangle}{E_{\tilde{A}-\tilde{B}} E_{\tilde{A}(000)-\tilde{A}(010)}} \tag{C.1.5}$$

or approximately

$$\propto \frac{\left\langle \tilde{A} \left| H_{RT} \right| \tilde{B} \right\rangle \left\langle \tilde{B} \left| H_{SO} \right| \tilde{A} \right\rangle}{\omega_2 E_{\tilde{A}-\tilde{B}}} \tag{C.1.6}$$

where ω_2 is the frequency of the bending mode oscillator. The probability is proportional to the square of the mixing matrix element and therefore:

$$P_{000-010} \propto \frac{2\left\{\left\langle \tilde{A}\left|H_{RT}\right|\tilde{B}\right\rangle \left\langle \tilde{B}\left|H_{SO}\right|\tilde{A}\right\rangle\right\}^2}{\left\{\omega_2 E_{\tilde{A}-\tilde{B}}\right\}^2}. \tag{C.1.7}$$

The mixing of the Π state with Σ and Δ states due to RT interaction can be estimated using the parameter $\triangle g_L$ which is the contribution to the orbital g-factor [303]. Assuming Van Vleck's unique perturber model and pure precession hypothesis [110] we obtain:

$$P_{000-010} = \frac{4\triangle g_L A_{SO}^2}{\omega_2^2} \tag{C.1.8}$$

where we have used

$$\triangle g_L = -\frac{1}{4\gamma_2}\sum_{\eta}\frac{(-1)^p\left|\left\langle \eta\left|V_{RT}\right|\eta'\right\rangle\right|^2}{(\triangle E)^2} \tag{C.1.9}$$

from eq. 24 in [303] which in the unique perturber approximation becomes [304]:

$$\triangle g_L \approx -\frac{1}{4\gamma_2}\frac{\left\{\left\langle \tilde{A}\left|V_{RT}\right|\tilde{B}\right\rangle\right\}^2}{\left(E_{\tilde{A}-\tilde{B}}\right)^2} \tag{C.1.10}$$

where $\gamma_2 = 2\pi c\omega_2/\hbar$ [303]. Also, in the pure precession approximation we obtain (eq. 3.4.18 and 3.4.20 in [110]):

$$\left\langle {}^2\Pi_{1/2}, v\left|H_{SO}\right|^2\Sigma_{1/2}^+, v'\right\rangle = \frac{1}{2}a_+ = \sqrt{2}A_{SO}. \tag{C.1.11}$$

Let's attempt to estimate the effect now. For SrOH $\triangle g_L = -g_K/\omega_2 \approx 5\times10^{-4}$, while $A_{SO}^2/\omega_2^2 \approx 0.5$. Therefore, $P_{000-010} \approx 1\times10^{-3}$.

Let's compare our order of magnitude estimation with the experimental results. From our measurements in Chapter 6, FCF for decay $\tilde{A}(000) \rightarrow \tilde{X}\left(02^00\right)$ is $\sim 5\times10^{-4}$. Therefore, FCF for decay $\tilde{A}\,(000) \rightarrow \tilde{X}\left(01^10\right)$ should be $\sim 6\times10^{-5}$ according the results in Ref. [113]. However, our estimation appears to be an order of magnitude larger than this prediction.

	CaOH	SrOH	BaOH
A_{SO}, cm^{-1}	66	263	635
$\triangle E_{\Sigma-\Pi}$, cm^{-1}	2024	1703	1463
$A_{SO}^2/\triangle E_{\Sigma-\Pi}^2$	0.001	0.02	0.2

Figure C.2.1: Comparison of some molecular constants for CaOH, SrOH, and BaOH.

C.2 Comparison of SrOH, CaOH and BaOH

In order to compare the spin-orbit vibronic coupling between different molecules we evaluate the parameter $A_{SO}^2/\triangle E_{\Sigma-\Pi}$ using measured spectroscopic data. Table C.2.1 summarizes the results. Notice that the forbidden decay channel $\tilde{A}\,(000) \rightarrow \tilde{X}\left(01^10\right)$ should be suppressed by a factor of 20 in CaOH compared to SrOH. This conclusion is consistent with previous experimental measurements on the strength of the forbidden $\tilde{X}\,(000) \rightarrow \tilde{A}\,(010)$ band for SrOH and CaOH [305]. Thus, potentially laser slowing and magneto-optical trapping of CaOH could be achieved without a need for repumping (010) vibrationally excited state.

Bibliography

[1] Lincoln D Carr, David DeMille, Roman V Krems, and Jun Ye. Cold and ultracold molecules: science, technology and applications. *New J. Phys.*, 11(5):055049, 2009.

[2] Hendrick L Bethlem, Giel Berden, Floris MH Crompvoets, Rienk T Jongma, André JA Van Roij, and Gerard Meijer. Electrostatic trapping of ammonia molecules. *Nature*, 406(6795):491–494, 2000.

[3] Jonathan D Weinstein, Robert deCarvalho, Thierry Guillet, Bretislav Friedrich, and John M. Doyle. Magnetic trapping of calcium monohydride molecules at millikelvin temperatures. *Nature*, 395(6698):148–150, 1998.

[4] Steven A Moses, Jacob P Covey, Matthew T Miecnikowski, Bo Yan, Bryce Gadway, Jun Ye, and Deborah S Jin. Creation of a low-entropy quantum gas of polar molecules in an optical lattice. *Science*, 350(6261):659–662, 2015.

[5] Roman V Krems. Cold controlled chemistry. *Phys. Chem. Chem. Phys.*, 10(28):4079–4092, 2008.

[6] Roman V Krems. Viewpoint: Ultracold controlled chemistry. *Physics*, 3:10, 2010.

[7] N Balakrishnan. Perspective: Ultracold molecules and the dawn of cold controlled chemistry. *J. Chem. Phys.*, 145(15):150901, 2016.

[8] Mikhail Lemeshko, Roman V Krems, John M Doyle, and Sabre Kais. Manipulation of molecules with electromagnetic fields. *Mol. Phys.*, 111:1648, 2013.

[9] Masato Morita, Jacek Kłos, Alexei A Buchachenko, and Timur V Tscherbul. Cold collisions of heavy $^2\Sigma$ molecules with alkali-metal atoms in a magnetic field: Ab initio analysis and prospects for sympathetic cooling of SrOH ($^2\Sigma$) by Li (^{2}S). *arXiv preprint arXiv:1702.05856*, 2017.

[10] Wolfgang Demtröder. *Molecular Physics: Theoretical Principles and Experimental Methods*. Weinheim: Wiley-VCH Verlag, 2003.

[11] David DeMille. Diatomic molecules, a window onto fundamental physics. *Phys. Today*, 68(12):34, 2015.

[12] Cheng Chin, VV Flambaum, and MG Kozlov. Ultracold molecules: new probes on the variation of fundamental constants. *New J. Phys.*, 11(5):055048, 2009.

[13] Paul Jansen, Hendrick L Bethlem, and Wim Ubachs. Tipping the scales: Search for drifting constants from molecular spectra. *J. Chem. Phys.*, 140(1):010901, 2014.

[14] C. J. Hogan. Why the universe is just so. *Rev. Mod. Phys.*, 72(4):11–49–1161, 2000.

[15] Mikhail G Kozlov and Sergei A Levshakov. Microwave and submillimeter molecular transitions and their dependence on fundamental constants. *Ann. Phys. (Berlin)*, 525(7):452–471, 2013.

[16] Alexander Shelkovnikov, Robert James Butcher, Christian Chardonnet, and Anne Amy-Klein. Stability of the proton-to-electron mass ratio. *Phys. Rev. Lett.*, 100(15):150801, 2008.

[17] Julija Bagdonaite, Paul Jansen, Christian Henkel, Hendrick L Bethlem, Karl M Menten, and Wim Ubachs. A stringent limit on a drifting proton-to-electron mass ratio from alcohol in the early universe. *Science*, 339(6115):46–48, 2013.

[18] S Truppe, RJ Hendricks, SK Tokunaga, HJ Lewandowski, MG Kozlov, Christian Henkel, EA Hinds, and MR Tarbutt. A search for varying fundamental constants using hertz-level frequency measurements of cold CH molecules. *Nat. Commun.*, 4, 2013.

[19] OW Greenberg. Particles with small violations of Fermi or Bose statistics. *Phys. Rev. D*, 43(12):4111, 1991.

[20] Peter F Bernath. *Spectra of Atoms and Molecules*. Oxford University Press, 2005.

[21] P Cancio Pastor, I Galli, G Giusfredi, D Mazzotti, and P De Natale. Testing the validity of Bose-Einstein statistics in molecules. *Phys. Rev. A*, 92(6):063820, 2015.

[22] Catalina Curceanu, JD Gillaspy, and Robert C Hilborn. Resource letter ss–1: The spin-statistics connection. *Am. J. Phys.*, 80(7):561–577, 2012.

[23] David DeMille, Sidney B Cahn, Dennis Murphree, David A Rahmlow, and Mikhail G Kozlov. Using molecules to measure nuclear spin-dependent parity violation. *Phys. Rev. Lett.*, 100(2):023003, 2008.

[24] ACME Collaboration. Order of magnitude smaller limit on the electric dipole moment of the electron. *Science*, 343(6168):269–272, 2014.

[25] TA Isaev, AV Zaitsevskii, and E Eliav. Laser-coolable polyatomic molecules with heavy nuclei. *arXiv preprint arXiv:1610.08243*, 2016.

[26] Martin Quack, Jürgen Stohner, and Martin Willeke. High-resolution spectroscopic studies and theory of parity violation in chiral molecules. *Annu. Rev. Phys. Chem.*, 59:741–769, 2008.

[27] Sean Tokunaga, RJ Hendricks, M Tarbutt, and B Darquié. High-resolution mid-infrared spectroscopy of buffer-gas-cooled methyltrioxorhenium molecules. *arXiv preprint arXiv:1607.08741*, 2016.

[28] G. K. Drayna. *Novel application of buffer-gas cooling to cold atoms, diatomic molecules, and large molecules*. PhD thesis, Harvard University, 2016.

[29] David DeMille. Quantum computation with trapped polar molecules. *Physical Review Letters*, 88(6):067901, 2002.

[30] Qi Wei, Sabre Kais, Bretislav Friedrich, and Dudley Herschbach. Entanglement of polar symmetric top molecules as candidate qubits. *J. Chem. Phys.*, 135(15):154102, 2011.

[31] Carmen M Tesch and Regina de Vivie-Riedle. Quantum computation with vibrationally excited molecules. *Phys. Rev. Lett.*, 89(15):157901, 2002.

[32] Daniel Weidinger and Martin Gruebele. Quantum computation with vibrationally excited polyatomic molecules: effects of rotation, level structure, and field gradients. *Mol. Phys.*, 105(13-14):1999–2008, 2007.

[33] Carmen M Tesch and Regina de Vivie-Riedle. Vibrational molecular quantum computing: Basis set independence and theoretical realization of the Deutsch–Jozsa algorithm. *J. Chem. Phys.*, 121(24):12158–12168, 2004.

[34] Kouichi Hosaka, Hiroyuki Shimada, Hisashi Chiba, Hiroyuki Katsuki, Yoshiaki Teranishi, Yukiyoshi Ohtsuki, and Kenji Ohmori. Ultrafast fourier transform with a femtosecond-laser-driven molecule. *Phys. Rev. Lett.*, 104(18):180501, 2010.

[35] A Micheli, GK Brennen, and P Zoller. A toolbox for lattice-spin models with polar molecules. *Nature Phys.*, 2(5):341–347, 2006.

[36] A. Micheli, G. Pupillo, H. P. Büchler, and P. Zoller. Cold polar molecules in two-dimensional traps: Tailoring interactions with external fields for novel quantum phases. *Phys. Rev. A*, 76(4):043604, 2007.

[37] Salvatore R Manmana, EM Stoudenmire, Kaden RA Hazzard, Ana Maria Rey, and Alexey V Gorshkov. Topological phases in ultracold polar-molecule quantum magnets. *Phys. Rev. B*, 87(8):081106, 2013.

[38] Bryce Gadway and Bo Yan. Strongly interacting ultracold polar molecules. *J. Phys. B*, 49(15):152002, 2016.

[39] Michael L Wall, Kenji Maeda, and Lincoln D Carr. Simulating quantum magnets with symmetric top molecules. *Ann. Phys. (Berlin)*, 525(10-11):845–865, 2013.

[40] ML Wall, Kenji Maeda, and Lincoln D Carr. Realizing unconventional quantum magnetism with symmetric top molecules. *New J. Phys.*, 17(2):025001, 2015.

[41] Daniel Greif, Thomas Uehlinger, Gregor Jotzu, Leticia Tarruell, and Tilman Esslinger. Short-range quantum magnetism of ultracold fermions in an optical lattice. *Science*, 340(6138):1307–1310, 2013.

[42] Bo Yan, Steven A Moses, Bryce Gadway, Jacob P Covey, Kaden RA Hazzard, Ana Maria Rey, Deborah S Jin, and Jun Ye. Observation of dipolar spin-exchange interactions with lattice-confined polar molecules. *Nature*, 501(7468):521–525, 2013.

[43] Simon Stellmer, Benjamin Pasquiou, Rudolf Grimm, and Florian Schreck. Laser cooling to quantum degeneracy. *Phys. Rev. Lett.*, 110(26):263003, 2013.

[44] K-K Ni, S Ospelkaus, MHG De Miranda, A Pe'er, B Neyenhuis, JJ Zirbel, S Kotochigova, PS Julienne, DS Jin, and J Ye. A high phase-space-density gas of polar molecules. *Science*, 322(5899):231–235, 2008.

[45] Goulven Quéméner and John L Bohn. Shielding $^2\Sigma$ ultracold dipolar molecular collisions with electric fields. *Phys. Rev. A*, 93(1):012704, 2016.

[46] TV Tscherbul and RV Krems. Controlling electronic spin relaxation of cold molecules with electric fields. *Phys. Rev. Lett.*, 97(8):083201, 2006.

[47] TV Tscherbul, Yu V Suleimanov, V Aquilanti, and RV Krems. Magnetic field modification of ultracold molecule–molecule collisions. *New J. Phys.*, 11(5):055021, 2009.

[48] TV Tscherbul, H-G Yu, and A Dalgarno. Sympathetic cooling of polyatomic molecules with S-state atoms in a magnetic trap. *Physical Review Letters*, 106(7):073201, 2011.

[49] Zhiying Li, Roman V Krems, and Eric J Heller. Collision dynamics of polyatomic molecules containing carbon rings at low temperatures. *Journal of Chemical Physics*, 141(10):104317, 2014.

[50] James FE Croft and John L Bohn. Non-sticking of helium buffer gas to hydrocarbons. *Phys. Rev. A*, 91(3):032706, 2015.

[51] Julia Piskorski, David Patterson, Sandra Eibenberger, and John M Doyle. Cooling, spectroscopy and non-sticking of trans-Stilbene and Nile Red. *ChemPhysChem*, 15(17):3800–3804, 2014.

[52] Garrett K Drayna, Christian Hallas, Kenneth Wang, Sergio R Domingos, Sandra Eibenberger, John M Doyle, and David Patterson. Direct time-domain observation of conformational relaxation in gas-phase cold collisions. *Angew. Chem. Int. Ed.*, 55(16):4957–4961, 2016.

[53] Florian Richter, Daniel Becker, Cédric Bény, Torben A Schulze, Silke Ospelkaus, and Tobias J Osborne. Ultracold chemistry and its reaction kinetics. *New J. Phys.*, 17(5):055005, 2015.

[54] K-K Ni, S Ospelkaus, D Wang, G Quéméner, B Neyenhuis, MHG De Miranda, JL Bohn, J Ye, and DS Jin. Dipolar collisions of polar molecules in the quantum regime. *Nature*, 464(7293):1324–1328, 2010.

[55] S Ospelkaus, K-K Ni, D Wang, MHG De Miranda, B Neyenhuis, G Quéméner, PS Julienne, JL Bohn, DS Jin, and J Ye. Quantum-state controlled chemical reactions of ultracold potassium-rubidium molecules. *Science*, 327(5967):853–857, 2010.

[56] Vijay Singh, Kyle S. Hardman, Naima Tariq, Mei-Ju Lu, Aja Ellis, Muir J. Morrison, and Jonathan D. Weinstein. Chemical reactions of atomic lithium and molecular calcium monohydride at 1 K. *Phys. Rev. Lett.*, 108:203201, 2012.

[57] Timur V Tscherbul and Roman V Krems. Tuning bimolecular chemical reactions by electric fields. *Phys. Rev. Lett.*, 115(2):023201, 2015.

[58] M. T. Hummon, T. V. Tscherbul an J. Kłos, H-I Lu, E. Tsikata, W. C. Campbell, A. Dalgarno, and J. M. Doyle. Cold N-NH collisions in a magnetic trap. *Physical Review Letters*, 106:053201, 2011.

[59] TV Tscherbul, J Kłos, and AA Buchachenko. Ultracold spin-polarized mixtures of $^2\Sigma$ molecules with S-state atoms: Collisional stability and implications for sympathetic cooling. *Physical Review A*, 84(4):040701, 2011.

[60] D. Jin and J. Ye. Polar molecules in the quantum regime. *Phys. Today*, 64(5):27, 2011.

[61] Eric Herbst and Ewine F van Dishoeck. Complex organic interstellar molecules. *Annual Review of Astronomy and Astrophysics*, 47:427–480, 2009.

[62] Robin J Shannon, Mark A Blitz, Andrew Goddard, and Dwayne E Heard. Accelerated chemistry in the reaction between the hydroxyl radical and methanol at interstellar temperatures facilitated by tunnelling. *Nat. Chem.*, 5(9):745–749, 2013.

[63] Alexandre Faure, Krzysztof Szalewicz, and Laurent Wiesenfeld. Potential energy surface and rotational cross sections for methyl formate colliding with helium. *J. Chem. Phys.*, 135:024301, 2011.

[64] Melanie Schnell and Gerard Meijer. Cold molecules: preparation, applications, and challenges. *Angew. Chem. Int. Ed.*, 48(33):6010–6031, 2009.

[65] TE Wall. Preparation of cold molecules for high-precision measurements. *J. Phys. B: At. Mol. Opt. Phys.*, 49(24):243001, 2016.

[66] Nitzan Akerman, Michael Karpov, Liron David, Etay Lavert-Ofir, Julia Narevicius, and Edvardas Narevicius. Simultaneous deceleration of atoms and molecules in a supersonic beam. *New J. Phys.*, 17(6):065015, 2015.

[67] Marina Quintero-Pérez, Paul Jansen, Thomas E Wall, Joost E van den Berg, Steven Hoekstra, and Hendrick L Bethlem. Static trapping of polar molecules in a traveling wave decelerator. *Phys. Rev. Lett.*, 110(13):133003, 2013.

[68] Yang Liu, Manish Vashishta, Pavle Djuricanin, Sida Zhou, Wei Zhong, Tony Mittertreiner, David Carty, and Takamasa Momose. Magnetic trapping of cold methyl radicals. *Phys. Rev. Lett.*, 118:093201, 2017.

[69] Nitzan Akerman, Michael Karpov, Yair Segev, Natan Bibelnik, Julia Narevicius, and Edvardas Narevicius. Trapping of molecular oxygen together with lithium atoms. *arXiv preprint arXiv:1611.00155*, 2016.

[70] Cunfeng Cheng, Aernout PP van der Poel, Paul Jansen, Marina Quintero-Pérez, Thomas E Wall, Wim Ubachs, and Hendrick L Bethlem. Molecular fountain. *Phys. Rev. Lett.*, 117(25):253201, 2016.

[71] Jonathan J Hudson, Dhiren M Kara, IJ Smallman, Ben E Sauer, Michael R Tarbutt, and Ed A Hinds. Improved measurement of the shape of the electron. *Nature*, 473(7348):493–496, 2011.

[72] Etay Lavert-Ofir, Yuval Shagam, Alon B Henson, Sasha Gersten, Jacek Kłos, Piotr S Żuchowski, Julia Narevicius, and Edvardas Narevicius. Observation of the isotope effect in sub-kelvin reactions. *Nat. Chem.*, 6(4):332–335, 2014.

[73] Frank Stienkemeier and Kevin K Lehmann. Spectroscopy and dynamics in helium nanodroplets. *J. Phys. B*, 39(8):R127, 2006.

[74] Frank Stienkemeier and Andrey F Vilesov. Electronic spectroscopy in He droplets. *J. Chem. Phys.*, 115(22):10119–10137, 2001.

[75] Mikhail Lemeshko and Richard Schmidt. Molecular impurities interacting with a many-particle environment: from ultracold gases to helium nanodroplets. *arXiv preprint arXiv:1703.06753*, 2017.

[76] Mikhail Lemeshko. Quasiparticle approach to molecules interacting with quantum solvents. *Phys. Rev. Lett.*, 118(9):095301, 2017.

[77] John M Doyle, Bretislav Friedrich, Jinha Kim, and David Patterson. Buffer-gas loading of atoms and molecules into a magnetic trap. *Phys. Rev. A*, 52(4):R2515, 1995.

[78] SE Maxwell, N Brahms, R. deCarvalho, DR Glenn, JS Helton, SV Nguyen, D Patterson, J Petricka, D DeMille, and JM Doyle. High-flux beam source for cold, slow atoms or molecules. *Physical Review Letters*, 95(17):173201, 2005.

[79] Wesley C Campbell and John M Doyle. Cooling, trap loading, and beam production using a cryogenic helium buffer gas. *Cold Polar Molecules: Creation and Applications*, 2009.

[80] Nicholas R Hutzler, Hsin-I Lu, and John M Doyle. The buffer gas beam: An intense, cold, and slow source for atoms and molecules. *Chemical Reviews*, 112(9):4803–4827, 2012.

[81] S Charles Doret, Colin B Connolly, Wolfgang Ketterle, and John M Doyle. Buffer-gas cooled Bose-Einstein condensate. *Phys. Rev. Lett.*, 103(10):103005, 2009.

[82] David Patterson and John M Doyle. Bright, guided molecular beam with hydrodynamic enhancement. *Journal of Chemical Physics*, 126:154307, 2007.

[83] Hsin-I Lu, Ivan Kozyryev, Boerge Hemmerling, Julia Piskorski, and John M Doyle. Magnetic trapping of molecules via optical loading and magnetic slowing. *Phys. Rev. Lett.*, 112(11):113006, 2014.

[84] Boerge Hemmerling, Garrett K Drayna, Eunmi Chae, Aakash Ravi, and John M Doyle. Buffer-gas loaded magneto-optical traps for Yb, Tm, Er and Ho. *New J. Phys.*, 16:063070, 2014.

[85] Alexander Prehn, Martin Ibrügger, Rosa Glöckner, Gerhard Rempe, and Martin Zeppenfeld. Optoelectrical cooling of polar molecules to submillikelvin temperatures. *Phys. Rev. Lett.*, 116(6):063005, 2016.

[86] Martin Zeppenfeld, Barbara G U Englert, Rosa Glöckner, Alexander Prehn, Manuel Mielenz, Christian Sommer, Laurens D van Buuren, Michael Motsch, and Gerhard Rempe. Sisyphus cooling of electrically trapped polyatomic molecules. *Nature*, 491:570–3, 2012.

[87] Charles H Townes and Arthur L Schawlow. *Microwave spectroscopy*. New York: Dover Publications, 1975.

[88] Peter F Bernath. *Spectra of Atoms and Molecules*. Oxford University Press, 2005.

[89] Steven Chu. The manipulation of neutral particles. *Rev. Mod. Phys.*, 70(3):685, 1998.

[90] William D Phillips. Nobel Lecture: Laser cooling and trapping of neutral atoms. *Rev. Mod. Phys.*, 70(3):721, 1998.

[91] Eric A Cornell and Carl E Wieman. Nobel Lecture: Bose-Einstein condensation in a dilute gas, the first 70 years and some recent experiments. *Rev. Mod. Phys.*, 74(3):875, 2002.

[92] Daniel Greif, Maxwell F. Parsons, Anton Mazurenko, Christie S. Chiu, Sebastian Blatt, Florian Huber, Geoffrey Ji, and Markus Greiner. Site-resolved imaging of a fermionic Mott insulator. *Science*, 351(6276):953–957, 2016.

[93] Waseem S Bakr, Amy Peng, M Eric Tai, Ruichao Ma, Jonathan Simon, Jonathon I Gillen, Simon Foelling, Lode Pollet, and Markus Greiner. Probing the superfluid–to–mott insulator transition at the single-atom level. *Science*, 329(5991):547–550, 2010.

[94] Juan J García-Ripoll, Peter Zoller, and J Ignacio Cirac. Quantum information processing with cold atoms and trapped ions. *J. Phys. B At. Mol. Opt. Phys.*, 38(9):S567, 2005.

[95] CS Wood, SC Bennett, Donghyun Cho, BP Masterson, JL Roberts, CE Tanner, and CE Wieman. Measurement of parity nonconservation and an anapole moment in cesium. *Science*, 275(5307):1759–1763, 1997.

[96] Paul Hamilton, Matt Jaffe, Philipp Haslinger, Quinn Simmons, Holger Müller, and Justin Khoury. Atom-interferometry constraints on dark energy. *Science*, 349(6250):849–851, 2015.

[97] Susannah M Dickerson, Jason M Hogan, Alex Sugarbaker, David MS Johnson, and Mark A Kasevich. Multiaxis inertial sensing with long-time point source atom interferometry. *Phys. Rev. Lett.*, 111(8):083001, 2013.

[98] Alexander D Cronin, Jörg Schmiedmayer, and David E Pritchard. Optics and interferometry with atoms and molecules. *Rev. Mod. Phys.*, 81(3):1051, 2009.

[99] Mehdi Hamamda, Pierre Pillet, Hans Lignier, and Daniel Comparat. Ro-vibrational cooling of molecules and prospects. *J. Phys. B*, 48(18):182001, 2015.

[100] E S Shuman, J F Barry, and D DeMille. Laser cooling of a diatomic molecule. *Nature*, 467(7317):820–823, September 2010.

[101] Matthew T. Hummon, Mark Yeo, Benjamin K. Stuhl, Alejandra L. Collopy, Yong Xia, and Jun Ye. 2D magneto-optical trapping of diatomic molecules. *Physical Review Letters*, 110:143001, 2013.

[102] V Zhelyazkova, A Cournol, TE Wall, A Matsushima, JJ Hudson, EA Hinds, MR Tarbutt, and BE Sauer. Laser cooling and slowing of CaF molecules. *Physical Review A*, 89(5):053416, 2014.

[103] Wenhao Bu, Tao Chen, Guitao Lv, and Bo Yan. Cold collision and high-resolution spectroscopy of buffer gas cooled BaF molecule. *Phys. Rev. A*, 95:032701, 2017.

[104] TA Isaev, S Hoekstra, and R Berger. Laser-cooled RaF as a promising candidate to measure molecular parity violation. *Phys. Rev. A*, 82(5):052521, 2010.

[105] Timur Isaev and Robert Berger. Polyatomic candidates for cooling of molecules with lasers from simple theoretical concepts. *Phys. Rev. Lett.*, 116(6):063006, 2016.

[106] Andrew M Ellis. Main group metal-ligand interactions in small molecules: New insights from laser spectroscopy. *Int. Rev. Phys. Chem.*, 20(4):551–590, 2001.

[107] Michael J. Dick. *Spectroscopy of selected calcium and strontium containing polyatomic molecules*. PhD thesis, University of Waterloo, 2007.

[108] Gerhard Herzberg. *Molecular spectra and molecular structure. Vol. 3: Electronic spectra and electronic structure of polyatomic molecules*, volume 3. New York: Van Nostrand, 1966.

[109] Wolfgang Quapp and Brenda P Winnewisser. What you thought you already knew about the bending motion of triatomic molecules. *J. Math. Chem.*, 14(1):259–285, 1993.

[110] Helene Lefebvre-Brion and Robert W Field. *The Spectra and Dynamics of Diatomic Molecules*. Academic Press, 2004.

[111] Robert C Hilborn, Zhu Qingshi, and David O Harris. Laser spectroscopy of the $\tilde{A}$-$\tilde{X}$ transitions of CaOH and CaOD. *J. Mol. Spectrosc.*, 97(1):73–91, 1983.

[112] Gerhard Herzberg. *Molecular spectra and molecular structure. Vol. 1: Spectra of diatomic molecules*. New York: Van Nostrand Reinhold, 1950, 2nd ed., 1950.

[113] CR Brazier and PF Bernath. Laser and Fourier transform spectroscopy of the $\tilde{A}^2\Pi$-$\tilde{X}^2\Sigma^+$ transition of SrOH. *Journal of Molecular Spectroscopy*, 114(1):163–173, 1985.

[114] Paul I. Presunka and John A. Coxon. Laser excitation and dispersed fluorescence investigations of the $\tilde{A}^2\Pi_{1/2}$-$\tilde{X}^2\Sigma^+$ system of SrOH. *Chem. Phys.*, 190:97–111, 1995.

[115] Charles H Townes and Arthur L Schawlow. *Microwave spectroscopy*. New York: Dover, 2013.

[116] Paul I Presunka and John A Coxon. Laser spectroscopy of the $\tilde{A}\ ^2\Pi$–$\tilde{X}^2\Sigma^+$ transition of SrOH: Deperturbation analysis of K-resonance in the v_2=1 level of the $\tilde{A}\ ^2\pi$ state. *J. Chem. Phys.*, 101(1):201–222, 1994.

[117] DA Fletcher, MA Anderson, WL Barclay Jr, and Lucy M Ziurys. Millimeter-wave spectroscopy of vibrationally excited ground state alkaline-earth hydroxide radicals ($\tilde{x}^2\sigma^+$). *J. Chem. Phys.*, 102(11):4334–4339, 1995.

[118] Mark Yeo, Matthew T Hummon, Alejandra L Collopy, Bo Yan, Boerge Hemmerling, Eunmi Chae, John M Doyle, and Jun Ye. Rotational state microwave mixing for laser cooling of complex diatomic molecules. *Phys. Rev. Lett.*, 114(22):223003, 2015.

[119] S Truppe, H Williams, M Hambach, N Fitch, TE Wall, EA Hinds, BE Sauer, and MR Tarbutt. A bright, cold, velocity-controlled molecular beam by frequency-chirped laser slowing. *New J. Phys.*, 19:022001, 2017.

[120] TE Sharp and HM Rosenstock. Franck-Condon factors for polyatomic molecules. *J. Chem. Phys.*, 41(11):3453–3463, 1964.

[121] DA Fletcher, KY Jung, CT Scurlock, and TC Steimle. Molecular beam pump/probe microwave-optical double resonance using a laser ablation source. *J. Chem. Phys.*, 98(3):1837–1842, 1993.

[122] Jun Nakagawa, Richard F Wormsbecher, and David O Harris. High-resolution laser excitation spectra of linear triatomic molecules: Analysis of the $\tilde{B}^2\Sigma^+$–$\tilde{X}^2\Sigma^+$ system of SrOH and SrOD. *J. Mol. Spectrosc.*, 97(1):37–64, 1983.

[123] Axel André, David DeMille, John M Doyle, Mikhail D Lukin, St Ex Maxwell, Peter Rabl, Robert J Schoelkopf, and Peter Zoller. A coherent all-electrical interface between polar molecules and mesoscopic superconducting resonators. *Nature Physics*, 2(9):636–642, 2006.

[124] John Weiner, Vanderlei S Bagnato, Sergio Zilio, and Paul S Julienne. Experiments and theory in cold and ultracold collisions. *Rev. Mod. Phys.*, 71(1):1, 1999.

[125] Brian C Sawyer, Benjamin K Stuhl, Mark Yeo, Timur V Tscherbul, Matthew T Hummon, Yong Xia, Jacek Kłos, David Patterson, John M Doyle, and Jun Ye. Cold heteromolecular dipolar collisions. *Physical Chemistry Chemical Physics*, 13(42):19059–19066, 2011.

[126] Benjamin K Stuhl, Matthew T Hummon, Mark Yeo, Goulven Quéméner, John L Bohn, and Jun Ye. Evaporative cooling of the dipolar hydroxyl radical. *Nature*, 492(7429):396–400, 2012.

[127] Moritz Kirste, Xingan Wang, H Christian Schewe, Gerard Meijer, Kopin Liu, Ad van der Avoird, Liesbeth MC Janssen, Koos B Gubbels, Gerrit C Groenenboom, and Sebastiaan YT van de Meerakker. Quantum-state resolved bimolecular collisions of velocity-controlled OH with NO radicals. *Science*, 338(6110):1060–1063, 2012.

[128] Andreas Osterwalder, Samuel A Meek, Georg Hammer, Henrik Haak, and Gerard Meijer. Deceleration of neutral molecules in macroscopic traveling traps. *Phys. Rev. A*, 81(5):051401, 2010.

[129] Sebastiaan YT van de Meerakker, Paul HM Smeets, Nicolas Vanhaecke, Rienk T Jongma, and Gerard Meijer. Deceleration and electrostatic trapping of OH radicals. *Phys. Rev. Lett.*, 94(2):023004, 2005.

[130] Jeremy M Sage, Sunil Sainis, Thomas Bergeman, and David DeMille. Optical production of ultracold polar molecules. *Phys. Rev. Lett.*, 94(20):203001, 2005.

[131] Eric R Hudson, Nathan B Gilfoy, Svetlana Kotochigova, Jeremy M Sage, and David DeMille. Inelastic collisions of ultracold heteronuclear molecules in an optical trap. *Phys. Rev. Lett.*, 100(20):203201, 2008.

[132] Wesley C Campbell, Timur V Tscherbul, Hsin-I Lu, Edem Tsikata, Roman V Krems, and John M Doyle. Mechanism of collisional spin relaxation in $^3\Sigma$ molecules. *Physical Review Letters*, 102(1):013003, 2009.

[133] Kenneth Maussang, Dima Egorov, Joel S Helton, Scott V Nguyen, and John M Doyle. Zeeman relaxation of CaF in low-temperature collisions with helium. *Physical Review Letters*, 94(12):123002, 2005.

[134] Wade G Rellergert, Scott T Sullivan, Steven J Schowalter, Svetlana Kotochigova, Kuang Chen, and Eric R Hudson. Evidence for sympathetic vibrational cooling of translationally cold molecules. *Nature*, 495(7442):490–4, March 2013.

[135] Wesley C Campbell, Gerrit C Groenenboom, Hsin-I Lu, Edem Tsikata, and John M Doyle. Time-domain measurement of spontaneous vibrational decay of magnetically trapped NH. *Phys. Rev. Lett.*, 100(8):083003, 2008.

[136] Yat Shan Au, Colin B Connolly, Wolfgang Ketterle, and John M Doyle. Vibrational quenching of the electronic ground state in ThO in cold collisions with ^{3}He. *Phys. Rev. A*, 90:032703, 2014.

[137] Julia Piskorski. *Cooling, Collisions and non-Sticking of Polyatomic Molecules in a Cryogenic Buffer Gas Cell*. PhD thesis, Harvard University, Cambridge, MA, 2014.

[138] Jonathan David Weinstein. *Magnetic trapping of atomic chromium and molecular calcium monohydride*. PhD thesis, Harvard University Cambridge, Massachusetts, 2001.

[139] John Barrett Hasted. *Physics of Atomic Collisions*. Washington: Butterworth & Co., 1972.

[140] Hsin-I Lu, J. Rasmussen, M. J. Wright, D. Patterson, and J. M. Doyle. Cold and slow molecular beam. *Phys. Chem. Chem. Phys.*, 13:18986–18990, 2011.

[141] Matthew S Beardah and Andrew M Ellis. Observation of several new electronic transitions of the SrOH free radical. *J. Chem. Phys.*, 110:11244–11254, 1999.

[142] R Pereira and Donald H Levy. Observation and spectroscopy of high-lying states of the CaOH radical: Evidence for a bent, covalent state. *J. Chem. Phys.*, 105(22):9733–9739, 1996.

[143] SM Skoff, RJ Hendricks, CDJ Sinclair, JJ Hudson, DM Segal, BE Sauer, EA Hinds, and MR Tarbutt. Diffusion, thermalization, and optical pumping of YbF molecules in a cold buffer-gas cell. *Phys. Rev. A*, 83(2):023418, 2011.

[144] MD Di Rosa. Laser-cooling molecules. *Eur. Phys. J. D*, 31(2):395–402, 2004.

[145] LR Hunter, SK Peck, AS Greenspon, S Saad Alam, and D DeMille. Prospects for laser cooling TlF. *Phys. Rev. A*, 85(1):012511, 2012.

[146] TE Wall, JF Kanem, JJ Hudson, BE Sauer, D Cho, MG Boshier, EA Hinds, and MR Tarbutt. Lifetime of the A($v = 0$) state and Franck-Condon factor of the A-X(0-0) transition of CaF measured by the saturation of laser-induced fluorescence. *Phys. Rev. A*, 78(6):062509, 2008.

[147] Xiujuan Zhuang, Anh Le, Timothy C Steimle, NE Bulleid, IJ Smallman, RJ Hendricks, SM Skoff, JJ Hudson, BE Sauer, EA Hinds, et al. Franck–Condon factors and radiative lifetime of the $A2\Pi_1/2$–$X2\Sigma_+$ transition of ytterbium monofluoride, YbF. *Phys. Chem. Chem. Phys.*, 13(42):19013–19017, 2011.

[148] Christopher J Foot. *Atomic Physics*. New York: Oxford University Press, 2004.

[149] I Kozyryev, L. Baum, K. Matsuda, P. Olson, B. Hemmerling, and J. M. Doyle. Supplementary Material, 2015.

[150] Michael David Oberlander. *Laser excited fluorescence studies of reactions of group 2 metals with oxygen containing molecules and of heavy group 15 clusters with fluorine*. PhD thesis, Ohio State University, 1995.

[151] RW Nicholls. Franck-Condon factor formulae for astrophysical and other molecules. *Astrophys. J. Suppl. S.*, 47:279–290, 1981.

[152] J-G Wang, MJ Dick, PM Sheridan, S Yu, and PF Bernath. Further spectroscopic investigations of the high energy electronic states of SrOH. *J. Mol. Spec.*, 245(1):26–33, 2007.

[153] John F Barry. *Laser cooling and slowing of a diatomic molecule*. PhD thesis, Yale University, 2013.

[154] E S Shuman, J F Barry, D R Glenn, and D DeMille. Radiative force from optical cycling on a diatomic molecule. *Physical Review Letters*, 103(22):223001, 2009.

[155] D. Egorov. *Buffer-gas cooling of diatomic molecules*. PhD thesis, Harvard University, 2004.

[156] Edem Tsikata, WC Campbell, MT Hummon, Hsin-I Lu, and J M Doyle. Magnetic trapping of NH molecules with 20 s lifetimes. *New J. Phys.*, 12(6):065028, 2010.

[157] Hsin-I Lu. *Magnetic trapping of molecules via optical loading and magnetic slowing*. PhD thesis, Harvard University, 2013.

[158] Dmitry Budker, Derek F Kimball, and David P DeMille. *Atomic physics: an exploration through problems and solutions*. Oxford University Press, USA, 2004.

[159] J. F. Barry, E. S. Shuman, and D. DeMille. A bright, slow cryogenic molecular beam source for free radicals. *Phys. Chem. Chem. Phys.*, 13:18936–18947, 2011.

[160] Peter F Bernath. Spectroscopy and photochemistry of polyatomic alkaline earth containing molecules. *Adv. Photochem.*, 23:1–62, 1997.

[161] Mark Yeo. *The Laser Cooling and Magneto-Optical Trapping of the YO Molecule*. PhD thesis, the University of Colorado, Boulder, 2015.

[162] Nikolai Kiesel, Florian Blaser, Uroš Delić, David Grass, Rainer Kaltenbaek, and Markus Aspelmeyer. Cavity cooling of an optically levitated submicron particle. *Proc. Natl. Acad. Sci. U.S.A.*, 110(35):14180–14185, 2013.

[163] Peter Asenbaum, Stefan Kuhn, Stefan Nimmrichter, Ugur Sezer, and Markus Arndt. Cavity cooling of free silicon nanoparticles in high vacuum. *Nat. Comm.*, 4, 2013.

[164] RW Peterson, TP Purdy, NS Kampel, RW Andrews, P-L Yu, KW Lehnert, and CA Regal. Laser cooling of a micromechanical membrane to the quantum backaction limit. *Phys. Rev. Lett.*, 116(6):063601, 2016.

[165] Jasper Chan, TP Mayer Alegre, Amir H Safavi-Naeini, Jeff T Hill, Alex Krause, Simon Gröblacher, Markus Aspelmeyer, and Oskar Painter. Laser cooling of a nanomechanical oscillator into its quantum ground state. *Nature*, 478(7367):89–92, 2011.

[166] Sandra Eibenberger, Xiaxi Cheng, JP Cotter, and Markus Arndt. Absolute absorption cross sections from photon recoil in a matter-wave interferometer. *Phys. Rev. Lett.*, 112(25):250402, 2014.

[167] Henrik Stapelfeldt, Hirofumi Sakai, E Constant, and Paul B Corkum. Deflection of neutral molecules using the nonresonant dipole force. *Phys. Rev. Lett.*, 79(15):2787, 1997.

[168] Rosa Glöckner, Alexander Prehn, Barbara GU Englert, Gerhard Rempe, and Martin Zeppenfeld. Rotational cooling of trapped polyatomic molecules. *Phys. Rev. Lett.*, 115(23):233001, 2015.

[169] John M Brown and Flemming Jørgensen. Vibronic energy levels of a linear triatomic molecule in a degenerate electronic state: a unified treatment of the Renner-Teller effect. *Adv. Chem. Phys.*, 52:117–180, 1983.

[170] Harold J Metcalf and Peter Van der Straten. *Laser cooling and trapping*. Springer Science & Business Media, 2012.

[171] EB Norrgard, DJ McCarron, MH Steinecker, MR Tarbutt, and D DeMille. Submillikelvin dipolar molecules in a radio-frequency magneto-optical trap. *Phys. Rev. Lett.*, 116(6):063004, 2016.

[172] Ye Cunyun. *Tunable external cavity diode lasers*. Hackensack: World Scientific, 2004.

[173] DJ Berkeland and MG Boshier. Destabilization of dark states and optical spectroscopy in Zeeman-degenerate atomic systems. *Phys. Rev. A*, 65(3):033413, 2002.

[174] Ivan Kozyryev, Louis Baum, Kyle Matsuda, Peter Olson, Boerge Hemmerling, and John M Doyle. Collisional relaxation of vibrational states of SrOH with He at 2 K. *New J. Phys.*, 17(4):045003, 2015.

[175] Boerge Hemmerling, Eunmi Chae, Aakash Ravi, Loic Anderegg, Garrett K Drayna, Nicholas R Hutzler, Alejandra L Collopy, Jun Ye, Wolfgang Ketterle, and John M Doyle. Laser slowing of CaF molecules to near the capture velocity of a molecular MOT. *J. Phys. B: At. Mol. Opt. Phys.*, 49:174001, 2016.

[176] John Rice. *Mathematical statistics and data analysis*. Belmont: Thomson Higher Education, 3rd edition, 2010.

[177] Trung Nguyen, Damian L. Kokkin, Timothy Steimle, Ivan Kozyryev, and John M. Doyle. The optical spectrum of SrOH re-visited: Zeeman effect, high-resolution spectrscopy and Franck-Condon factors. In *International Symposium on Molecular Spectroscopy*, 2015.

[178] Gad Fischer. *Vibronic coupling: The interaction between the electronic and nuclear motions*. New York: Academic Press, 1984.

[179] MA Chieda and EE Eyler. Prospects for rapid deceleration of small molecules by optical bichromatic forces. *Phys. Rev. A*, 84(6):063401, 2011.

[180] L Aldridge, SE Galica, and EE Eyler. Simulations of the bichromatic force in multilevel systems. *Phys. Rev. A*, 93(1):013419, 2016.

[181] SE Galica, L Aldridge, and EE Eyler. Four-color stimulated optical forces for atomic and molecular slowing. *Phys. Rev. A*, 88(4):043418, 2013.

[182] CR Brazier, LC Ellingboe, S Kinsey-Nielsen, and PF Bernath. Laser spectroscopy of alkaline earth monoalkoxide free radicals. *J. Am. Chem. Soc.*, 108(9):2126–2132, 1986.

[183] Benjamin K Stuhl, Brian C Sawyer, Dajun Wang, and Jun Ye. Magneto-optical trap for polar molecules. *Phys. Rev. Lett.*, 101(24):243002, 2008.

[184] JF Barry, DJ McCarron, EB Norrgard, MH Steinecker, and D DeMille. Magneto-optical trapping of a diatomic molecule. *Nature*, 512(7514):286–289, 2014.

[185] DJ McCarron, EB Norrgard, MH Steinecker, and D DeMille. Improved magneto–optical trapping of a diatomic molecule. *New J. Phys.*, 17(3):035014, 2015.

[186] S Truppe, HJ Williams, M Hambach, L Caldwell, NJ Fitch, EA Hinds, BE Sauer, and MR Tarbutt. Molecules cooled below the Doppler limit. *arXiv preprint arXiv:1703.00580*, 2017.

[187] L. Anderegg, B. L. Augenbraun, E. Chae, N. R. Hutzler, A. Ravi, A. L. Collopy, J. Ye, W. Ketterle, and J. M. Doyle. Radio-frequency and DC dual frequency magneto-optical trapping of CaF. *to be submitted*, 2017.

[188] Ivan Kozyryev, Louis Baum, Kyle Matsuda, Boerge Hemmerling, and John M Doyle. Radiation pressure force from optical cycling on a polyatomic molecule. *J. Phys. B: At. Mol. Opt. Phys.*, 49(13):134002, 2016.

[189] Olivier Emile, Robin Kaiser, Christoph Gerz, Hartmut Wallis, Alain Aspect, and Claude Cohen-Tannoudji. Magnetically assisted Sisyphus effect. *J. Phys. II France*, 3(12):1709–1733, 1993.

[190] B Sheehy, SQ Shang, P Van Der Straten, S Hatamian, and H Metcalf. Magnetic-field-induced laser cooling below the doppler limit. *Phys. Rev. Lett.*, 64(8):858, 1990.

[191] A Aspect, J Dalibard, A Heidmann, C Salomon, and C Cohen-Tannoudji. Cooling atoms with stimulated emission. *Phys. Rev. Lett.*, 57(14):1688, 1986.

[192] S Padua, C Xie, R Gupta, Herman Batelaan, T Bergeman, and H Metcalf. Transient laser cooling. *Phys. Rev. Lett.*, 70(21):3217, 1993.

[193] Martin Zeppenfeld, Michael Motsch, Pepijn WH Pinkse, and Gerhard Rempe. Optoelectrical cooling of polar molecules. *Phys. Rev. A*, 80(4):041401, 2009.

[194] Paul D Lett, William D Phillips, SL Rolston, Carol E Tanner, RN Watts, and CI Westbrook. Optical molasses. *J. Opt. Soc. Am. B*, 6(11):2084–2107, 1989.

[195] MR Tarbutt, BE Sauer, JJ Hudson, and EA Hinds. Design for a fountain of ybf molecules to measure the electron's electric dipole moment. *New J. Phys.*, 15(5):053034, 2013.

[196] R Gupta, S Padua, C Xie, Herman Batelaan, and H Metcalf. Simplest atomic system for sub-Doppler laser cooling. *J. Opt. Soc. Am. B*, 11(4):537–541, 1994.

[197] M Prentiss and A Cable. Slowing and cooling an atomic beam using an intense optical standing wave. *Phys. Rev. Lett.*, 62(12):1354, 1989.

[198] SQ Shang, B Sheehy, H Metcalf, P Van der Straten, and G Nienhuis. Velocity-selective resonances and sub-Doppler laser cooling. *Phys. Rev. Lett.*, 67(9):1094, 1991.

[199] MD Hoogerland, HFP De Bie, HCW Beijerinck, EJD Vredenbregt, KAH Van Leeuwen, P Van der Straten, and HJ Metcalf. Force, diffusion, and channeling in sub-doppler laser cooling. *Phys. Rev. A*, 54(4):3206, 1996.

[200] B Klöter, C Weber, D Haubrich, D Meschede, and H Metcalf. Laser cooling of an indium atomic beam enabled by magnetic fields. *Phys. Rev. A*, 77(3):033402, 2008.

[201] JA Devlin and MR Tarbutt. Three-dimensional Doppler, polarization-gradient, and magneto-optical forces for atoms and molecules with dark states. *New J. Phys*, 18:123017, 2016.

[202] A Aspect, R Kaiser, N Vansteenkiste, and CI Westbrook. Laser manipulation of neutral atoms. *Phys. Scripta*, 1995(T58):69, 1995.

[203] Alain Aspect. Manipulation of neutral atoms. Experiments. *Phys. Rep.*, 219(3):141–152, 1992.

[204] Harold J Metcalf and Peter van der Straten. Laser cooling and trapping of atoms. *J. Opt. Soc. Am. B*, 20(5):887–908, 2003.

[205] Claude Cohen-Tannoudji. Laser cooling and trapping of neutral atoms: theory. *Phys. Rep.*, 219(3-6):153–164, 1992.

[206] Jean Dalibard and Claude Cohen-Tannoudji. Laser cooling below the doppler limit by polarization gradients: simple theoretical models. *J. Opt. Soc. Am. B*, 6(11):2023–2045, 1989.

[207] MD Hoogerland, HCW Beijerinck, KAH van Leeuwen, P van der Straten, and HJ Metcalf. Magnetically induced laser cooling for Ne*: approaching the recoil limit. *Europhys. Lett.*, 19(8):669, 1992.

[208] B Sheehy, S-Q Shang, P Van Der Straten, and H Metcalf. Collimation of a rubidium beam below the Doppler limit. *Chem. Phys.*, 145(2):317–325, 1990.

[209] MD Hoogerland, JPJ Driessen, EJD Vredenbregt, HJL Megens, MP Schuwer, HCW Beijerinck, and KAH Van Leeuwen. Bright thermal atomic beams by laser cooling: A 1400-fold gain in beam flux. *Appl. Phys. B*, 62(4):323–327, 1996.

[210] J Söding, R Grimm, Yu B Ovchinnikov, Ph Bouyer, and Ch Salomon. Short-distance atomic beam deceleration with a stimulated light force. *Phys. Rev. Lett.*, 78(8):1420, 1997.

[211] H Ball, MW Lee, SD Gensemer, and MJ Biercuk. A high-power 626 nm diode laser system for Beryllium ion trapping. *Rev. Sci. Instrum.*, 84(6):063107, 2013.

[212] I Kozyryev, L. Baum, K. Matsuda, and J. M. Doyle. Proposal for laser cooling of complex polyatomic molecules. *ChemPhysChem*, 17:3641, 2016.

[213] Kazuya Yamashita, Kouhei Hanasaki, Akihiro Ando, Masahiro Takahama, and Toshiya Kinoshita. All-optical production of a large Bose-Einstein condensate in a double compressible crossed dipole trap. *Phys. Rev. A*, 95(1):013609, 2017.

[214] J Lee, J Chen, LV Skripnikov, AN Petrov, AV Titov, NS Mosyagin, and AE Leanhardt. Optical spectroscopy of tungsten carbide for uncertainty analysis in electron electric-dipole-moment search. *Phys. Rev. A*, 87(2):022516, 2013.

[215] R Grimm, Yu B Ovchinnikov, AI Sidorov, and VS Letokhov. Observation of a strong rectified dipole force in a bichromatic standing light wave. *Phys. Rev. Lett.*, 65(12):1415, 1990.

[216] Harold J Metcalf and Peter Van der Straten. *Laser cooling and trapping*. Springer Science & Business Media, 2012.

[217] MA Chieda and EE Eyler. Prospects for rapid deceleration of small molecules by optical bichromatic forces. *Phys. Rev. A*, 84(6):063401, 2011.

[218] Leonid Yatsenko and Harold Metcalf. Dressed-atom description of the bichromatic force. *Phys. Rev. A*, 70(6):063402, 2004.

[219] Leland Aldridge. *The Bichromatic Force in Multi-Level Systems*. PhD thesis, University of Connecticut, 2016.

[220] A.M. Jayich, A.C. Vutha, M.T. Hummon, J.V. Porto, and W.C Campbell. Continuous all-optical deceleration and single-photon cooling of molecular beams. *Physical Review A*, 89:023425, 2014.

[221] A Goepfert, I Bloch, D Haubrich, F Lison, R Schütze, R Wynands, and D Meschede. Stimulated focusing and deflection of an atomic beam using picosecond laser pulses. *Phys. Rev. A*, 56(5):R3354, 1997.

[222] Martin E Carrera-Patio and R Stephen Berry. Entropy production in stopping atoms with laser light. *Phys. Rev. A*, 34(6):4728, 1986.

[223] SJ Van Enk and G Nienhuis. Entropy production and kinetic effects of light. *Phys. Rev. A*, 46(3):1438, 1992.

[224] Harold Metcalf. Entropy exchange in laser cooling. *Phys. Rev. A*, 77(6):061401, 2008.

[225] M Partlow, X Miao, J Bochmann, M Cashen, and H Metcalf. Bichromatic slowing and collimation to make an intense helium beam. *Phys. Rev. Lett.*, 93(21):213004, 2004.

[226] P Bouyer, P Lemonde, M Ben Dahan, A Michaud, C Salomon, and J Dalibard. An atom trap relying on optical pumping. *EPL*, 27(8):569, 1994.

[227] AML Oien, IT McKinnie, PJ Manson, WJ Sandle, and DM Warrington. Cooling mechanisms in the sodium type-II magneto-optical trap. *Phys. Rev. A*, 55(6):4621, 1997.

[228] Benjamin K Stuhl, Brian C Sawyer, Dajun Wang, and Jun Ye. Magneto-optical trap for polar molecules. *Phys. Rev. Lett.*, 101(24):243002, 2008.

[229] John Barry, Daniel McCarron, Eric Norrgard, Matthew Steinecker, and David DeMille. Magneto-optical trapping of a diatomic molecule. *Nature*, 512:286–289, 2014.

[230] MR Tarbutt. Magneto-optical trapping forces for atoms and molecules with complex level structures. *New J. Phys.*, 17(1):015007, 2015.

[231] Eunmi Chae, Loic Anderegg, Benjamin L Augenbraun, Aakash Ravi, Boerge Hemmerling, Nicholas R Hutzler, Alejandra L Collopy, Jun Ye, Wolfgang Ketterle, and John M Doyle. One-dimensional magneto-optical compression of a cold caf molecular beam. *New J. Phys.*, 19(3):033035, 2017.

[232] Peter F Bernath. Spectroscopy and photochemistry of polyatomic alkaline earth containing molecules. *Adv. Photochem.*, 23:1–62, 1997.

[233] MR Tarbutt. Magneto-optical trapping forces for atoms and molecules with complex level structures. *New J. Phys.*, 17(1):015007, 2015.

[234] CR Brazier and PF Bernath. Laser and fourier transform spectroscopy of the a-x transition of sroh. *J. Mol. Spectrosc.*, 114(1):163–173, 1985.

[235] Immanuel Bloch. Ultracold quantum gases in optical lattices. *Nat. Phys.*, 1(1):23–30, 2005.

[236] Mingwu Lu, Nathaniel Q Burdick, and Benjamin L Lev. Quantum degenerate dipolar fermi gas. *Phys. Rev. Lett.*, 108(21):215301, 2012.

[237] K Aikawa, A Frisch, M Mark, S Baier, A Rietzler, R Grimm, and F Ferlaino. Bose-Einstein condensation of erbium. *Phys. Rev. Lett.*, 108(21):210401, 2012.

[238] Andrew D Ludlow, Martin M Boyd, Jun Ye, Ekkehard Peik, and Piet O Schmidt. Optical atomic clocks. *Rev. Mod. Phys.*, 87(2):637, 2015.

[239] Andrew D Ludlow and Jun Ye. Progress on the optical lattice clock. *C. R. Phys.*, 16(5):499–505, 2015.

[240] Mark Saffman, TG Walker, and Klaus Mølmer. Quantum information with rydberg atoms. *Rev. Mod. Phys.*, 82(3):2313, 2010.

[241] Iulia Buluta, Sahel Ashhab, and Franco Nori. Natural and artificial atoms for quantum computation. *Rep. Prog. Phys.*, 74(10):104401, 2011.

[242] Lawrence W Cheuk, Matthew A Nichols, Melih Okan, Thomas Gersdorf, Vinay V Ramasesh, Waseem S Bakr, Thomas Lompe, and Martin W Zwierlein. Quantum-gas microscope for fermionic atoms. *Phys. Rev. Lett.*, 114(19):193001, 2015.

[243] Ahmed Omran, Martin Boll, Timon A Hilker, Katharina Kleinlein, Guillaume Salomon, Immanuel Bloch, and Christian Gross. Microscopic observation of pauli blocking in degenerate fermionic lattice gases. *Phys. Rev. Lett.*, 115(26):263001, 2015.

[244] Immanuel Bloch, Jean Dalibard, and Sylvain Nascimbene. Quantum simulations with ultracold quantum gases. *Nat. Phys.*, 8(4):267–276, 2012.

[245] IM Georgescu, S Ashhab, and Franco Nori. Quantum simulation. *Rev. Mod. Phys.*, 86(1):153, 2014.

[246] Denis V Seletskiy, Seth D Melgaard, Stefano Bigotta, Alberto Di Lieto, Mauro Tonelli, and Mansoor Sheik-Bahae. Laser cooling of solids to cryogenic temperatures. *Nat. Photon.*, 4(3):161–164, 2010.

[247] Galina Nemova and Raman Kashyap. Laser cooling of solids. *Rep. Prog. Phys.*, 73(8):086501, 2010.

[248] J F Barry, E S Shuman, E B Norrgard, and D Demille. Laser radiation pressure slowing of a molecular beam. *Phys. Rev. Lett.*, 108:103002, 2012.

[249] S Truppe, H Williams, M Hambach, N Fitch, TE Wall, EA Hinds, BE Sauer, and MR Tarbutt. A bright, cold, velocity-controlled molecular beam by frequency-chirped laser slowing. *arXiv preprint arXiv:1605.06055*, 2016.

[250] I Kozyryev, L. Baum, K. Matsuda, Benjamin L Augenbraun, L. Anderegg, Alex Sedlack, and John M. Doyle. Sisyphus laser cooling of a polyatomic molecule. *Phys. Rev. Lett.*, 118:173201, 2017.

[251] YV Stadnik and VV Flambaum. Can dark matter induce cosmological evolution of the fundamental constants of Nature? *Phys. Rev. Lett.*, 115(20):201301, 2015.

[252] Ken Van Tilburg, Nathan Leefer, Lykourgos Bougas, and Dmitry Budker. Search for ultralight scalar dark matter with atomic spectroscopy. *Phys. Rev. Lett.*, 115(1):011802, 2015.

[253] Eduardo Berrios, Martin Gruebele, Dmytro Shyshlov, Lei Wang, and Dmitri Babikov. High fidelity quantum gates with vibrational qubits. *J. Phys. Chem. A*, 116(46):11347–11354, 2012.

[254] Martin Quack. *Fundamental symmetries and symmetry violations from high-resolution spectroscopy*, volume 1. Wiley Online Library, 2011.

[255] Yuan-Pin Chang, Daniel A Horke, Sebastian Trippel, and Jochen Küpper. Spatially-controlled complex molecules and their applications. *Int. Rev. Phys. Chem.*, 34(4):557–590, 2015.

[256] Hendrick L Bethlem, Floris MH Crompvoets, Rienk T Jongma, Sebastiaan YT van de Meerakker, and Gerard Meijer. Deceleration and trapping of ammonia using time-varying electric fields. *Phys. Rev. A*, 65(5):053416, 2002.

[257] Takamasa Momose, Yang Liu, Sida Zhou, Pavle Djuricanin, and David Carty. Manipulation of translational motion of methyl radicals by pulsed magnetic fields. *Phys. Chem. Chem. Phys.*, 15(6):1772–1777, 2013.

[258] R Fulton, Alexis I Bishop, and Peter F Barker. Optical Stark decelerator for molecules. *Phys. Rev. Lett.*, 93(24):243004, 2004.

[259] Sotir Chervenkov, Xing Wu, Josef Bayerl, A Rohlfes, Thomas Gantner, Martin Zeppenfeld, and Gerhard Rempe. Continuous centrifuge decelerator for polar molecules. *Phys. Rev. Lett.*, 112(1):013001, 2014.

[260] David Patterson and John M Doyle. A slow, continuous beam of cold benzonitrile. *Phys. Chem. Chem. Phys.*, 17(7):5372–5375, 2015.

[261] Ben Spaun, P Bryan Changala, David Patterson, Bryce J Bjork, Oliver H Heckl, John M Doyle, and Jun Ye. Continuous probing of cold complex molecules with infrared frequency comb spectroscopy. *Nature*, 533(7604):517–520, 2016.

[262] MolView, 2016.

[263] LC O'Brien, CR Brazier, and PF Bernath. High-resolution laser spectroscopy of strontium monomethoxide, sroch3. *J. Mol. Spec.*, 130(1):33–45, 1988.

[264] D Forthomme, C Linton, AG Read, DW Tokaryk, AG Adam, LE Downie, AD Granger, and WS Hopkins. Unravelling the visible spectrum of strontium monomethoxide. *J. Mol. Spec.*, 270(2):108–115, 2011.

[265] P Crozet, F Martin, AJ Ross, C Linton, MJ Dick, and AG Adam. The $\tilde{A}^2$E–$\tilde{X}^2$A$_1$ system of $CaOCH_3$. *J. Mol. Spec.*, 213(1):28–34, 2002.

[266] M Elhanine, R Lawruszczuk, and B Soep. Laser spectroscopy of metallic free radicals: the observation of the C–X vibronically allowed electronic transition for Ca–OCH_3, Ca–OC_2H_5 and Ca–CCH. *Chem. Phys. Lett.*, 288(5):785–792, 1998.

[267] Paul J Dagdigian, Howard W Cruse, and Richard N Zare. Radiative lifetimes of the alkaline earth monohalides. *J. Chem. Phys.*, 60(6):2330–2339, 1974.

[268] E Bright Wilson, John Courtney Decius, and Paul C Cross. *Molecular Vibrations: The Theory of Infrared and Raman Vibrational Spectra*. New York: Dover Publications, 1955.

[269] I Kozyryev, L. Baum, K. Matsuda, and John M. Doyle. Supporting information for proposal for laser cooling of complex polyatomic molecules. *ChemPhysChem*, 17(22), 2016.

[270] RF Wormsbecher and RD Suenram. Laser spectroscopy and chemiluminescence from the monomethoxides of Ca, Sr, and Ba. *J. Mol. Spec.*, 95(2):391–404, 1982.

[271] Saibei Zhao and SN Ghosh. Vibrational frequency and force field constant calculation of CH_3OH and its 9 isotopomers by GF matrix method. *Int. J. Infrared Millimeter Waves*, 16(3):547–577, 1995.

[272] CJ Whitham, SA Beaton, Y Ito, and JM Brown. Laser excitation spectroscopy of the $\tilde{B}^2A_1$–$\tilde{X}^2A_1$ transition of the $CaOCH_3$ radical. *J. Mol. Spec.*, 191(2):286–294, 1998.

[273] Wencui Peng, Lin Zhou, Shitong Long, Jin Wang, and Mingsheng Zhan. Locking laser frequency of up to 40 GHz offset to a reference with a 10 GHz electro-optic modulator. *Opt. Lett.*, 39(10):2998–3001, 2014.

[274] PM Sheridan, MJ Dick, J-G Wang, and PF Bernath. High-resolution spectroscopic investigation of the $\tilde{B}^2A_1$–$\tilde{X}^2A_1$ transitions of $CaCH_3$ and $SrCH_3$. *J. Phys. Chem. A*, 109(46):10547–10553, 2005.

[275] Kei Ichi C Namiki, J Scott Robinson, and Timothy Steimle. A spectroscopic study of $CaOCH_3$ using the pump/probe microwave and the molecular beam/optical Stark techniques. *J. Chem. Phys.*, 109(13):5283–5289, 1998.

[276] Chien-Yu Lien, Christopher M Seck, Yen-Wei Lin, Jason HV Nguyen, David A Tabor, and Brian C Odom. Broadband optical cooling of molecular rotors from room temperature to the ground state. *Nat. Commun.*, 5, 2014.

[277] Matthieu Viteau, Amodsen Chotia, Maria Allegrini, Nadia Bouloufa, Olivier Dulieu, Daniel Comparat, and Pierre Pillet. Optical pumping and vibrational cooling of molecules. *Science*, 321(5886):232–234, 2008.

[278] D Egorov, WC Campbell, Bretislav Friedrich, SE Maxwell, E Tsikata, LD van Buuren, and JM Doyle. Buffer-gas cooling of NH via the beam loaded buffer-gas method. *EPJ D*, 31(2):307–311, 2004.

[279] Eric R Hudson, HJ Lewandowski, Brian C Sawyer, and Jun Ye. Cold molecule spectroscopy for constraining the evolution of the fine structure constant. *Phys. Rev. Lett.*, 96(14):143004, 2006.

[280] Ian C Lane. Ultracold hydrogen and deuterium production via Doppler-cooled Feshbach molecules. *Phys. Rev. A*, 92:022511, 2015.

[281] Ian C Lane. Ultracold fluorine production via doppler cooled bef. *Phys. Chem. Chem. Phys.*, 14(43):15078–15087, 2012.

[282] Mingkai Fu, Haitao Ma, Jianwei Cao, and Wensheng Bian. Extensive theoretical study on electronically excited states of calcium monochloride: Molecular laser cooling and production of ultracold chlorine atoms. *J. Chem. Phys.*, 144(18):184302, 2016.

[283] Nathan Wells and Ian C Lane. Prospects for ultracold carbon via charge exchange reactions and laser cooled carbides. *Phys. Chem. Chem. Phys.*, 13(42):19036–19051, 2011.

[284] Dale G Fried, Thomas C Killian, Lorenz Willmann, David Landhuis, Stephen C Moss, Daniel Kleppner, and Thomas J Greytak. Bose-einstein condensation of atomic hydrogen. *Phys. Rev. Lett.*, 81(18):3811, 1998.

[285] Benjamin K Stuhl, Matthew T Hummon, Mark Yeo, Goulven Quéméner, John L Bohn, and Jun Ye. Evaporative cooling of the dipolar hydroxyl radical. *Nature*, 492(7429):396–400, 2012.

[286] Heinz G Floss and Sungsook Lee. Chiral methyl groups: small is beautiful. *Acc. Chem. Res.*, 26(3):116–122, 1993.

[287] JW Cornforth and JW Redmond. Asymmetric methyl groups, and the mechanism of malate synthase. *Nature*, 221:1212–1213, 1969.

[288] J Lüthy, J Retey, and D Arigoni. Preparation and detection of chiral methyl groups. *Nature*, 221(5187):1213, 1969.

[289] Anna Schweifer and Friedrich Hammerschmidt. Formal and improved synthesis of enantiopure chiral methanol. *Tetrahedron*, 64(32):7605–7610, 2008.

[290] Robert Berger, Martin Quack, Achim Sieben, and Martin Willeke. Parity-violating potentials for the torsional motion of methanol (CH_3OH) and its isotopomers (CD_3OH, $^{13}CH_3OH$, CH_3OD, CH_3OT, CHD_2OH, and CHDTOH). *Helv. Chim. Acta*, 86(12):4048–4060, 2003.

[291] Katherine C Thompson and Paula Margey. Hydrogen bonded complexes between nitrogen dioxide, nitric acid, nitrous acid and water with SiH_3OH and $Si(OH)_4$. *Phys. Chem. Chem. Phys.*, 5(14):2970–2975, 2003.

[292] Mark S Gordon, Robert Damrauer, and Michèle Krempp. Gas-phase acidity computations of silanols and their sulfur analogs. *J. Phys. Chem.*, 97(30):7820–7822, 1993.

[293] Robert Damrauer, Roger Simon, and Michele Krempp. Effect of substituents on the gas-phase acidity of silanols. *J. Am. Chem. Soc.*, 113(12):4431–4435, 1991.

[294] Hiroshi Kumagai. Development of a continuous-wave, deep-ultraviolet, and single-frequency coherent light source-challenges toward laser cooling of silicon. *IEEE J. Quantum Electron.*, 10(6):1252–1258, 2004.

[295] MR Tarbutt and TC Steimle. Modeling magneto-optical trapping of CaF molecules. *Phys. Rev. A*, 92(5):053401, 2015.

[296] A.M. Jayich, A.C. Vutha, M.T. Hummon, J.V. Porto, and W.C Campbell. Continuous all-optical deceleration and single-photon cooling of molecular beams. *Physical Review A*, 89:023425, 2014.

[297] Ekaterina Ilinova, Jonathan Weinstein, and Andrei Derevianko. Stimulated deceleration of diatomic molecules on multiple rovibrational transitions with coherent pulse trains. *New J. Phys.*, 17(5):055003, 2015.

[298] TV Tscherbul, TA Grinev, H-G Yu, A Dalgarno, Jacek Kłos, Lifang Ma, and Millard H Alexander. Cold collisions of polyatomic molecular radicals with S-state atoms in a magnetic field: An ab initio study of He+$CH_2(\tilde{X})$ collisions. *Journal of Chemical Physics*, 137:104302, 2012.

[299] Xiujuan Zhuang, Anh Le, Timothy C Steimle, Ramya Nagarajan, Varun Gupta, and John P Maier. Visible spectrum of titanium dioxide. *Phys. Chem. Chem. Phys.*, 12(45):15018–15028, 2010.

[300] Anh Le, Timothy C Steimle, Varun Gupta, Corey A Rice, John P Maier, Sheng H Lin, and Chih-Kai Lin. The visible spectrum of zirconium dioxide, ZrO_2. *J. Chem. Phys.*, 135(10):104303, 2011.

[301] George B Arfken and Hans J Weber. *Mathematical methods for physicists*. Boston: Elsevier, 1999.

[302] A.V. Gorokhov. Franck-condon integrals for linear-bent absorptive trnasitions in triatomic molecules. *Izvestiya Vysshikh Uchebnyhk Zavedenii Fizika*, 1971.

[303] JM Brown. The effective Hamiltonian for the Renner-Teller effect. *J. Mol. Spec.*, 68(3):412–422, 1977.

[304] PSH Bolman and JM Brown. The Renner-Teller effect and vibronically induced bands in the electronic spectrum of NCO. *Chem. Phys. Lett.*, 21(2):213–216, 1973.

[305] J. A. Coxon, M. Li, and P. I. Presunka. Laser spectroscopy of the $(010)^2\Sigma^+,^2\Sigma^- - -$ $(000)^2\Sigma^+$ parallel bands in the $\tilde{A}^2\Pi - \tilde{X}^2\Sigma^+$ system of CaOH. *J. Mol. Spec.*, 164:118–128, 1994.